Flame-Wall Interactions at Elevated Pressure Studied with Advanced Laser Diagnostics

Vom Fachbereich Maschinenbau
der Technischen Universität Darmstadt

zur Erlangung des Grades eines
Doktors der Ingenieurwissenschaften (Dr.-Ing.)
genehmigte

D i s s e r t a t i o n

von

Pascal Johe, M.Sc.

aus Mainz

Berichterstatter:	Prof. Dr. habil. Andreas Dreizler
Mitberichterstatter:	Prof. Dr.-Ing. Dirk Geyer
Tag der Einreichung:	23. Januar 2024
Tag der mündlichen Prüfung:	23. April 2024

Darmstadt 2024

Johe, Pascal:
"Flame-Wall Interactions at Elevated Pressure Studied with Advanced Laser Diagnostics"

Darmstadt, Technische Universität Darmstadt

Jahr der Veröffentlichung der Dissertation auf TUprints: 2024

URN: urn:nbn:de:tuda-tuprints-273590
URI: https://tuprints.ulb.tu-darmstadt.de/id/eprint/27359

Tag der mündlichen Prüfung: 23.04.2024

Erklärung

Hiermit erkläre ich an Eides statt, dass ich die vorliegende Dissertation selbstständig verfasst und keine anderen als die von mir angegebenen Hilfsmittel verwendet habe. Ich erkläre außerdem, dass ich bisher noch keinen Promotionsversuch unternommen habe.

Pascal Johe Darmstadt, den 16. Januar 2024

Danksagung

Nach fünf ereignisreichen, teils anstrengenden, lehrreichen und vor allem schönen Jahren als Wissenschaftlicher Mitarbeiter am Institut für Reaktive Strömungen und Messtechnik möchte ich an dieser Stelle meine große Dankbarkeit gegenüber einer Reihe an Personen ausdrücken, die mich auf diesem Weg begleitet, unterstützt und somit zu dieser Dissertation beigetragen haben.

Ganz zu Beginn möchte mich herzlichst bedanken bei meinem Doktorvater und fachlichem Betreuer Prof. Dr. habil. Andreas Dreizler, dafür dass er es mir ermöglicht hat, solch einer spannenden und erfüllenden Forschungstätigkeit in einem überaus angenehmen und produktiven Arbeitsumfeld nachgehen zu können. Seine Unterstützung durch die vielen Gespräche, Ratschläge und Diskussionen, für die er sich immer Zeit genommen hat, waren von unschätzbarem Wert. Weiterhin gilt mein großer Dank Prof. Dr.-Ing. Dirk Geyer, Leiter des Labors für Optische Diagnosemethoden und Erneuerbare Energien an der Hochschule Darmstadt, für die Übernahme des Koreferats dieser Dissertation.

Zudem möchte ich mich bei meinen Kolleginnen und Kollegen bedanken für die durchweg freundliche und solidarische Arbeitsatmosphäre, welche stets durch die Bereitschaft zur gegenseitigen Unterstützung geprägt war. Besonders hervorheben möchte ich an dieser Stelle meine beiden Vorgänger am Fachgebiet. Bei Dr.-Ing. Florian Zentgraf möchte ich mich herzlichst bedanken für die umfassende thematische Einarbeitung, die vielen wertvollen Tipps für die Laborarbeit, seine Unterstützung beim Messbetrieb, sein hilfreiches Feedback zu Publikationen sowie für die vielen fachlichen Diskussionen und privaten Gespräche. Dankbar bin ich zudem Dr.-Ing. Max Greifenstein für die umfängliche Einweisung in den Betrieb des Druckbrennerkammerprüfstandes mit all seinen Eigenheiten sowie für seinen fachlichen Rat bei verschiedensten Fragestellungen.

Weiterhin möchte ich mich bedanken bei dem Sekretariatskollegium, namentlich Marion Müller und Angela Berger, für die Unterstützung in organisatorischen Fragen, sowie bei dem gesamten IT-Team, für die Fortentwicklung und Instandhaltung der IT-Infrastruktur, von der ich sehr profitiert habe. Zu großem Dank verpflichtet bin ich darüber hinaus dem Team der feinmechanischen Werkstatt des RSM um Roland Berntheisel und Dirk Feldmann. Durch ihre hervorragenden Arbeit bei der Fertigung des Prüfstandes, welcher für die durchgeführten Untersuchungen genutzt wurde, haben sie einen wichtigen Teil zu dieser Arbeit beigetragen.

Zum Schluss möchte ich mich bei meiner Familie, meinen Eltern Sabine und Axel, sowie meinem Bruder Patrick, für die fortwährende Unterstützung während meiner langjährigen Ausbildung und in allen Lebensbereichen bedanken. Besonders dankbar bin ich meiner Freundin Caroline für den uneingeschränkten Rückhalt, der mir vor allem in den stressigen Zeiten die nötige Aufmunterung gegeben hat.

Darmstadt, 16. Januar 2024 Pascal Johe

Abstract

Despite the ongoing progress in electrification driven by the indispensable substitution of fossil fuels with renewable energy sources, the thermochemical conversion of chemical energy carriers is expected to continue playing an important role in the energy transition. This underlines the necessity for continual development of low-emission combustion technologies, grounded in a comprehensive understanding of the underlying physical processes through ongoing fundamental research efforts. Within this cumulative dissertation, the complex phenomenon of flame-wall interaction (FWI), which is an essential aspect of practical combustion systems, is investigated experimentally using advanced laser diagnostics. FWI involves the mutual interaction between chemical reaction, solid surface and fluid flow and is associated with undesired effects, such as reduced efficiency and increased pollutant emissions. The main objective of this thesis, which includes three peer-reviewed publications, is the investigation of fundamental aspects of FWI at elevated pressures and increased Reynolds numbers, mimicking operating conditions of practical combustion systems.

Experiments are carried out within a novel, enclosed test rig – the *pressurized side-wall quenching (SWQ) burner* – which provides a reproducible, generic configuration of a premixed flame interacting with a cold, solid wall. This test rig was designed, built and commissioned within the scope of this thesis and is presented in detail. The process under investigation is examined at operating pressures ranging between atmospheric and 5 bar absolute and Reynolds numbers up to 20,000 using various laser diagnostics. Limitations of such measurement techniques resulting from the complex test rig design and process-inherent challenges arising with increasing pressure are reported.

First, a characterization of the turbulent flow field and the combustion dynamics is conducted using velocity data and spatial fields of the instantaneous flame front positions, provided by high-speed and low-speed particle image velocimetry measurements and planar, laser-induced fluorescence of the hydroxyl radical (OH-PLIF). This involves the inspection of the inflow and the near-wall flow field under non-reacting and reacting conditions, as well as the examination of the transient flame front motion. Building on this, turbulent flame propagation close to the wall is further analyzed in terms of the flame surface density (FSD), a central quantity in numerical combustion modeling, which is derived from measured flame front positions (OH-PLIF) following two common approaches. Furthermore, the near-wall thermochemistry of the turbulent flame quenching process is explored through simultaneous measurements of the gas-phase temperature and mole fractions of CO_2 and CO by means of dual-pump coherent anti-Stokes Raman spectroscopy and laser-induced fluorescence of CO. These measurements represent the first reported attempt to investigate the thermochemistry of FWI at pressures above atmospheric by means of multi-parameter laser diagnostics.

This cumulative dissertation presents novel insights into the impact of elevated pressure and increased Reynolds numbers on turbulent FWI and provides experimental data for model validation. It furthermore, contributes to the FWI research community by exploring the limits of state-of-the-art laser diagnostics for measurements in pressurized, near-wall reactive flows.

Kurzfassung

Trotz der fortschreitenden Elektrifizierung, angetrieben durch die unverzichtbare Substitution fossiler Brennstoffe durch erneuerbare Energiequellen, wird der thermochemischen Umwandlung chemischer Energieträger weiterhin eine wichtige Rolle innerhalb der Energiewende zugeschrieben. Dies unterstreicht die Notwendigkeit einer kontinuierlichen Entwicklung emissionsarmer Verbrennungstechnologien auf der Grundlage eines umfassenden Verständnisses der zugrundeliegenden physikalischen Prozesse durch fortwährende Grundlagenforschung. Im Rahmen dieser kumulativen Dissertation wird das komplexe Phänomen der Flammen-Wand-Interaktion (FWI), welches ein wesentlicher Aspekt praktischer Verbrennungssysteme ist, experimentell mit Hilfe moderner Laserdiagnostik untersucht. Bei der FWI handelt es sich um die gegenseitige Wechselwirkung zwischen chemischer Reaktion, Festkörperoberfläche und Gasströmung, die mit unerwünschten Effekten, wie vermindertem Wirkungsgrad und erhöhten Schadstoffemissionen, einhergeht. Das Hauptziel dieser Arbeit, die drei begutachtete Veröffentlichungen umfasst, ist die Untersuchung grundlegender Aspekte von FWI bei praxisrelevanteren Bedingungen, wie erhöhten Drücken und erhöhten Reynoldszahlen.

Die Experimente wurden in einem neuartigen, geschlossenen Prüfstand - dem *pressurized side-wall quenching (SWQ) burner* - durchgeführt, der eine reproduzierbare, generische Konfiguration einer vorgemischten Flamme in Wechselwirkung mit einer kalten, festen Wand bietet. Dieser Prüfstand wurde im Rahmen dieser Arbeit entworfen, gebaut und in Betrieb genommen und wird im Detail vorgestellt. Der Flammenlöschprozess wird bei Betriebsdrücken zwischen atmosphärisch und 5 bar absolut und Reynoldszahlen bis zu 20.000 mit verschiedenen Laserdiagnoseverfahren untersucht. Die Grenzen solcher Messtechniken für die Untersuchung dieses Prozesses, welche sich aus dem komplexen Aufbau des Prüfstandes und aus prozessimmanenten Herausforderungen bei steigendem Druck ergeben, sind in dieser Arbeit dokumentiert.

Zunächst erfolgt eine Charakterisierung des turbulenten Strömungsfeldes und der Verbrennungsdynamik anhand von Geschwindigkeitsdaten und räumlichen Feldern der instantanen Flammenfrontpositionen, die durch Particle Image Velocimetry-Messungen und planare, laserinduzierte Fluoreszenz des Hydroxylradikals (OH-PLIF) bereitgestellt werden. Dies beinhaltet die Untersuchung der Einströmung und des wandnahen Strömungsfeldes unter nicht-reagierenden und reagierenden Bedingungen sowie die Untersuchung der transienten Flammenfrontbewegung. Darauf aufbauend wird die turbulente Flammenausbreitung in Wandnähe anhand der Flammenflächendichte, einer zentralen Größe in der numerischen Verbrennungsmodellierung, weiter analysiert, die aus gemessenen Flammenfrontpositionen (OH-PLIF) nach zwei gängigen Ansätzen abgeleitet wird. Darüber hinaus wird die wandnahe Thermochemie des turbulenten Flammenlöschprozesses durch gleichzeitige Messungen der Gasphasentemperatur und der Molenbrüche von CO_2 und CO mit Hilfe der dual-pump kohärenten Anti-Stokes Raman-Spektroskopie und der laserinduzierten Fluoreszenz von CO untersucht. Diese Messungen stellen die erste dokumentierte Bestrebung dar, die Thermochemie von FWI bei erhöhten Drücken mit Hilfe von Multi-Parameter-Laserdiagnostiken zu untersuchen.

Diese kumulative Dissertation präsentiert neue Erkenntnisse über die Auswirkungen von erhöhtem Druck und erhöhten Reynoldszahlen auf turbulente FWI und liefert experimentelle Daten zur Modellvalidierung. Darüber hinaus leistet sie einen Beitrag zur FWI-Forschung, indem sie die Grenzen moderner Laserdiagnostik für wandnahe Messungen in reaktiven Strömungen bei erhöhten Drücken auslotet.

Contents

List of Figures

List of Tables

Nomenclature

Lowercase Latin Letters		**Unit**
c	Reaction progress variable	-
d_F	Minimum distance between probe volume location and flame front	m
h	Planck's constant	Js
$\vec{k}$	Wave vector	m^{-1}
l	Characteristic length scale	m
l_k	Kolmogorov length scale	m
n_s	Number of crossings per unit length	m^{-1}
p	Pressure	bar
s	Position along a curve	m
t	Time-averaged area of the turbulent flame front	s
u'	Velocity fluctuation	m/s
u_B	Bulk velocity	m/s
u_L	Laminar flame speed	m/s
u^+	Dimensionless velocity	-
u_T	Turbulent flame speed	m/s
z_τ	Wall friction velocity	m/s
u_x, u_y, u_z	x-, y- and z-component of velocity	m/s
$u_{x,0}$	Free-stream velocity	m/s
w	Mass fraction	-
x,y,z	Spatial coordinates	m
x_c	Conditioned x-coordiante	m
x_Q	Average axial position of flame quenching	m
y^+	Dimensionless wall distance	-

Uppercase Latin Letters		**Unit**
$\bar{A}$	Time-averaged area of the turbulent flame front	m^2
A_T	Overall area of the turbulent flame front	m^2
COV	Coefficient of variation	-
Da	Damköhler number	-
E	Energy	J
F	Frequency distribution	-
F_c	Cumulative frequency distribution	-
K	Gladstone-Dale constant	$m^/$ kg
Ka	Karlovitz number	-

L	Integral length scale	m
L_c	Length of a curve	m
L_s	Integral length scale of flame front wrinkling	m
Ma	Mach number	-
N	Number of samples	-
P	Flame front perimeter	m
R	Two-point correlation of velocity	m^2 / s^4
R	Specific gas constant	$J/(kg \cdot K)$
Re	Reynolds number	-
Re_t	Turbulent Reynolds number	-
T	Temperature	K
T_b	Temperature of the burnt gas mixture	K
T_u	Temperature of the unburnt gas mixture	K
X	Mole fraction	-
Y	Mass Fraction	-

Lowercase Greek Letters **Unit**

$\alpha, \beta, \gamma, \delta, \theta$	Geometric angle	$^\circ$
δ_d	Displacement thickness	m
δ_F	Laminar flame thickness	m
δ_g	Geometric boundary layer thickness	m
δ_Q	Quenching distance	m
δ_t	Thickness of turbulent flame brush	m
η	Dynamic viscosity	$kg/(m \cdot s)$
κ	Von Kármán constant	-
κ	Curvature estimate	-
λ	Wavelength	nm
ν	Kinematic viscosity	m^2/s
ν	Frequency of electromagnetic radiation	Hz
ν_E	Frequency of exciting electromagnetic wave	Hz
ν_F	Frequency of emitted fluorescence	Hz
ρ	Density	kg/m^3
σ_s	Orientation factor	-
ϕ	Equivalence ratio	-
ϕ	Fluorescence quantum yield	-

Uppercase Greek Letters **Unit**

Σ	Flame surface density	m^{-1}
Σ'	Flame front-conditioned FSD	m^{-1}

Indices

b	burnt

CF	Co-flow
crit	critical
F	Fuel
RMS	Root mean square
u	uburnt

Abbreviations

BML	Bray-Moss-Libby
CA	Control area
CARS	Coherent anti-Stokes Raman spectroscopy
CE	Canny-Edge (filter)
DNS	Direct numerical simulation
DP-CARS	Dual-pump CARS
FOV	Field-of-view
FSD	Flame surface density
FWI	Flame-wall interaction
GHG	Greenhouse gas
HOQ	Head-on quenching
HS	High-speed
HS	High resolution
IEA	International Energy Agency
IW	Interrogation window
LES	Large-eddy simulation
LIF	Laser-induced fluorescence
LII	Laser-induced incandescence
LS	Low-speed
LS	Low resolution
MFC	Mass flow controller
MZQ	Mulit-zone quenching
NZE	Net Zero Emissions
PIV	Particle image velocimetry
PLIF	Planar laser-induced fluorescence
RET, VET	Rotational/vibrational energy transfer
RSM	Fachgebiet für Reaktive Strömungen und Messtechnik
SIF	Spark-induced fluorescence
SWQ	Side-wall quenching
TG	Turbulence-generating grid
UV	Ultraviolet

List of Publications

Publications Included in this Dissertation

This cumulative dissertation is based on the following publications:

I. **P. Johe**, F. Zentgraf, M. Greifenstein, M. Steinhausen, C. Hasse, A. Dreizler. Characterization of flow field and combustion dynamics in a novel pressurized side-wall quenching burner using high-speed PIV/OH-PLIF measurements. *International Journal of Heat and Fluid Flow,* 94:108921, 2022. https://doi.org/10.1016/j.ijheatfluidflow.2021.108921

II. **P. Johe**, F. Zentgraf, M. Greifenstein, R. S. Barlow, A. Dreizler. Laser-based investigation of flame surface density and mean reaction rate during flame-wall interaction at elevated pressure. *Proceedings of the Combustion Institute,* 39(2):2159–2168, 2023. https://doi.org/10.1016/j.proci.2022.09.016

III. **P. Johe**, F. Zentgraf, M. Greifenstein, B. Böhm, A. Dreizler. Effects of elevated pressure on thermochemical states of turbulent flame-wall interaction studied by multi-parameter laser diagnostics. *Combustion and Flame*, 260:113214, 2024. https://doi.org/10.1016/j.combustflame.2023.113214

Publications not Included in this Dissertation

Publications and conference papers not included in this dissertation:

IV. M. Greifenstein, F. Zentgraf, **P. Johe**, B. Böhm, M. Steinhausen, C. Hasse, A. Dreizler. Measurements of the local equivalence ratio and its impact on the thermochemical state in laminar partially premixed boundary layer flames. *Experiments in Fluids,* 65, 7, 2024. https://doi.org/10.1007/s00348-023-03747-z

V. F. Zentgraf, **P. Johe**, A. Nicolas, R. S. Barlow, B. Böhm, B. Peterson, A. Dreizler. On the Evolution of Turbulent Boundary Layers during Flame-Wall Interaction Investigated by Highly Resolved Laser Diagnostics. *Combustion and Flame*, 261:113276, 2024. https://doi.org/10.1016/j.combustflame.2023.113276

VI. F. Zentgraf, **P. Johe**, A. D. Cutler, R. S. Barlow, B. Böhm, A. Dreizler. Classification of flame prehistory and quenching topology in a side-wall quenching burner at low-intensity turbulence by correlating transport effects with CO_2, CO and temperature. *Combustion and Flame,* 239:111681, 2022. https://doi.org/10.1016/j.combustflame.2021.111681

VII. F. Zentgraf, **P. Johe**, M. Steinhausen, C. Hasse, M. Greifenstein, A. D. Cutler, R. S. Barlow, A. Dreizler. Detailed assessment of the thermochemistry in a side-wall quenching burner by simultaneous quantitative measurement if CO_2, CO and temperature using laser diagnostics. *Combustion and Flame,* 235:111707, 2022. https://doi.org/10.1016/j.combustflame.2021.111707

VIII. F. Zentgraf, **P. Johe**, D. Escofet-Martin, R. S. Barlow, B. Böhm, B. Peterson, A. Dreizler. On the evolution of turbulent boundary layers during side-wall quenching. *30. Deutscher Flammentag für nachhaltige Verbrennung, Hannover-Garbsen 28.–29.09.2021, Online-Tagungsband*, pages 1100–1105, 2021.

IX. F. Zentgraf, **P.Johe**, D. Escofet-Martin, R. S. Barlow, B. Böhm, B. Peterson, A. Dreizler. Highly Resolved Near-Wall Boundary Layer Measurements in a Side-Wall Quenching Burner. *13th International ERCOFTAC symposium on engineering, turbulence, modelling and measurements (ETMM)*, Rhodes, Greece, 2021.

X. F. Zentgraf, **P. Johe**, H. Hoche, B. Göckel, S. Becker, M. Oechsner, A. Dreizler. Assessment of the impact of multiple mild-steam decontaminations on the protection performance of disposable KN95 filtering facepiece respirators. *Infection Prevention in Practice,* 3(2):100136, 2021. https://doi.org/10.1016/j.infpip.2021.100136

XI. **P. Johe**, F. Zentgraf, M. Greifenstein, M. Steinhausen, C. Hasse, A. Dreizler. Introducing a Novel Pressurized Side-Wall Quenching Burner: Characterization of the Combustion Dynamics. *10th European Combustion Meeting*, Naples, Italy, 2021.

Chapter 1

Introduction

1.1 Motivation

Anthropogenic climate change, induced by an increasing abundance of greenhouse gases (GHG) in the Earth's atmosphere [1, p. 8], poses a significant challenge to society and industry worldwide. Severe impacts on ecosystems, human life and infrastructure due to more frequent and intense weather extremes and other phenomenons are already observed and can be attributed to climate change with increasing confidence [2, p. 44]. Therefore, in order to limit human-induced global warming and related consequences, in December 2015, 195 countries defined the common objective of limiting the mean global temperature increase to well below 2°C and preferably to 1.5°C by reaching net zero GHG emissions until the middle of the 21st century, as stated in the *Paris Agreement*. To achieve this goal, a substantial reduction in the use of fossil fuels is inevitable. According to the *International Energy Agency's (IEA) World Energy Outlook*, proposing a pathway to such a *Net Zero Emissions (NZE)* scenario, there is a projected decline in the share of fossil fuels in the total global energy supply from 80 % in 2021 to about one third in 2030, and less than 20 % by 2050 [3, p. 133]. This decline, however, is closely linked to a consistent increase in the adoption of so-called *low-emission fuels*, such as bioenergy, hydrogren and hydrogen-based fuels, which are crucial for reducing carbon emissions of energy systems where electrification is not feasible. In particular, these chemical energy carriers are predicted to play a vital role for long-distance transportation, such as aviation and shipping, and high-temperature industrial processes [3, p. 135]. Furthermore, with the rapidly increasing share of volatile renewable energy sources, which reinforces the need for flexible power generation, these low-emission fuels are assigned an essential contribution to electricity security through their use in thermal power plants [3, p. 140]. Against this background, it is therefore expected that chemical energy carriers and their thermochemical conversion in combustion systems will continue to play a significant role in the energy sector in the medium and long term. The development of efficient combustion systems featuring low-emission characteristics is thus considered an important aspect of the transition of the energy sector imposing the need for fundamental research to deepen the understanding of the underlying combustion processes.

An essential aspect of practical combustion systems, often relying on enclosed combustion, such as gas turbines and internal combustion engines, is the phenomenon of flame-wall interaction (FWI) which involves the complex mutual interaction of chemical reaction,

(turbulent) flow and solid surface. As the chemical reaction takes place in a confined space, these processes are often unavoidable and occur as the propagating flame approaches the wall. Due to the significant difference between adiabatic flame temperature and wall surface temperature, FWI is characterized by high near-wall temperature gradients leading to undesired heat losses which, in turn, reduce durability, diminish thermodynamic efficiency and cause quenching of chemical reactions near the wall [4, p. 349]. This can result in an increased emission of pollutants such as unburned hydrocarbons and carbon monoxide. Thus, a thorough comprehension of these processes is considered crucial for designing more sustainable combustion systems, necessitating fundamental research into the governing phenomena. Considering typical operating conditions in practical combustion systems, fundamental research on FWI at increased turbulence and elevated pressure is of particular interest.

1.2 State of Research on Flame-Wall Interaction

The phenomenon of FWI may involve both, non-premixed as well as premixed flames. Since the latter is of primary interest within the context of this thesis, the literature review given in this section is limited to studies dealing with premixed FWI only. Fundamental research on FWI of premixed flames is commonly carried out using two generic flame quenching configurations (see also section 2.3) which are characterized by a flame that propagates either towards (*head-on quenching*, HOQ) or alongside (*side-wall quenching*, SWQ) a solid wall. As recently reviewed by Dreizler and Böhm [5], studies related to FWI cover various aspects, such as thermal properties, like quenching distances and heat fluxes, flame-flow interactions, flame front characteristics and thermochemistry. The literature review given in this section is intended to provide a summary of the current state of research on FWI of premixed flames focusing on experimental studies and with an emphasis on publications considering effects of elevated pressure.

Thermal properties of FWI were investigated experimentally in the past in a number of studies considering effects of equivalence ratio, wall properties and fuels [5]. Quenching distances at atmospheric pressure were measured in tubes and parallel plates with varying diameter/plate distance [6, 7]. More recently, the quenching distance was derived for HOQ and SWQ configurations at laminar and turbulent flow conditions using planar laser-induced fluorescence of the OH radical (OH-PLIF) [8, 9] and based on near-wall average temperature profiles obtained from coherent anti-Stokes Raman spectroscopy (CARS) measurements [9–11]. In the latter three studies, the data obtained was further used to determine wall heat fluxes based on measured near-wall temperature gradients, assuming one-dimensional heat conduction. Transient wall heat fluxes at pressures near atmospheric were also derived from time-resolved measurements of the instantaneous wall temperatures, using resistance type thermometers and thermocouples, which were subsequently provided to an unsteady heat conduction model, e.g. [12, 13]. Effects of pressure on these thermal properties were investigated by Bellenoue at al. [14], Sotton et al. [15] and Boust et al. [16] for HOQ and SWQ configurations in a constant-volume chamber based on direct measurements of the quenching distance at pressures up to 3.5 bar using chemiluminescence-based flame front imaging. These studies, which applied further

parameter variations, showed a decreasing quenching distance at increasing pressure in accordance to previous studies on flame quenching between parallel plates and in internal combustion engines, e.g. [17, 18]. By simultaneous measurements of the wall heat flux for pressures up to 17 bar using a heat flux gauge, which revealed a disproportional increase in this pressure range reaching values up to 2 MW/m^2, Sotton et al. and Boust et al. were able to review existing relations for prediction of the quenching distance [15] and derive a analytical model for thermal flame quenching [16]. To overcome limitations of the optical diagnostics used for quenching distance measurements, further experiments were carried out by this group using an electrical ionization current probe, as reported by Karrer et al. [19], for measurements of the quenching distance at pressures up to 16 bar, carried out by Labuda et al. [20]. Further studies on wall heat fluxes in an SWQ configuration were carried out by Escofet-Martin et al. [21] and Ojo et al. [22] using a fixed-volume chamber using advanced laser diagnostics. They applied hybrid fs/ps rotational coherent anti-Stokes Raman spectroscopy (HRCARS) and Phosphor thermometry, yielding wall-normal temperature profiles and wall temperatures, to examine wall heat losses that occur as the flame propagates through a quiescent gas mixture that is compressed to 2 bar due to the heat release.

Flame-flow interactions close to a solid wall were investigated at atmospheric pressure focusing on the evolution of the stretch rate [23] and the effect of local stretch on flame speed [24] both in a head-on quenching flame in an atmospheric pressure vessel using high-speed and time-resolved particle image velocimetry (PIV). Further studies were carried out in a similar atmospheric HOQ burner, to investigate flame propagation and flame displacement speeds [8] and in a atmospheric SWQ burner focusing on the interaction of the flame with the turbulent boundary layer [9]. The same SWQ configuration was used in a subsequent study to examine the impact of the reaction on the near-wall flow with special attention to the inner layer of the turbulent boundary layer. The PIV setup applied in this study allowed for resolving the turbulent boundary layer down to the viscous sublayer, which remained unaffected from the chemical reactions [25]. The impact of the wall on flame front characteristics, such as the flame brush and the flame surface density, was moreover examined at atmospheric pressure in the same SWQ burner using OH-PLIF imaging [26] and in a similar SWQ configuration using laser tomography of the flame [27]. In all of these three studies, an increase of the flame surface density close to the wall was observed. Regarding experiments at elevated pressure, Boust et al. [28] carried out high-speed PIV measurements of a spark-ignited, tumbling methane-air mixture in constant-volume vessel at 2 bar pressure before ignition. They observed decreasing turbulence intensities close to the wall as the flame front propagated through the region-of-interest. Based on simultaneous heat flux measurements, they further concluded that the wall heat losses are influenced by the large-scale velocity magnitude. Influences of turbulence intensity could not be determined. In a more recent study of the same group based on high-speed PIV measurements in the unburned gas mixture in a constant-volume chamber at pressures up to 58 bar, Padhiary et al. [29] showed that turbulent flow motion causes increased wall heat fluxes and they moreover observed that, with rising pressure, wall heat fluxes of turbulent FWI even more exceed those at laminar conditions.

The first experiments on thermochemistry during FWI were carried out in a SWQ configuration comprised of an isothermal cold plate positioned in the laminar exhaust gas flow of a McKenna-type burner based on Raman-scattering measurements yielding local gas-phase temperatures and relative hydrocarbon number densities [30, 31]. More recently, multi-line NO laser-induced fluorescence (LIF) thermometry as well as single-photon and two-photon LIF of OH, CH_2O and CO was used in a similar configuration to assess the laminar boundary layer [32]. Experiments on HOQ were also conducted in the past by applying spark-induced fluorescence (SIF) yielding temperature profiles across the laminar flame propagating within a combustion chamber at pressures between 0.5 bar and atmospheric [33]. Additional studies on atmospheric, laminar FWI were performed in a HOQ and an SWQ burner using two-photon CO-LIF as well as CARS and dual-pump CARS, respectively, for a simultaneous quantification of gas-phase temperature, mole fractions of CO [9–11] and mole fractions of CO_2 [34]. Furthermore, in another study on a similar SWQ configuration, one-dimensional imaging of temperature and major species was achieved by application of ultrabroadband CARS [35]. While some of the most recent investigations mentioned above covered the thermochemistry of turbulent FWI to some extent [10, 11], there is only one study known to the author focusing on the assessment of turbulence-chemistry interaction [36]. The experimental investigation of thermochemical states during turbulent FWI at elevated pressure, however, is an entirely unexplored domain, to the author's best knowledge.

The state of research of numerical simulations, which is summarized only briefly here, is similar to that of experimental studies with respect to the investigation of FWI at turbulent flow conditions and elevated pressure. Various aspects of FWI at laminar flow conditions and atmospheric pressure in HOQ and SWQ configurations were investigated in a larger number of studies in the past using on-step chemistry approaches [37–39], tabulated reaction manifolds [40–45] and detailed chemistry [46–49] to describe the reaction chemistry. The number of studies that cover FWI at turbulent flow conditions (and atmospheric pressure), in contrast, seems to be smaller, but has also increased over the last years: Quenching distances, wall heat fluxes, flame surface density, turbulent fluxes and further fluid mechanical aspects of turbulent FWI in HOQ and SWQ configurations were investigated using large-eddy simulations (LES) implementing tabulated chemistry manifolds [50, 51] and direct numerical simulations (DNS) based on one-step chemistry approaches [52–57] and a detailed chemistry mechanism [58]. Furthermore, thermochemical properties of turbulent FWI have been examined more recently in a few studies using DNS (detailed chemistry) [59] and LES (tabulated reaction manifolds) [60, 61]. Regarding the effect of elevated pressure, however, numerical studies are scarce and mostly limited to atmospheric flow conditions. Westbrook et al. [62], for example, investigated quenching of laminar methane and methanol flames in a HOQ configuration at pressures up to 40 atm based on a one-dimensional DNS using detailed chemistry to study the effect of pressure, and other parameters, on the quenching distance to derive flame speed correlations for this quantity. More recently, head-on quenching of a more complex fuel, namely iso-octane, at pressures up to 20 atm, was examined by Hasse et al. [63], also based on a one-dimensional detailed chemistry DNS which revealed, amongst other findings, a slower oxidation of fuel and intermediate hydrocarbons for increased pressure. Further DNS studies (one-dimensional, detailed chemistry) on laminar flame quenching (HOQ) at

elevated pressures up to 2 bar and up to 20 bar, respectively, were conducted by Owston et al. [64] for H_2/O_2 and Yenerdag et al. [65] for methane flames. The only numerical study known to the author that treats turbulent FWI at elevated pressure was carried out by Niemietz et al. [66] and is related to gas turbine combustion. Within this study, a lean methane/air flame at 4 bar interacting with isothermal walls, similar to an SWQ configuration, is examined based on a DNS using a finite rate chemistry approach to identify the main influences on carbon monoxide emissions.

1.3 Aim and Structure of this Work

1.3.1 Aim

This thesis aims to expand experimental research on fundamental aspects of premixed Flame-Wall Interaction towards more realistic operating conditions, such as elevated pressures and increased Reynolds numbers. For this purpose, the following specific objectives were pursued during this work.

Development and characterization of a novel, enclosed test rig
Fundamental research on pressurized FWI requires a reproducible flame quenching configuration at well-defined boundary conditions in an enclosed environment. To achieve this, a customized test rig is required that additionally meets further demands in terms of applicability of measurement techniques – more specifically, optical diagnostics, which are the method of choice for such investigations – and suitability for numerical simulations. Therefore, within the scope of this thesis, a novel enclosed test rig was designed, incorporating experiences gained in past experimental and numerical studies conducted by the group. After commissioning of the test rig, the flow field and combustion characteristics were characterized for three operating cases.

Identification of laser diagnostic limitations
The application of optical diagnostics to investigate near-wall combustion phenomena is complicated, but offers the exceptional possibility of in-situ, non-invasive and highly-resolved measurements of varying parameters. With increasing operating pressure, however, further difficulties arise from more complex test rig designs and process-inherent challenges. Therefore, the experiments carried out within this thesis also serve to evaluate the feasibility of optical diagnostics for the investigation of pressurized FWI and to identify associated limitations.

Assessment of turbulent, pressurized FWI
Increased turbulence and elevated pressure induce enhanced wrinkling of the flame front affecting the interaction of fluid mechanical and chemical processes which in turn has an impact on near-wall thermochemical states. At the core of this work is the process-oriented research on turbulent FWI at elevated pressure which aims at acquiring novel insights into the coupled processes at conditions closer to reality. For this purpose, the flow field, the flame front geometry and thermochemical states are measured experimentally using a set of laser diagnostics.

Providing experimental data for model validation
Despite their importance for model validation in numerical combustion simulation, experimental data of FWI are only available to a limited extent. The experimental studies conducted within this work aim to help address this lack of experimental FWI data. Therefore, the acquired data is shared publically on the institutional repository of Technical University of Darmstadt *TUdatalib* [67–69].

1.3.2 Structure

This cumulative dissertation is based on three peer-reviewed publications, as summarized in the **List of Publications**.

The structure of this thesis mirrors the fundamental stages of the research project on pressurized FWI conducted within this work at the Institute for Reactive Flows and Diagnostics (RSM) at TU Darmstadt. These stages can be associated with the specific objectives defined above. After a brief introduction into the theoretical background, including fundamentals on near-wall flows, premixed combustion and laser diagnostics, this thesis is divided into four main chapters covering the introduction of the newly developed test rig (chapter 3), a summary of the experimental methodology applied for near-wall measurements (chapter 4), the characterization of the flow field and combustion characteristics (chapter 5) and process-oriented investigations on pressurized FWI (chapter 6).

Chapter 3 and 4 present the experimental methodology applied within this work, starting with a comprehensive description of the novel *pressurized side-wall quenching (SWQ) burner* test rig which provides the basis for the subsequent experimental research. This test rig was designed, built and commissioned within the scope of this thesis and was firstly introduced in **Paper I**. In Chapter 4, the laser diagnostic setups of two different experiments for (high-speed) velocimetry and flame front visualization (**Paper I**) and multi-parameter thermochemistry measurements (**Paper III**) are outlined. Subsequently, limitations of these diagnostics in the context of near-wall measurements in reactive flows at elevated pressure are reported and discussed.

Chapter 5, based on results of **Paper I**, provides a characterization of the non-reactive and reactive flow field yielding inflow boundary conditions and properties of the near-wall flow. Furthermore, the combustion process is characterized in terms of flame front dynamics, statistics and topologies.

In chapter 6, the pressurized FWI process under investigation is examined in terms of two different aspects of (turbulent) premixed combustion. First, the flame surface density and further flame front characteristics are analyzed focusing on influences of the wall and increasing operating pressure (up to 5 bar absolute), based on results first published in **Paper II** and the evaluation of unpublished data. Then, the near-wall thermochemistry is investigated, based on results of **Paper III**, and effects of elevated pressure are discussed.

This thesis finally concludes with a summary of the results and an outlook for future work.

Chapter 2

Theoretical Background

The purpose of this chapter is to provide an introduction into the theoretical background of this thesis. Fundamental aspects of near-wall turbulent flows, premixed combustion and laser diagnostics relevant to this work are presented. For further information on these topics the reader is referred to the literature cited in this chapter.

2.1 Near-Wall Turbulent Flows

Fluid flows bounded by one or more solid surfaces arise in a large variety of technical applications and therefore play an important role within fluid dynamics. This may involve external flows, such as the flow around airfoils, road vehicles or buildings, as well as internal flows within pipes, ducts and nozzles [72, p. 264] [73, p. 1], but also within combustion devices, such as gas turbines or internal combustion engines. Fundamental characteristics of near-wall flows are elucidated in the following based on comprehensive descriptions in the textbooks by Spurk and Aksel [71], Schlichting and Gersten [70] and Pope [72].

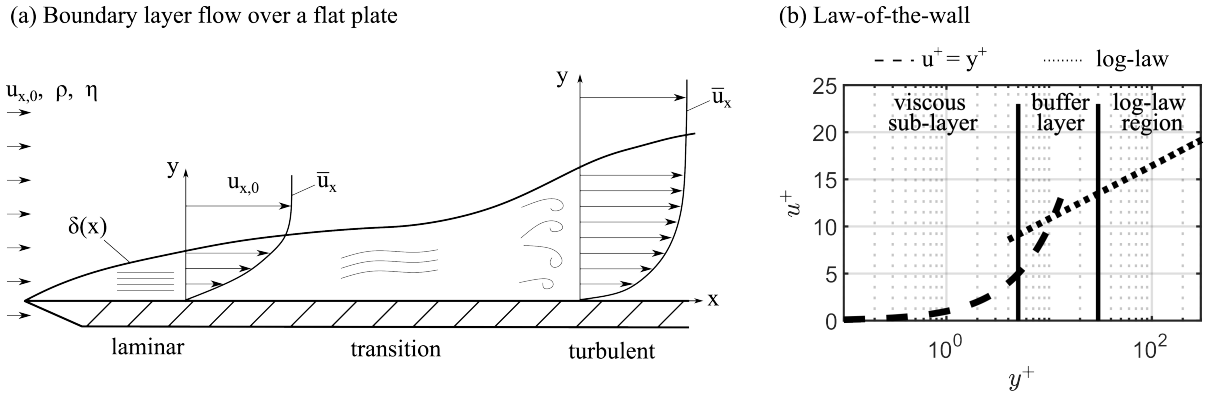

Figure 2.1: Illustration of near-wall turbulent flow characteristics: (a) schematic of the boundary layer over a flat plate transitioning from laminar to turbulent flow conditions and (b) Normalized velocity profiles in the semi-logarithmic u^+/y^+-space for a visualization of the universal law of the wall [70, p. 420][71, p. 239].

The fluid flow in all of the above-mentioned examples is characterized by fluid motion in the vicinity of a solid wall, to some extent, comparable to the non-reacting flow over a flat plate as, depicted in Fig. 2.1. This generic flow configuration is of fundamental importance within the theory of near-wall flows and is particularly well suited to elucidate basic properties and characteristics. As depicted in Fig. 2.1, the (mean) flow is (nearly) aligned parallel to the surface of the plate and oriented mainly in x-direction. The motion of the fluid is described by the velocities u_x, u_y and u_z in the three coordinate directions x, y and z, respectively, and the density is denoted by ρ. Far off the wall, the (mean) velocity is constant and equivalent to the so-called *free-stream velocity* $u_{x,0}$. The flow is treated as incompressible, which is a valid assumption for many flow configurations under technically relevant conditions, provided that the ratio of the flow velocity and the sound velocity of the medium, i.e. the Mach number Ma, is well below 0.2 [74, p. 392]. Furthermore, the flow is assumed to be isothermal and incompressible with a constant density ρ and shall exhibit Newtonian behavior with a constant dynamic viscosity η. The incompressible, isothermal flow of a Newtonian fluid over a flat plate is thus governed by the parameters $u_{x,0}$, ρ and η. Using a characteristic length scale, i.e. the length of the flat plate l, these parameters may be combined to the dimensionless Reynolds number Re, which is given in Eq. 2.1 for the specific flow configuration described above [70, p. 31].

$$Re = \frac{u_{x,0}\rho l}{\eta} \tag{2.1}$$

This dimensionless quantity is of central importance within fluid dynamics and can be derived for any flow configuration using a characteristic length and velocity of the flow and the fluid's density and viscosity. In general, it serves as indicator for the dominating forces in the fluid flow as it gives the ratio of inertial and viscous forces. Correspondingly, at low Re, viscous forces dominate while at high Re the fluid motion is predominantly governed by inertial forces [70, p. 7]. In the case of a near-wall flow, like the flow over a flat plate, however, in a region close to the wall viscous forces play an important role. Due to the viscous behavior of the fluid, the velocity of the flow is zero right at the surface of the wall, generally referred to as no slip-condition, and increases with the distance from the wall approaching the free-stream velocity, as depicted in Fig. 2.1. This region of monotonically increasing velocity is called *boundary layer* and separates the surface of the wall from the *outer flow*. The spatial dimensions of the boundary layer are frequently described by either the geometric boundary layer thickness δ_g or the displacement thickness δ_d, as given in Eq. 2.2 and 2.3, respectively. While δ_g is defined by the distance from the wall at which the mean velocity is equal to some percentage, e.g. 99%, of the free-stream velocity $u_{x,0}$, δ_d may be interpreted as measure for the displacement of the streamlines of the outer flow due to the boundary layer [72, p. 299].

$$\delta_{g,99\%} = y(u = 0.99 \cdot u_{x,0}) \tag{2.2}$$

$$\delta_d = \int_0^\infty \left(1 - \frac{u}{u_{x,0}}\right) dy \tag{2.3}$$

Regardless of the definition used, the thickness of the boundary layer significantly depends on the flow condition which can be laminar or turbulent and increases with the distance from the leading edge of the plate. For the flow configuration depicted in Fig. 2.1, the flow within the boundary layer is initially laminar and hence exhibits a layered structure of fluid motion without any convective transport of mass or momentum perpendicular to the flow direction. Within this region, the laminar boundary layer exhibits a characteristic wall-normal velocity (streamwise component) profile, commonly referred to as *Blasius profile* [70, p. 31]. At some position along the plate, however, small instabilities in the flow develop and initiate the transition into a fully turbulent flow which is characterized by irregular velocity fluctuations superimposed on the mean flow motion. This fully turbulent boundary layer flow can be observed downstream of a certain position x_{crit}, which can be estimated from the critical Reynolds number $Re_{crit} = (u_{x,0}\rho x_{crit})/\eta$. For the flow over a flat plate, Re_{crit} commonly takes values between $3 \cdot 10^5$ and $3 \cdot 10^6$, depending on the pressure distribution and the turbulence intensity in the outer flow and the roughness of the wall [70, p. 33].

With the flow turning turbulent, the thickness of the boundary layer considerably increases and the wall-normal mean velocity profile of a fully turbulent boundary layer develops. Due to the turbulent fluctuations resulting in an increased momentum transfer, the turbulent velocity profile shows a more homogeneous shape compared to the laminar Blasius profile [73, p. 165]. Correspondingly, close to the wall surface, wall-normal gradients of the mean streamwise velocity are increased in the turbulent flow resulting in higher wall shear stresses and friction drag [75, p. 192]. Within a certain distance from the wall, inside the boundary layer, the turbulent flow exhibits a velocity distribution which is characteristic for many turbulent wall-bounded flows, therefore referred to as *universal law of the wall*. It is defined as $u^+ = f_\mathrm{w}(y^+)$ based on a dimensionless velocity u^+ and wall distance y^+, which are derived as given in in the following

$$u^+ = \frac{\bar{u}_x}{u_\tau} \qquad y^+ = \frac{y}{\delta_\nu} = \frac{y \cdot u_\tau}{\nu} \qquad u_\tau = \sqrt{\nu \left.\frac{d\bar{u}_x}{dy}\right|_{y=0}} \tag{2.4}$$

where $\bar{u}_x$ is the mean velocity in streamwise direction, u_τ is the *wall friction velocity*, and ν is the fluids kinematic viscosity. The universal law of the wall thus basically states that the mean velocity profile solely depends on u_τ and δ_ν which are suitable velocity scales and lengthscales of the region close to the wall [72, p. 272]. Depending on y^+, the function f_w can be expressed in different forms and the near-wall flow may be subdivided correspondingly into separate regions. While within the *viscous sublayer*, generally associated with $y^+ < 5$, the velocity profile can be described by a linear relation, farther away from the wall, the so-called *log law* holds:

$$y^+ < 5: \; u^+(y^+) = y^+ \qquad\qquad y^+ > 30: \; u^+(y^+) = \frac{1}{\kappa}\ln y^+ + B \tag{2.5}$$

According to Pope [72, p. 274], the von Kármán constant κ and the constant B in the log law generally take values within 5% of $\kappa = 0.41$ and constant $B = 5.2$. At dimensionless wall distances $5 < y^+ < 30$ a transition between both aforementioned regions takes place within a *buffer layer* [72, p. 275]. The resulting characteristic structure of the velocity distribution $u^+(y^+)$ is illustrated in Fig. 2.1 using a semi-logarithmic representation.

As the flow in the boundary layer turns turbulent, it shows characteristics of turbulent motion which involves velocity fluctuations on a wide range of length scales. In order to quantify the characteristic size of the larger flow structures within the turbulent flow the integral length scale L can be derived from two-point correlations. According to Pope [72, p. 196], the longitudinal two-point correlation of the x-component of the velocity in x-direction R_{xx} can be calculated as in Eq. 2.6

$$R_{xx} = \overline{u'_x(x+r,y,z,t) \cdot u'_x(x,y,z,t)} \tag{2.6}$$

$$L_{xx} = \int_0^\infty R_{xx} \,/\, \overline{u'_x \cdot u'_x} dr \tag{2.7}$$

where $u'_x = u_x - \bar{u}_x$ denotes the velocity fluctuation in the sense of the Reynolds decomposition [72, p. 83]. The longitudinal length scale L_{xx} can subsequently derived according to Eq. 2.7 by integration of the normalized two-point correlation function.

2.2 Premixed Combustion

Premixed combustion refers to the self-sustaining process of thermochemical energy conversion governed by exothermic chemical reactions between a fuel and an oxidizer in a homogeneous mixture of both. Fundamental aspects of this process relevant to this thesis are presented in this section following outlines in the textbooks by Warnatz et al. [76], Turns [77] and Peters [78].

2.2.1 Combustion Chemistry

The overall oxidative conversion of methane into major product species during combustion in air is specified by the global reaction defined as follows.

$$CH_4 + 2O_2 \longrightarrow CO_2 + 2H_2O \tag{2.8}$$

This reaction equation indicates the ratio between the amounts of fuel (CH_4) and oxidizer (O_2 or air), commonly quantified in terms of mole fractions X or mass fractions w, required to achieve a complete conversion of both reactants. Using this *stoichiometric ratio*, a given fuel-oxidizer mixture is characterized based on the *equivalence ratio*

$$\phi = \frac{(w_{fuel}/w_{air})}{(w_{fuel}/w_{air})_{stoichiometric}} \tag{2.9}$$

as *lean* ($\phi < 1$), stoichiometric ($\phi = 1$) or *rich* ($\phi > 1$) mixture [77, p. 19].

The global reaction defined in Eq. 2.8, however, represents a significant simplification of the combustion chemistry, as it actually results from a set of *elementary reactions* taking place during the combustion process and involving many intermediate species. In the case of methane, complex reaction mechanisms including 325 elementary reactions and 53 species (e.g. *GRI-Mech 3.0* mechanism [79]) are available.

2.2.2 Structure of Laminar, Premixed Flames

A premixed flame is characterized by the localized combustion of a homogeneous fuel/oxidizer mixture within a distinct region of chemical reaction. Inside the flame, heat is released during the thermochemical conversion of the unburned reactants causing spatial changes of temperature and involved species mole fractions [77, p. 254 ff.]. The resulting flame structure is illustrated exemplarily by spatial profiles of these state variables in a stationary, freely-propagating, laminar, lean premixed ($\phi = 0.8$) methane/air flame, depicted in Fig. 2.2 for atmospheric and 3 bar pressure. As the flame is assumed to be one-dimensional, temperature and species mole fraction profiles only depend on the spatial coordinate z which is oriented perpendicular to the planar flame front. The unburned gas mixture moves in z-direction approaching the flame at *laminar flame speed* u_L – which is equivalent to the velocity of a flame propagating through a quiescent gas mixture – causing the flame front to remain spatially stationary [77, p. 254 ff.]. In general, the laminar flame speed depends on the temperature and mixture composition of the unburned gas and, for any hydrocarbon fuel [80, p. 6], exhibits a non-linear, negative dependence on pressure [77, p. 277].

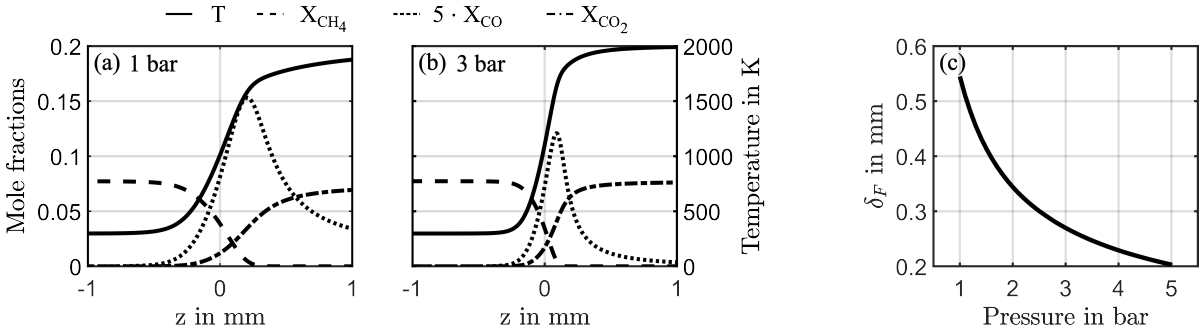

Figure 2.2: Spatial profiles of temperature and mole fractions of CH_4, CO and CO_2 in a stationary, freely-propagating, laminar, lean premixed ($\phi = 0.8$) methane/air flame at (a) atmospheric and (b) 3 bar pressure, derived from CANTERA simulations. The evolution of δ_F with pressure according to Eq. 2.10 is shown in (c).

Commonly, the flame region, as depicted in Fig. 2.2, is divided into three different zones. Moving in positive z-direction, the unburned gas mixture first passes a *preheat zone* characterized by only little heat release. Within this region, the temperature increases due to diffusive transport of heat from the subsequent *reaction zone*, where the major part of chemical energy is converted into heat. The reaction zone is dominated by fast-chemistry reactions involving fuel depletion and formation of major combustion products as well as intermediate species, such as CO. Within the *recombination zone* or *post-flame zone* the final burnout of CO to CO_2 takes place and equilibrium state is reached [77, p. 255 ff.] [81, p. 152].
The thickness of this flame structure, i.e. the *laminar flame thickness* δ_F, can serve as a characteristic length scale of the flame and may be determined from Eq. 2.10 based on the maximum spatial temperature gradient $\max(\partial T/\partial x)$ in the flame and the temperature difference between the burned and unburned gas mixture $T_b - T_u$ [63].

$$\delta_F = \frac{T_b - T_u}{\max(\partial T/\partial x)} \tag{2.10}$$

For the flames depicted in Fig. 2.2, this equation yields a reduction of the laminar flame thickness from about 0.55 mm to 0.27 mm with the pressure in the unburned gas mixture being increased from 1 to 3 bar, as shown in Fig. 2.2(c). Correspondingly, Fig. 2.2(a) and (b) show a considerably narrower structure for the flame at higher pressure featuring increased spatial gradients. This behavior of reducing flame thicknesses is an important aspect complicating experimental measurements in a pressurized flame.

2.2.3 Turbulent Combustion Regimes and Flame Properties

The combustion process in a premixed, turbulent reacting flow can show varying characteristics resulting from the complex interaction of the turbulent flow field and the chemical reaction. A classification can be made by means of regime diagrams which are commonly based on the comparison of characteristic length and velocity scales of the propagating flame and the turbulent flow. For the regime diagram shown in Fig. 2.3, first introduced by Borghi [82, p. 122] and later on modified by Peters [83], the turbulence intensity u', the laminar flame speed u_L, a macroscopic turbulent length scale, e.g. the integral length scale of turbulence L, and the laminar flame thickness δ_F are used. Based on (1) a turbulent Reynolds number Re_t, derived according to Eq. 2.1 using u' as characteristic velocity and L as characteristic length, (2) a turbulent Damköhler number

$$Da = \frac{u_L L}{u' \delta_F} \tag{2.11}$$

and (3) a turbulent Karlovitz number

$$Ka = \frac{\delta_F^2}{l_k^2} \tag{2.12}$$

which is derived using the Kolmogorov length scale l_k, different regimes of combustion are defined in a double logarithmic coordinate space of the ratios (u'/u_L) and (L/δ_F). The dimensionless quantities Re_t, Da and Ka can be expressed as functions of these ratios such that the relations $Re_t = 1$, $Da = 1$ and $Ka = 1$, which define the boundaries

of these regimes, are represented by lines within the diagram.
Based on Re_t, a fundamental distinction between the regime of *laminar flames* ($Re_t < 1$) and the domain of turbulent combustion ($Re_t > 1$) is made. The latter is further subdivided into the following regimes associated with varying combustion characteristics:

- Within the *flamelet* regime ($Re_t > 1$, $Da > 1$, $Ka < 1$), the turbulent flow field causes a large-scale wrinkling of the flame front, but does not affect the structure of the reactive-diffusive flame layer as, following the definition of Ka in Eq. 2.12, the size of even the smallest turbulent eddies is larger than the thickness of the laminar flame. The reaction zone may, therefore, be understood as a locally laminar premixed flame, a *flamelet*. With regard to numerical simulation, these properties allow the application of the *flamelet*-concept, a widely used modeling approach. This regime can be further subdivided based on the ratio u'/u_L.
  - For $u'/u_L < 1$, within the regime of *wrinkled flamelets*, only weak flame front wrinkling is observed, since the laminar flame propagation with u_L outweighs turbulent fluctuations characterized by u'.
  - Within the regime of *corrugated flamelets* ($u'/u_L > 1$), however, larger turbulent structures can substantially affect the flame propagation resulting in higher level of flame front wrinkling.
- The regime of *distributed reaction zones* ($Re_t > 1$, $Da > 1$, $Ka > 1$) is separated from the flamelet regime by the line $Ka = 1$. Correspondingly, as the size of the smallest turbulent structures falls below δ_F, they may advance into the reactive-diffusive flame layer resulting in a broadening of the flame front and local flame extinction.
- Within the *well-stirred reactor* regime ($Re_t > 1$, $Da < 1$, $Ka > 1$), turbulent mixing is faster than the chemical reaction, as $Da < 1$, leading to an even broader reaction zone as turbulent structures substantially influence the flame structure.

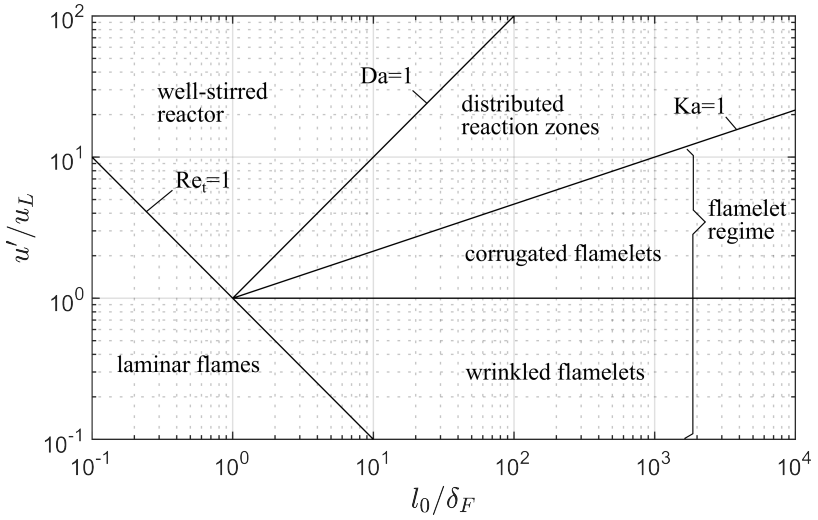

Figure 2.3: Regime diagram of premixed combustion by Borghi in a modified version by Peters [83].

Within the context of this work, besides the regime of laminar flames, only the flamelet regime is of relevance. As described above, the turbulent flame associated with the flamelet regime, features a thin reaction zone, which exhibits a convoluted shape due the interaction with the turbulent flow field. In contrary to a stationary, laminar flame, rapid fluctuations of the turbulent flame front location are observed within a certain spatial area which is often referred to as *flame brush*. Furthermore, the wrinkled flame front shape, results in a substantially increased surface area which allows for higher fuel consumption rates. Assuming that the flame front locally propagates with the laminar flame speed, neglecting effects of curvature and other influences on u_F, a turbulent flame speed u_T may be defined as

$$u_T = u_F \frac{A_T}{\bar{A}} \tag{2.13}$$

based on the overall area of the turbulent flame front A_T and the area of the time-averaged flame front $\bar{A}$ [76, p. 233].

2.3 Flame-Wall Interaction

The mutual interaction between a flame, the laminar or turbulent flow and a nearby solid surface is generally referred to as *flame-wall interaction (FWI)*. This interaction process occurs in a variety of practical combustion systems and is of particular importance for devices that incorporate combustion within an enclosed chamber. Due to large temperature gradients at locations where the flame approaches the cold surface of the wall, heat is removed from the combustion process and transferred to the wall resulting in large wall heat fluxes and local quenching of the chemical reaction. This may give rise to undesirable effects such as decreased efficiency, promotion of pollutant formation and reduced durability [84, p. 327].

Research on various aspects of FWI is typically carried out using generic experimental configurations which can be classified into the extreme cases of *head-on quenching (HOQ)* and *side-wall quenching (SWQ)*, depending on the orientation of the flame front and the direction of its propagation with respect to the wall. The geometrical configuration of both of these cases of FWI are schematically illustrated in Fig. 2.4. In the case of HOQ, the flame front is oriented parallel to the wall and approaches it as it propagates

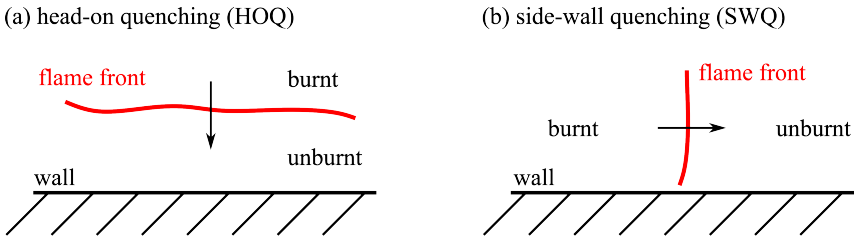

Figure 2.4: Generic configurations of flame-wall interaction: (a) HOQ, (b) SWQ.

perpendicular to the wall's surface. This is always a transient event, as, after ignition, the flame propagates through a premixed mixture until it is thermally quenched close to the surface of the wall when heat losses exceed heat release rates of the chemical reaction. The SWQ configuration, in contrast, is characterized by a flame front which is oriented perpendicular to the wall and propagates parallel to its surface. Within most experimental SWQ burner devices, however, the angle between flame front and wall surface at the position of FWI can also take values smaller than 90°, especially for turbulent flow conditions [5].
An inherent characteristic and also prerequisite of FWI is the close proximity of the flame to the wall which is quantified by means of the minimum distance between the reaction zone and the wall's surface, commonly denoted as *quenching distance* δ_Q. This quantity depends on parameters of the surface, like wall temperature and wall material, as well as on properties of the combustible medium, such as initial temperature and equivalence ratio, and generally decreases with increasing pressure [5, 14]. Boust et al. [28], for example, report a reduction of δ_Q for both configurations of FWI from about 0.6 mm to 0.2 mm (HOQ) and from 0.85 mm to 0.25 mm (SWQ) for a laminar methane/air flame with equivalence ratio of 0.7, when pressure is increased from slightly below 0.1 MPa to about 0.3 MPa.

Beyond these geometrical characteristics, the research area of FWI moreover involves further aspects on thermal, fluid-mechanical and thermochemical properties, as summarized in section 1.2.

2.4 Laser Diagnostics

The purpose of this section is to provide a brief introduction into the laser diagnostics techniques applied within this work focusing on basic aspects most relevant to the experimental implementation of those. For further information on these diagnostics the reader is referred to the textbooks cited in this section and the relevant literature.

2.4.1 Particle Image Velocimetry

This section gives a short overview of Particle Image Velocimetry (PIV) following the outlines in the textbook by Raffel et al.[85]. As illustrated in Fig. 2.5, which presents a typical planar PIV setup, the principle of flow velocity measurements with PIV relies on the imaging of *tracer particles*, which are present within the flow under investigation and illuminated with a suitable light source. The light that is scattered off the particles, which are moving with the fluid flow, is captured on at least two frames (i.e. PIV images) separated in time by a short, well-defined time interval Δt. From these PIV images, the spatially resolved particle displacement, resulting from the particle motion during the time interval Δt, is then derived by cross-correlation of both frames within so-called *interrogation windows* (IW) and subsequent identification of the correlation peak for each IW. Finally, the flow velocity field is computed from the particle displacement and Δt

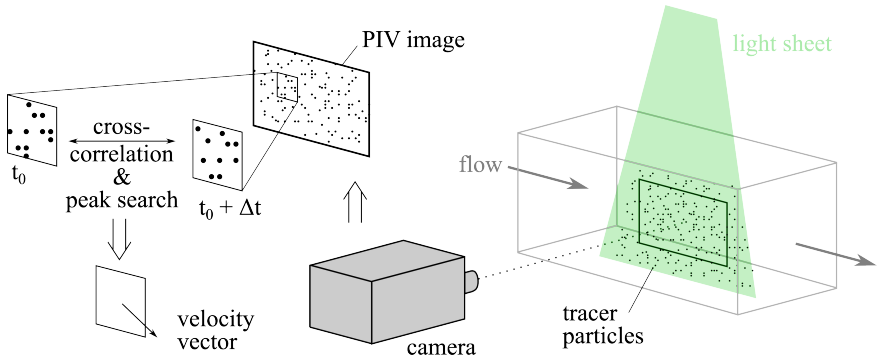

Figure 2.5: Schematic of the principle of PIV including an illustration of a common planar PIV setup and basic steps of the evaluation procedure [85, p. 8].

yielding one velocity vector for each IW.
To obtain meaningful velocity data, the diagnostic setup as well as parameters of the image acquisition sequence need to be adapted to the individual flow configuration under investigation. Amongst others, this involves the following aspects [85, p. 9 ff.]:

- Suitable tracer particles that show a high ability to follow the fluid motion need to be carefully selected. In the case of solid, chemically inert particles, that are commonly used in gaseous reacting flows, this can often only be achieved by using particles of small size (diameter typically in the order of 1 μm) [85, p. 11], which, however, also results in reduced amount of scattered light, as predicted by Mie's theory [85, p. 43].
- High power light sources, such as lasers, are therefore needed for illumination of small tracer particles. A common approach is to use dual-cavity lasers providing one short laser pulse for each PIV image separated in time by Δt. In this case, both laser pulses, which are formed into light sheets, must exhibit similar beam characteristics and need to be spatially overlapped within the field-of-view.
- The time separation Δt needs to be adjusted to achieve a sufficient particle displacement while minimizing the number of particles leaving the illuminated area during the time interval Δt due to out-of-plane motion.
- Parameters of the evaluation algorithm, such as the size and the number of IWs, need to be optimized to obtain the desired accuracy.

2.4.2 Laser-Induced Fluorescence

In this section a brief description of the laser-induced fluorescence (LIF) technique is given following the outlines of Hanson et al. [87] and Eckbreth [88]. The underlying process of LIF involves the resonant absorption of a photon by a molecule, leading to the transition from its ground state S_0 into a higher, electronically excited, energy state S_1, and the subsequent spontaneous emission of light, i.e. fluorescence, when the molecule relaxes into its ground state again. This process is outlined in Fig. 2.6 using an energy scheme that illustrates the difference in energy E between distinct electronic, vibrational, and

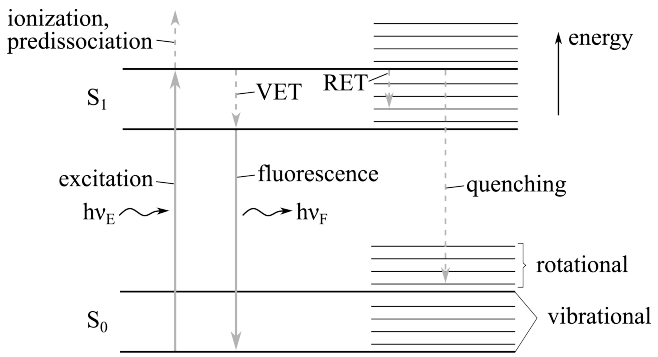

Figure 2.6: Illustration of the LIF process and the involved radiative and non-radiative energy transfer between rotation, vibrational and electronic energy states [86].

rotational energy states of the molecule. Excitation of the molecule is typically achieved using a narrowband laser tuned to certain frequency ν_E to match the photon energy $h\nu_E$ (h: Planck's constant) to the energy difference of the targeted transition, which allows for selective probing of specific molecules. Besides relaxation due to spontaneous emission of a photon with energy $h\nu_F$, de-excitation of the molecule can involve further non-radiative relaxation processes. These are rotational and vibrational energy transfer (RET and VET), i.e. the spontaneous relaxation to lower vibrational and rotational energy states of the electronically excited state and energy transfer to a colliding molecule, denoted as collisional quenching. Moreover, in some cases, molecules in the excited state may undergo photoionization or dissociation. All these processes are summarized in the fluorescence quantum yield ϕ which basically gives the ratio of the number of photons that are emitted by fluorescence to the number of photons which are absorbed [86]. Typically, the spontaneous fluorescence emission occurs in combination with RET and VET resulting in a red-shift of the emitted fluorescence ν_F compared to the excitation frequency ν_E.
As can be seen from Eq. 2.14, the intensity of the emitted fluorescence signal F is proportional to the fluorescence quantum yield ϕ and the state population of the ground state N_1 prior to laser excitation, which depends on temperature via the Boltzmann distribution [88, p. 391].

$$F \propto N_1(T) \cdot \phi(T,p,X_i) \tag{2.14}$$

This allows for both, species concentration and temperature measurements using LIF. Such quantitative measurements are, however, challenging due to the dependency of ϕ on temperature, pressure and composition of the gas mixture. While these quantities could be measured by applying further diagnostic techniques, other approaches exist, such as predissociative LIF, which avoid effects of quenching [88, p. 391].

Within this work, two-photon LIF is applied for quantitative measurements of carbon monoxide mole fractions (CO-LIF). The calibration procedure used for quantification of the fluorescence signal is outlined in section 4.2. Furthermore, LIF is used for flame front visualization based on qualitative planar imaging of the hydroxyl radical (OH-PLIF).

2.4.3 Coherent anti-Stokes Raman Spectroscopy

This section briefly summarizes the basic aspects of coherent anti-Stokes Raman Spectroscopy (CARS) based on descriptions by Hanson et al. [87] and Eckbreth [88]. The basic principle of CARS involves the nonlinear interaction of three laser beams at frequencies ω_1, ω_2 and ω_3 with the medium, i.e. an ensemble of molecules, resulting in the generation of a forth electromagnetic wave at frequency ω_4 due to an oscillating polarization. As illustrated in the energy scheme in Fig. 2.7(a), this process can be pictured as the excitation of a molecule by the laser with frequency ω_1, denoted as pump laser, to a virtual state followed by the transition to an excited ro-vibrational state by stimulated emission with the so-called Stokes beam with frequency ω_2. The molecule is then again excited to a virtual state by the laser with frequency ω_3, denoted as probe beam, which subsequently results in the emission of the CARS signal at ω_4, satisfying the conservation of energy in Eq. 2.15 [88, p. 282], as the molecules de-excites back to the ground state.

$$\omega_4 = \omega_1 - \omega_2 + \omega_3 \tag{2.15}$$

$$\Delta\vec{k} = \vec{k_1} - \vec{k_2} + \vec{k_3} - \vec{k_4} = 0 \tag{2.16}$$

In order to probe specific Raman resonances, the frequency difference $\omega_1 - \omega_2$ furthermore needs to be adjusted to match with rotational and/or vibrational transitions of the molecule. Using a broadband Stokes laser, multiple transitions can be accessed simultaneously enabling single-pulse measurements.

Besides energy, also momentum is conserved during the CARS process which is expressed by Eq. 2.16 [88, p. 311] yielding a relation between the wave vectors $\vec{k_i}$ of the four waves participating in the process. This leads to a geometric constraint, commonly referred to as *phase-matching condition*, which requires the beams to overlap at a specific angle in the measurement volume, as illustrated in Fig. 2.7(b), to achieve efficient signal generation. Geometrical arrangements which are commonly applied to achieve this condition are *coliniear CARS* ($\alpha = \beta = \gamma = \delta = 0$) and *BOXCARS*, the latter being illustrated in Fig. 2.7(b).

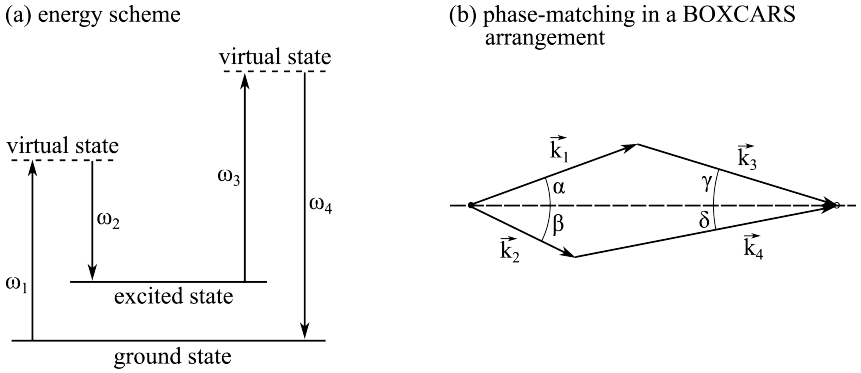

Figure 2.7: Illustration of the CARS process: (a) energy scheme and (b) phase-matching in a BOXCARS arrangement [88, p. 285].

Dependencies of the CARS signal intensity I_4 from parameters of the process are expressed in Eq. 2.17 [88, p. 290]. While I_4 increases with laser intensities I_i of the pump, Stokes and probe beam and the interaction length l squared, it decrease in case of deviations from the phase-matching condition which are associated with $\Delta\vec{k} > 0$.

$$I_4 \propto I_1 I_2 I_3 l^2 \left(\frac{\sin \Delta k l/2}{\Delta k l/2} \right)^2 \tag{2.17}$$

The fundamental CARS process described above can be further enhanced to the dual-pump CARS process allowing to probe ro-vibrational transitions of two molecules at the same time. This is possible by a suitable selection of the laser frequencies ω_1 and ω_3 ensuring that also the frequency difference $\omega_1 - \omega_3$ matches to ro-vibrational transitions of a second molecule. In this scenario, the two lasers with frequencies ω_1 and ω_3 switch roles between both interaction processes with the two different molecules. The Stokes laser with frequency ω_2 maintains the same role for both processes [88, p. 356].

In a typical diagnostic setup for (dual-pump) CARS measurements based on a BOXCARS arrangement, phase-matching of the laser beams within the measurement volume is commonly achieved by aligning the beams parallel and guiding them through a common lens. The generated CARS signal, which carries information about the Boltzmann distribution from the initial state and exhibits laser-like characteristics, is guided into a spectrometer to be spectrally resolved. Evaluation of the CARS signal is typically achieved using spectral fitting codes, such as CARSFT [89] and the algorithms by Cutler et al. [90] and Greifenstein and Dreizler [91]. These algorithms rely on matching synthetic spectra, calculated from a physical model, to the experimental data through residual minimization by optimization of certain degrees of freedom. This finally yields information on temperature and/or species concentration. Within the scope of this work, a dual-pump CARS approach is applied to probe N_2 and CO_2 for simultaneous measurement of gas-phase temperature and mole fraction of CO_2.

Chapter 3

Pressurized Side-Wall Quenching Burner

In this chapter, the pressurized side-wall quenching (SWQ) burner test rig, which was used for experimental investigations on FWI at elevated pressure within this cumulative dissertation, is presented in detail. This test rig was developed, constructed and commissioned within the scope of this thesis and was firstly introduced in **Paper I**.

3.1 Test Rig

Fig. 3.1(a) shows an overview of the *pressurized side-wall quenching burner*. The test rig can be subdivided into the test rig enclosure, shown in dark gray, and the SWQ burner unit, colored in light gray.

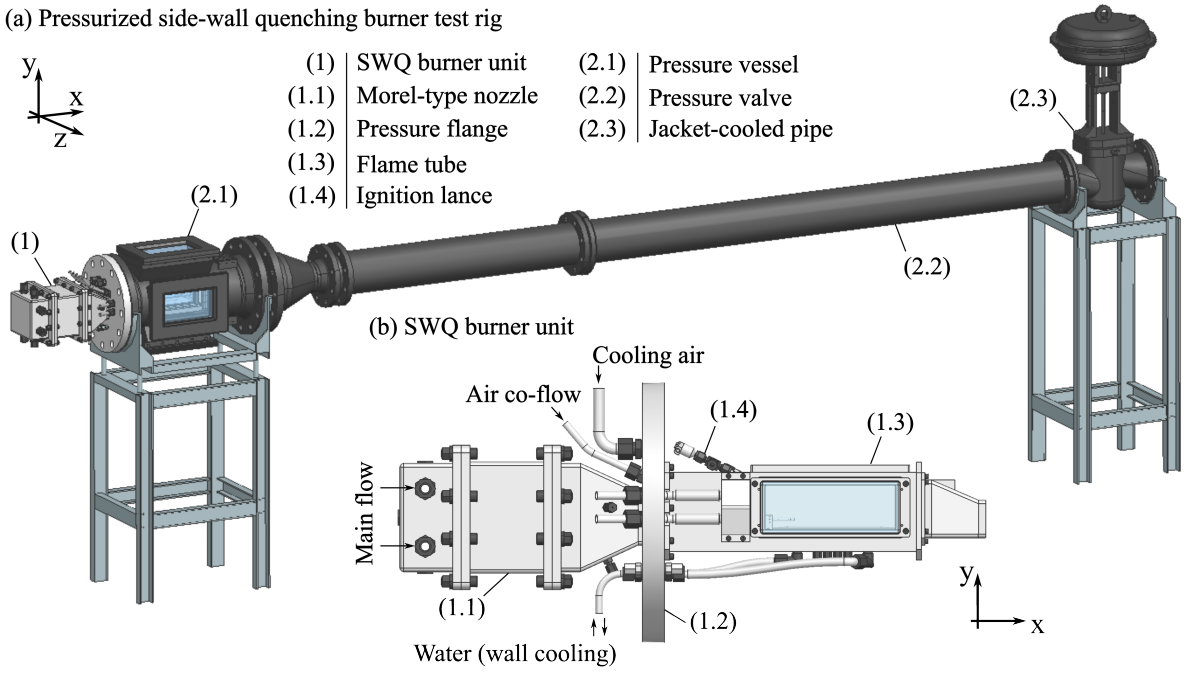

Figure 3.1: Pressurized SWQ burner test rig: (a) overview and (b) detailed view of SWQ burner unit.

The test rig enclosure is composed of a pressure vessel, which is equipped with three removable quartz glass windows (one on either side and one at the top; *Heraeus, SQ1*), and a pneumatic pressure valve (*Samson AG, Bauart 250*) both connected via a jacket-cooled pipe. This fraction of the test rig was previously part of the *single sector model gas turbine* test stand which was constructed by J. Hermann during his PhD studies [92] and used for investigations on flame-cooling air interaction by him and M. Greifenstein [91]. These components and parts of the infrastructure were reused within the design of the pressurized side-wall quenching burner rig presented within this work.

A detail view of the SWQ burner unit, which was designed and constructed[1] within the scope of this thesis, is shown in Fig. 3.1(b). Its design is inspired by the proven concept of the unconfined, *atmospheric side-wall quenching burner* that was extensively used at RSM for investigations of FWI under atmospheric conditions within the dissertations of Jainski [93], Kosaka [11] and Zentgraf [34]. As shown in Fig. 3.1(b), the burner unit is composed of a Morel-type nozzle and a flow channel, in the following referred to as flame tube, both connected to a stainless-steel pressure flange. In the assembled state, the right part of the SWQ burner unit is enclosed by the pressure vessel and fixed to it by screw connections at the pressure flange. All gas and liquid flows entering the test rig during operation are summarized in Fig. 3.1.

During operation, the main flow composed of air mixed with methane is guided into the SWQ burner unit through four inlet ports (two on each side). Cooling air is fed into the test rig via two ports at the top and four further ports, two on each side of the SWQ burner unit. A co-flow air mass flow is guided into the test rig through five inlet ports. Domestic water for wall cooling drawn from laboratory's water supply is de-ionized and filtered before entering the test rig.

The inner structure of the the test rig is illustrated by sectional views in Fig. 3.2. After entering the inlet plenum of the SWQ burner unit, the premixed air/methane main flow is guided through a fine square mesh (mesh size: $\approx 0.5\,\mathrm{mm}$) placed between two hexagonal grids (width of one hexagon: $\approx 3\,\mathrm{mm}$), a honeycomb structure (width of one hexagon: $\approx 3\,\mathrm{mm}$) and a second similar grid/mesh/grid combination to achieve flow homogenization. The flow is then accelerated within the Morel-type nozzle as the flow cross-sectional area reduces from $120 \times 135\,\mathrm{mm}^2$ to approximately $30 \times 60\,\mathrm{mm}^2$ (corner radius in both upper corners: 5 mm, see Fig. 3.2(c)) at the nozzle outlet, corresponding to a contraction ratio of 9. This nozzle design ensures an almost top-hat velocity profile at the nozzle outlet, where the premixed main flow enters into the flame tube. By inserting a removable turbulence-generating grid (TG; perforated plate with 3.8 mm bore diameter and 51% solidity) into the flow path of the main flow, increased turbulence intensities can be achieved especially within the boundary layer (see section 5). Quartz glass windows (*Sico Technology GmbH, SQ1*) on both sides and at the top of the flame tube enable optical access into it. At the bottom side of the flame tube, the flow is bounded by the the stainless-steel quenching wall which features a flat surface smoothly merging with the surface of the Morel-type nozzle yielding a continuous flow boundary between flow homogenization and quenching wall without prominent edges that might evoke flow

[1]The SWQ burner unit was manufactured by the RSM's workshop led by R. Berntheisel and D. Feldmann. Their contribution to this work is thankfully acknowledged here.

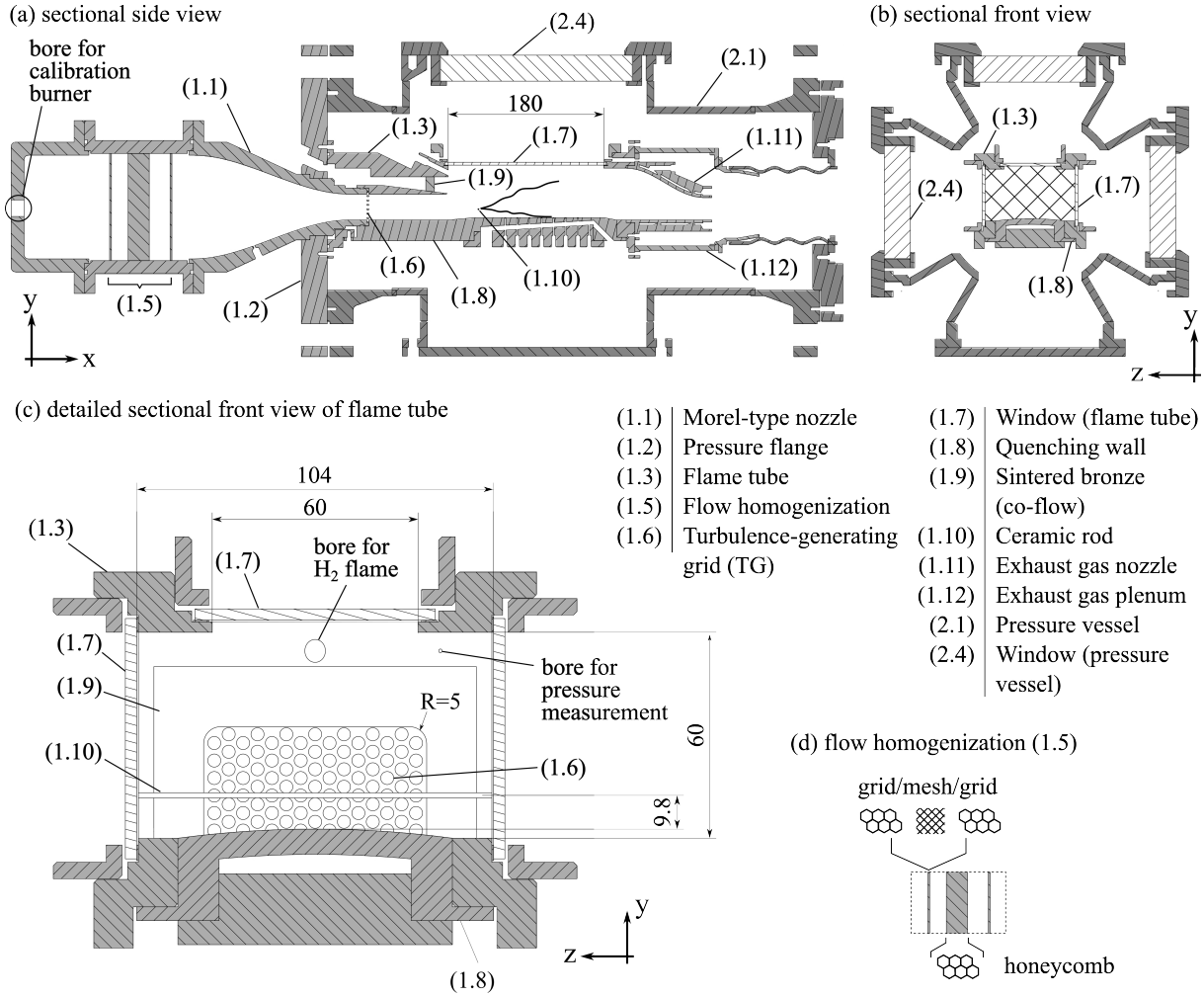

Figure 3.2: Sketch of pressurized SWQ burner: (a) sectional side view, (b) sectional front view, (c) detailed sectional front view of flame tube, (d) elements for flow homogenization. Dimensions are given in millimeters.

disturbances. Downstream of the nozzle outlet, the flat surface of the quenching wall smoothly converts into a convex surface which is cylindrically curved in the y-z-plane (300 mm radius) allowing for enhanced optical access to the near-wall FWI process. The resulting shape of the flow cross-section within the flame tube is illustrated by the hatched area in the front sectional view in Fig. 3.2(b). An enlarged view of the flame tube cross-section is additionally depicted in Fig. 3.2(c). As shown in this illustration, the premixed main flow is surrounded on three sides by the air co-flow which enters the flame tube through an inverted U-shaped, flat, sintered bronze structure for homogenization (see also Fig. 3.2(a)). This co-flow serves the purposes of (1) minimizing shear effects and reducing recirculation zones at the nozzle outlet and (2) shielding the quartz glass windows from the reacting main flow. In this way, thermal load on the windows is reduced and, during particle-based measurements, such as PIV, seeding particle deposition on the windows' surfaces is slowed down. The inverted U-shaped area surrounding the co-flow cross-section in Fig. 3.2(c) represents an inner surface of the flame tube. This surface exhibits two bore holes, one for injection of a hydrogen pilot flame using the ignition lance (see Fig. 3.1(b)

and Fig. 3.2(a)) and one for measurements of the internal, static pressure. After ignition of the premixed main flow, a V-shaped flame is stabilized on a ceramic rod of 1 mm diameter positioned 9.8 mm above the surface of the quenching wall and 36 mm downstream of the nozzle outlet. Moving in downstream direction, the lower branch of this flame gradually approaches the quenching wall and extinguishes locally in the vicinity of the solid surface resulting in a side-wall quenching process. As depicted in Fig. 3.2(a–c), the quenching wall features a cooling duct which is continuously flushed with ambient-temperature water (provided by the wall cooling water flow) for temperature stabilization. The cooling duct is inclined by 3° with respect to the direction of gravity (i.e. negative y-direction) to ensure that air bubbles, if any are present, are transported with the cooling water flow to the outlet of the cooling duct, preventing their accumulation at axial positions where flame quenching takes place. Instead, air bubbles would accumulate at the highest position of the wall cooling system located close to the outlet of the cooling duct and be removed with the coolant flow. Using a type-K sheath thermocouple positioned at the cooling duct outlet, air accumulations at this position can be detected if temperatures exceed the boiling point of water. Local wall temperatures are monitored using five additional sheath thermocouples (type K, 1.5 mm diameter) mounted in bores about 0.4 mm beneath the surface of the quenching wall. Farther downstream, the hot exhaust gases resulting from the combustion process exit the flame tube through an exhaust gas nozzle (rectangular cross-section reduced from $60 \times 94\,\mathrm{mm}^2$ to $26 \times 38\,\mathrm{mm}^2$; contraction ratio of 5.7) used to accelerate the gaseous flow into the exhaust gas plenum. Internal cooling channels within the exhaust gas nozzle can be flushed with deionized water for cooling purposes, which was not necessary for the operating conditions relevant to this thesis (see section 3.3) due to low thermal loads. Cooling of the pressure vessel and the flame tube is ensured by the cooling air flow entering the test rig through the pressure flange of the SWQ burner unit (see Fig. 3.1). This cooling air flow is guided alongside the windows of the flame tube into the exhaust gas plenum. There, it is mixed with the hot combustion products issuing from the flame tube to lower the temperature of the gaseous mixture, which then exits the test rig through the exhaust pipe and the pressure valve.

Calibrated thermal mass flow controllers (MFC, *Bronckhorst*) are used to control the mass flows of the air/methane main flow and the air co-flow. The cooling air flow is determined based on a differential pressure measurement at an orifice plate and regulated using a pneumatic valve. Measurement of the static pressure inside the flame tube is carried out by means of a pressure transducer (*PSI Pressure Systems, Model 9116*) connected via a pressure measurement hose to the 1-mm bore in the flame tube, shown in Fig. 3.2(c).

3.2 Calibration Burner

For calibration and validation of the optical diagnostics, a calibration burner providing a stable, laminar flame even at elevated pressure was used since laminar flame operation could not be achieved with the enclosed test rig. This burner was designed and used by M. Greifenstein before for a similar purpose [91]. The burner consisted of two co-axial pipes carrying N_2 in the outer and a premixed methane/air mixture in the inner pipe (8 mm inner diameter). At the outlet of the inner pipe, a V-flame was stabilized on

a 1-mm steel-rod. The burner was positioned inside the flame tube of the pressurized SWQ burner by inserting it through a bore in the base plate of the inlet plenum (see Fig. 3.2) after removing the honeycomb, grids and meshes for flow homogenization, the turbulence-generating grid and the ceramic rod. The V-flame of the calibration burner was positioned far off the quenching wall of the flame tube to ensure adiabatic conditions. A sketch of the calibration burner can be found in [91].

3.3 Operating Conditions

In this section the operating conditions of the pressurized SWQ burner for the experiments carried out within the scope of this thesis are defined. The strategy for the selection of operating cases involving operating pressures varying between $p = 1\,\text{bar}$ and $p = 5\,\text{bar}$ absolute is outlined in Fig. 3.3. This graphic shows the relation between key parameters of the SWQ process and operating pressure. In Fig. 3.3(a), the ratio of bulk velocity u_B of the premixed methane/air main flow (quotient of volume flow rate and flow cross-sectional area at the flame tube's inlet) and laminar flame speed u_L obtained from the adiabatic simulation (see section 4.2) is plotted as a function of p for three different constant Reynolds numbers Re. The latter is defined according to Eq. 2.1 with the hydraulic diameter of the nozzle outlet $d_H = 40.7\,\text{mm}$ as characteristic length and u_B as characteristic velocity using fluid properties of the premixed methane/air mixture at 20 °C. Since growing p leads to an increase of the density of the gaseous medium, u_B decreases if Re is kept constant. As the reduction of u_L with increasing pressure (see section 2.2.2) is less pronounced, this results in a decrease of u_B/u_L. This ratio, in turn, affects the average axial position x_Q where flame quenching occurs and the average angle α between flame front and surface of the quenching wall (see schematic in Fig. 3.3(b)). The impact of varying pressure on these geometric quantities, derived from simple geometric considerations, is illustrated in Fig. 3.3(c).
From these illustrations on pressure dependencies, it is evident that at high Re, low

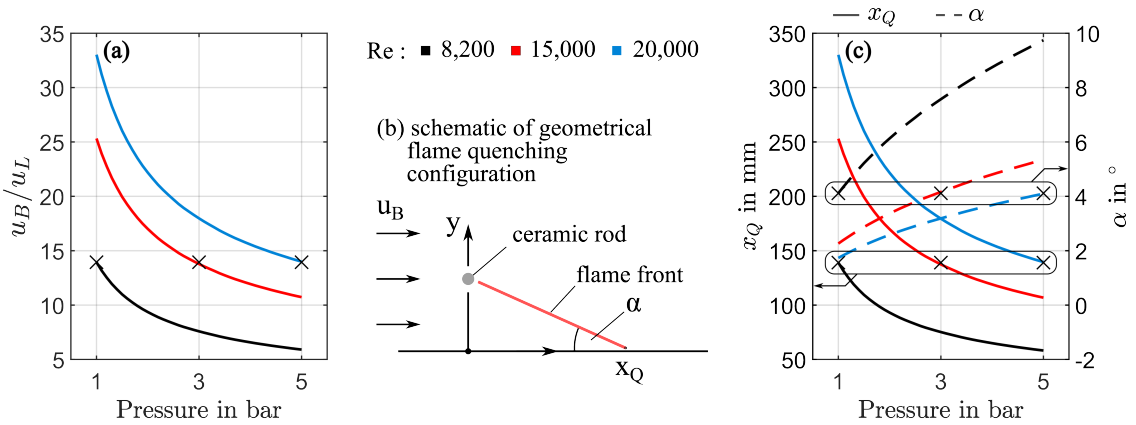

Figure 3.3: Selection of operating conditions: (a) ratio of bulk velocity u_B and laminar flame speed u_L and (c) axial position of flame quenching x_Q (solid lines) and angle α between flame front and wall surface (dashed lines) as functions of pressure. A schematic of the geometrical flame quenching configuration is shown in (b). Functional relations are shown for three Re.

Table 3.1: Operating conditions.

p	TG	u_B	u_L	$u_{B,CF}$	ϕ	Re	T_{wall}
bar	-	m/s	m/s	m/s	-	-	K
1	yes	3.8	0.27	3.8	0.8	8,200	319
3	yes	2.3	0.17	2.3	0.8	15,000	359
5	yes	1.8	0.13	1.8	0.8	20,000	370

operating pressures p result in high u_B/u_L which leads to a shallow angle α between flame front and quenching wall at axial positions x_Q outside the optically accessible area or even blowoff of the flame. For low Re, in contrast, u_B/u_L takes significantly smaller values which results in flashbacks of the flame at high operating pressures. Due to these constraints, operation at constant Re, which is a common approach for the design of flow experiments, can not be achieved for the relevant pressure range. Instead, operating cases are defined by keeping the ratio u_B/u_L constant, aiming at consistency in x_Q and α which are considered important parameters of the FWI process. These operating cases are visualized in Fig. 3.3(a) and (c) by black crosses. A summary of the operating conditions for these operating cases is given in Tab. 3.1. Similar to u_B, the flow rate of the air co-flow is defined by its bulk velocity $u_{B,CF}$. In all operating cases, the burner was operated with turbulence-generating grid (TG) and the equivalence ratio ϕ was kept constant at 0.8.

Chapter 4

Experimental Methodology

Two different experiments were carried out for this cumulative dissertation to investigate turbulent FWI at elevated pressure by means of (1) velocimetry measurements and flame front visualization and (2) multi-parameter thermochemistry measurements. Major aspects of both experiments are summarized in section 4.1 and 4.2 and further details can be found in **Paper I** and **Paper III**, respectively. Limitations of the diagnostic setups with regard to its application to the SWQ process under investigation are summarized and discussed in section 4.3.

4.1 Velocimetry and Flame Front Visualization

Particle image velocimetry (PIV) and planar laser-induced fluorescence of the hydroxyl radical (OH-PLIF) were applied simultaneously for two-component, two-dimensional velocity measurements of the reactive and non-reactive flow and flame front visualization. The measurements were carried out at low-speed (LS, 50 Hz) and high-speed (HS, 5 kHz) repetition rates and at two different axial positions in the central plane of the burner (x/y-plane) – close to the ceramic rod and farther downstream, where FWI occurs. A schematic of the optical setup is shown in Fig. 4.1(a–b). The test rig-fixed coordinate system used to indicate measurement locations is shown in Fig. 4.1(b).

For PIV, a pair of laser sheets was introduced into the flame tube through the windows on the upper side of the test rig to illuminate alumina tracer particles (Al_2O_3, $d_{50} = 1-1.7\,\mu$m) seeded to the premixed main flow. Mie-scattering of the particles was recorded through the windows on one side of the test rig using two different detection systems (high-speed camera, distance rings, camera lens) to obtain both, images with a lower resolution (LR) and a larger field-of-view (FOV) covering the full height of the Morel-type nozzle and images with a higher resolution (HR) to resolve smaller structures in the flow field. For these two optical setups, one camera pixel (LR: 20 μm, HR: 13.5 μm) corresponded to $\approx 40\,\mu$m (LR) or $\approx 12\,\mu$m (HR), respectively, in the object plane of the FOV. Velocity vector fields were derived from pre-processed (spatially calibrated and filtered) particle images in a multi-pass processing procedure with decreasing interrogation window size using the commercial software DaVis (LaVision GmbH). During post-processing, spurious vectors were removed by outlier detection based on a median filtering operation.

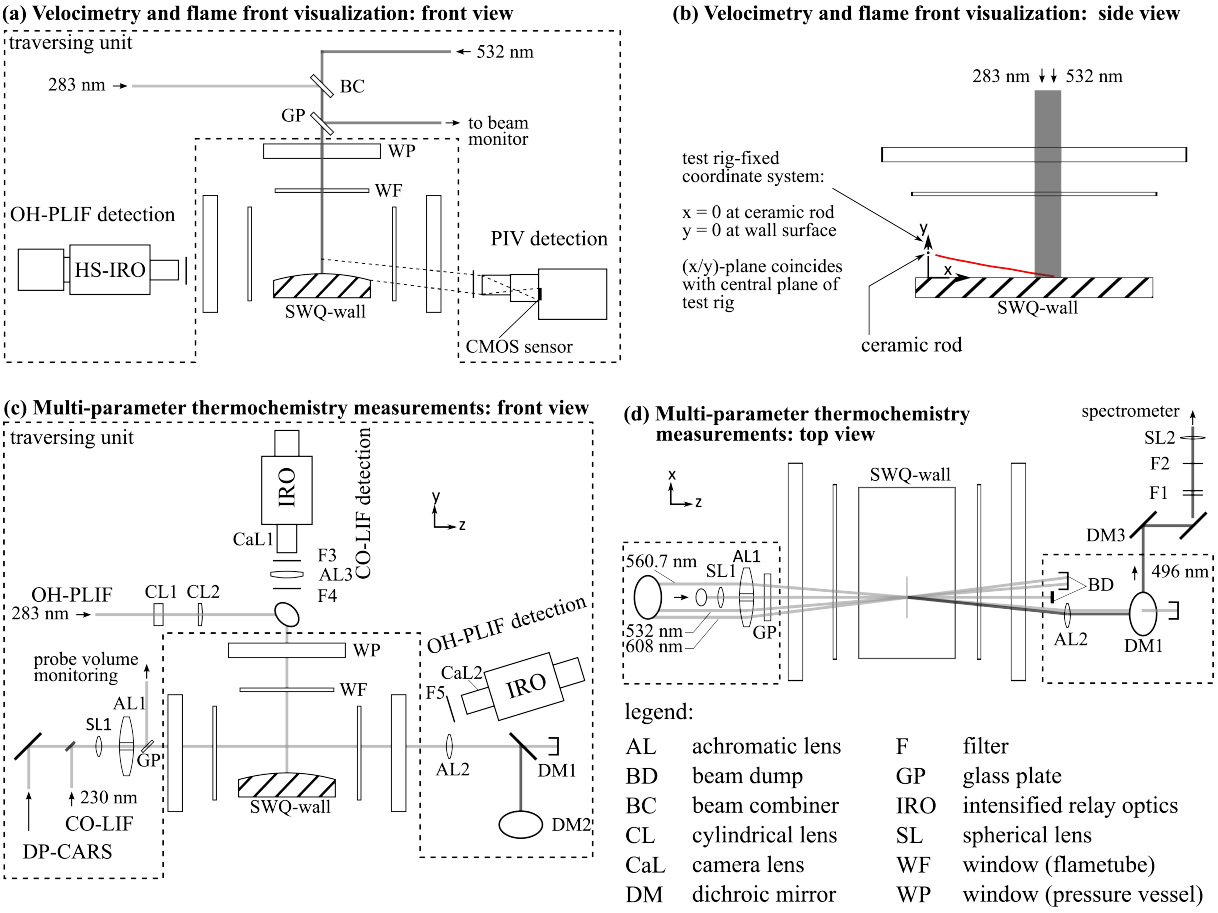

Figure 4.1: Schematics of both laser diagnostic setups: (a) front view and (b) side view of velocimetry and flame front visualization setup. (c) front view and (d) side view of setup for multi-parameter thermochemistry measurements. Adapted from [94, 95].

For OH-PLIF, excitation of the $Q_1(6)$ transition of the hydroxyl radical was achieved by guiding a UV ($\lambda = 282.93\,\text{nm}$) laser light sheet from above into the test rig using a beam combiner to overlap it with the light sheets for PIV. An intensified high-speed camera equipped with an interference filter ($305 - 340\,\text{nm}$ transmission) was used to capture the emitted fluorescence signal perpendicular to the light sheet through the windows on one side of the test rig. The detection system provided images of the spatial OH distribution in a FOV of $35 \times 35\,\text{mm}^2$ with one pixel ($20\,\mu\text{m}$) corresponding to approximately $35\,\mu\text{m}$ in physical space. The spatial resolution was about $250\,\mu\text{m}$ (25% MTF), estimated from recordings of a siemens star target. Flame front detection was carried out using the OH-PLIF images by identification of spatial gradients in the OH distribution, which are assumed to indicate the location of the reaction zone. The processing procedure used for this purpose was implemented in MATLAB (The MathWorks Inc.) and involved a block-matching and 3D filtering algorithm [96] for spatial noise suppression with preservation of spatial gradients and Canny-Edge (CE) filtering for edge (i.e. spatial gradient) detection. The lower CE filter threshold was defined based on the frequency distribution of spatial gradient magnitudes resulting from image noise.

The position of the wall within the obtained velocity fields was deduced from spatially calibrated, averaged particle raw images exhibiting a small stripe of high intensity resulting from light scattered on the wall's surface (see Fig. 4.2). Spatial mapping of velocity fields and flame front locations was subsequently achieved using images of a calibration target recorded with both systems.

4.2 Multi-Parameter Thermochemistry Measurements

Ro-vibrational dual-pump coherent anti-Stokes Raman spectroscopy (DP-CARS) of N_2 and CO_2 and two-photon laser-induced fluorescence of carbon monoxide (CO-LIF) were applied for quantitative, pointwise measurements of gas-phase temperature, CO_2 and CO mole fractions. Planar laser-induced fluorescence of the hydroxyl radical (OH-PLIF) was performed for flame front visualization providing information on the location of the DP-CARS/CO-LIF probe volume with respect to the position of the reaction zone. The individual laser diagnostic techniques were temporally synchronized and measurements were carried out at 10 Hz repetition rate. Measurements at varying (nominal) wall distances ($0.1 \leq y \leq 4$ mm) could be realized by moving a major part of the optical diagnostic setup using a traversing unit. A schematic of the optical setup is shown in Fig. 4.1(c–d).

For DP-CARS, the three laser beams (pump/probe lasers: $\lambda_1 = 532$ nm, $\lambda_2 = 560.7$ nm; Stokes laser: $\lambda_3 = 608$ nm) were aligned parallel to each other, focused by a common spherical, achromatic lens and introduced into the test rig through the windows on one side to overlap in a planar BOXCARS arrangement oriented parallel to the surface of the quenching wall. The size of the DP-CARS probe volume was about 50 μm in lateral direction and approximately 0.9 mm in principal beam direction (i.e. interaction length of the three laser beams). The coherent signal originating from the DP-CARS probe volume was collected on the other side of the test rig and guided to the spectrometer using a second achromatic lens and dichroic mirrors for separation from overlapping excitation laser beams. A spherical lens was used to focus the signal beam through the slit of a Czerny-Turner spectrometer equipped with a 2400 lines/mm 1st-order grating and spectra (in a wavelength range of about 493 to 499 nm) were recorded with a backside-illuminated, cooled CCD camera with one pixel corresponding to 0.19 cm^{-1} in wavenumber domain. Pre-processing of single-shot spectra involved removal of flawed spectra, mean background subtraction, normalization to an averaged non-resonant signal (obtained from recordings in pure methane), square root extraction and a dispersion calibration. Applying a spectral fitting algorithm [90] to the pre-processed single-shot spectra subsequently yielded temperature and CO_2 mole fraction values. Post-processing included removal of unphysical samples based on a thresholding criterion applied to the simulated spectra and additional calibration of CO_2 mole fractions using a temperature dependent calibration function derived from experimental data measured in the laminar, unbounded flame of the calibration burner (section 3.2) and data provided

by a CANTERA simulation [79]. This simulation of a one-dimensional, adiabatic, freely-propagating, laminar flame was carried out using the GRI3.0 mechanism [97] and is in the following referred to as *adiabatic simulation*.

Two-photon excitation in the Hopfield-Birge bands of CO for CO-LIF measurements was achieved by focusing a narrow-band, wavelength-stabilized dye laser ($\lambda = 230.09\,\mathrm{nm}$) through the windows on one side into the test rig to overlap it with the DP-CARS probe volume. The spot size of the laser beam at this position was about $130\,\mu\mathrm{m}$ in diameter. Fluorescence emission resulting from transition in the Ångström bands was recorded through the upper windows of the test rig using an intensified CCD camera equipped with an interference bandpass filter ($480 - 500\,\mathrm{nm}$ transmission). Operating the camera with 4×4 hardware binning resulted in one pixel corresponding to about $80\,\mu\mathrm{m}$ in physical space. Processing of the raw signal involved background and baseline correction, integration of the two-dimensional signal in a region of 0.9 mm (corresponds to interaction length of DP-CARS probe volume), correction for the local gas density (based on the gas-phase temperature provided by the DP-CARS technique) and correction for influences resulting from reflections of the fluorescence signal at the quenching wall. Shot-to-shot laser energy correction was only applied to certain data sets due to an undetected failure of the energy monitoring system. Validity of the calibration procedure was still assumed, as discussed in **Paper III** and the corresponding supplementary material. Conversion of the pre-processed LIF signal into quantitative CO mole fractions was finally achieved using a temperature-dependent calibration function derived from experimental data measured in the laminar, unbounded flame of the calibration burner (section 3.2) and data provided by a CANTERA simulation (adiabatic simulation).

Planar OH-LIF measurements were carried out by excitation of the $Q_1(6)$ transition of OH and recording of the subsequent fluorescence emission using an optical setup similar to that described in section 4.1. Differences in the geometric arrangement (inclination of UV laser light sheet and detection system) mainly resulted from additional space limitations. Moreover, as the measurements were carried out at low- instead of high-speed repetition rate, the optical setups comprised differing technical equipment. This resulted in slightly changed imaging characteristics of the detection system (one $12.9\,\mu\mathrm{m}$ pixel corresponding to $54\,\mu\mathrm{m}$ in physical space). The processing procedure for detection of flame front positions based on the OH-PLIF raw images followed the procedure described in section 4.1. The obtained flame front positions were subsequently used to derive the minimum distance d_F between probe volume location and the flame front, as shown in Fig. 6 in **Paper III**, for every individual sample. This quantity was defined to be negative, if the probe volume was located in the unburned gas and positive, if it was located in the burned gas region.

Spatial matching of the different techniques was achieved by guiding the laser beams for DP-CARS and CO-LIF through a 100-μm pinhole positioned in the central plane of the burner and subsequently taking images of the same pinhole with the CO-LIF and OH-PLIF detection systems. The position of the wall's surface with respect to the DP-CARS/CO-LIF probe volume was subsequently identified by slowly moving the probe

volume closer to the wall until abruptly breakdowns occurred. At elevated pressure, however, this procedure could only be used under non-reacting conditions. In the reacting flow, the laser beams are stochastically deflected due to increased beam steering, resulting in a more continuous increase of breakdowns rather than an abrupt one. This results in a reduced accuracy of the determination of the position of the wall's surface, as thermal expansion of the wall is not accounted for. Correspondingly, the distance of the probe volume with respect to the wall given in this thesis are to be understood as *nominal* wall distance.

4.3 Limitations of Optical Diagnostic Techniques

In this section limitations of the optical diagnostics applied for near-wall measurements of flame-wall interaction at elevated pressure are briefly reported. As the interactions between propagating flame and wall occur on small length and time scales, experimental investigations of FWI are always difficult [5]. With increasing pressure, these scales tend to further decrease (e.g., reduction of laminar flame thickness and quenching distance, see section 2.2.2 and 2.3), further complicating the application of experimental techniques. Furthermore, near-wall measurements are subject to beam steering effects, i.e. the undesired refraction of light due to gradients of the refractive index normal to the direction of propagation, which are known to be a major challenge of combustion research with optical diagnostics, in general. While the influence of these effects on optical diagnostics, such as CARS [98], laser-induced incandescence (LII) [99] and PIV [100, 101], i.a., have been occasionally investigated, they still remain an open issue in combustion research. With increasing pressure, beam steering effects further intensify, as can be deduced from Eq. 4.1 which is adopted from [100] and derived using the *Gladstone-Dale relation* and the equation of state of a perfect gas. Eq. 4.1 yields an approximation of the deflection angle α of a light ray from its direction of propagation (z-direction) as it travels through a reaction zone with a laminar flame thickness δ_F exhibiting gradient components of temperature T in a direction x normal to z. This equation is used here for a rough estimation of the influence of beam steering effects with rising pressure.

$$tan(\alpha) \approx \frac{K \cdot p}{R} \left[\frac{1}{T^2} \frac{\partial T}{\partial x} \right]_{max} \cdot 3\delta_F \tag{4.1}$$

Using a Gladstone-Dale constant of $K = 2.98 \cdot 10^{-4}\,\mathrm{m^3/kg}$, as in [100], the specific gas constant of dry air $R = 287\,\mathrm{J/(kg \cdot K)}$ and values for $[1/T^2 \cdot \partial T/\partial x]_{max}$ and δ_F derived from the adiabatic simulation (section 4.2) using Eq. 2.10, an almost linear increase of α with p is estimated for the operating cases under investigation ($\alpha_{1\ bar} \approx 0.06°$; $\alpha_{3\ bar} \approx 0.15°$; $\alpha_{5\ bar} \approx 0.24°$). Correspondingly, a significant increase of beam steering with rising pressure is expected which matches with the observations presented in the following.

Figure 4.2 illustrates the rising impact of beam steering effects in the reacting flow at increasing operating pressure on the image quality of PIV raw images (HR setup). For this purpose, one example PIV raw image is shown for each operating case with the instantaneous flame front position visualized as red line. While at 1 bar the individual

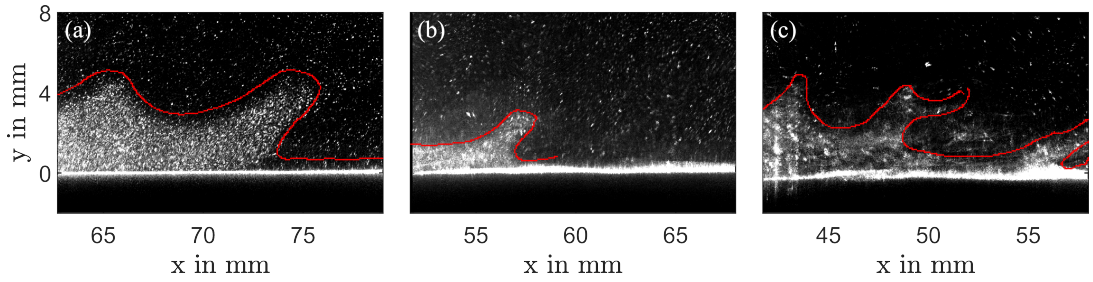

Figure 4.2: Example particle raw images recorded at (a) 1 bar, (b) 3 bar and (c) 5 bar, illustrating the increasing impact of beam steering at elevated pressure.

particles illuminated by the laser light sheet are sharply imaged, a significant blurring of the particle images can be observed at 3 bar, which is further intensified at 5 bar because of the increasing deflection of light (see Eq. 4.1). Due to this significant degradation of image quality, particle raw images of the reacting flow in the 5 bar case were not used for PIV post-processing. Close to the wall, at elevated operating pressure, these effects cause the surface of the wall to be imaged as a blurred stripe of high intensity rather than a sharp line, as it is observed for the 1 bar case, impairing the accuracy of the determination of the wall surface position (see section 4.1 and **Paper I**). With regard to the OH-PLIF measurements carried out within this work, increasing operating pressure primarily resulted in a reduction of the fluorescence signal due to increased electronic quenching and pressure broadening of the absorption lines [102]. Reduced spatial gradients of the fluorescence signal, however, did not affect the determination of the flame front position using the algorithm described in section 4.1. Considering the decrease of quenching distances δ_Q with increasing pressure (section 2.3), an accurate measurement of δ_Q was not possible with the optical setup used, although the detection system was aligned to achieve the maximum possible magnification.

Limitations of the DP-CARS/CO-LIF setup with regard to its application for near-wall measurements of turbulent FWI at elevated pressure are summarized in Fig. 4.3. While measurements in the unbounded flame of the calibration burner, which is mostly unaffected by beam steering effects, provided convincing results with regard to accuracy and precision (presented in **Paper III**), rising beam steering effects at increasing pressure again turned out to be a major challenge of near-wall measurements.

Regarding the DP-CARS technique, the favorable increase of signal intensity at higher pressure (see supplementary material of **Paper III** for sample DP-CARS spectra) was outweighed by increased beam steering resulting in distorted wavefronts and a changing overlap of the laser beams within the probe volume. This in turn, negatively affected the DP-CARS spectra and degraded the accuracy and precision of the system. In some cases, this led to clearly distorted spectra (see example DP-CARS spectra in Fig. 4.3(a)), which needed to be excluded from the post-processing procedure. Close to the wall, beam steering, moreover, caused deflected laser beams to occasionally impinge on the quenching wall. The emitted intense broadband radiation resulted in an increased baseline of the corresponding DP-CARS spectrum and regions of saturated pixels in the

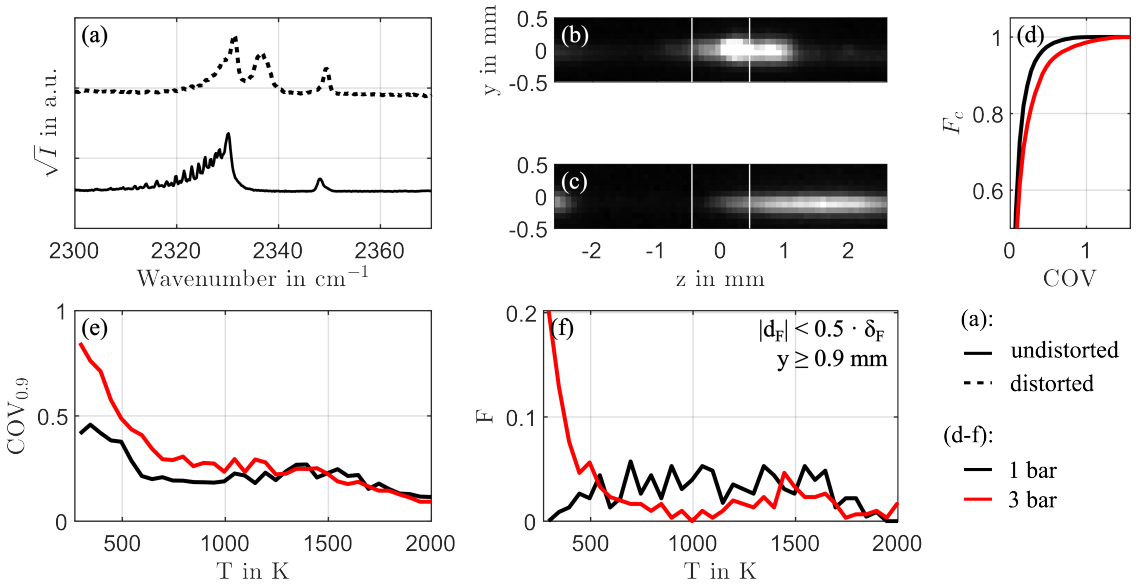

Figure 4.3: Limitations of DP-CARS/CO-LIF setup: (a) distorted and undistorted single-shot DP-CARS spectrum, (b–c) example CO-LIF raw images with saturation and inhomogeneous fluorescence signal, (d) cumulative frequency F_c for COV of CO-LIF raw signal, (e) 90%-quantiles of COV values and (f) frequency of temperatures measured close to the reaction zone. Data in (e) and (f) derived in $\Delta T = 50\,\mathrm{K}$ wide bins.

CO-LIF raw image, as shown in Fig. 4.3(a) and (b). Overall, the ratio of DP-CARS samples that could not be evaluated during post-processing due to these effects was $\approx 28\%$ at 1 bar and $\approx 42\%$ at 3 bar. As described in section 4.2 and 6.2, beam steering at small wall distances and 3 bar furthermore impeded the determination of the wall position with respect to the DP-CARS/CO-LIF probe volume in the reacting flow and prevented measurements at nominal wall distances $y < 0.4\,\mathrm{mm}$.

Besides beam steering, also the finite spatial resolution of the DP-CARS/CO-LIF setup turned out to presumably have an increasing impact on the accuracy of the measurements. This is illustrated in Fig. 4.3 based on an evaluation of the homogeneity of the fluorescence signal in direction of beam propagation (z-direction) in CO-LIF raw images, which is quantified by the coefficient of variance (COV). The COV was calculated from the background-corrected fluorescence signal within the same region of $\Delta z = 0.9\,\mathrm{mm}$ (visualized by white vertical lines in Fig. 4.3(b–c)), which was used within the CO-LIF post-processing procedure. An example CO-LIF raw image with a COV value of ≈ 0.8 is shown in Fig. 4.3(c) and the cumulative frequency (F_c) distribution of the COV of all samples is given in Fig. 4.3(d) for the 1 bar and the 3 bar case. Comparing both operating cases, it is evident that in the 3 bar case the distribution is shifted towards larger COV, which could be attributed to decreased length scales with respect to the size of the probe volume. As large COV indicate an inhomogeneous gas mixture within the probe volume, corresponding X_{CO} values result from averaging of multiple thermochemical states. For the DP-CARS measurement, an inhomogeneous mixture within the overlapped probe volume causes a significant decrease of the measured temperature as the signal depends on the number density of participating molecules squared [103]. Correspondingly, individ-

ual samples with high COV values are associated with low temperatures, as can be seen from the evolution of 90%-quantiles $\mathrm{COV}_{0.9}$ with temperature, derived in $\Delta T = 50\,\mathrm{K}$ wide bins and shown in Fig. 4.3(e). This, in turn, causes low temperatures to be over-represented within the statistical ensemble of thermochemical states obtained from the DP-CARS measurements. This is shown in Fig. 4.3(f) visualizing frequency distributions of temperatures measured closed to the reaction zone ($|d_F| < 0.5 \cdot \delta_F$) and at wall distances $y \geq 0.9$ to reduce the impact of wall heat losses on this analysis. Furthermore, the CO-LIF technique tends to underestimate $\mathrm{X_{CO}}$ as the instantaneous temperature measured with DP-CARS is used for a density-correction of the fluorescence signal. Correspondingly, thermochemical states with highest $\mathrm{X_{CO}}$ in the turbulent flame would be underrepresented within the statistical ensemble obtained from the measurement if it is increasingly affected by inhomogeneous mixtures within the probe volume.

Chapter 5

Characterization of Flow Field and Combustion Dynamics

This chapter provides a characterization of the flow field and the combustion dynamics of the novel pressurized SWQ burner based on a summary of the main results of **Paper I** for the 1 bar and 3 bar case. These results are supplemented with unpublished data of the 5 bar case. First, the non-reacting flow is characterized close to the outlet of the Morel-type nozzle, yielding a specification of the inflow boundary conditions, and at axial positions where FWI occurs focusing on the near-wall region. Next, characteristics of the near-wall flow field under reacting conditions are presented followed by a statistical evaluation of the turbulent flame front. Last, flame front dynamics are investigated and characteristic near-wall flame front topologies are presented.

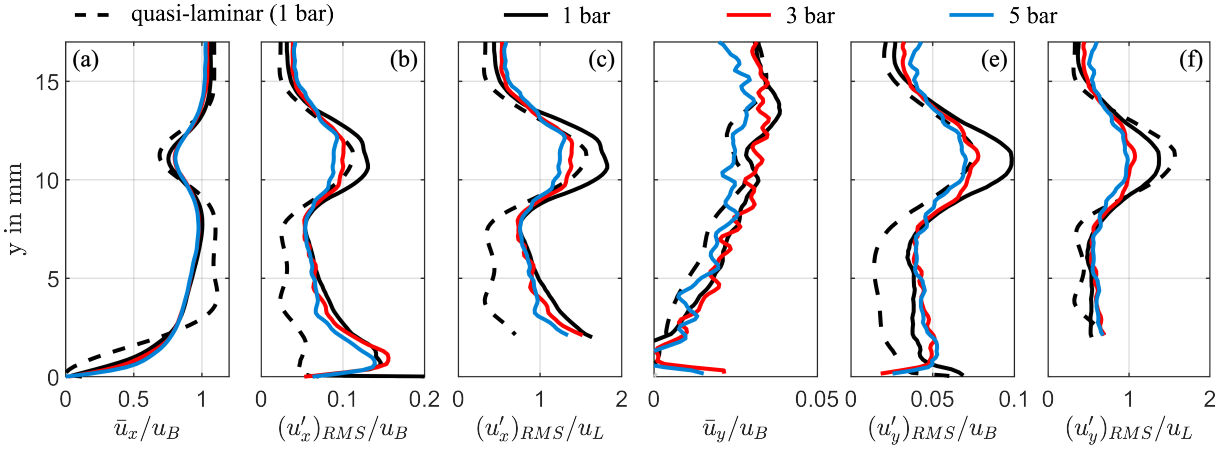

Figure 5.1: Inflow boundary conditions characterized by wall-normal profiles of ensemble-averaged velocity (a,d) and RMS of velocity fluctuations (b,c,e,f) at $x = 30\,\text{mm}$. Velocity data is normalized with the bulk velocity u_B and the laminar flame speed u_L of the corresponding operating case.

5.1 Non-Reacting Flow

5.1.1 Inflow Boundary Conditions

A characterization of the non-reacting flow field close to the Morel-type nozzle outlet was carried out based on low-speed (LS, 50 Hz repetition rate) and low-resolution velocity data provided by PIV measurements (section 4.1). For each operating case, velocity data within a region between $x = 29\,\text{mm}$ to $x = 31\,\text{mm}$ downstream of the ceramic rod was extracted from 500 statistically independent PIV samples and averaged in x-direction to obtain 500 individual wall-normal velocity profiles at $x = 30\,\text{mm}$. This axial position was selected as it is located downstream of the axial region where the surface of the quenching wall transitions from a flat into a convex, cylindrically curved shape (see section 3.1). A statistical evaluation of the data in terms of ensemble-averaged values $\bar{u}$ and root mean squares (RMS) of the instantaneous fluctuations $(u')_{RMS}$ is presented for both (streamwise and wall-normal) velocity components u_x and u_y in Fig. 5.1. Profiles are shown for each operating case defined in Tab. 3.1. Additionally, a *quasi-laminar* case, which corresponds to operation under the conditions of the 1 bar case just without turbulence-generating grid (TG), is included in Fig. 5.1. Velocities are normalized with the bulk velocity u_B to enhance comparability and with the laminar flame speed u_L (see Tab. 3.1) for a rough classification into combustion regimes.

For the ensemble-averaged streamwise velocity $\bar{u}_x$, normalization with u_B causes the profiles of all operating cases in Fig. 5.1(a), except for the quasi-laminar operation, to almost coincide in one line. Moving from large to small wall distances, $\bar{u}_x$ is almost constant at $y > 15\,\text{mm}$, resulting in a nearly top-hat profile, and then drops within the region of the wake of the ceramic rod ($8\,\text{mm} < y < 15\,\text{mm}$). Closer to the wall, the effect of the TG on the flow field becomes clearly visible. While the flow in the quasi-laminar case features a nearly top-hat profile ($4\,\text{mm} < y < 8\,\text{mm}$), the flow field in the other cases seems to be already influenced by the turbulent boundary layer induced by the TG. Furthermore, in close vicinity of the wall ($y < 4\,\text{mm}$), increased turbulence generated by the TG causes appreciably steeper near-wall velocity gradients than in the quasi-laminar case. Correspondingly, as depicted in Fig. 5.1(b), normalized velocity fluctuations within the region of the turbulent boundary layer are significantly increased by a factor of about 2 (at $y = 4\,\text{mm}$) up to about 4 (at $y = 1\,\text{mm}$) for the operation cases with TG, which again differ little from each other. Turbulence intensities $(u')_{RMS}/\bar{u}_x$ (shown in **Paper I**) within the region $4\,\text{mm} < y < 8\,\text{mm}$, where $\bar{u}_x$ is almost constant, are about 6% (with TG) and 3% (quasi-laminar). As shown in Fig. 5.1(c), the ratio $(u')_{RMS}/u_L$ takes values below and above 1 within this region, suggesting that, under reacting conditions, the process could be associated with the transition between wrinkled and corrugated flamelets in the Borghi-Peters regime diagram (section 2.2.3). Profiles of the wall-normal velocity component are given in Fig. 5.1(d–f) for a complete characterization of the flow, but will not be further discussed here.

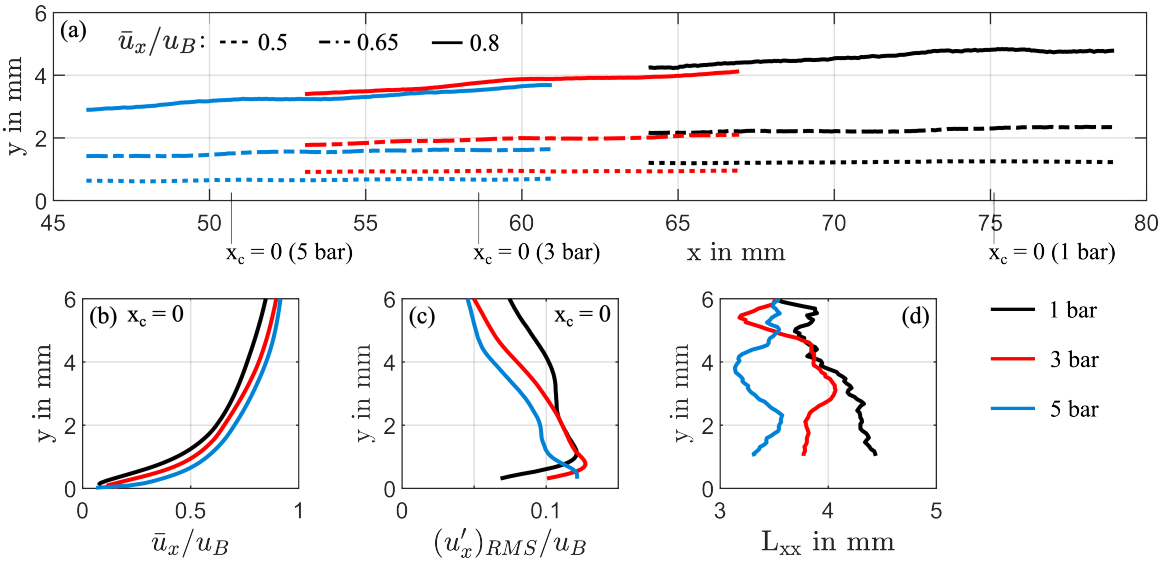

Figure 5.2: Non-reacting near-wall flow field: (a) iso-contours of the normalized mean streamwise velocity for $\bar{u}_x/u_B = [0.5; 0.65; 0.8]$. Wall-normal profiles of (a) mean normalized streamwise velocity, (b) RMS of velocity fluctuations and (c) longitudinal integral length scale at $x_c = 0$.

5.1.2 Near-Wall Flow

The isothermal, non-reacting flow was further examined at axial positions where flame quenching occurs during operation with combustion using velocity data provided by PIV measurements at high resolution and low-speed repetition rate (see section 4.1). A summary of characteristics of the turbulent boundary layer flow is given in Fig. 5.2 for each operating case defined in Tab. 3.1.

In Fig. 5.2(a), iso-contours of the normalized, ensemble-averaged streamwise velocity component are plotted for $\bar{u}_x/u_B = [0.5; 0.65; 0.8]$. The iso-contours of each operating case are shown within different FOVs as, under reacting conditions, flame quenching occurred at slightly varying axial position. Due to differing turbulent flame speeds caused by varying levels of flame wrinkling (see section 5.2.3 and 6.1), the average axial position of flame quenching was shifted in upstream direction by a few millimeter for increasing operating pressure, although u_B/u_L was kept constant for each operating case (section 3.3). From the diagram shown in Fig. 5.2(a) it can be concluded that the growing (in streamwise direction) turbulent boundary layers exhibit decreasing boundary layer thicknesses at increasing operating pressure, as iso-contours are shifted towards the wall. This is in good accordance with fundamental theory on the turbulent boundary layer on a flat plate (section 2.1) predicting a slow reduction of the boundary layer thickness δ at a given position x from the leading edge of the plate with increasing Re following the relation $\delta/x \propto 1/\ln Re$ [70, p. 34]. As iso-contours are closer to the wall, this is associated with increased (normalized) near-wall velocity gradients at higher operating pressure, which is also evident from wall-normal profiles of $\bar{u}_x/u_B$ shown in Fig. 5.2(b). These profiles are extracted from the two-dimensional velocity data at the streamwise position with the highest probability to detect a flame front close to the wall (in the case of reacting con-

ditions). This position represents the origin of a second streamwise coordinate x_c, which is introduced in **Paper I** (see also section 5.2.2) to allow for better comparison of the individual operating cases. By transforming $\bar{u}_x$ and y into the dimensionless quantities u^+ and y^+ following Eq. 2.4−2.5, the thickness of the viscous sublayer ($y^+ = 5$) could be identified for the 1 bar (about 450 μm) and the 3 bar case (about 300 μm). While for these two operating cases the viscous sublayer could be resolved down to $y^+ = 2$, this was not possible for the 5 bar case as the viscous sublayer thickness was further reduced. Wall-normal profiles of normalized velocity fluctuations derived at the same axial position x_c are shown in Fig. 5.2(c). In all three operating cases, velocity fluctuations increase towards the wall, but no clear trend with increasing pressure can be observed. Longitudinal integral length scales L_{xx} derived according to Eq. 2.6 and 2.7 are presented in Fig. 5.2(d). The shown profiles visualize L_{xx} as a function of y for the most upstream position in the FOV of each operating case, to make use of the data in the whole FOV for the two-point correlation. At wall distances $y < 4$ mm, a clear trend of decreasing L_{xx} with increasing operation pressure can be seen. Correspondingly, the flow field at higher operating pressures is characterized by a reduced size of the larger eddies.

5.2 Reacting Flow

5.2.1 Near-Wall Flow

Similar to the non-reacting flow, characteristics of the turbulent boundary layer under reacting conditions were assessed based on velocity data provided by PIV measurements with the high-resolution setup conducted at low-speed repetition rate (see section 4.1). However, due to beam steering effects increasingly affecting the measure-

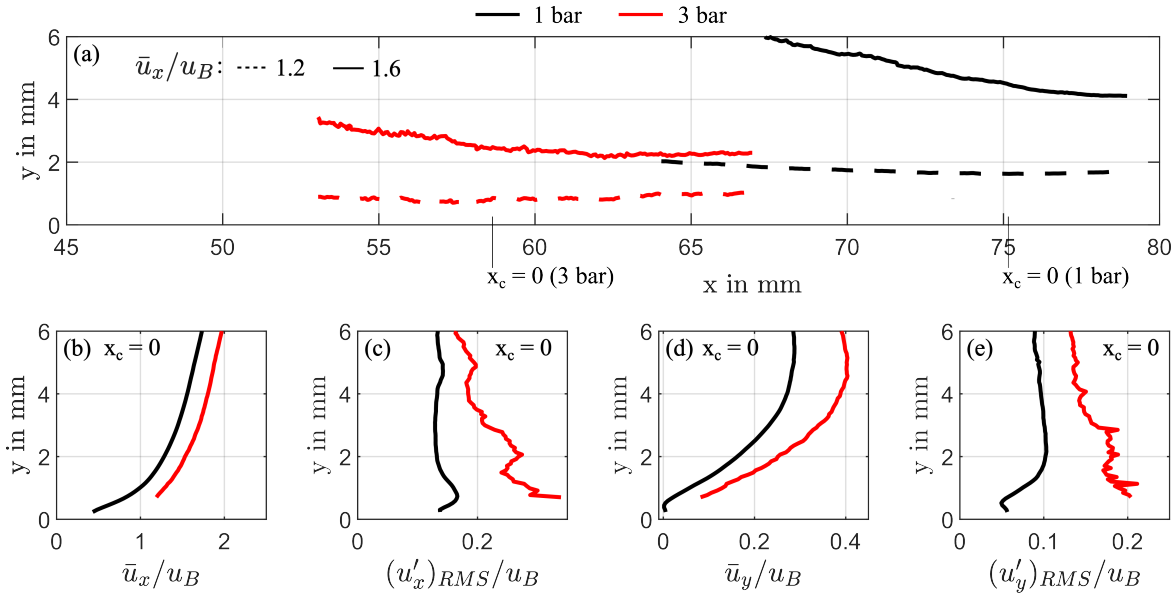

Figure 5.3: Reacting near-wall flow field: (a) iso-contours of the normalized mean streamwise velocity for $\bar{u}_x/u_B = [1.2; 1.6]$. Wall-normal profiles of mean normalized (b) streamwise, (d) wall-normal velocity component and RMS of fluctuations of (c) streamwise, (e) wall-normal velocity component.

ments, as shown in section 4.3, velocity data of the 5 bar case were not considered for analysis. A summary of the results for the 1 bar and the 3 bar case is presented in Fig. 5.3.

Due to the heat release of the chemical reaction accompanied with a significant increase in temperature and a reduction of the gas density, ensemble-averaged streamwise velocities exceed the bulk velocity u_B resulting in normalized velocities $\bar{u}_x/u_B$ larger than 1. Correspondingly, iso-contours of $\bar{u}_x/u_B$ are shown in Fig. 5.3(a) for $\bar{u}_x/u_B = [1.2; 1.6]$ to match the increased velocities. The impact of the combustion on the near-wall flow is clearly evident, as iso-contours are first compressed in streamwise direction and seem to expand again further downstream. In the 3 bar case, both iso-contours are located closer to the wall and to each other compared to corresponding iso-contours of the 1 bar case. Correspondingly, wall-normal profiles of $\bar{u}_x/u_B$ at $x_c = 0$ presented in Fig. 5.3(b), exhibit higher normalized velocities in the 3 bar case for a given wall distance. The same holds true for the wall-normal component of the normalized velocity, shown in Fig. 5.3(d). These observations imply an increased acceleration of the flow close to the wall due to the heat release in the 3 bar case. Normalized velocity fluctuations, shown in Fig. 5.3(c) and (e) for the streamwise and wall-normal direction, respectively, are also significantly increased compared to the non-reacting flow (Fig. 5.2(c)), which could be attributed to fluctuations of the flame front position and the increased velocity of the mean flow motion. Comparing both operating cases, normalized velocity fluctuations are higher in the 3 bar case. As corresponding profiles of the non-reacting flow were quite similar for all operating cases, this could imply an increased impact of the flame on the flow field at elevated pressure.

5.2.2 Flame Front Statistics

A statistical evaluation of the turbulent flame front close to the ceramic rod and in the region of FWI was carried out based on flame front positions extracted from 1000 OH-PLIF images (for each FOV) acquired at low-speed repetition rate (50 Hz).

A summary of this analysis for the region close to the ceramic rod is outlined in Fig. 5.4. Each column corresponds to one operating case (1 bar, 3 bar and 5 bar) with operating pressure increasing from left to right. In the upper row, two-dimensional flame front frequency distributions, in the following referred to as *flame brushes*, are shown. These distributions were derived by averaging binary images of the instantaneous flame fronts, indicating the flame front positions by 1's in an array of 0's, which yielded the frequency of flame front occurrences within the statistical ensemble for every position in the FOV. The y-coordinates with the highest frequency of a flame front occurrence for each position in x-direction in the FOV, derived from the spatially smoothed flame brush, are visualized by a red, dashed line. Another representation of the turbulent flame brush is depicted in the middle row of Fig. 5.5 using iso-contour plots of the mean reaction progress variable $\bar{c}$. The spatial distribution of $\bar{c}$ was derived by averaging binary images of the instantaneous spatial reaction progress c indicating regions of unburned and burned gas by $c = 1$ and $c = 0$, respectively. These two-dimensional fields of $\bar{c}$ were

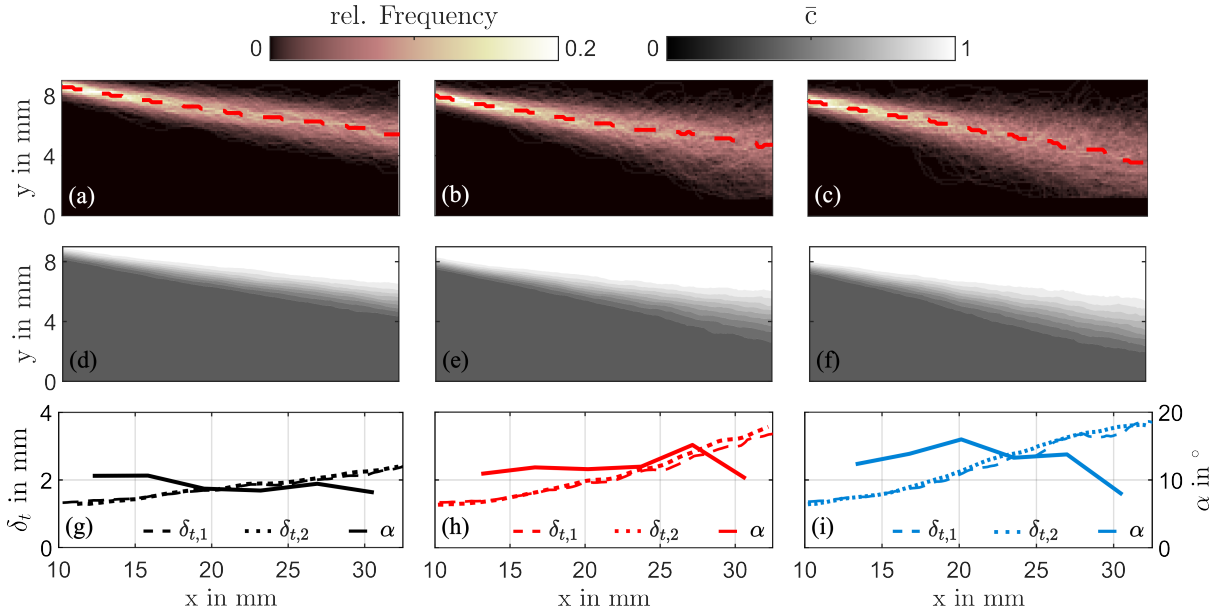

Figure 5.4: Turbulent flame brush close to the ceramic rod: (a–c) spatial distribution of flame front frequency, (d–f) spatial distribution of mean reaction progress variable, (g–i) flame brush thickness and local angle of $\bar{c} = 0.1$ iso-contour with respect to x-axis. Left column: 1 bar; middle: 3 bar; right: 5 bar.

used within the processing procedures for the derivation of the flame surface density, presented in section 6.1.

From these $\bar{c}$-iso-contour, the thicknesses δ_t of the turbulent flame brush were determined using two commonly used definitions: $\delta_{t,1} = 1/max[\partial\bar{c}/\partial y]$ defined as the inverse of the maximum wall normal gradient of $\bar{c}$ [104] and $\delta_{t,2}$, which quantifies the vertical distance between $\bar{c} = 0.9$ and $\bar{c} = 0.1$ [105]. Both are plotted as a function of x in the lower row in Fig. 5.5. As can be also observed from the flame brushes (upper row) and the spatial distributions of $\bar{c}$ (middle row), in each operating case, the flame brushes widen in downstream direction due to the interaction with the turbulent flow field, resulting in an increase of the turbulent flame brush thickness. Comparing δ_t of the different operating cases at a given axial position, this growth of flame brush thickness in downstream direction seems to be fastest in the 5 bar case. Assuming that this corresponds in average to a larger overall area of the turbulent flame front, the ratio of turbulent flame speed and laminar flame speed most likely increases with operating pressure (Eq. 2.13). Correspondingly, the angle between the average flame front and the x-axis (visualized in Fig. 5.4 by the local angle α of the $\bar{c} = 0.1$ iso-contours with respect to the x-axis) also increases with operating pressure resulting in slightly different geometrical configurations for the three operating cases.

Corresponding results of this analysis for the region of FWI were derived as described above and are presented in a similar manner (left: 1 bar; middle: 3 bar; right: 5 bar) in Fig. 5.5. Unlike Fig. 5.4, the conditioned x-coordinate x_c, which was already mentioned before, is used here. This coordinate was deduced from one-dimensional (in x-direction) frequency distributions, derived from the flame brushes by summing up frequency values

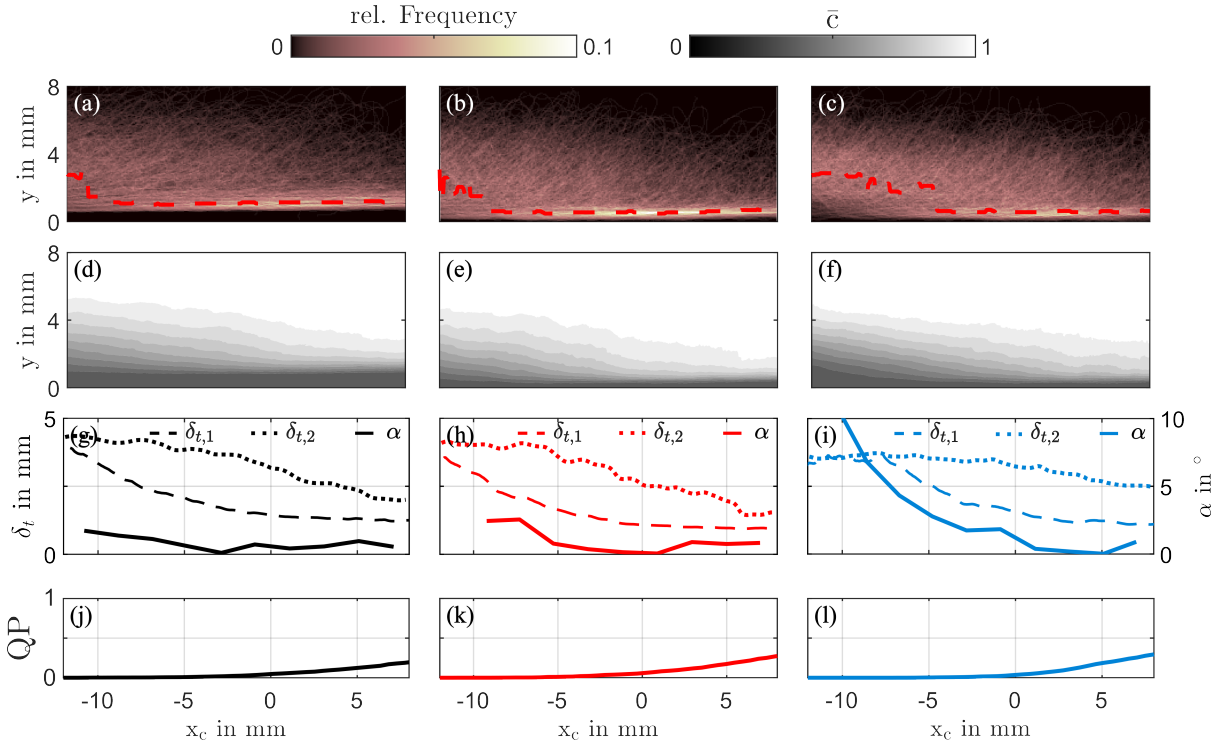

SWQ	HOQ	MZQ	SWQ	HOQ	MZQ	SWQ	HOQ	MZQ
8.8	84.3	6.8	8.4	84.9	6.6	17.8	73.5	8.7

Figure 5.5: Near-wall turbulent flame brush: (a–c) spatial distribution of flame front frequency, (d–f) spatial distribution of mean reaction progress variable, (g–i) flame brush thickness and local angle of $\bar{c} = 0.1$ iso-contour with respect to x-axis, (j–l) quenching probability. Ratio of quenching scenarios in % in the table at the bottom. Left column: 1 bar; middle: 3 bar; right: 5 bar.

within $\Delta x = 700\,\mu$m wide bins (see also **Paper I**). Defining $x_c = 0$ mm at the x-position of the maximum value in the one-dimensional frequency distribution, this conditioned x-coordinate indicates the streamwise position with respect to the location of the highest frequency of flame front occurrence. It is used throughout this cumulative thesis and the included publications for a better comparison of the three operating cases. With increasing operating pressure, this position is shifted in negative x-direction (1 bar: $x = 75.1$ mm; 3 bar: $x = 58.6$ mm; $x = 50.7$ mm). Correspondingly, the angle between wall and flame front takes in average the largest value for the 5 bar case (see Fig. 5.4) and flame fronts are observed with a higher probability at larger wall distances for a given streamwise position $x_c < 0$ (see red, dashed line). As evident from the flame brushes (upper row), independent of operating case, maximum frequency values are observed at axial locations around $x_c = 0$ in a thin, elongated region close to the wall. Comparing the 1 bar case with the operating cases at elevated pressure, this region is shifted towards the wall which is in good accordance with experiments in the literature (see section 2.3) showing the reduction of measured quenching distances at increasing pressure [28]. Within the two-dimensional fields of $\bar{c}$, these regions of high frequencies of flame front occurrences, observed at $x_c \geq 0$, correspond to a reduced distance between adjacent iso-contours. Regarding the flame brush thickness, similar trends can be observed for all operating cases: Far upstream the

flame brush is wide exhibiting an almost constant thickness $\delta_{t,2} \approx 4\,\mathrm{mm}$ and narrows down farther downstream. While in the 5 bar case also $\delta_{t,1}$ remains constant before it starts to decrease (at about $x_c > -7\,\mathrm{mm}$), in the other operating cases $\delta_{t,1}$ already monotonically decreases upstream of this position. This could again be attributed to the slightly different geometrical configurations characterized by larger (in average) angle between flame front and wall at increasing pressure, causing $\delta_{t,1}$ to be first impacted by the presence of the wall at larger x_c. As an instantaneous flame front is more often closer to the wall at increasing x_c, the probability of local flame quenching increases, as visualized in Fig. 5.5(j–l) by the quenching probability QP. It quantifies the ratio of instantaneous OH-PLIF images in which no flame front was detected by the algorithm (section 4.1) downstream of a given streamwise position. The table at the bottom of Fig. 5.5 summarizes the ratio of three different quenching scenarios, defined in the following section 5.2.3 based on certain characteristics of the near-wall flame front topology.

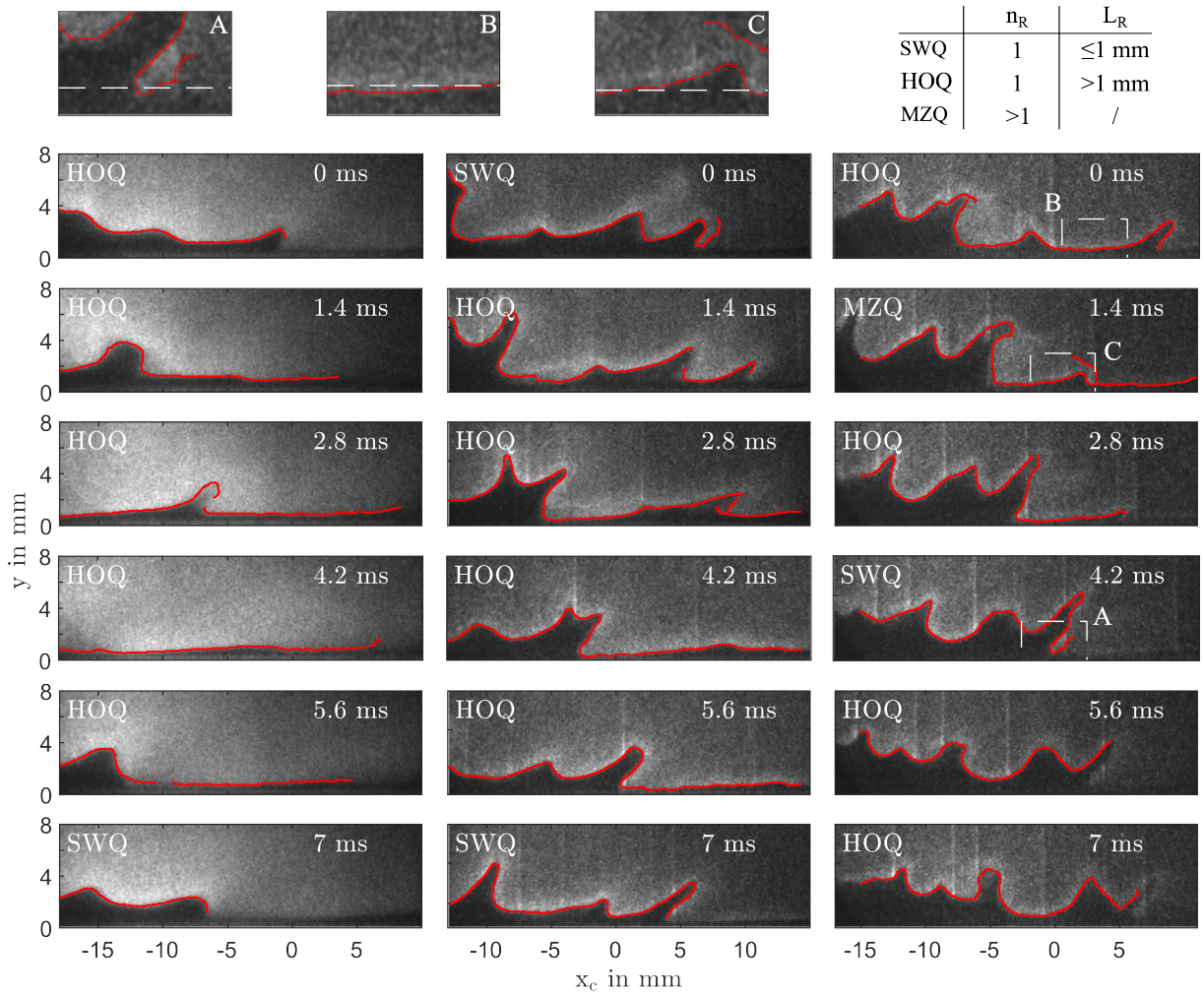

Figure 5.6: Transient near-wall flame front motion illustrated by means of time series of OH-PLIF images with the flame front highlighted as red line. Left column: 1 bar; middle: 3 bar; right: 5 bar.

5.2.3 Flame Front Topologies and Dynamics

Figure 5.6 illustrates the transient motion of the near-wall flame front for each operating case (left column: 1 bar; middle: 3 bar; right: 5 bar) by means of example sequences of six consecutive OH-PLIF raw images provided by high-speed repetition rate (5 kHz) measurements (section 4.1). Every seventh image of a 7 ms time sequence is shown resulting in a time separation of 1.4 ms between two consecutive single-shot images. Flame front positions detected by the post-processing algorithm are highlighted as red line.
Based on the topology of the flame front in close proximity to the surface of the wall, the individual, instantaneous realizations of the side-wall quenching process were classified into three *quenching scenarios*, similar to [34], which appear alternately over time:

- In the side-wall quenching (SWQ)-like scenario the interaction of flame front and wall is limited to a small, almost point-like region (i.e. the quenching point), where the reaction is quenched locally.
- The head-on (HOQ)-like scenario is characterized by one single, extended (in wall-parallel direction) flame front segment which interacts with the wall.
- In the multi-zone quenching (MZQ) scenario the interaction of flame and wall occurs in multiple regions which are spatially separated by pockets of unburned gas.

An automated classification of the individual FWI events was carried out applying the criteria given in Fig. 5.6 based on the number n_R and lengths L_R of unconnected flame front segments in a wall-parallel region close to the wall which was defined by the section of the flame front positioned at minimum wall distance. This procedure is illustrated by one magnified view of the near-wall flame front for each quenching scenario. The quenching scenarios assigned to the individual events presented in Fig. 5.6 are indicated by labels in each OH-PLIF image. As evident from the image sequences, the transient evolution of the near-wall flame front topology is in general characterized by convective transport of large-scale structures, i.e. convex and concave curved flame front segments, in streamwise direction. These structures result from fluctuating turbulent motions interacting with the flame front and are increasingly pronounced as operating pressure is increased. Approaching the wall, the wrinkling of the flame front decreases as pockets of unburned gas are consumed by the reaction resulting in HOQ-like or MZQ events. Due to heat losses to the wall, the extended near-wall reaction zone extinguishes which initiates the transition to a SWQ-like event.

Chapter 6

Experimental Investigation of FWI at Elevated Pressure

In this chapter, the main results of the process-related research on flame-wall interactions at elevated pressure, carried out within the scope of this cumulative dissertation, are summarized. In the first part of this chapter, an analysis of the flame surface density (FSD), first published in **Paper II** for the 1 bar and 3 bar case, is presented. The results are supplemented with unpublished data of the 5 bar case and the analysis is further expanded by including a second approach for the determination of the FSD. In the second part of this chapter, an analysis of thermochemical states during flame-wall interaction at 1 bar and 3 bar operating pressure, first published in **Paper III**, is presented.

6.1 Flame Surface Density

In turbulent, premixed combustion modeling based on the flamelet concept, the flame surface density (FSD) Σ, representing the flame surface area per unit volume, is commonly used to model the mean reaction rate $\bar{\dot{\omega}}$ as the product of Σ, the density of the unburnt mixture ρ_u, the fuel mass fraction $Y_{F,u}$ and the average consumption speed along the flame front s_c [4, p. 224][78, p. 51]:

$$\bar{\dot{\omega}} = \rho_u Y_{F,u} s_c \Sigma \tag{6.1}$$

As the FSD yields a measure for flame front wrinkling due to the turbulent flow field, this approach provides the advantage of decoupling influences of turbulence-combustion interactions, represented by Σ, from complex chemistry effects, included in s_c, on $\bar{\dot{\omega}}$ [4, p. 224]. According to [78, p. 51], the FSD may either be modeled (1) by an algebraic formulation based on a flame crossing frequency (see Eq. 6.3), which was initially used within the *Bray-Moss-Libby (BML)* model for turbulent combustion [106], or (2) using an unclosed transport equation (Σ-equation) stemming from Pope [107] and Candel and Poinsot [108]. Several closures for this equation were proposed in the past [109] including approaches that account for wall quenching by means of a sink term for the FSD [52, 54] derived from DNS data showing the importance of quenching effects on Σ. Inaccuracies of the standard closures for the Σ-equation when applied to FWI were more recently

confirmed by further DNS studies (on a head-on quenching flame) and modifications were proposed [110]. Model development and validation was supported in the past with experimental investigations on FSD carried out mainly in unbounded flames, e.g. [111–113] including experiments at elevated pressure [114, 115]. The impact of walls on the FSD, in contrast, were examined by experiments only occasionally [26, 27] and studies are limited to atmospheric pressure, to the author's best knowledge. For the derivation of the FSD from experimental data, different approaches can be found in the literature, as summarized in [116]. Within the scope of this thesis, two of these approaches were applied.

Figure 6.1 illustrates these two approaches used to derive the flame surface density (FSD) and further flame front characteristics. For this purpose, instantaneous flame front positions and spatial distributions of the reaction progress c extracted from 1000 OH-PLIF images (for each operating case) recorded at low-speed repetition rate (50 Hz, see section 4.1) were used. The first approach, used before, for example, in [26, 117, 118], is outlined on the left in Fig. 6.1. It is based on the determination of the flame front perimeter P in so-called control areas (CA) of size Δx^2 to subsequently derive Σ according to Eq. 6.2. For the following analysis, Δx^2 was set to $0.5 \times 0.5\,\mathrm{mm}^2$ in accordance to recommendations by Donbar et al. [118] as outlined in **Paper II**.

$$\Sigma = \lim_{\Delta x \to 0} \frac{P}{\Delta x^2} \tag{6.2}$$

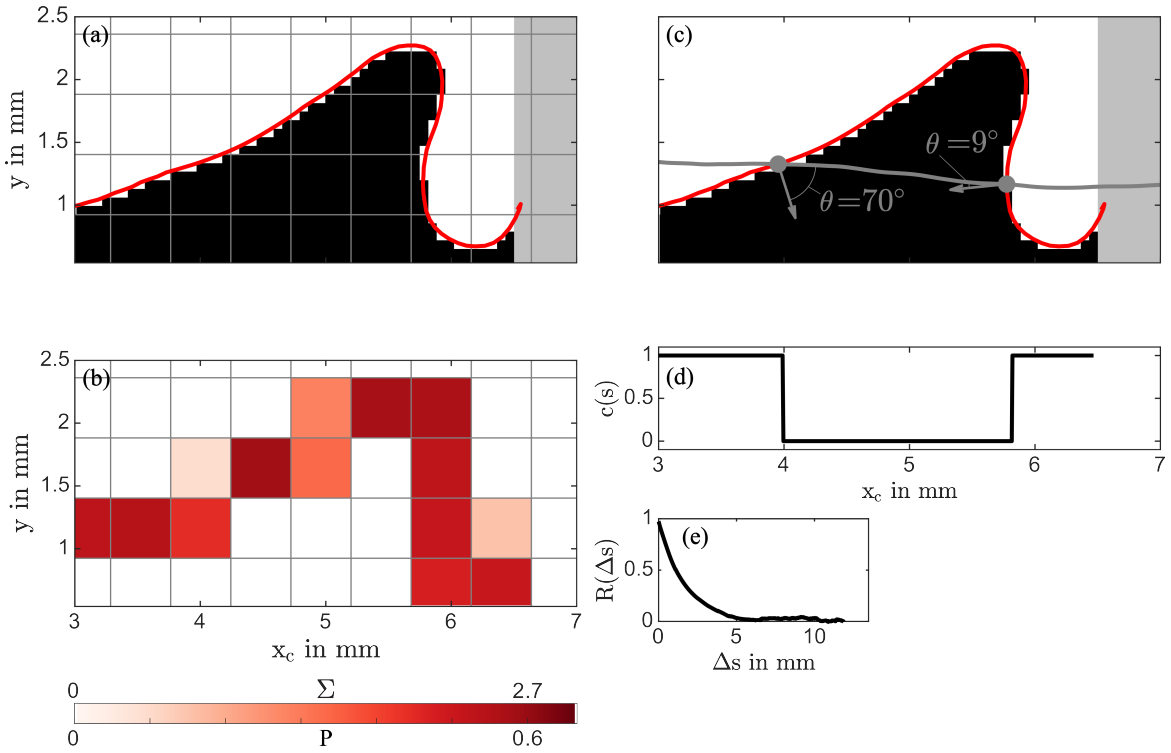

Figure 6.1: Illustration of CA-approach (left) and BML-approach (right). (a) Calculation of flame front perimeter P in CAs to derive (b) spatial distribution of Σ. (c) Identification of intersections between instantaneous flame front with $\bar{c}$ iso-contour. (d-e) Calculation of auto-correlation $R(\Delta s)$ from $c(s)$.

In order to derive P in each CA the flame front contour was first smoothed using a savitzky-golay filtering algorithm yielding a steady flame front shape, as illustrated by the red line in Fig. 6.1(a) and (c) for the selected sample. In a next step, intersections with the boundaries (gray lines) of the individual CAs were identified to calculate the length of the curve section (i.e. the flame front perimeter P) between both intersections. Based on this, an estimate of the curvature κ of the flame front within a CA was calculated by dividing P by the shortest distance between both intersection points. The resulting spatial distribution of P and Σ, comprising values greater than zero only in CAs that contain a section of the flame front, is illustrated in Fig. 6.1(b). To account for quenching of the flame at the wall, two definitions (Σ and Σ_R) of the FSD were used, similar to [26]. These definitions only differ in regions where the flame is already quenched at the wall (visualized by gray coloring in Fig. 6.1(a)), as $\Sigma = \mathrm{NaN}$ and $\Sigma_R = 0$ at these positions. Correspondingly, after ensemble-averaging all distributions of the instantaneous FSD Σ and Σ_R in a last step yielding the mean FSD $\overline{\Sigma}$ and $\overline{\Sigma}_R$, this causes $\overline{\Sigma}_R$ to be either equal to or smaller than $\overline{\Sigma}$. This approach is in the following referred to as *CA-approach*.

The second approach applied to derive the FSD following descriptions in [119] is outlined on the right in Fig. 6.1 for the same pre-processed OH-PLIF image sample and originates from the algebraic formulation initially used within the BML model. Within this approach, the FSD is given as a function of the mean reaction progress variable $\bar{c}$ and defined as the quotient of (1) the mean number of crossings $\bar{n}_s$ per unit length of the instantaneous flame fronts with an iso-contour of $\bar{c}$ and (2) an orientation factor σ_s calculated as the mean cosine value $\overline{\cos\theta}$ of the angles θ between the normal to the instantaneous flame front and the same $\bar{c}$-iso-contour at the positions of intersection:

$$\overline{\Sigma} = \frac{\bar{n}_s}{\sigma_s} = \frac{g\bar{c}(1-\bar{c})}{\sigma_s L_s} \tag{6.3}$$

This equation may be rewritten using the integral length scale of flame front wrinkling L_s and a model constant g, which is in the order of unity [4, p. 227].

In a first step, the algorithm for the derivation of these quantities involved the determination of the number and positions of intersections of the instantaneous, smoothed (savitzky-golay filtered) flame front with each $\bar{c}$-iso-contour for $\bar{c}$ ranging from 0.1 to 0.9 in steps of 0.1. These iso-contours were derived as described in section 5.2.2 and their spatial distribution is illustrated in the middle row of Fig. 5.5 for each operating case. In Fig. 6.1, crossings of the iso-contour for $\bar{c} = 0.8$ with the flame front of the selected sample are highlighted as gray dots. By dividing the number of intersections by the length of the instantaneous flame front, n_s was subsequently deduced for the given sample. In a next step, the normal to the flame front and the tangent to the $\bar{c}$-iso-contour at all intersection points were estimated by fitting a linear polynomial through adjacent points on each curve. From this, θ and $\cos\theta$ were derived subsequently. Evaluating Eq. 6.3 using the ensemble-averages $\bar{n}_s$ and $\sigma_s = \overline{\cos\theta}$ then yielded the mean FSD $\overline{\Sigma}$ for each $\bar{c}$. As stated on the right hand side of Eq. 6.3, $\overline{\Sigma}$ is also related to the integral length scale of flame front wrinkling L_s which was subsequently derived by further post-processing of the data according to [119]. For this purpose, a two-dimensional interpolation was carried out on

each instantaneous distribution of c at the positions along each $\bar{c}$-iso-contour of length L_c yielding 0-1 square wave functions $c(s)$ as presented for the selected sample in Fig. 6.1(d). The mean autocorrelation $R^*(\Delta s)$ was then derived as

$$R^*(\Delta s) = \frac{1}{N} \sum_{N} f_w(\Delta s) \sum_{s=0}^{L_c} c(s)c(s+\Delta s) \tag{6.4}$$

$$R(\Delta s) = \frac{R^*(\Delta s) - \bar{c}^2}{\bar{c}(1-\bar{c})} \tag{6.5}$$

$$L_s = \int_0^{\Delta s_0} R(\Delta s) d\Delta s \tag{6.6}$$

by averaging the autocorrelation functions over $N = 1000$ samples using a weighting function $f_w(\Delta s) = 1/(L_c - \Delta s)$. Subsequently, $R^*(\Delta s)$ was normalized to $R(\Delta s)$ according to Eq. 6.5 (for more detailed information on f_w and the normalization function the reader is referred to [119]). In a last step, L_s was calculated using Eq. 6.6 by integration of $R(\Delta s)$ from $\Delta s = 0$ to $\Delta s_{0.1}$, the smallest value of Δs, where $R(\Delta s) \leq 0.1$. This approach is in the following referred to as *BML-approach*.

Results of the evaluation following both approaches carried out on the flame brush close to the ceramic rod (see Fig. 5.4) are summarized in Fig. 6.2. As the impact of the wall on flame propagation is assumed to be low at these streamwise positions, the results in this figure are intended to provide the FSD of the undisturbed flame serving as a reference for the analysis of the FSD of the flame interacting with the wall, presented later in this section. For this purpose, profiles of $\overline{\Sigma}$ derived from the CA-approach (solid lines) are presented as a function of y and $\bar{c}$ at two different streamwise positions $x = 20\,\text{mm}$ and $x = 30\,\text{mm}$. The latter were derived by interpolating $\overline{\Sigma}(x,y)$ on an equally spaced $\bar{c}(x_c,y)$-grid and subsequently averaging $\overline{\Sigma}(x,\bar{c})$ in streamwise direction within segments of $\Delta x_c = 2\,\text{mm}$ length. Profiles of $\overline{\Sigma}(\bar{c})$ provided by the BML-approach are visualized as dashed-dotted lines. Additionally, the integral length scale of flame front wrinkling L_s is given for each operating case. In the spatial domain, the profiles of $\overline{\Sigma}$ are symmetric with respect to the maximum exhibiting a narrow shape at $x = 20\,\text{mm}$, which broadens farther downstream at $x = 30\,\text{mm}$, as the thickness of the flame brush increases (see Fig. 5.4). These profiles are similar to those observed in an unbounded V-flame [113] and a side-wall quenching V-flame at large wall distances [9]. With increasing operating pressure, the peak location is shifted towards the wall since the flame brush is located closer to the wall and the maximum value of $\overline{\Sigma}$ decreases as the flame brush thickness increases. In the

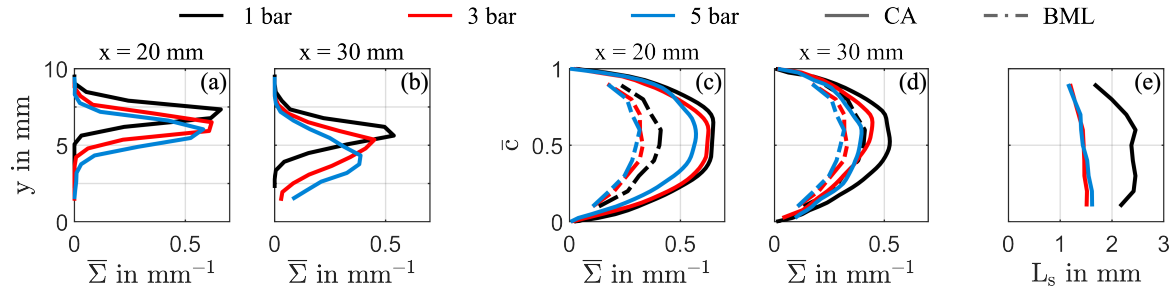

Figure 6.2: Profiles of mean FSD within the region close to the ceramic rod as a function of (a-b) y and (c-d) $\bar{c}$. Integral lengthscales of flame front wrinkling in (e).

$\bar{c}$-space, profiles of $\overline{\Sigma}$ take a nearly parabolic shape as predicted in the BML-formulation in Eq. 6.3 and are comparable in shape to those previously found in unbounded V-flames [27, 111, 117] and Bunsen flames [112, 120]. Comparing profiles of both approaches, $\overline{\Sigma}$ values derived from the second approach are clearly reduced at $x = 20\,\text{mm}$, but differences almost vanish at $x = 30\,\text{mm}$. Deviations between both approaches were also reported in [116] for a freely-propagating flame and may result from a reduced accuracy of the BML-approach in regions where the flame is only slightly wrinkled [116], i.e. close to the ceramic rod. Integral length scales of flame front wrinkling L_s are almost independent of $\bar{c}$ similar to results from experiments on a Bunsen flame [119]. With increasing operating pressure, L_s decreases and thus exhibits the same trend as the longitudinal integral length scale L_{xx} (see Fig. 5.1).

Figure 6.3 summarizes the results obtained from analysis of the data in the region of FWI following the CA-approach. Profiles of $\overline{\Sigma}$ and $\overline{\Sigma}_R$ at five different streamwise positions between $x_c = -10$ and $x_c = 8\,\text{mm}$ are presented for each operating case as a function of y (upper row) and $\bar{c}$ (middle row). $\overline{\Sigma}(\bar{c})$ and $\overline{\Sigma}_R(\bar{c})$ were derived as describe above. The impact of the wall on $\overline{\Sigma}$ and $\overline{\Sigma}_R$ is clearly evident from the evolution of corresponding profiles in downstream direction: At $x_c = -10\,\text{mm}$, where the frequency of flame front occurrence close to the wall is not yet significantly increased (see flame brush in Fig. 5.5), the profiles indicate a broad distribution of the FSD in the spatial domain. As the quenching probability is close to zero (see Fig. 5.5), profiles of $\overline{\Sigma}$ and $\overline{\Sigma}_R$ are indistinguishable. For the 5 bar case, the distribution exhibits a nearly symmetric

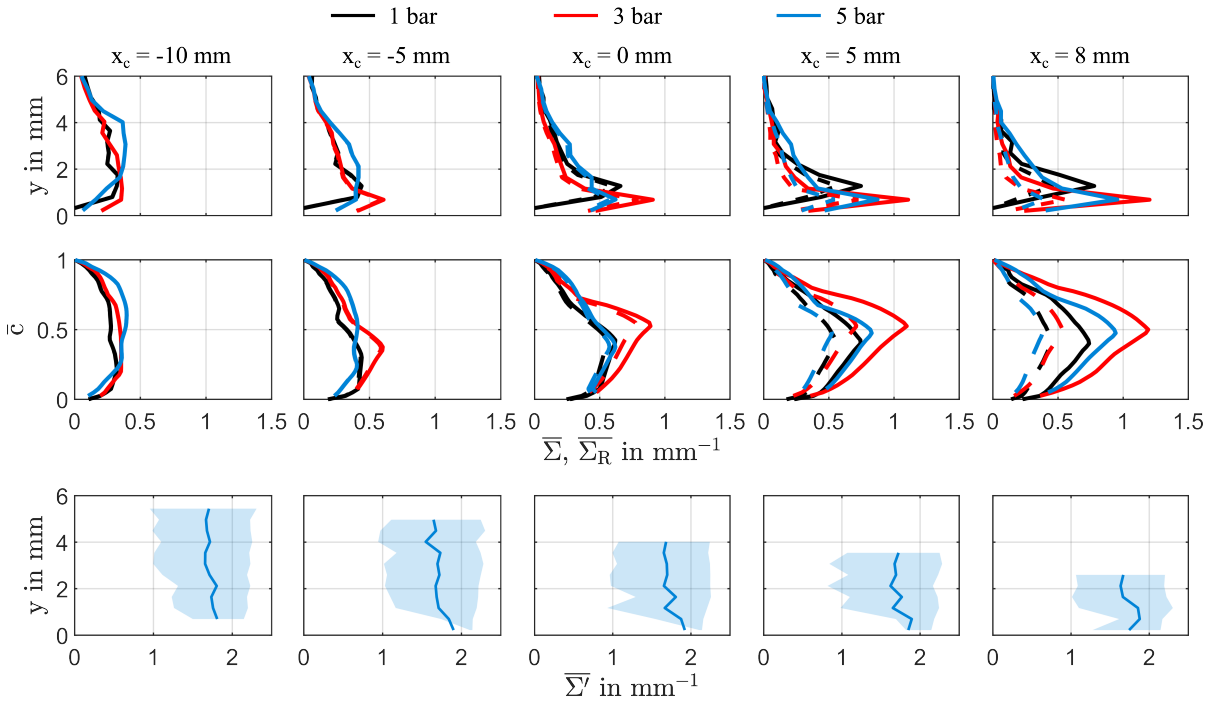

Figure 6.3: Evolution of the FSD (derived following the CA-approach) in streamwise direction: profiles of mean FSD $\overline{\Sigma}$ (solid) and $\overline{\Sigma_R}$ (dashed) as functions of y (top row) and $\bar{c}$ (middle row). Wall-normal profiles of flame front-conditioned FSD $\overline{\Sigma'}$ (lower row, only 5 bar case is shwown here). Boundaries of colored areas indicate 0.25- and 0.75-quantiles of Σ'.

shape as observed for an unbounded V-flame [113] and a side-wall quenching V-flame at large wall distances [9]. The corresponding profile in the $\bar{c}$-space shows a nearly parabolic shape as it was observed closer to the ceramic rod in Fig. 6.2. Profiles of the two other operating cases (1 bar and 3 bar) on the contrary deviate more clearly from those of unbounded flames indicating a stronger influence of the wall on flame propagation already at this streamwise position which also causes a stronger reduction of the flame brush thickness $\delta_{t,1}$ (see Fig. 5.5). Farther downstream, the profiles in the spatial domain exhibit a clearly asymmetric shape with the maximum being shifted towards the wall and increasing in downstream direction. As outlined in **Paper II**, based on a *flame front-conditioned* evaluation of the FSD (for the 1 bar and 3 bar case), this increase of $\overline{\Sigma}$ close to the wall is rather due to a decrease of the flame brush thickness, corresponding to an increasing frequency of flame front occurrences close to the wall (see Fig. 5.5), than due to increased flame front wrinkling. On the contrary, an evaluation of κ for the flame front in the whole field yielded a 95%-quantile $\kappa_{0.95}$ of 1.028 (1 bar), 1.066 (3 bar) and 1.086 (5 bar), respectively, suggesting that the influence of local flame front curvature on $\overline{\Sigma}$ and $\overline{\Sigma}_R$ might increase with operating pressure but remains low for all operating cases. Comparing the estimates of the integral lengthscale of flame front wrinkling L_s, presented below in Fig. 6.4, with the CA size Δx, this is a result one would expect. Based on the flame front-conditioned FSD $\overline{\Sigma'}$ (CAs without flame front are omitted within the ensemble-average) presented in **Paper II** for the 1 bar and 3 bar case, it was concluded that flame front wrinkling is rather reduced close to the wall, as in most cases the flame front takes an elongated wall-parallel shape (corresponding to $P = \Delta x$ and $\Sigma = 1/\Delta x = 2\,\mathrm{mm}^{-1}$), similar to observations made in an atmospheric, side-wall quenching V-flame [9]. Results of this flame front-conditioned evaluation carried out on data of the 5 bar case are presented in the lower row of Fig. 6.3 showing similar trends as for the other operating cases since $\overline{\Sigma'}$ approaches $1/\Delta x$ close to the wall. At $x_c = 5\,\mathrm{mm}$ and $x_c = 8\,\mathrm{mm}$, however, a higher variability of Σ' is observed as the interquartile range, visualized by the colored area, is increased and the 25%-quantile is shifted to lower values. This corresponds to an increased number of instantaneous flame fronts deviating from a wall-parallel shape at the given streamwise position close to the wall including samples where the flame front passes the CA only partly resulting in smaller values of P and Σ. Correspondingly, the maximum value of $\overline{\Sigma}$ (profiles in upper row) in the 5 bar case is slightly reduced compared to the 3 bar case, due to (1) a larger flame brush thickness $\delta_{t,1}$ (see Fig. 5.5) and (2) a slightly reduced $\overline{\Sigma'}$. The mean FSD $\overline{\Sigma}(\bar{c})$ also exhibits a significant change with increasing x_c as the maximum value increases and profiles first become (more) asymmetric before taking a nearly symmetric shape again ($x_c = 8\,\mathrm{mm}$). Both observations, asymmetric [9] and symmetric shapes [27] of $\overline{\Sigma}(\bar{c})$ in side-wall quenching V-flames were previously reported. In the latter case, the profiles even retained a parabolic shape. This is obviously not the case for the profiles presented in Fig. 6.3 which, however, could be due to high spatial gradients $\partial\bar{c}/\partial y$ and the limited resolution of the optical setup. As the probability of flame quenching increases in downstream direction, $\overline{\Sigma}$ and $\overline{\Sigma}_R$ start to deviate at $x_c \geq 0\,\mathrm{mm}$. Comparing corresponding profiles at $x_c = 5\,\mathrm{mm}$ and $x_c = 8\,\mathrm{mm}$, the difference between $\overline{\Sigma}$ and $\overline{\Sigma}_R$ is significantly more pronounced for both operating cases at pressures above atmospheric.

Supplementing the results of the CA-approach, Fig. 6.4 summarizes outcomes of the analysis following the BML-approach including results on the FSD and further characteristics of the flame front topology in the region of FWI. As described above, this analysis yields the FSD and other quantities only as functions of $\bar{c}$ which are derived for the whole FOV. Thus, the impact of the wall on the flame propagation is reflected by (1) the evolution of these quantities with decreasing $\bar{c}$, which may be interpreted as a wall-normal coordinate, and (2) differences compared to the results obtained from the analysis of the turbulent flame front close to the ceramic rod (see Fig. 6.2). Comparing frequency distributions $F(\theta)$ of the acute angle θ between flame front normal and $\bar{c}$-isoline shown for $\bar{c} = 0.8$ (solid lines) and $\bar{c} = 0.2$ (dashed-dotted lines), the growing number of wall-parallel flame fronts close to the wall is evident: For $\bar{c} = 0.2$, the frequency distributions of θ are broad and indicate a decreasing frequency for $\theta \to 90°$, which corresponds to a flame front aligned parallel to the $\bar{c}$-isoline at the position of intersection. This, in turn, roughly corresponds to a wall-parallel flame front, as the local angle between $\bar{c}$-isolines and the wall surface are small and further decrease in downstream direction (see Fig. 5.5). For $\bar{c} = 0.8$, in contrast, the frequency of larger angles θ significantly increases as the distributions show a distinct maximum for $\theta \approx 75°$. This observation is in good accordance with the results of the analysis of the flame-front conditioned FSD, shown in Fig. 6.3. From the ensemble of θ values, $1/\overline{\cos\theta}$ was derived in a next step. This quantity increases for $\bar{c} \to 0$ as θ in average takes larger values. Using $1/\overline{\cos\theta}$ and the mean number of crossings per unit length n_s, $\overline{\Sigma}$ was subsequently derived and is presented in Fig. 6.4. In contrast to the $\overline{\Sigma}(\bar{c})$-profiles derived with the CA-approach in Fig. 6.3, $\overline{\Sigma}$ is not significantly increased compared to the FSD closer to the ceramic rod (Fig. 6.2) and, hence, rather no impact of the wall is observed here. This might be due to the fact that $\overline{\Sigma}$ is derived for the full FOV which includes regions where the flame is still rather unaffected by the wall. Comparing profiles of L_s in Fig. 6.4 with corresponding profiles in Fig. 6.2, relaminarization is observed as are L_s higher in the region of FWI.

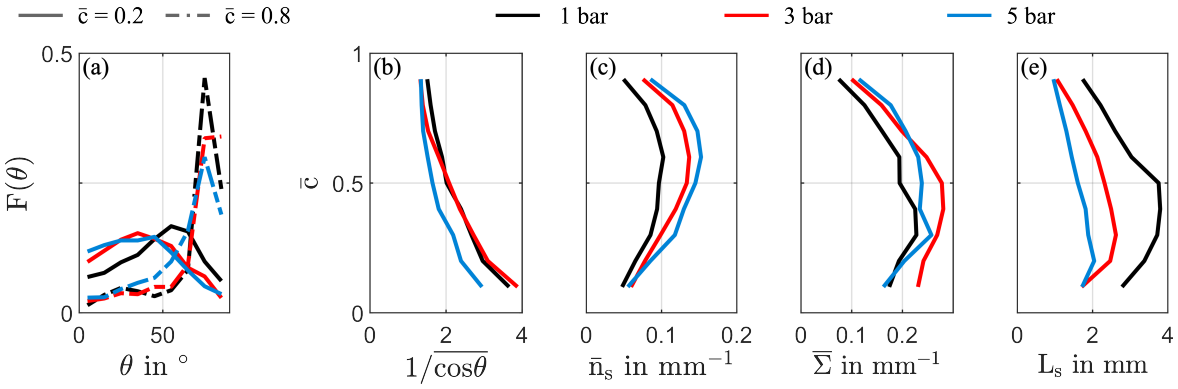

Figure 6.4: FSD and geometric properties of the flame front deduced from the BML-approach: (a) frequency distributions of θ calculated in bins of 10° width. Profiles of (b) $1/\cos\theta$, (c) $\bar{n}_s$, (d) $\overline{\Sigma}$ and (e) L_s as functions of $\bar{c}$.

6.2 Near-Wall Thermochemistry

During FWI, not only topological characteristics, such as the flame surface density, are affected by the presence of the wall, but also the thermochemical structure of the flame, as shown in section 2.2.2 for a laminar, freely-propagating flame, is modified. Caused by the coupling of chemical reactions with convective heat and mass transport, local thermochemical states in the vicinity of the wall are influenced [5]. While first experimental investigations on the thermochemistry during FWI, showing the impact of the wall on combustion, date back to the 1980s, the number of experimental studies is still very limited, as reviewed in [5] and summarized in section 1.2. To the best of the author's knowledge, except for [36], all of the mentioned studies focused on FWI at laminar flow conditions only or addressed the impact of turbulence only to some extent [10, 11]. The only studies known to the author which include experiments on FWI at elevated pressure are focused on turbulent boundary layer phenomena [21, 22]. The near-wall thermochemistry measurements presented in the following are therefore assumed to be the first attempt to explore thermochemical states during FWI at elevated pressure.

Results of the near-wall thermochemistry measurements (section 4.2) are presented in Fig. 6.5 by means of scatter plots visualizing correlations of the gas-phase temperature T and mole fractions X_{CO} and X_{CO_2} of carbon monoxide and carbon dioxide. The individual single-shot samples are color-coded with the minimum distance d_F between the probe volume location and the flame front, indicating the local instantaneous reaction progress through the sign (unburned: $d_F < 0$; burned: $d_F > 0$). Thermochemical states of an adiabatic laminar flame derived from the adiabatic simulation (CANTERA, see section 4.2) are visualized as red line and shown for reference. The measurements were carried out at 1 bar and 3 bar operating pressure and results for both operating cases are summarized in Fig. 6.5. Due to increasing beam steering effects impairing accuracy and precision of the measurement techniques and impeding an accurate determination of the probe volume position (see section 4.3), no measurements were performed for the 5 bar operating case. Furthermore, beam steering results in an increasing number of deflected laser beams impinging on the quenching wall and causing an intense broadband radiative emission which could potentially damage the detection systems. For this reason, in the 3 bar case measurements were only carried out at nominal wall distances $y \geq 0.4\,\mathrm{mm}$. For the 1 bar case, scatter plots of thermochemical states are shown for nominal wall distances down to $y = 0.1\,\mathrm{mm}$. Additional scatter plots showing thermochemical states at wall distances $y > 0.85\,\mathrm{mm}$ as well as correlations of X_{CO} and X_{CO_2} may be found in **Paper III**.

Comparing both operating cases in Fig. 6.5, similar trends can be observed for (1) the evolution of scatter plots with increasing wall distance y and (2) the distribution of thermochemical states for increasing d_F at a fixed wall distance. Regarding the latter, a positive correlation between T and d_F is observed for $d_F < 0$ which in average can be associated with a flame front approaching the wall and the probe volume, respectively. Considering that the HOQ-like is the predominant quenching scenario (see Fig. 5.5 and

description of quenching scenarios in section 5.2.3), the statistically independent scatter might approximately recreate the thermochemistry of a transient head-on quenching event, as it was investigated in [10]. In the 3 bar case, this correlation is less distinct, most likely due to beam steering effects impairing the spatial matching of the DP-CARS and OH-PLIF diagnostics and thus affecting correlations of T, X_{CO} and X_{CO_2} with d_F. For thermochemical states measured clearly in the burned gas ($d_F > 0$) and close to the

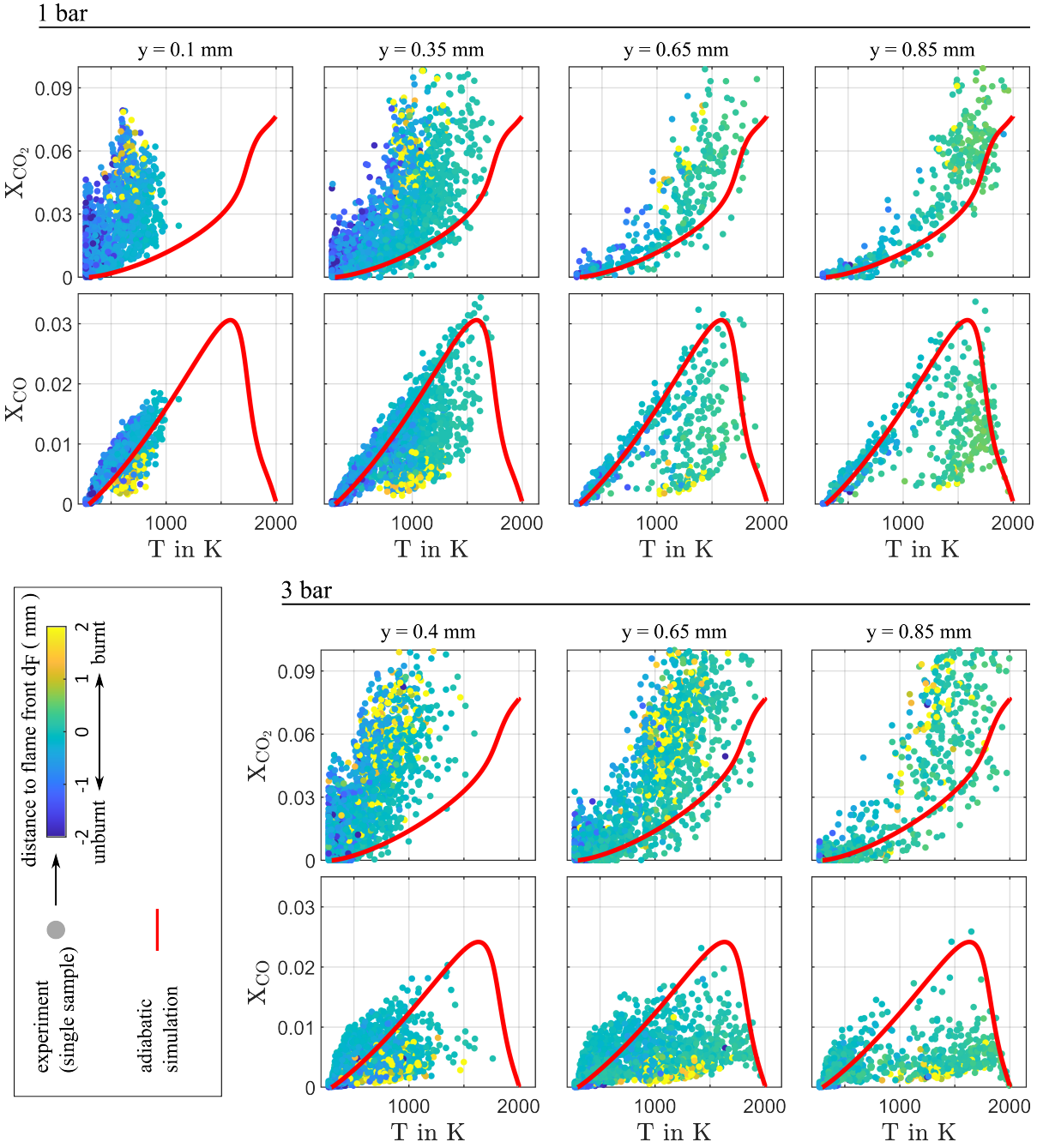

Figure 6.5: Thermochemical states of FWI at atmospheric and elevated pressure (3 bar) under turbulent flow conditions at varying wall distances visualized by means of correlations of X_{CO_2}/T and X_{CO}/T. Adapted from [95].

wall, temperatures decrease again with increasing d_F. These states are either related to an SWQ-like event or to measurements downstream of an HOQ-like flame.
From thermochemical states measured at minimum nominal wall distance, the impact of wall heat losses on thermochemistry is clearly evident, as most samples significantly deviate from the trace of the adiabatic simulation and maximum temperature values clearly fall below the adiabatic flame temperature. An interesting observation in that regard is the existence of thermochemical states featuring high X_{CO_2} at low temperatures, which are observed for both operating cases almost exclusively in the unburned gas mixture and in some cases far away from the flame front. This observation is in agreement with results of thermochemistry measurements in a similar, unconfined SWQ flame [34]. In this study, these thermochemical states could be attributed to a transport mechanism that involved the transport of hot exhaust gases in upstream direction passing the gap between flame tip and the wall. Considering the similarity of both SWQ configurations, similar transport effects could be the reason for the existence of such thermochemical states in the SWQ process under investigation in this thesis. Comparing both operating cases, the existence of such thermochemical states of high X_{CO_2} and low T seem to vanish in the 3 bar case at larger wall distances than in the 1 bar case. This could imply increased convective transport and enhanced turbulent mixing at higher pressure. Regarding correlations of T and X_{CO}, heat losses to the wall, moreover, result in maximum X_{CO} values being significantly reduced compared to the adiabatic simulation and cause CO production and oxidation branches to almost coincide. Similar to observations made in previous studies on atmospheric FWI (laminar & turbulent, SWQ & HOQ) [10, 11, 26, 36], the oxidation branch is more strongly affected by heat losses due to larger chemical time scales of the CO oxidation process compared to CO production [11]. The CO production branch, however, is also slightly shifted towards lower temperatures, which matches with results on an atmospheric SWQ flame [26, 34], but is different from results of the transient HOQ flame [10] showing almost no influence of heat losses on the CO production. For the 3 bar case (at $y = 0.4\,\mathrm{mm}$), the impact of heat losses on the CO production branch seems to be even more pronounced. With increasing wall distance, the influence of wall heat losses decreases as measured thermochemical states approach the trace of the adiabatic simulation. Since maximum X_{CO} values of the adiabatic simulation are reached in the 1 bar case at $y = 0.35\,\mathrm{mm}$ (and at larger wall distances), but not in the 3 bar case (for $y = 0.4\,\mathrm{mm}$), a stronger influence of wall heat losses on the near-wall thermochemistry could be assumed for the higher operating pressure. However, as the region in the state space below the peak of the adiabatic simulation is still filled only very sparsely with experimental scatter at $y > 0.4\,\mathrm{mm}$ (where the impact of heat losses successively diminishes), it needs to be considered, that also properties of the optical measurement technique and the FWI process itself could cause these states to be probed less frequently: As spatial locations of high X_{CO} are associated with high spatial temperature gradients, increased beam steering at higher pressure could result in a rising number of distorted single-shot samples for these thermochemical states. Furthermore, increased flame front wrinkling, which presumably is accompanied by a higher variation of the local 3D flame front orientation, and a reduced thickness of the reaction zone, could result in an inhomogeneous mixture within the CO-LIF probe volume for an increased number of samples. A more comprehensive description of the limitations of the diagnostic technique

with regard to the presented measurements may be found in section 4.3 and in **Paper III**.

For a specific analysis focusing on differences between both operating cases, the experimental data was further examined using conditioned averages derived from the single-shot scatter in the (X_{CO_2}/T)-state space. For this purpose, temperatures and CO_2 mole fractions were divided into bins of $\Delta X_{CO_2} = 0.01$ and subsequently averaged. Individual samples with an inhomogeneous signal within the DP-CARS/CO-LIF probe volume (COV > 0.2) were excluded from the analysis. The effects, described in section 4.3, that could cause a bias towards lower temperatures should therefore not affect the data used in this analysis. Figure 6.6 shows the distribution of these conditioned averages in the state space for nominal wall distances $y \leq 0.85\,\text{mm}$ (left) and $y \geq 2\,\text{mm}$ (right) for both the 1 bar and the 3 bar operating case. Adiabatic simulations, which are quite similar for both operating cases, are also shown. Comparing conditioned averages of both operating cases for similar wall distances (same symbol for both cases), it is evident that at small wall distances thermochemical states are shifted further towards lower temperatures at 3 bar and thus differ more clearly from the adiabatic simulation. This suggests that the near-wall thermochemistry is more strongly affected by heat losses to the wall in the 3 bar case. At larger wall distances, as the impact of heat losses diminishes and conditioned averages approach the adiabatic simulation, differences between both operating cases are less pronounced.

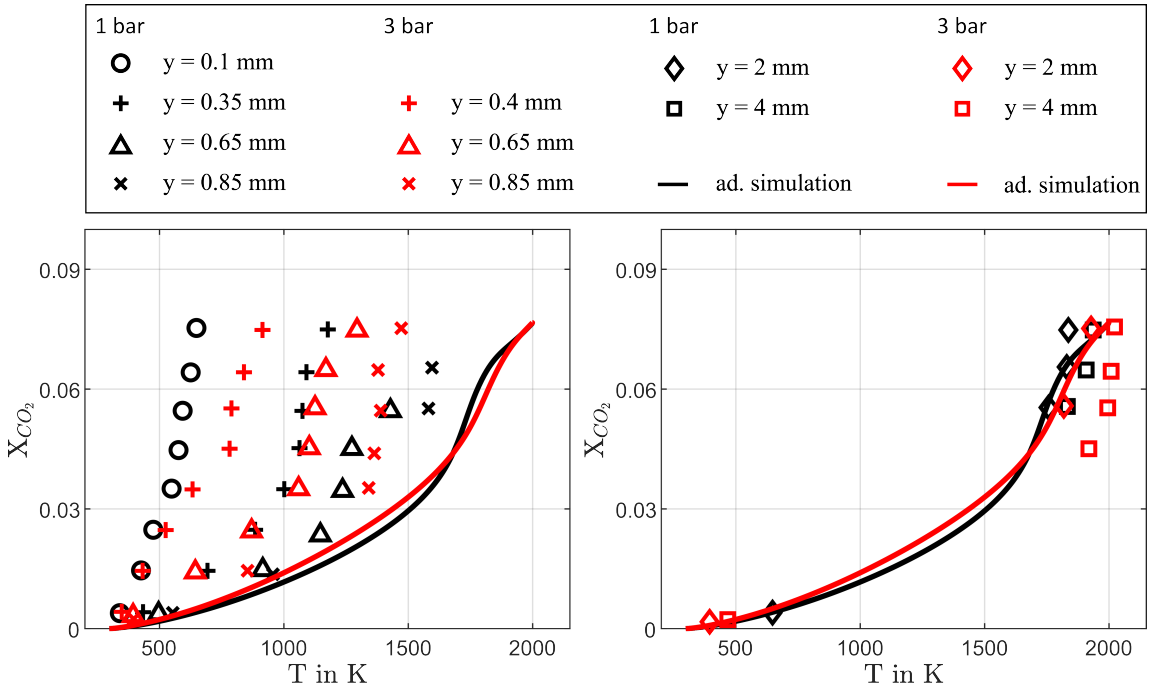

Figure 6.6: Comparison of conditional averaged (within bins of $\Delta X_{CO_2} = 0.01$) thermochemical states of turbulent FWI at atmospheric and 3 bar pressure shown in the X_{CO_2}/T-state space for nominal wall distances $y \leq 0.85\,\text{mm}$ (left) and $y \geq 2\,\text{mm}$ (right). Conditional averages are only plotted for bins comprising at least 30 individual samples. Adapted from [95].

Chapter 7

Summary and Outlook

7.1 Summary

This cumulative dissertation addresses the experimental investigation of turbulent flame-wall interaction (FWI) at elevated pressures and increased Reynolds numbers using advanced laser diagnostics. Experiments were conducted in a novel enclosed test rig, the pressurized side-wall quenching (SWQ) burner, which was designed, built and commissioned within the scope of this thesis. To allow for investigations of effects of elevated pressure on FWI, three different operating cases were defined, with the governing parameter being pressure, varied between atmospheric and 5 bar and the Reynolds number ranging from 8,200 to 20,000. For the investigation of the side-wall quenching process, two comprehensive experimental campaigns were carried out, which involved the application of high- and low-speed particle image velocimetry (PIV) and planar laser-induced fluorescence (LIF) of the hydroxyl radical (OH-PLIF) as well as low-speed LIF of carbon monoxide (CO-LIF) and dual-pump coherent anti-Stokes Raman spectroscopy (DP-CARS). Based on these measurements, first, a characterization of the flow field and the turbulent flame front was conducted based on velocity fields (PIV) and flame front positions (OH-PLIF). This involved the specification of the inflow and the near-wall flow field under non-reacting conditions, which revealed a reduction of the turbulent boundary layer thickness at increasing pressure and Reynolds number, as expected from theory. Under reacting conditions, a compression of the turbulent boundary layer towards the wall due to the impact of the flame was observed, which was more pronounced at elevated pressure. From the instantaneous flame front positions, geometric properties of the turbulent flame brush were examined and transient near-wall flame front motion, which involves the transition between characteristic near-wall flame front topologies, was shown. The flame front position data was subsequently further used for an analysis of the flame surface density (FSD) based on two different approaches to derive this quantity. Results of both approaches clearly showed a relaminarization of the turbulent flame front during FWI which was associated with an increase of flame front segments aligned parallel to the wall surface and the increase of the integral lengthscale of flame front wrinkling. Regarding absolute values of the FSD, however, significant differences between the results of both approaches were evident. While a clear increase in the FSD close to the wall was observed from the first approach, especially for operations at pressures above atmospheric, there was no evident impact of the wall on the FSD derived from the second approach. Furthermore, the near-wall thermochemistry of the turbulent FWI process was explored

based on simultaneous measurements of gas-phase temperature and mole fractions of CO_2 (both obtained from DP-CARS) and CO (CO-LIF). To the author's best knowledge these measurements represent the first experimental implementation of multi-parameter laser diagnostics to probe near-wall thermochemical states of FWI at elevated pressure. From these measurements, the impact of wall heat losses on the flame's thermochemistry at atmospheric and elevated pressure was clearly evident. Close to the wall, temperatures were shifted towards lower values and highest mole fractions of CO cleary fell below peak concentrations of the adiabatic flame. Based on simultaneously measured flame front positions (OH-PLIF), thermochemical states of high CO_2 mole fractions and low temperatures could be identified in the unburned mixture, which supported the theory on near-wall exhaust gas recirculation (EGR), recently proclaimed in a study on an unconfined SWQ burner. A comparison of conditional-averaged thermochemical states measured at atmospharic and 3 bar pressure, finally suggested an increased impact of wall heat losses on thermochemistry at elevated pressure, as temperatures were shifted towards lower values at similar wall distances. Regarding the implementation of the mentioned laser techniques, an important aspect of this work was furthermore the identification of limitations of these diagnostics with respect to the investigation of FWI at elevated pressures. Influences of enhanced beam steering as well as finite resolution effects, which become more pronounced as lengthscales are reduced, turned out to have an serious impact on these diagnostic techniques. Thus, at least for the experimental setups used within this work, limits of their feasibility became clear from the experiences gained within this work.

7.2 Outlook

The experiments and findings presented within this work revealed trends of increasing pressure and Reynolds number on certain aspects of a turbulent side-wall quenching flame. This involved analyses of the flame surface density, thermochemical states and properties of the averaged, reacting turbulent flow field. Further research efforts could include more detailed investigations on the interaction of the instantaneous turbulent flow with the flame and the alteration of the inner layer of the turbulent boundary layer due to the chemical reaction. Furthermore, regarding the exploration of the near-wall thermochemistry, the implementation of laser diagnostic approaches that allow for quantitative measurements of additional species would of course be desirable. However, as discussed within this thesis, near-wall laser diagnostic measurements of such a flame quenching processes become more and more challenging with increasing pressure, as lengthscales are reduced and beam steering effects intensify. This affects accuracy and precision of the applied techniques and complicates the interpretation of the data. Correspondingly, in addition to its actual research focus on the FWI process itself, future work would also need to address methodological aspects dealing with the aforementioned effects. This could involve the optimization of the experimental setup allowing for a mitigation of their influence on the measurement process as well as the estimation of associated uncertainties.

Bibliography

[1] WMO P. Taalas. *State of the global climate 2020*, volume 12464 of *WMO*. World Meteorological Organization (WMO), Genf, 2021.

[2] Intergovernmental Panel on Climate Change. *Climate Change 2022 – Impacts, Adaptation and Vulnerability*. Cambridge University Press, 2023.

[3] International Energy Agency. World Energy Outlook 2022: License: CC BY 4.0 (report); CC BY NC SA 4.0 (Annex A), 2022. https://www.iea.org/reports/world-energy-outlook-2022.

[4] T. Poinsot D. Veynante. *Theoretical and numerical combustion*. Edwards, Philadelphia, 2. ed. edition, 2005.

[5] A. Dreizler B. Böhm. Advanced laser diagnostics for an improved understanding of premixed flame-wall interactions. *Proceedings of the Combustion Institute*, 35(1):37–64, 2015.

[6] M. E. Harris, J. Grumer, G. von Elbe, B. Lewis. Burning velocities, quenching, and stability data on nonturbulent flames of methane and propane with oxygen and nitrogen. *Symposium on Combustion and Flame, and Explosion Phenomena*, 3(1):80–89, 1948.

[7] J. Jarosiński. Flame quenching by a cold wall. *Combustion and Flame*, 50:167–175, 1983.

[8] M. Rißmann, C. Jainski, M. Mann, A. Dreizler. Flame-Flow Interaction in Premixed Turbulent Flames During Transient Head-On Quenching. *Flow, Turbulence and Combustion*, 98(4):1025–1038, 2017.

[9] C. Jainski, M. Rißmann, B. Böhm, A. Dreizler. Experimental investigation of flame surface density and mean reaction rate during flame–wall interaction. *Proceedings of the Combustion Institute*, 36(2):1827–1834, 2017.

[10] M. Mann, C. Jainski, M. Euler, B. Böhm, A. Dreizler. Transient flame–wall interactions: Experimental analysis using spectroscopic temperature and CO concentration measurements. *Combustion and Flame*, 161(9):2371–2386, 2014.

[11] H. Kosaka. *Experimental Investigation of Flame-Wall Interaction by Laser-based Diagnostics*. Universitäts- und Landesbibliothek Darmstadt, Darmstadt, 2018.

[12] S. R. Vosen, R. Greif, C. K. Westbrook. Unsteady heat transfer during laminar flame quenching. *Symposium (International) on Combustion*, 20(1):75–83, 1985.

[13] W. M. Huang, S. R. Vosen, R. Greif. Heat transfer during laminar flame quenching: Effect of fuels. *Symposium (International) on Combustion*, 21(1):1853–1860, 1988.

[14] M. Bellenoue, T. Kageyama, S. A. Labuda, J. Sotton. Direct measurement of laminar flame quenching distance in a closed vessel. *Experimental Thermal and Fluid Science*, 27(3):323–331, 2003.

[15] J. Sotton, B. Boust, S. A. Labuda, M. Bellenoue. HEAD-ON QUENCHING OF TRANSIENT LAMINAR FLAME: HEAT FLUX AND QUENCHING DISTANCE MEASUREMENTS. *Combustion Science and Technology*, 177(7):1305–1322, 2005.

[16] B. Boust, J. Sotton, M. Bellenoue. Unsteady heat transfer during the turbulent combustion of a lean premixed methane–air flame: Effect of pressure and gas dynamics. *Proceedings of the Combustion Institute*, 31(1):1411–1418, 2007.

[17] R. Friedman W. C. Johnston. Pressure Dependence of Quenching Distance of Normal Heptane, Iso-Octane, Benzene, and Ethyl Ether Flames. *The Journal of Chemical Physics*, 20(5):919–920, 1952.

[18] W. A. Daniel. Flame quenching at the walls of an internal combustion engine. *Symposium (International) on Combustion*, 6(1):886–894, 1957.

[19] M. Karrer, M. Bellenoue, S. Labuda, J. Sotton, M. Makarov. Electrical probe diagnostics for the laminar flame quenching distance. *Experimental Thermal and Fluid Science*, 34(2):131–141, 2010.

[20] S. Labuda, M. Karrer, J. Sotton, M. Bellenoue. Experimental Study of Single-Wall Flame Quenching at High Pressures. *Combustion Science and Technology*, 183(5):409–426, 2011.

[21] D. Escofet-Martin, A. O. Ojo, N. T. Mecker, M. A. Linne, B. Peterson. Simultaneous 1D hybrid fs/ps rotational CARS, phosphor thermometry, and CH* imaging to study transient near-wall heat transfer processes. *Proceedings of the Combustion Institute*, 38(1):1579–1587, 2021.

[22] A. O. Ojo, D. Escofet-Martin, J. Collins, G. Falconetti, B. Peterson. Experimental investigation of thermal boundary layers and associated heat loss for transient engine-relevant processes using HRCARS and phosphor thermometry. *Combustion and Flame*, 233:111567, 2021.

[23] F. Foucher, S. Burnel, C. Mounaim-Rousselle, M. Boukhalfa, B. Renou, M. Trinité. Flame wall interaction: effect of stretch. *Experimental Thermal and Fluid Science*, 27(4):431–437, 2003.

[24] E. C. Fernandes I. S. Guerreiro. Time-resolved description of a flame front propagation toward an inclined wall - The effect of local stretch on flame speed. *13th International Symposium on Applications of Laser Techniques to Fluid Mechanics, Lisbon, Portugal*, 2006.

[25] F. Zentgraf, P. Johe, M. Steinhausen, C. Hasse, M. Greifenstein, A. D. Cutler, R. S. Barlow, A. Dreizler. Detailed assessment of the thermochemistry in a side-wall quenching burner by simultaneous quantitative measurement of CO 2 , CO and temperature using laser diagnostics. *Combustion and Flame*, 235:111707, 2022.

[26] C. Jainski, M. Rißmann, B. Böhm, J. Janicka, A. Dreizler. Sidewall quenching of atmospheric laminar premixed flames studied by laser-based diagnostics. *Combustion and Flame*, 183:271–282, 2017.

[27] B. Tayebi, C. Galizzi, J. F. Leone, D. Escudié. Topology structure and flame surface density in flame-wall interaction. *5th European Thermal-Sciences Conference, The Netherlands*, 2008.

[28] B. Boust, J. Sotton, S. A. Labuda, M. Bellenoue. A thermal formulation for single-wall quenching of transient laminar flames. *Combustion and Flame*, 149(3):286–294, 2007.

[29] A. Padhiary, G. Pilla, J. Sotton, M. Bellenoue. Effect of Pressure and Turbulence Intensity on the Heat Flux During Flame Wall Interaction (FWI). *Flow, Turbulence and Combustion*, 111(4):1345–1370, 2023.

[30] C. W. Clendening, W. Shackleford, R. Hilyard. Raman scattering measurements in a side-wall quench layer. *Symposium (International) on Combustion*, 18(1):1583–1590, 1981.

[31] M. Saffman. Parametric studies of a side wall quench layer. *Combustion and Flame*, 55(2):141–159, 1984.

[32] T. Fuyuto, H. Kronemayer, B. Lewerich, J. Brübach, T. Fujikawa, K. Akihama, T. Dreier, C. Schulz. Temperature and species measurement in a quenching boundary layer on a flat-flame burner. *Experiments in Fluids*, 49(4):783–795, 2010.

[33] B. Saggau. Temperature profile measurements at head-on quenched flame fronts in confined CH4/Air and CH3OH/Air mixtures. *Symposium (International) on Combustion*, 20(1):1291–1297, 1985.

[34] F. Zentgraf. *Investigation of Reaction and Transport Phenomena during Flame-Wall Interaction Using Laser Diagnostics*. PhD thesis, Technische Universität Darmstadt, 2022.

[35] A. Bohlin, C. Jainski, B. D. Patterson, A. Dreizler, C. J. Kliewer. Multiparameter spatio-thermochemical probing of flame–wall interactions advanced with coherent Raman imaging. *Proceedings of the Combustion Institute*, 36(3):4557–4564, 2017.

[36] F. Zentgraf, P. Johe, A. D. Cutler, R. S. Barlow, B. Böhm, A. Dreizler. Classification of flame prehistory and quenching topology in a side-wall quenching burner at low-intensity turbulence by correlating transport effects with CO 2 , CO and temperature. *Combustion and Flame*, 239:111681, 2022.

[37] G. Desoutter, B. Cuenot, C. Habchi, T. Poinsot. Interaction of a premixed flame with a liquid fuel film on a wall. *Proceedings of the Combustion Institute*, 30(1):259–266, 2005.

[38] M. Enomoto. Head-on Quenching of a Premixed Flame on the Single Wall Surface. *JSME International Journal Series B*, 44(4):624–633, 2001.

[39] O. A. Ezekoye R. Greif. A comparison of one and two dimensional flame quenching: heat transfer results. *National conference and exposition on heat transfer, Atlanta (GA), USA*, 1993.

[40] D. V. Efimov, P. de Goey, J. A. van Oijen. QFM: quenching flamelet-generated manifold for modelling of flame–wall interactions. *Combustion Theory and Modelling*, 24(1):72–104, 2020.

[41] S. Ganter, C. Straßacker, G. Kuenne, T. Meier, A. Heinrich, U. Maas, J. Janicka. Laminar near-wall combustion: Analysis of tabulated chemistry simulations by means of detailed kinetics. *International Journal of Heat and Fluid Flow*, 70:259–270, 2018.

[42] A. Heinrich, F. Ries, G. Kuenne, S. Ganter, C. Hasse, A. Sadiki, J. Janicka. Large Eddy Simulation with tabulated chemistry of an experimental sidewall quenching burner. *International Journal of Heat and Fluid Flow*, 71:95–110, 2018.

[43] M. Steinhausen, Y. Luo, S. Popp, C. Strassacker, T. Zirwes, H. Kosaka, F. Zentgraf, U. Maas, A. Sadiki, A. Dreizler, C. Hasse. Numerical Investigation of Local Heat-Release Rates and Thermo-Chemical States in Side-Wall Quenching of Laminar Methane and Dimethyl Ether Flames. *Flow, Turbulence and Combustion*, 106(2):681–700, 2021.

[44] C. Strassacker, V. Bykov, U. Maas. REDIM reduced modeling of quenching at a cold wall including heterogeneous wall reactions. *International Journal of Heat and Fluid Flow*, 69:185–193, 2018.

[45] C. Strassacker, V. Bykov, U. Maas. Reduced modeling of Flame-Wall-Interactions of premixed isooctane-air systems including detailed transport and surface reactions. *Proceedings of the Combustion Institute*, 38(1):1063–1070, 2021.

[46] F. Dabireau, B. Cuenot, O. Vermorel, T. Poinsot. Interaction of flames of H2 + O2 with inert walls. *Combustion and Flame*, 135(1-2):123–133, 2003.

[47] P. Popp, M. Smooke, M. Baum. Heterogeneous/homogeneous reaction and transport coupling during flame-wall interaction. *Symposium (International) on Combustion*, 26(2):2693–2700, 1996.

[48] P. Popp M. Baum. Analysis of wall heat fluxes, reaction mechanisms, and unburnt hydrocarbons during the head-on quenching of a laminar methane flame. *Combustion and Flame*, 108(3):327–348, 1997.

[49] T. Zirwes, T. Häber, F. Zhang, H. Kosaka, A. Dreizler, M. Steinhausen, C. Hasse, A. Stagni, D. Trimis, R. Suntz, H. Bockhorn. Numerical Study of Quenching Distances for Side-Wall Quenching Using Detailed Diffusion and Chemistry. *Flow, Turbulence and Combustion*, 106(2):649–679, 2021.

[50] A. Heinrich, S. Ganter, G. Kuenne, C. Jainski, A. Dreizler, J. Janicka. 3D Numerical Simulation of a Laminar Experimental SWQ Burner with Tabulated Chemistry. *Flow, Turbulence and Combustion*, 100(2):535–559, 2018.

[51] M. Steinhausen, T. Zirwes, F. Ferraro, A. Scholtissek, H. Bockhorn, C. Hasse. Flame-vortex interaction during turbulent side-wall quenching and its implications for flamelet manifolds. *Proceedings of the Combustion Institute*, 39(2):2149–2158, 2023.

[52] T. Poinsot, D. Haworth, G. Bruneaux. Direct simulation and modeling of flame-wall interaction for premixed turbulent combustion. *Combustion and Flame*, 95(1-2):118–132, 1993.

[53] G. Bruneaux. Flame-wall interaction simulation in a turbulent channel flow. *Combustion and Flame*, 107(1-2):27–36, 1996.

[54] G. Bruneaux, T. Poinsot, J. H. Ferziger. Premixed flame–wall interaction in a turbulent channel flow: budget for the flame surface density evolution equation and modelling. *Journal of Fluid Mechanics*, 349:191–219, 1997.

[55] T. M. Alshaalan C. J. Rutland. Turbulence, scalar transport, and reaction rates in flame-wall interaction. *Symposium (International) on Combustion*, 27(1):793–799, 1998.

[56] T. Alshaalan C. J. Rutland. Wall heat flux in turbulent premixed reacting flow. *Combustion Science and Technology*, 174(1):135–165, 2002.

[57] U. Ahmed, N. Chakraborty, M. Klein. Scalar Gradient and Strain Rate Statistics in Oblique Premixed Flame–Wall Interaction Within Turbulent Channel Flows. *Flow, Turbulence and Combustion*, 106(2):701–732, 2021.

[58] A. Gruber, R. Sankaran, E. R. Hawkes, J. H. Chen. Turbulent flame–wall interaction: a direct numerical simulation study. *Journal of Fluid Mechanics*, 658:5–32, 2010.

[59] R. Palulli, D. Brouzet, M. Talei, R. Gordon. A comparative study of flame-wall interaction and flame-cooling air interaction. *International Journal of Heat and Fluid Flow*, 92:108888, 2021.

[60] M. Steinhausen, T. Zirwes, F. Ferraro, S. Popp, F. Zhang, H. Bockhorn, C. Hasse. Turbulent flame-wall interaction of premixed flames using Quadrature-based Moment Methods (QbMM) and tabulated chemistry: An a priori analysis. *International Journal of Heat and Fluid Flow*, 93:108913, 2022.

[61] Y. Luo, M. Steinhausen, D. Kaddar, C. Hasse, F. Ferraro. Assessment of flamelet manifolds for turbulent flame-wall interactions in large-eddy simulations. *Combustion and Flame*, 255:112923, 2023.

[62] C. K. Westbrook, A. A. Adamczyk, G. A. Lavoie. A numerical study of laminar flame wall quenching. *Combustion and Flame*, 40:81–99, 1981.

[63] C. Hasse, M. Bollig, N. Peters, H. A. Dwyer. Quenching of laminar iso-octane flames at cold walls. *Combustion and Flame*, 122(1-2):117–129, 2000.

[64] R. Owston, V. Magi, J. Abraham. Interactions of hydrogen flames with walls: Influence of wall temperature, pressure, equivalence ratio, and diluents. *International Journal of Hydrogen Energy*, 32(12):2094–2104, 2007.

[65] B. Yenerdag, Y. Minamoto, K. Aoki, M. Shimura, Y. Nada, M. Tanahashi. Flame–wall interactions of lean premixed flames under elevated, rising pressure conditions. *Fuel*, 189:8–14, 2017.

[66] K. Niemietz, L. Berger, M. Huth, A. Attili, H. Pitsch. Direct numerical simulation of flame-wall interaction at gas turbine relevant conditions. *Proceedings of the Combustion Institute*, 39(2):2209–2218, 2023.

[67] P. Johe, F. Zentgraf, M. Greifenstein, M. Steinhausen, C. Hasse, A. Dreizler. Public Supplementals: Characterization of flow field and combustion dynamics in a novel pressurized side-wall quenching burner using highspeed PIV/OH-PLIF measurements, 2021. https://tudatalib.ulb.tu-darmstadt.de/handle/tudatalib/3369.

[68] P. Johe, F. Zentgraf, M. Greifenstein, R. Barlow, A. Dreizler. Public Supplementals: Laser-based investigation of flame surface density and mean reaction rate during flame-wall interaction at elevated pressure, 2022. https://tudatalib.ulb.tu-darmstadt.de/handle/tudatalib/3607.

[69] P. Johe, F. Zentgraf, M. Greifenstein, B. Böhm, A. Dreizler. Public Supplementals: Effects of elevated pressure on thermochemical states of turbulent flame-wall interaction studied by multi-parameter laser diagnostics, 2024. https://tudatalib.ulb.tu-darmstadt.de/handle/tudatalib/4066.

[70] H. Schlichting K. Gersten. *Boundary-Layer Theory*. Springer Berlin Heidelberg and Imprint: Springer, Berlin Heidelberg, 9th ed. 2017 edition, 2017.

[71] J. H. Spurk N. Aksel. *Strömungslehre: Einführung in die Theorie der Strömungen*. Springer eBook Collection. Springer Vieweg, Berlin, Germany, 9., vollständig überarbeitete auflage edition, 2019.

[72] S. B. Pope. *Turbulent flows*. Cambridge University Press, Cambridge, first published 2000, 5th printing 2019 edition, 2019.

[73] J. Zierep K. Bühler. *Grundzüge der Strömungslehre: Grundlagen, Statik und Dynamik der Fluide : mit 202 Abbildungen und zahlreichen Übungen*. Lehrbuch. Springer Vieweg, Wiesbaden, 11., überarbeitete und erweiterte auflage edition, 2018.

[74] F. Durst. *Fluid mechanics: An introduction to the theory of fluid flows*. Graduate texts in physics. Springer, Berlin and Heidelberg, second extended edition edition, 2022.

[75] S. Bschorer. *Technische Strömungslehre: Lehr- und Übungsbuch*. Lehrbuch. Springer Vieweg, Wiesbaden and Heidelberg, 11., überarbeitete und erweiterte auflage edition, 2018.

[76] J. Warnatz. *Combustion: Physical and Chemical Fundamentals, Modeling and Simulation, Experiments, Pollutant Formation*. Springer-Verlag Berlin Heidelberg, Berlin, Heidelberg, 4th edition edition, 2006.

[77] S. R. Turns. *An introduction to combustion: Concepts and applications*. McGraw-Hill series in mechanical engineering. WCB/McGraw-Hill, Boston, 2nd ed. international edition, 2006.

[78] N. Peters. *Turbulent combustion*. Cambridge monographs on mechanics. Cambridge University Press, Cambridge, 2009.

[79] D. G. Goodwin, R. L. Speth, H. K. Moffat, B. W. Weber. Cantera: An Object-oriented Software Toolkit for Chemical Kinetics, Thermodynamics, and Transport Processes: Version 2.1.0. 10.5281/zenodo.170284, 2021. http://www.cantera.org.

[80] C. K. Westbrook F. L. Dryer. Chemical kinetic modeling of hydrocarbon combustion. *Progress in Energy and Combustion Science*, 10(1):1–57, 1984.

[81] I. Glassman, R. A. Yetter, N. G. Glumac. Flame phenomena in premixed combustible gases. In *Combustion*, pages 147–254. Elsevier, 2015.

[82] R. Borghi. On the Structure and Morphology of Turbulent Premixed Flames. In C. Casci C. Bruno, editors, *Recent Advances in the Aerospace Sciences*, pages 117–138. Springer US, Boston, MA, 1985.

[83] N. Peters. Laminar flamelet concepts in turbulent combustion. *Symposium (International) on Combustion*, 21(1):1231–1250, 1988.

[84] T. Poinsot D. Veynante. *Theoretical and Numerical Combustion*. Edwards, 2001.

[85] M. Raffel, C. J. Kähler, J. Kompenhans, F. Scarano, S. T. Wereley, C. E. Willert. *Particle Image Velocimetry: A Practical Guide*. Springer International Publishing and Imprint: Springer, Cham, 3rd ed. 2018 edition, 2018.

[86] C. Schulz V. Sick. Tracer-LIF diagnostics: quantitative measurement of fuel concentration, temperature and fuel/air ratio in practical combustion systems. *Progress in Energy and Combustion Science*, 31(1):75–121, 2005.

[87] R. K. Hanson, C. S. Goldenstein, R. M. Spearrin. *Spectroscopy and Optical Diagnostics for Gases*. Springer International Publishing and Imprint: Springer, Cham, 1st ed. 2016 edition, 2016.

[88] A. Eckbreth. *Laser Diagnostics for Combustion Temperature and Species*. Gordon and Breach Publishers, Netherlands, 1995.

[89] R. E. Palmer. The CARSFT computer code calculating coherent anti-Stokes Raman spectra: User and programmer information.

[90] A. D. Cutler, E. C. A. Gallo, L. M. L. Cantu. WIDECARS spectra fitting in a premixed ethylene–air flame. *Journal of Raman Spectroscopy*, 47(4):416–424, 2016.

[91] M. Greifenstein A. Dreizler. MARSFT: Efficient fitting of CARS spectra using a library–based genetic algorithm. *Journal of Raman Spectroscopy*, 52(3):655–663, 2021.

[92] J. Hermann. *Laseroptische Untersuchung der Flamme-Kühlluft-Interaktion in einer effusionsgekühlten Brennkammer*. Ph.d. thesis, Technische Universität Darmstadt, 2017.

[93] C. Jainski. *Experimentelle Untersuchung der turbulenten Flamme-Wand-Interaktion*. Optimus, Göttingen, 1. auflage edition, 2016.

[94] P. Johe, F. Zentgraf, M. Greifenstein, M. Steinhausen, C. Hasse, A. Dreizler. Characterization of flow field and combustion dynamics in a novel pressurized side-wall quenching burner using high-speed PIV/OH-PLIF measurements. *International Journal of Heat and Fluid Flow*, 94:108921, 2022.

[95] P. Johe, F. Zentgraf, M. Greifenstein, B. Böhm, A. Dreizler. Effects of elevated pressure on thermochemical states of turbulent flame-wall interaction studied by mulit-parameter laser diagnostics. *Combustion and Flame (accepted for publication)*, 2023.

[96] K. Dabov, A. Foi, V. Katkovnik, K. Egiazarian. Image denoising with block-matching and 3D filtering. In E. R. Dougherty, J. T. Astola, K. O. Egiazarian, N. M. Nasrabadi, S. A. Rizvi, editors, *Image Processing: Algorithms and Systems, Neural Networks, and Machine Learning*, SPIE Proceedings, page 606414. SPIE, 2006.

[97] G. P. Smith, D. M. Golden, M. Frenklach, N. W. Moriarty, B. Eiteneer, M. Goldenberg, C. T. Bowman, R. K. Hanson, S. Song, W. Gardinier Jr., et al. GRI-Mech 3.0, 2011. http://www.me.berkeley.edu/gri mech.

[98] B. Hemmerling. Beam-steering effects in turbulent high-pressure flames. In M. Tacke W. Stricker, editors, *Combustion Diagnostics*, SPIE Proceedings, pages 32–37. SPIE, 1997.

[99] Z. W. Sun, Z. T. Alwahabi, D. H. Gu, S. M. Mahmoud, G. J. Nathan, B. B. Dally. Planar laser-induced incandescence of turbulent sooting flames: the influence of beam steering and signal trapping. *Applied Physics B*, 119(4):731–743, 2015.

[100] A. Stella, G. Guj, J. Kompenhans, M. Raffel, H. Richard. Application of particle image velocimetry to combusting flows: design considerations and uncertainty assessment. *Experiments in Fluids*, 30(2):167–180, 2001.

[101] M. Raffel F. Kost. Investigation of aerodynamic effects of coolant ejection at the trailing edge of a turbine blade model by PIV and pressure measurements. *Experiments in Fluids*, 24(5-6):447–461, 1998.

[102] B. Atakan, J. Heinze, U. E. Meier. OH laser-induced fluorescence at high pressures: spectroscopic and two-dimensional measurements exciting the A-X (1,0) transition. *Applied Physics B: Lasers and Optics*, 64(5):585–591, 1997.

[103] J. Garman. Spatial averaging effects in CARS thermometry of a nonpremixed flame. *Combustion and Flame*, 115(4):481–486, 1998.

[104] M. Namazian, I. G. Shepherd, L. Talbot. Characterization of the density fluctuations in turbulent V-shaped premixed flames. *Combustion and Flame*, 64(3):299–308, 1986.

[105] J. P. Dumont, D. Durox, R. Borghi. Experimental study of the mean reaction rates in a turbulent premixed flame. *Combustion Science and Technology*, 89(1-4):219–251, 1993.

[106] K. Bray J. B. Moss. A unified statistical model of the premixed turbulent flame. *Acta Astronautica*, 4(3-4):291–319, 1977.

[107] S. B. Pope. The evolution of surfaces in turbulence. *International Journal of Engineering Science*, 26(5):445–469, 1988.

[108] S. M. Candel T. J. Poinsot. Flame Stretch and the Balance Equation for the Flame Area. *Combustion Science and Technology*, 70(1-3):1–15, 1990.

[109] D. Veynante L. Vervisch. Turbulent combustion modeling. *Progress in Energy and Combustion Science*, 28(3):193–266, 2002.

[110] J. Sellmann, J. Lai, A. M. Kempf, N. Chakraborty. Flame surface density based modelling of head-on quenching of turbulent premixed flames. *Proceedings of the Combustion Institute*, 36(2):1817–1825, 2017.

[111] I. G. Shepherd. Flame surface density and burning rate in premixed turbulent flames. *Symposium (International) on Combustion*, 26(1):373–379, 1996.

[112] B. Deschamps, A. Boukhalfa, C. Chauveau, I. Gökalp, I. G. Shepherd, R. K. Cheng. An experimental estimation of flame surface density and mean reaction rate in turbulent premixed flames. *Symposium (International) on Combustion*, 24(1):469–475, 1992.

[113] D. Veynante, J. Piana, J. M. Duclos, C. Martel. Experimental analysis of flame surface density models for premixed turbulent combustion. *Symposium (International) on Combustion*, 26(1):413–420, 1996.

[114] F. Halter, C. Chauveau, I. Gökalp, D. Veynante. Analysis of flame surface density measurements in turbulent premixed combustion. *Combustion and Flame*, 156(3):657–664, 2009.

[115] G. G. Lee, K. Y. Huh, H. Kobayashi. Measurement and analysis of flame surface density for turbulent premixed combustion on a nozzle-type burner. *Combustion and Flame*, 122(1-2):43–57, 2000.

[116] B. Renou, A. Mura, E. Samson, A. Boukhalfa. Characterization of the local flame structure and the flame surface density for freely propagating premixed flames at various lewis numbers. *Combustion Science and Technology*, 174(4):143–179, 2002.

[117] D. Veynante, J. M. Duclos, J. Piana. Experimental analysis of flamelet models for premixed turbulent combustion. *Symposium (International) on Combustion*, 25(1):1249–1256, 1994.

[118] J. M. Donbar, J. F. Driscoll, C. D. Carter. Reaction zone structure in turbulent nonpremixed jet flames—from CH-OH PLIF images. *Combustion and Flame*, 122(1-2):1–19, 2000.

[119] T. C. Chew, K. Bray, R. E. Britter. Spatially resolved flamelet statistics for reaction rate modeling. *Combustion and Flame*, 80(1):65–82, 1990.

[120] B. M. Deschamps, G. J. Smallwood, J. Prieur, D. R. Snelling, Ö. Gülder. Surface density measurements of turbulent premixed flames in a spark-ignition engine and a bunsen-type burner using planar laser-induced fluorescence. *Symposium (International) on Combustion*, 26(1):427–435, 1996.

Appendix A

Journal Publications

A.1 Paper I

Characterization of flow field and combustion dynamics in a novel pressurized side-wall quenching burner using high-speed PIV/OH-PLIF measurements

P. Johe, F. Zentgraf, M. Greifenstein, M. Steinhausen, C. Hasse, A. Dreizler. Characterization of flow field and combustion dynamics in a novel pressurized side-wall quenching burner using high-speed PIV/OH-PLIF measurements. *International Journal of Heat and Fluid Flow,* 94:108921, 2022. https://doi.org/10.1016/j.ijheatfluidflow.2021.108921

Declaration on the contribution to the scientific publication
Erklärung zum Eigenanteil der wissenschaftlichen Veröffentlichung

Pascal Johe, M.Sc.

Paper

P. Johe, F. Zentgraf, M. Greifenstein, M. Steinhausen, C. Hasse, A. Dreizler: Characterization of flow field and combustion dynamics in a novel pressurized side-wall quenching burner using high-speed PIV/OH-PLIF measurements.
International Journal of Heat and Fluid Flow, Volume 94, 108921 (2022).
https://doi.org/10.1016/j.ijheatfluidflow.2021.108921

Co-Authors

Florian Zentgraf, Dr.-Ing.
Max Greifenstein, Dr.-Ing.
Matthias Steinhausen, M.Sc.
Christian Hasse, Prof. Dr.-Ing.
Andreas Dreizler, Prof. Dr. habil.

Individual Contributions

- **Pascal Johe**
  - Developed and conceptualized the novel pressurized side-wall quenching burner test rig for investigation of flame-wall interaction processes at elevated pressure.
  - Operated the test rig and performed experiments.
  - Conducted post-processing and analysis of the recorded experimental data sets.
  - Served as main and corresponding author of the paper, performed literature research, wrote the manuscript and managed the review process.
- **Florian Zentgraf**
  - Advised on the development of the novel test rig.
  - Supported P. Johe setting up and conducting the experiments.
  - Proofread the manuscript.
- **Max Greifenstein and Matthias Steinhausen**
  Advised on the development of the novel test rig; proofread of the manuscript.
- **Christian Hasse and Andreas Dreizler**
  Advised on the development of the novel test rig; supported the interpretation and discussion of the results, proofread the manuscript.

Overall Contribution of Pascal Johe

A leading role in the development of the novel test rig and conduction of the experiments, data analysis and main author of the manuscript.

Use of paper contents in other dissertations

This publication is not the subject of any ongoing or completed dissertation.

International Journal of Heat and Fluid Flow 94 (2022) 108921

Contents lists available at ScienceDirect

International Journal of Heat and Fluid Flow

journal homepage: www.elsevier.com/locate/ijhff

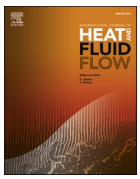

Characterization of flow field and combustion dynamics in a novel pressurized side-wall quenching burner using high-speed PIV/OH-PLIF measurements

Pascal Johe [a,*], Florian Zentgraf [a], Max Greifenstein [a], Matthias Steinhausen [b], Christian Hasse [b], Andreas Dreizler [a]

[a] Technical University of Darmstadt, Department of Mechanical Engineering, Reactive Flows and Diagnostics, Otto-Berndt-Str. 3, Darmstadt 64287, Germany
[b] Technical University of Darmstadt, Department of Mechanical Engineering, Simulation of Thermo-Fluid Systems, Otto-Berndt-Str. 2, Darmstadt 64287, Germany

ARTICLE INFO

Keywords:
Flame-wall interaction
Pressurized combustion
Turbulence
Side-wall quenching
PIV
LIF

ABSTRACT

A novel, pressurized side-wall quenching (SWQ) burner test rig enabling investigations on flame-wall interactions (FWI) of a fully premixed V-shaped flame at conditions mimicking some characteristics of practical devices, e.g. increased pressures and Reynolds numbers, is introduced within this study. Two operating cases featuring turbulent flow conditions at atmospheric and 3 bar operating pressure are defined and characterized based on velocity fields and flame front positions provided by simultaneous high-speed particle image velocimetry (PIV) and planar laser-induced fluorescence of the OH radical (OH-PLIF). For non-reacting conditions, profiles of mean velocities and mean velocity fluctuations are measured in addition to near-wall flow fields at locations where FWI occurs for chemically reacting conditions. For reacting conditions, near-wall flows are characterized in the vicinity of the quenching zone. Based on measured fluctuations of the streamwise velocity component, the turbulent flame is classified at the transition from the wrinkled to the corrugated flamelet regime. Using the derived flame front positions, the instantaneous flame-wall interaction is classified into SWQ-like, head-on quenching (HOQ)-like and multi-zone quenching events and the transition between these scenarios is identified by means of OH-PLIF image sequences. A statistical analysis of the flame front topology is performed based on the flame brush and deduced frequency distributions. Statistically significant differences between both operating cases are confirmed by chi-squared homogeneity tests.

1. Introduction

Chemical energy carriers synthesized from renewable energy are expected to have an increasing contribution to a CO_2-neutral energy supply which is crucial to limit human-induced global warming (Dreizler et al., 2021). Due to high energy densities, chemical energy carriers have the potential to serve as long-term storage with high capacity and to compensate production fluctuations of renewable energy sources like wind and photovoltaics. Moreover, in some sectors, like base load electricity supply, shipping and air traffic as well as high-temperature industrial processes, the thermochemical conversion of chemical energy carriers is likely to remain a relevant technically feasible alternative. Consequently, the development of highly efficient combustion technology featuring low pollutant emissions is still of great importance. One key aspect of many applied combustion systems, such as internal combustion engines and gas turbines, is the quenching of premixed flames at cooled solid surfaces, denoted as flame-wall interaction (FWI). Due to the high near-wall temperature gradient causing undesirable wall heat losses, the thermodynamic efficiency is reduced and chemical reaction processes are quenched close to the wall resulting in an increased emission of pollutants like unburned hydrocarbons and carbon monoxide (CO). A comprehensive understanding of these processes is therefore indispensable for the design of more sustainable combustion systems and fundamental research on the governing phenomena is required. In the past, various aspects of FWI have been investigated in atmospheric flames using generic experimental configurations (Dreizler and Böhm, 2015). Depending on the flame propagating normal or parallel to the wall, these experiments are classified into head-on quenching (HOQ) and side-wall quenching (SWQ) configurations, respectively. Quenching distances and wall heat fluxes, for example, were investigated

* Corresponding author.
E-mail address: johe@rsm.tu-darmstadt.de (P. Johe).

https://doi.org/10.1016/j.ijheatfluidflow.2021.108921
Received 1 October 2021; Received in revised form 13 December 2021; Accepted 20 December 2021
Available online 7 January 2022

Fig. 1. Overall view of the novel SWQ test rig: (1) SWQ burner unit, (2) pressure vessel with exhaust gas pipe, (3) pressure valve.

thoroughly for HOQ and SWQ in a stagnant gas mixture (Sotton et al., 2005) and in a gas flow (Boust et al., 2007b) using constant volume vessels. The effect of varying equivalence ratios on these FWI properties was subsequently examined in further studies using a similar experimental setup (Boust et al., 2007a). More recently, FWI has been investigated for forced laminar flames to unravel the impact of flame dynamics on quenching distances and exhaust CO emissions (Rivera et al., 2019). Interactions of the flame with different wall coating materials with regard to quenching distances and flame structure were investigated in a premixed flame using a slit burner and surface analysis of the coatings were performed to examine chemical quenching mechanisms (Li et al., 2019). Further studies also focussing on the influence of wall chemical effects in hydrogen and DME weak flames were carried out using a micro flow reactor (Fan et al., 2021; Wan et al., 2019). Interactions of the near-wall flow field with the flame were investigated in an HOQ burner (Rißmann et al., 2017) and supplemented with measurements of temperature profiles (Bohlin et al., 2015) as well as thermochemical states (Mann et al., 2014). Comparable studies were recently carried out using an SWQ configuration (Bohlin et al., 2017; Jainski et al., 2017; Zentgraf et al., 2021b).

Experimental investigations on FWI in a pressurized environment on the contrary are rare and limited only to some aspects of flame quenching. Boust et al. (2007a) and Karrer et al. (2010), for example, investigated the influence of increasing pressure (up to 6 bar) onto the quenching distance for an initially stagnant gas mixture in an HOQ and a SWQ configuration using a constant volume vessel. Temperature profile measurements in a laminar flame (HOQ) at variable pressure ranging from 0.5 to 1.0 bar were carried out by Saggau (1985) to evaluate heat transfer coefficients from the near-wall temperature gradient. Ojo et al. (2021) and Escofet-Martin et al. (2021) recently used a fixed-volume chamber to investigate thermal boundary layers and transient heat transfer processes in a methane/air flame propagating through the stagnant gas mixture (initially at 1 bar) which is compressed to 2 bar due to the heat release. Detailed assessments of thermochemical states and the near-wall flow field during FWI, however, do not exist to the best of the authors' knowledge. Considering typical operating conditions of practical combustion devices, further investigations on FWI with regard to increased operating pressures are therefore of particular interest to extend our phenomenological understanding and to provide validation data for numerical simulations. For this reason, a novel, pressurized side-wall quenching burner enabling investigations on FWI at increased pressures (up to 5 bar) was designed and is introduced in this study. As a basis for future process-related studies, the novel burner is described in detail and characterized in terms of inflow boundary conditions, the near-wall flow field and combustion dynamics using data provided by simultaneous high-speed particle image velocimetry (PIV) and planar laser-induced fluorescence of the hydroxyl radical (OH-PLIF) measurements.

To facilitate further investigations, underlying data of selected figures as well as computer-aided design (CAD) data of the 3D geometry of

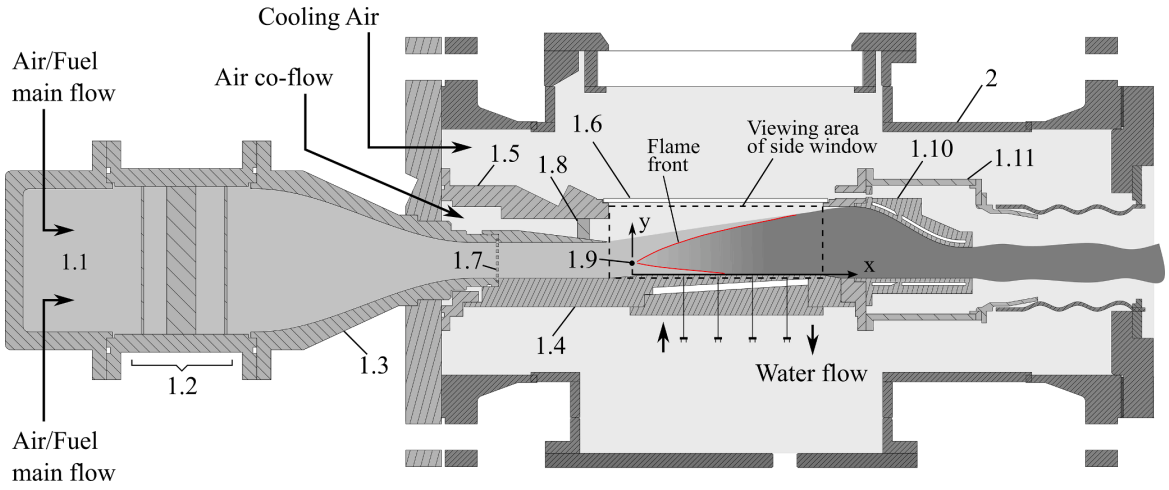

Fig. 2. Detailed sectional side view of the pressurized SWQ burner unit. Direction of gravity coincides with negative y-direction.

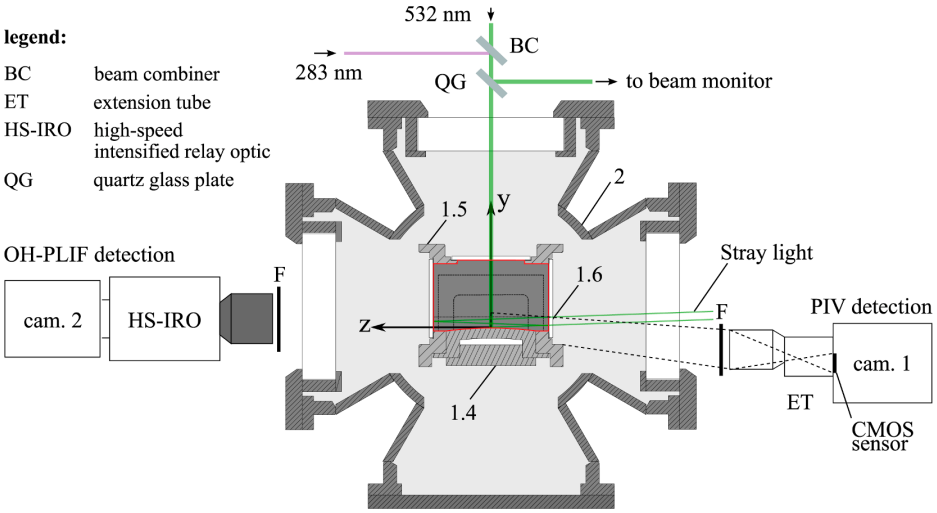

Fig. 3. Detailed sectional front view of the pressurized SWQ burner unit with applied laser optical setup.

the test rig (on request) are available on the institutional repository of Technical University of Darmstadt *TUdatalib* (*https://tudatalib.ulb.tu-darmstadt.de/handle/tudatalib/3369*).

2. The novel pressurized side-wall quenching burner

2.1. Test rig

The design of the novel burner test rig introduced in this study is based on the combination of the proven concepts of two existing burner configurations, (1) the atmospheric SWQ burner and (2) the single sector model gas turbine combustor rig. Both burners were investigated extensively in past studies, e.g. Kosaka et al. (2020), Zentgraf et al. (2021a), Greifenstein et al. (2019), Greifenstein and Dreizler (2021), and gained experiences and know-how were incorporated in the design process of the new burner test rig. Furthermore, findings and experience from previous numerical works on the atmospheric SWQ configuration (Ganter et al., 2017; Heinrich et al., 2018) were taken into account during the design process to optimize the burner design in terms of its suitability for numerical investigations.

Fig. 1 shows an overall view of the test rig which can be subdivided into its three main components: the newly developed SWQ burner unit (1) which was adapted to the already existing pressure vessel (2) and the pressure valve (3). Optical access to the SWQ burner unit is provided by three removable quartz glass windows, one on the top, and one on either side of the vessel allowing the application of laser-based diagnostics and imaging techniques. The pressure valve which is connected to the pressure vessel through an exhaust pipe is used to control the internal pressure. The thermal load of the valve is reduced by cooling down the exhaust gas using a glycol/water jacket cooling applied to the exhaust pipe. The overall horizontal length of the test rig is about 4.5 m.

A sectional side view showing the SWQ burner unit in detail is depicted in Fig. 2. During reacting operation, a fully premixed fuel/dried-air flow is supplied to the inlet plenum (1.1) of the SWQ burner unit and guided through honeycombs and a set of meshes of various grid spacing for flow homogenization (1.2). The gas flow then enters the flame tube through a converging Morel type nozzle (1.3) with a rectangular cross-section (approximately 30×60 mm^2 at nozzle outlet) and a contraction ratio of 9. A stainless-steel quenching wall (1.4) whose upper surface smoothly merges with the surface of the Morel nozzle is positioned at the bottom of the flame tube (1.5) and quartz glass windows (1.6) at three sides (top, left, right) of the flame tube allow for optical access. At the nozzle outlet the quenching wall presents a flat surface which transitions into a convex, cylindrically curved surface (300 mm radius in y-z-plane) further downstream ensuring improved optical access close to the wall, similar to the atmospheric SWQ burner (e.g. Zentgraf et al., 2021b; Kosaka et al., 2020). The resulting flow cross-section of the flame tube (60×100 mm^2) is highlighted as red line in Fig. 3. A removable turbulence-generating grid (TG, 1.7) designed as a perforated plate (bore diameter 3.8 mm, solidity 51 %) is positioned in the main flow 90 mm upstream the nozzle exit to increase turbulence intensities. To minimize shear effects and recirculation zones at the nozzle exit a dried air co-flow is led through a flat sintered bronze structure (1.8) into the flame tube surrounding the central main flow. Shielding of the quartz glass windows from the reacting fuel/air main flow by the co-flow moreover aids to avoid damages to the windows by minimizing the thermal load. In addition, during particle-based measurements, e.g. PIV, contamination of the windows is reduced, lowering the frequency of cleaning breaks and extending measurement intervals, respectively.

The fully premixed fuel/air flow is ignited using a spark ignited hydrogen pilot flame which is extinguished after the ignition procedure. The V-shaped main flame is then stabilized on a ceramic rod (1.0 mm diameter, 1.9) placed 10 mm above the quenching wall and 36 mm downstream of the nozzle exit. The lower flame branch of the V-shaped flame impinges on the surface of the quenching wall resulting in a side-wall quenching process. The temperature of the quenching wall is stabilized by circulating water through a cooling duct which is inclined by 3° relative to the direction of gravity (negative y-direction) to avoid accumulations of air bubbles at axial positions where quenching occurs. In case air bubbles are formed they will accumulate at the highest position of the wall cooling system close to the outlet of the cooling duct and are removed with the coolant. A thermocouple positioned close to the outlet is used to check for air accumulations which are heated up significantly faster than the coolant due to a lower heat capacity. Five additional thermocouples (type K, 1.5 mm diameter) are mounted in bores about 0.4 mm beneath the wall surface to measure the local wall temperature values and their spatial homogeneity to finally control and well-reproduce the burner operation.

An exhaust gas nozzle with internal cooling channels (rectangular cross-section, contraction ratio 6, 1.10) at the exit of the flame tube is used to accelerate the hot combustion products into the exhaust plenum (1.11). During operation with high thermal load, deionized ambient-temperature water can be fed into the internal cooling channels to

Table 1
Operating conditions. Laminar flame speeds are received from CANTERA simulations, see section 4.1.

p	TG	u_B	s_l	$u_B/u_{B,CF}$	ϕ	Re
bar	–	m/s	m/s	–	–	–
1	yes	3.8	0.2725	1	0.8	8,200
3	yes	2.3	0.167	1	0.8	15,000
1	no	3.8	0.2725	1	0.8	8,200

avoid overheating and damage to the nozzle. Cooling of the pressure vessel, the flame tube and the quartz glass windows is achieved by feeding a cooling air flow into the pressure vessel which is guided alongside the windows into the exhaust plenum. The exhaust gas/cooling air gas mixture then enters the exhaust pipe and exits it through the pressure valve.

Mass flows of main air, fuel and co-flow air are controlled using calibrated thermal mass flow controllers (MFC, Bronkhorst). A pneumatic valve operated in a feedback loop is used to control the cooling air flow rate which is determined by measuring the differential pressure across an orifice plate. The flame tube internal static pressure is measured by means of a pressure transmitter (PSI Pressure Systems, Model 9116) connected via a pressure measurement hose to a 1.0 mm diameter bore in the flame tube above the co-flow inlet. The test rig control software including a closed loop control algorithm to control the flame tube internal pressure is implemented in LabVIEW (National Instruments).

2.2. Operating conditions

The operating conditions of the burner test rig are summarized in Table 1. The governing parameter is the flame tube internal pressure p as its impact on FWI processes is in the focus of this and future investigations. The flow rate of the premixed fuel/air main flow and the air co-flow are defined in terms of their bulk velocities u_B and $u_{B,CF}$ with regard to the corresponding flow cross-section at the inlet of the flame tube, i.e., the ratio of volume flow rate and area. By keeping the ratio of bulk velocity u_B and laminar burning velocity s_l constant (leading to a variation of the Reynolds number), the streamwise position (x-direction) where flame quenching occurs is nearly the same for all measured conditions. Operation at constant Reynolds numbers, as in previous parameter studies on FWI at atmospheric conditions, is not possible since varying pressures would result in changing u_B/s_l ratios as both quantities show different pressure dependencies (linear vs. power-law (Wu et al., 2016)). Considering the relevant pressure range, this would either result in flashback events at high pressures or the absence of SWQ events within the optically accessible region at low pressures. The latter results from increasing u_B/s_l ratios causing the flame to strike the wall at an increasingly shallow angle at further downstream positions close to the exhaust gas nozzle. To minimize shear effects $u_B/u_{B,CF}$ is set to unity. The temperature of the quenching wall is stabilized at 353 K.

In total, three operating cases are defined in Table 1 for this study, using methane as fuel. In the first two cases, the burner test rig is operated with turbulence grid to achieve increased turbulence intensities. Moreover, the utilization of the turbulence grid is intended to provide a better comparability of both flows at different Reynolds numbers as the grid-generated turbulence should outweigh the turbulence of the incident flow. The Reynolds numbers given in Table 1 are derived based on the hydraulic diameter of the nozzle exit, the bulk flow velocity u_B and the kinematic viscosity at 25 °C. This study will focus on these first two operating cases, in the following to be referred as turbulent cases, as (1) increased turbulence is an inherent property of the novel test rig at most operating conditions (particularly at higher pressures and Reynolds numbers, respectively) and (2) conditions closer to real technical combustion systems are characterized by increased turbulence. The third operating case serves as quasi-laminar reference case and will only be considered with regard to the inflow boundary conditions (section 4.1) of the non-reacting flow to obtain a thorough characterization of the burner. During this operating case the burner is operated without the turbulence grid.

3. Experimental approach

3.1. Laser diagnostics

Two-component, two-dimensional velocimetry and flame front visualization measurements were applied simultaneously using particle image velocimetry (PIV) and planar laser-induced fluorescence of the hydroxyl radical (OH-PLIF). Both systems were operated at low-speed (50 Hz) and high-speed (5 kHz) repetition rates to acquire statistically independent data and to resolve transient phenomena, respectively. Synchronization of all components was ensured using a pulse generator (Quantum Composer Inc., 9529 Series) and a timing unit (LaVision GmbH, HSCv2). For the characterization of the inflow boundary conditions, PIV images were acquired at low resolution (LR) and within a large field-of-view (FOV) covering the full height of the Morel nozzle outlet. Subsequently, the magnification of the PIV detection system was increased (high resolution, HR) to capture the flow field in the FWI with higher spatial resolution. Fig. 3. shows the main elements of the used laser optical setup. The test-rig-fixed coordinate system used in the PIV and OH-PLIF images is depicted in Fig. 2 and Fig. 3. The coordinate system is anchored at the surface of the quenching wall within the symmetry plane of the flame tube (z = 0 mm) with the y-axis oriented in wall-normal and the x-axis in wall-parallel, streamwise direction. The origin of the x-axis is defined by the position of the ceramic rod. All images were recorded at the symmetry plane (z = 0 mm) of the flame tube (x-y-plane). A traversing unit was used to move both, the PIV and the OH-PLIF detection system, as well as a part of the laser optics, enabling various FOV positions along the x-axis.

For PIV, alumina particles (Al_2O_3, Martoxid MR52, $d_{50} = [1, 1.7\ \mu m]$) were seeded to the premixed main flow using a customized fluidized bed seeder. They were illuminated by means of two individual diode-pumped solid state Nd:YAG lasers (Edgewave GmbH, Innoslab IS16II-E) formed into light sheets with a thickness of approximately 650 µm (LR) and 300 µm (HR), respectively. Two cylindrical lenses (LR: $f = -100$ mm & $f = 750$ mm; HR: $f = -100$ mm & $f = 300$ mm) were used to first expand the beams in x-direction and subsequently focus them in z-direction to achieve the desired sheet thickness. The laser pulse separation was varied between 30 and 55 µs. Mie-scattering of the particles was captured using a high-speed CMOS camera (LR: Vision Research, Phantom v711; HR: Vision Research, Phantom v2640) equipped with a 180 mm macro lens (Sigma APO Macro EX DG IF HSM, f/8). With the low-resolution setup, one camera pixel (20 µm) corresponded to ≈ 40 µm in physical space. For the high-resolution setup, the magnification was increased resulting in one camera pixel (13.5 µm) corresponding to ≈ 12 µm in physical space. The optical axis of the objective lens was positioned slightly below the surface of the quenching wall to reduce the collection of stray light which is scattered at the cylindrical surface of the wall and reflected multiple times from the windows (sketched as thin green lines originating from the laser beam impinging on the surface of the quenching wall). By shifting the optical axis of the CMOS camera slightly further, below the axis of the objective lens, the desired FOV could still be achieved. This approach is widely used in professional photography (*tilt-shift photography*), but, to the authors' best knowledge, has not yet been applied for stray light suppression in scientific imaging. Additionally, a bandpass filter (520–544 nm transmission) was mounted to the objective lens to supress flame luminosity and ambient light.

Velocity vector fields were derived from the recorded particle raw images using the software DaVis 10.0.5 (LaVision GmbH). Mapping of the pixel scale to the test-rig-fixed coordinate system was achieved by calibration using recordings of a spatially defined calibration target plate (LaVision GmbH, 058–5). To improve the results of the PIV

algorithm, a sliding average subtraction and a min/max filtering operation (24 pixel and 5 pixel filter length, respectively) were applied within an image pre-processing step to the calibrated particle images. The processing of the particle images recorded with the low-resolution setup was based on an interrogation window size (IRW) of 16 × 16 pixel (≈ 640 μm IRW size, 160 μm vector spacing with 75 % overlap). For the processing of the higher resolved particle images, the IRW was increased to 24 × 24 pixel (≈288 μm IRW size, 72 μm vector spacing with 75 % overlap) to keep the number of particles within an IRW sufficiently high for a robust vector field calculation. Spurious vectors were detected and removed using an 11 × 11 median filter. In the reacting flow, these vectors mainly resulted from low seeding densities in the post-flame region and defocused image regions caused by significant beam steering effects (especially in the 3 bar case) due to high density gradients caused by the flame.

OH-PLIF measurements were carried out for a qualitative visualization of the spatial hydroxyl radical distribution, yielding a measure for the reaction zone. The $Q_1(6)$ transition at 35334.38 cm^{-1} was excited using the emission of a frequency doubled dye laser (Sirah Laserstechnik GmbH, Allegro) operated with Rhodamine 6G dissolved in Ethanol which was optically pumped by a diode pumped solid state Nd:YAG laser (Edgewave GmbH, Innoslab IS 8II-E). The pulse energy of the resulting UV beam (~283 nm) was about 0.3 mJ/pulse (at 10 kHz) at the exit of the laser. Two spherical lenses (f = − 75 mm and f = 200 mm) forming a telescope were utilized to initially expand and collimate the UV beam. Subsequently, the beam was formed into a light sheet of 80 μm thickness by two cylindrical lenses (f = − 100 mm and f = 300 mm) used to expand it in x-direction and focus it in z-direction. The UV radiation was guided into the test rig by means of high reflective dielectric mirrors and overlapped with the PIV light sheets using a beam combiner. Small fractions of the beams reflected at a quartz glass plate positioned after the beam combiner were used to verify the overlap using a beam monitor. The emitted fluorescence signal was recorded using a high-speed CMOS camera (Photron Fastcam SA-X2) equipped with a dual-stage high-speed image intensifier (LaVision GmbH, HS-IRO, 200 ns gate), a 100 mm UV lens (Sodern CERCO 2073, f/2.8) and an interference filter (305–340 nm transmission). The detection optics were placed as close as possible to the quartz glass window of the pressure vessel to provide the maximum achievable magnification. The resulting FOV of the OF-PLIF system was 35 × 35 mm^2 with ≈ 35 μm in physical space corresponding to a one camera pixel (20 μm). Using recordings of a siemens star target, a spatial resolution of about 250 μm (25 % MTF) was derived.

Spatial calibration of the OH-PLIF raw images was performed within DaVis 10.0.5 software similar to the particle image calibration using recordings of the same calibration target plate (LaVision GmbH, 50.8). Subsequently, the instantaneous flame front positions were extracted from the calibrated OH-PLIF images using a processing procedure implemented in MATLAB 2020b (The MathWorks, Inc.). In a first step, to reduce computing time the image is cropped to the region of interest close to the wall containing the flame front and resampled by a 2 × 2 binning. Spatial noise is subsequently reduced using a block-matching and 3D filtering (BM3D) algorithm (Dabov et al., 2006). By collaborative filtering of 3D data arrays consisting of similar 2D image fragments (blocks) grouped together, this filter enables noise attenuation and preserving of shared and unique features of the processed blocks at the same time. Applied to the OH-PLIF images this filter showed compelling results in terms of noise reduction and preserving of gradients in the vicinity of the flame front. Considering decreasing signal-to-noise ratios of the OH signal at higher pressures due to pressure broadening of the absorption line, these filter characteristics are of increasing importance. In a last step, the flame front is extracted using a Canny-edge (CE) filter (Canny, 1986). This filter detects edges in the input image based on local maxima of the signal gradient preserving strong edges with gradient values exceeding a high threshold and rejecting weak edges with gradient values below a low threshold. Edges with gradient values above

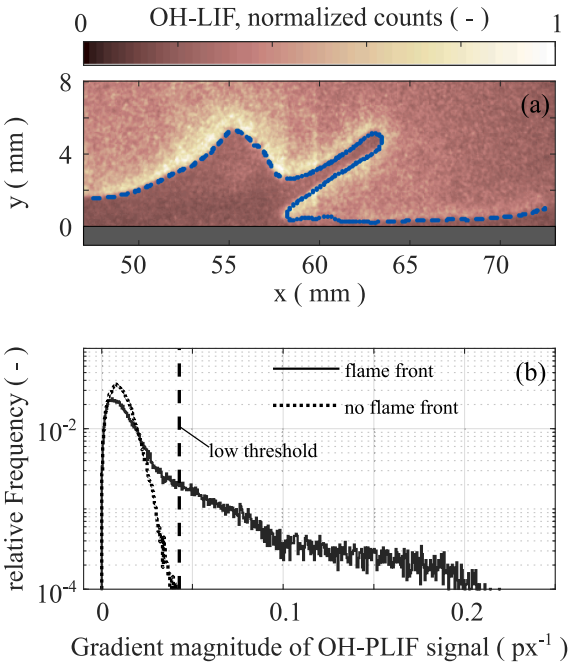

Fig. 4. Detection of flame front traces. (a) arbitrary OH-PLIF image (3 bar operating case) with detected flame front (dashed blue line); (b) Frequency distribution of gradient magnitude values of OH-PLIF signals in regions with and without flame front. (For interpretation of the references to colour in this figure legend, the reader is referred to the web version of this article.)

the low threshold are included into the output if they are connected to strong edges. Within the described flame front tracking algorithm, the low threshold was determined individually for every input image based on the frequency distribution of the gradient magnitude values (normalized by the maximum values) in an image area without flame front. Assuming that these image areas only contain image noise the low threshold was set to the 99 %-quantile of the related frequency distribution multiplied with a safety factor of 1.5 to minimize the detection of flawed flame fronts. An arbitrary OH-PLIF raw image (recorded at 3 bar) with the detected flame front visualized as dashed blue line (a) and the related frequency distribution (b) are shown in Fig. 4. For comparison, the frequency distribution of gradient magnitude values in an image area with flame front is also shown in Fig. 4(b). As the detection of the flame front in image areas with small signal gradients, e.g. close to the wall, depends to a certain extent on the low threshold, its influence is estimated by means of a sensitivity analysis presented in the appendix (Appendix). On the contrary, the flame front detection is less sensitive to the high threshold which was empirically set to 0.6.

The position of the quenching wall within the acquired velocity vector fields was determined using an average particle image derived from (spatially calibrated) particle raw images of the corresponding data set. As the incident PIV light sheet is scattered by the surface of the wall and by alumina particles adhering to it, the wall surface can be identified by a small stripe of high intensity. Within this study, the position of the maximum intensity within this small stripe was used to approximate the position of the quenching wall. By matching OH-PLIF recordings to the PIV images with the aid of images of a knife edge recorded with both systems, the position of the wall was transferred to the OH-PLIF images.

3.2. *Experimental uncertainties*

The processing of the particle raw images described above was

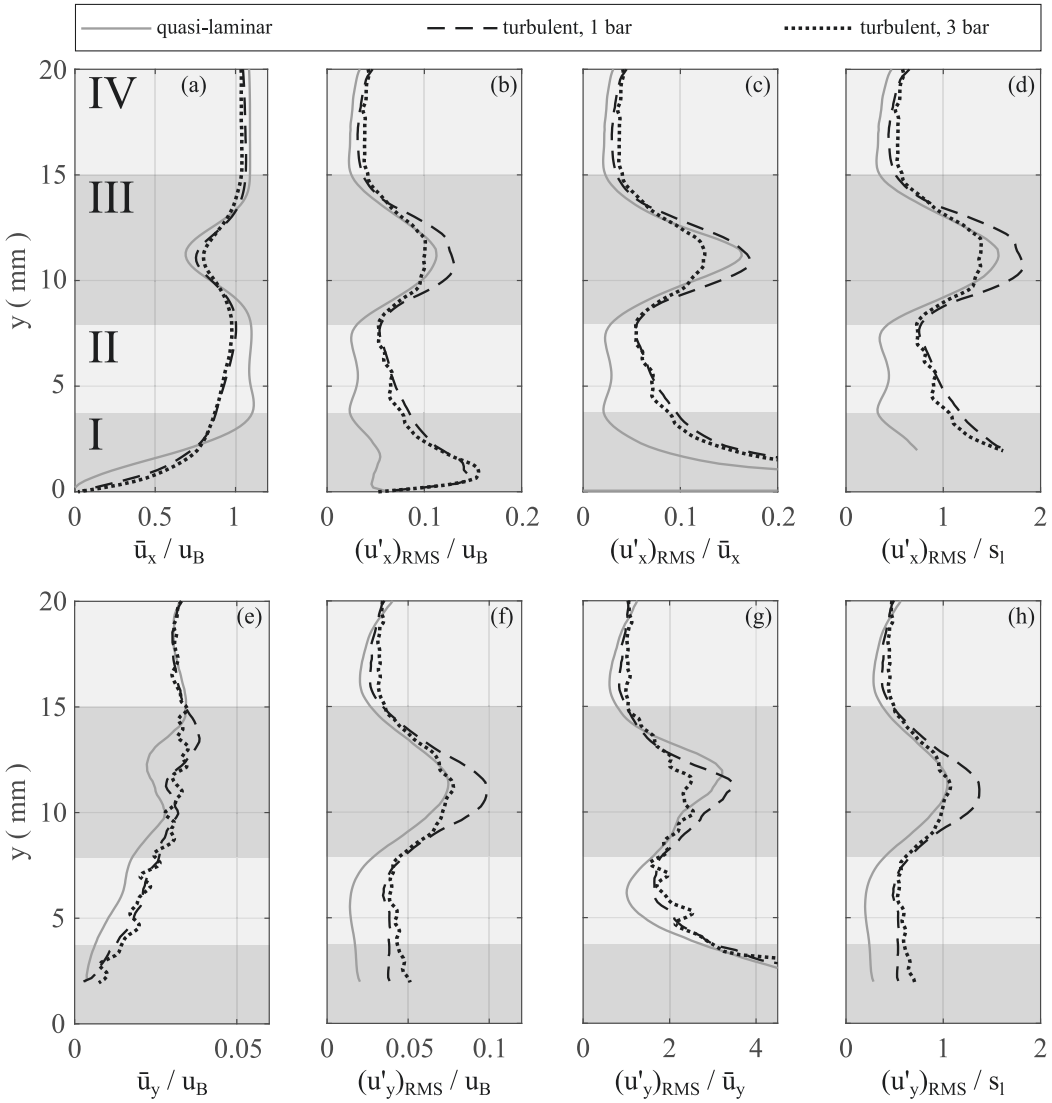

Fig. 5. Inflow boundary conditions characterized by: wall-normal profiles of mean normalized velocities (a, e), normalized RMS of fluctuations (b ,d, f, h) and turbulence intensities (c, g) in the non-reacting flow derived from 500 samples (in each operating case) recorded at 50 Hz repetition rate. Streamwise components in a – d, wall-normal components in e – h. Profiles at $x = 30$mm.

iteratively optimized to maximize correlation values and minimize velocity uncertainty values given by the PIV algorithm. In the 3 bar case at reacting conditions, the average uncertainty of the velocity magnitude in an individual vector field was approximately 0.3 m/s. Uncertainties of velocity values derived from PIV images recorded in the non-reacting flow or at atmospheric pressure were lower.

The uncertainty of the detected flame front positions is assumed to be dominated by the limited resolution of the OH-PLIF detection system and the impact of the algorithm used for flame front detection is presumed to be negligible.

The uncertainty of the absolute quenching wall position in the velocity fields of the non-reactive flows mainly results from the detection procedure described above. As the intensity peak close to the quenching wall covers several pixels, the identification of the wall surface by visual inspection includes a certain error e_R . This error is estimated by assessing the full width at half maximum (FWHM) of the intensity peak. In the non-reactive flow, the FWHM of this peak is about 100 µm. Considering velocity fields of reactive flows, the individual PIV recordings are strongly affected by beam steering effects causing an additional stochastic shift of the apparent quenching wall position in every individual image. This results in an increased FWHM of the intensity peak close to the wall within the corresponding average particle image and therefore, an increased error e_R. As these beam steering effects are less pronounced in the reactive flow at atmospheric conditions, the FWHM value in the respective particle image is not noticeably increased. At increasing pressures however, the influence of beam steering effects appreciably intensifies resulting in a broadened intensity peak (FWHM $\approx$ 170 µm) in the 3 bar operating case. Considering the matching of images of both laser diagnostic systems, there is a second contribution e_M to the uncertainty of the quenching wall position in the OH-PLIF images originating from the determination of the knife edge position. Due to the limited optical resolution of both systems, the

position of the knife edge can only be determined with limited accuracy. The related error of the knife edge position is estimated based on the width of the corresponding intensity edge (10 % to 90 % contrast) of about 60 μm (PIV) and 140 μm (OH-PLIF), respectively. Both individual errors related to the determination of the knife edge position are added up to $e_M = 200$ μm to get a worst-case estimation of the error associated to the matching procedure. A worst-case estimation of the uncertainty of the quenching wall position in the OH-PLIF images is eventually derived by summing up the individual errors resulting in 300 μm for the 1 bar case and 370 μm for the 3 bar case. With regard to the relative position of the quenching wall comparing two individual data sets, the uncertainty is assumed to be considerably smaller as quenching wall positions are determined based on the same procedure.

4. Results

4.1. Inflow boundary conditions

The inflow boundary conditions of the novel burner test rig are characterized by means of wall-normal profiles of mean velocities and root mean square values (RMS) of velocity fluctuations at x = 30 mm in the non-reacting flow, summarized in Fig. 5. Profiles are shown for both turbulent operating cases (1 bar: black dashed line, 3 bar: black dotted line) and the quasi-laminar reference case (grey solid line). Plots in the top row refer to the streamwise (x-direction) velocity component, whereas profiles in the bottom row relate to the wall-normal (y-direction) velocity component. The underlying velocity data are derived from 500 statistically independent PIV images (in each operating case) recorded with the low-resolution setup at 50 Hz repetition rate. Profiles of ensemble-averaged values of the streamwise velocity component u_x normalized with the bulk velocity u_B (Table 1) are depicted in Fig. 5(a). Based on these profiles, the incident flow is sectioned into four distinct regions (I-IV): Close to the wall (I), the flow is characterized by the boundary layer and $\overline{u}_x$ increases with increasing wall distances. Comparing the profiles in close vicinity to the wall, it is evident that the flow features a steeper near-wall velocity gradient in the turbulent cases due to increased turbulence generated by the turbulence grid. At higher wall distances (II), $\overline{u}_x$ is almost constant in the quasi-laminar case resulting in a nearly top-hat profile. In the turbulent cases however, the flow is still influenced by the boundary layer. In region III the profiles show an appreciable drop in $\overline{u}_x$ due to the wake of the ceramic rod comprising eddies produced by vortex shedding at the rod and transported with the flow in x-direction (Kármán vortex street). Far from the wall (IV, y > 15 mm) the influence of the wake is no longer apparent resulting in a nearly top-hat profile in all three cases. Comparing both turbulent cases, it should be noted that both profiles show an almost identical shape in all four regions. The same holds true (except for region III) for root mean squares (RMS) of the instantaneous velocity fluctuations $(u'_x)_{RMS}$ normalized with the bulk velocity u_B , the local ensemble averaged velocity $\overline{u}_x$ and the laminar flame speed s_l , shown in Fig. 5(b), (c) and (d), respectively. Considering only the turbulent cases, three different contributions can be assigned to the velocity fluctuations shown based on the defined regions: the undisturbed grid-generated turbulence in region IV, the wake of the ceramic rod in region III and the evolving turbulent boundary layer (superimposed by grid-generated turbulence) in region I and II. By comparing the profiles of both operating cases at 1 bar (quasi-laminar and turbulent) in Fig. 5(b), the impact of the turbulence grid on the incident flow is evident as velocity fluctuations are appreciably smaller in the quasi-laminar case at all wall distances (except for region III). Especially in region I and II, the influence of the turbulence grid on the flow is notable as it induces the development of the turbulent boundary layer causing the velocity fluctuations to differ by a factor of 2 or more. In region IV, where velocity fluctuations are dominated only by grid-generated turbulence, the differences in the velocity fluctuations are less pronounced. Corresponding turbulence levels $(u'_x)_{RMS}/\overline{u}_x$ are shown in Fig. 5(c). In the region with undisturbed grid-generated turbulence (IV) the turbulence level is about 3.0 % (turbulent, 1 bar) and 3.7 % (turbulent, 3 bar), respectively, whereas closer to the wall in region II values range between 5.4 % and 9.6 % (turbulent, 1 bar and 3 bar). Turbulence levels in the quasi-laminar case vary between 2.1 % (region IV) and 3 % (region II). At decreasing wall distances within region I, turbulence levels strongly increase, as mean velocities tend to zero. For a first rough classification of the combustion process (discussed later on) in the Borghi-Peters regime diagram (Peters, 1988), profiles of the $(u'_x)_{RMS}/s_l$ ratio are shown in Fig. 5(d). Based on past studies on FWI at atmospheric conditions showing that the laminar flame speed s_l of the freely propagating flame is only valid at wall distances y > 2 mm (Jainski et al., 2017a), a comparable near-wall behaviour of s_l is assumed for the FWI experiments at 1 bar operating pressure within this study. Considering decreasing quenching distances at increasing pressure (Boust et al., 2007a), s_l might be unaffected by the wall even at smaller wall distances, in the 3 bar operating case. Therefore, $(u'_x)_{RMS}/s_l$ ratios are only calculated at wall distances y > 2 mm, where s_l is not yet influenced by the presence of the wall. Assuming laminar flame speeds of $s_l = 0.2725\text{m/s}$ (1 bar) and $s_l = 0.167\text{m/s}$ (3 bar), provided by CANTERA simulations (Goodwin et al., 2021) in conjunction with the GRI-MECH 3.0 mechanism (Smith et al., 2011), $(u'_x)_{RMS}/s_l$ ratios vary between 0.5 (region IV) and 1.6 (region I, y = 2 mm) in the turbulent cases, indicating that the combustion processes is at the transition from the wrinkled to the corrugatedflamelet regime. Since velocity fluctuations in the non-reacting flow were used to avoid bias by flame intermittency, this is an approximation since no influences from the combustion process were considered.

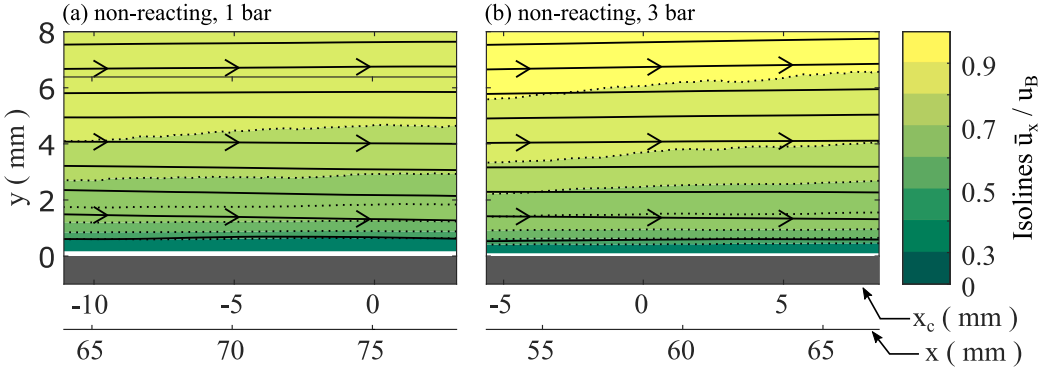

Fig. 6. Isolines (dashed lines) of the averaged, streamwise velocity component $\overline{u}_x$ overlaid with streamlines (solid lines with arrows) of the non-reacting flow for (a) the 1 bar and (b) the 3 bar operating case obtained from 500 samples (in each case) recorded at 50 Hz repetition rate.

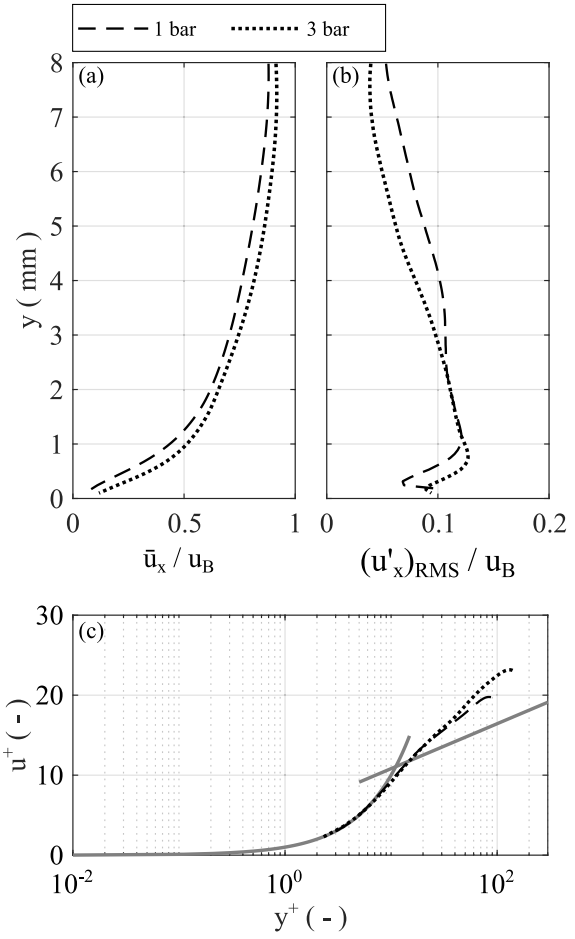

Fig. 7. Wall-normal profiles of mean normalized velocities (a), normalized RMS of fluctuations (b). Normalized $u^+(y^+)$ profiles of the turbulent boundary layer (c). Profiles at $x_c = 0$mm in the non-reacting flow derived from 500 Samples recorded at 50 Hz.

Corresponding profiles of the wall-normal velocity component u_y are depicted in Fig. 5(e), (f), (g) and (h) for a complete characterization of the incident flow. The plots are sectioned into the same four regions. As can be seen from Fig. 5(e), the flow on average shows a slight movement into the wall-normal direction at velocities at about one order of magnitude smaller than the corresponding streamwise velocity component. Fluctuations of both velocity components, $(u'_y)_{RMS}$ and $(u'_x)_{RMS}$ however are in the same order differing only by a factor of about 2 (Fig. 5(b) and (f)). The corresponding wall-normal profiles of both velocity components are characterized by a similar shape and the above-mentioned contributions to the velocity fluctuations are again recognizable in Fig. 5(f). Turbulence levels are about 100 % and above as $\bar{u}_y$ and $(u'_y)_{RMS}$ values are in the same order of magnitude (Fig. 5(g)). Based on $(u'_y)_{RMS}/s_l$ ratios, shown in Fig. 5(h), slightly smaller than corresponding $(u'_x)_{RMS}/s_l$ values, the flame would be classified as wrinkled flamelet.

4.2. Near-wall flow characterization

In the following, the turbulent flow is characterized in the region where quenching occurs, focussing on the local flow field close to the wall using velocity data from 500 (in each non-reacting case) and 1000 (in each reacting case) PIV images recorded with the HR-setup at 50 Hz repetition rate. Although u_B/s_l was kept constant for both operating cases (see section 2.2), caused by different flame propagation speeds quenching occurs at slightly different positions. In a first step, the corresponding non-reacting flow is discussed. Subsequently, the reacting flow field is presented.

4.2.1. Non-reacting case

Isolines of the ensemble averaged streamwise velocity component $\bar{u}_x$ normalized with the bulk velocity u_B (dotted lines) are shown for both turbulent cases in Fig. 6, superimposed with streamlines indicating the flow direction. The isolines are plotted for normalized velocities of 0.3 to 0.9 (in 0.1 steps). Based on statistically independent (50 Hz) OH-PLIF recordings of the flame in the corresponding reacting case, a second streamwise coordinate x_c is introduced, indicating the position in the near-wall region with the highest probability of a flame front to be detected at $x_c = 0$ mm (conditioned to axial position of mean quenching location). This coordinate is intended to allow for a better comparison of both flow fields, especially in the reacting case, as the flow is highly influenced by the presence of the flame. The mean position of the flame front therefore needs to be considered when comparing both reacting flow fields. The evaluation of the x_c -coordinate will be discussed in detail in section 4.3.

As already observed in section 4.1, the non-reacting flow is oriented almost entirely in streamwise direction indicated by the plotted streamlines in Fig. 6. The $\bar{u}_x$ values increase with increasing wall distance whereas the wall-normal velocity gradient decreases indicated by the growing distance of adjacent isolines. Comparing isolines of both non-reacting cases, it is evident that the wall-normal velocity gradient close to the wall is higher in the flow at 3 bar pressure as isolines are located closer to each other in this case. In Fig. 7, wall-normal profiles of the normalized velocity $\bar{u}_x/u_B$ are depicted for $x_c = 0$ mm . Boundary layer thicknesses deduced from the shown profiles are about $\delta_{99} \approx 6.8$ mm (1 bar, $u_\infty/u_B \approx 0.88$) and $\delta_{99} \approx 6.5$mm (3 bar, $u_\infty/u_B \approx 0.92$), respectively. This is in accordance with observations on turbulent boundary layers (evolved from a laminar boundary layer due to laminar/turbulent-transition) on a flat plate (Schlichting and Gersten, 2017). At a given distance x from the leading edge of the plate, the thickness of the boundary layer δ decreases slowly with increasing Re showing an asymptotic relation ($\delta/x \sim 1/\ln Re$) for high Re. In Fig. 7(c) profiles of the mean velocity at the same position are plotted in dimensionless coordinates u^+ and y^+ on a semi-logarithmic scale. The dimensionless values are derived from the averaged streamwise velocity component $\bar{u}_x$ and the wall-normal coordinate y using the kinematic viscosity ν , the friction velocity u_τ and the following equations:

$$u^+ = \bar{u}_x/u_\tau$$

$$y_+ = y \cdot u_\tau/\nu$$

$$u_\tau = \sqrt{\nu \cdot [d\bar{u}_x/dy]_{y=0\text{mm}}}$$

For comparison, the linear law

$$u^+ = y^+$$

and the logarithmic law of the wall

$$u^+ = 1/\kappa \cdot \ln(y^+) + B$$

following Pope (2012) are plotted as grey solid lines. According to Pope (2012), the parameters κ and B were set to 0.41 and 5.2, respectively. Close to the wall up to $y^+ = 7$, the profiles are in good agreement with the linear law of the viscous sublayer. The thickness of the viscous sublayer, usually associated with $y^+ = 5$, is about 450 µm in the 1 bar case, well consistent with a previous study on an atmospheric SWQ

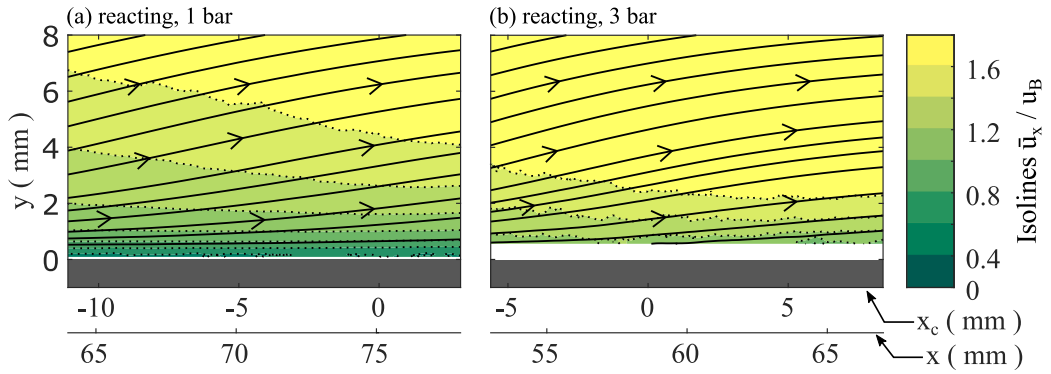

Fig. 8. Isolines (dashed lines) of the averaged, streamwise velocity component u_x overlaid with streamlines (solid lines) of the reacting flow for (a) the 1 bar and (b) the 3 bar operating case obtained from 1000 samples (in each case) recorded at 50 Hz repetition rate.

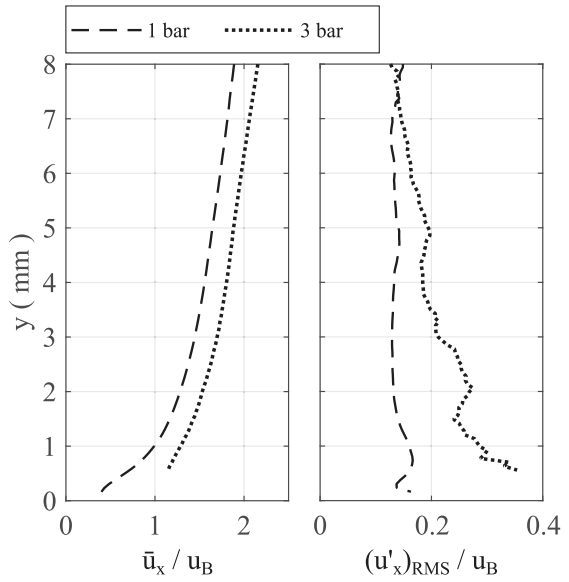

Fig. 9. Wall-normal profiles of mean normalized velocities (a), normalized RMS of fluctuations (b) $x_c = 0$mm in the reacting flow.

configuration (Zentgraf et al., 2021a). In the 3 bar case it is about 300 µm. As the velocity profiles are plotted down to $y^+ = 2$, Fig. 7(c) confirms, that the optical setup is capable to resolve the viscous sublayer of the turbulent flow. In the log-law region ($y^+ > 30$), however, the profiles clearly deviate from the logarithmic law of the wall, as measured u^+ values exceed the corresponding theoretical value. In Fig. 7(b), profiles of the corresponding mean velocity fluctuations (RMS) at $x_c = 0$ mm are shown. Compared to the profiles at the inlet of the flame tube (Fig. 5, the near-wall peak has broadened resulting in a more homogenous profiles close to the wall. Comparing the profiles of both operating cases in Fig. 7 (b), normalized velocity fluctuations in the vicinity of the wall (y < 1 mm) appear to be higher at 3 bar. At larger wall distances (y < 3 mm), however, the opposite is observed.

4.2.2. Reacting case

In Fig. 8, the reacting flow field is shown by means of isolines of the ensemble averaged streamwise velocity component $\overline{u}_x$ normalized with the bulk velocity u_B for both turbulent cases similar to Fig. 6. In the 1 bar case, the velocity vectors closest to the wall are located at $y = 100$ µm . In the 3 bar case, however, considerably increased beam steering effects impeded the evaluation of velocity vectors from the particle raw images below $y = 550$ µm wall distance. Comparing these plots with the flow fields of the non-reacting cases, the impact of the flame is apparent as the flow is accelerated through the flame resulting in normalized velocities greater than one and an appreciably increased wall-normal velocity component indicated by the streamlines. To fit the increased velocities, the isolines are plotted for normalized velocities of 0.4 to 1.6 with steps of 0.2. It is observed, that the isolines contract in streamwise direction approaching $x_c = 0$ mm due to the presence of the flame. Further downstream, the isolines appear to slightly expand again. Comparing both operating cases, it is evident, that corresponding isolines associated with normalized velocities between 1.0 and 1.6 are located closer to the wall at 3 bar operating pressure. The same is observed from wall-normal profiles of $\overline{u}_x/u_B$ at $x_c = 0$ mm depicted in Fig. 9(a) showing higher normalized velocities in the 3 bar case at all wall distances y. This suggests a higher acceleration of the gas flow due to the flame in the 3 bar case. Considering the appreciably higher normalized velocity in the vicinity of the wall ($y = 550$ µm) at 3 bar, the wall-normal gradient of $\overline{u}_x/u_B$ close to the wall is likely to be higher similar to the observations in the non-reacting flow. The impact of the flame on mean velocity fluctuations (RMS) is outlined in Fig. 9(b). Compared to the non-reacting conditions (Fig. 7), overall velocity fluctuations are significantly increased in both operating cases. In the 3 bar case, $(u'_x)_{RMS}/u_B$ values significantly increase with decreasing wall distance. This is likely due to fluctuations of the flame front position close to the wall. In the 1 bar case, however, the influence of flame front fluctuations is appreciably smaller, as mean velocity fluctuations are almost constant except for a slight increase close to the wall. Far from the wall, where the flow field is barely affected by flame front fluctuations (see section 4.3), $(u'_x)_{RMS}/u_B$ values are nearly equal in both operating cases and increased by a factor of about 2.5–3.5 compared to the non-reacting flows.

4.3. Quenching phenomena and flame front statistics

Within this section, the combustion dynamics and the quenching topology of the side-wall quenching process are characterized for both turbulent operating cases based on OH-PLIF recordings and the extracted flame front positions. In a first step, the temporal evolution of the near-wall flame front topology is discussed by means of example OH-PLIF image sequences taken from data sets recorded at 5 kHz repetition rate. The sequences, showing every fifth image of the underlying data, are depicted in Fig. 10. The instantaneous flame front, which was detected using the algorithm described in section 3.2, is highlighted as blue dashed line. Based on the topology of the flame front close to the wall, the instantaneous flame-wall interaction events are classified into three cases. The selected example image sequences show the evolution

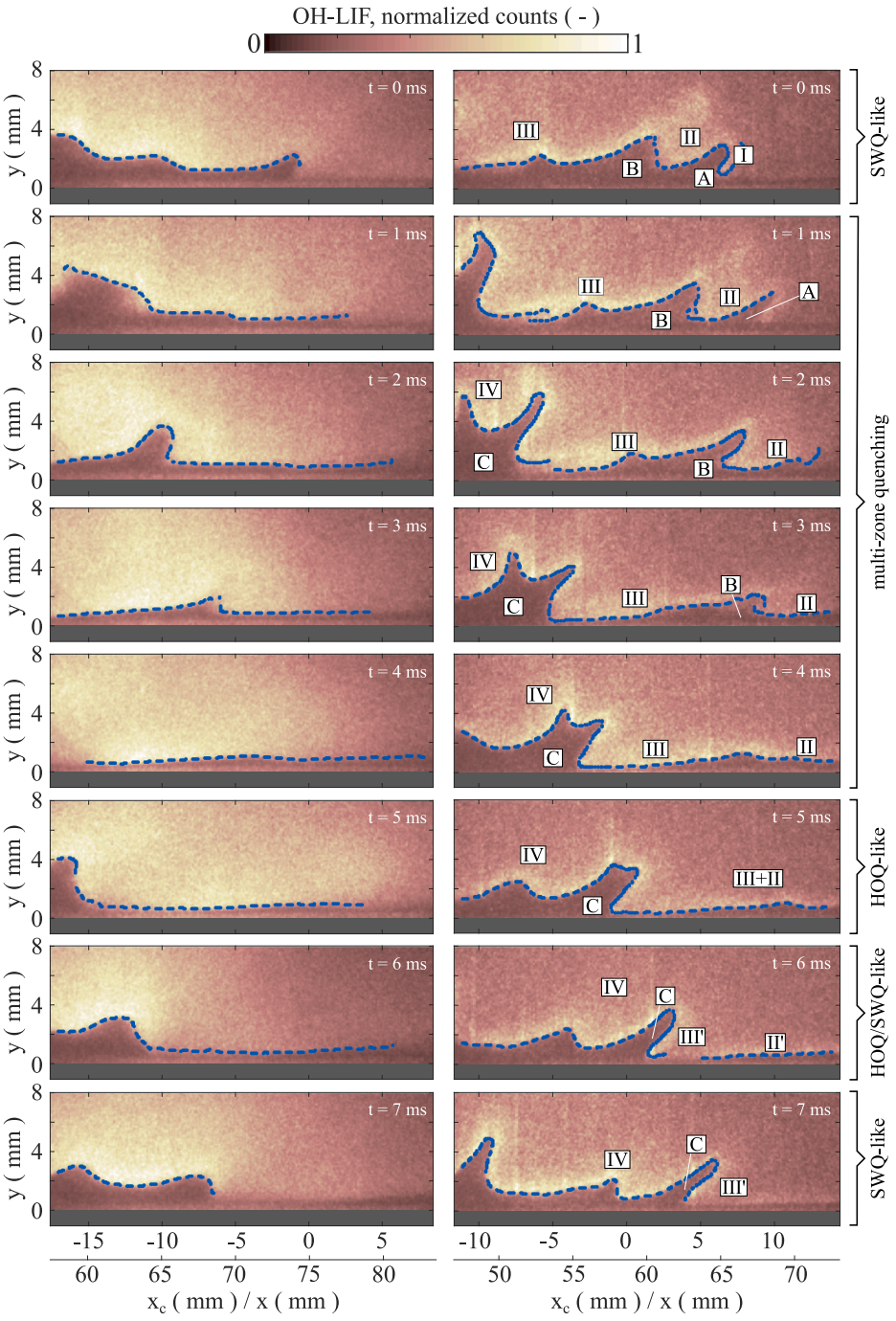

Fig. 10. Evolution of near-wall flame front shown by OH-PLIF raw image sequences. Detected flame fronts highlighted as blue dashed line. 1 bar operating case on the left, 3 bar operating case on the right. (For interpretation of the references to colour in this figure legend, the reader is referred to the web version of this article.)

of the flame front between these FWI cases. To allow comparisons of the general flame front topologies at both operating pressures, sequences are shown for the 1 bar and the 3 bar operating case. However, as the fundamental process of both transient sequences is comparable, the focus is on the 3 bar case in the following. At the beginning of the sequence at $t = 0$ ms , the zone of flame-wall interaction is limited to a small area at about $x = 65$ mm and the near-wall flame front (I) is oriented almost perpendicular to the wall. In accordance with the nomenclature in a previous study (Zentgraf et al., 2021a), this FWI event is therefore called *SWQ-like scenario*. Upstream of the quenching zone, two new reaction zones (II, III) are approaching the wall, while in the unburnt gas, two pockets of fresh gas (A, B) bounded by the curved flame

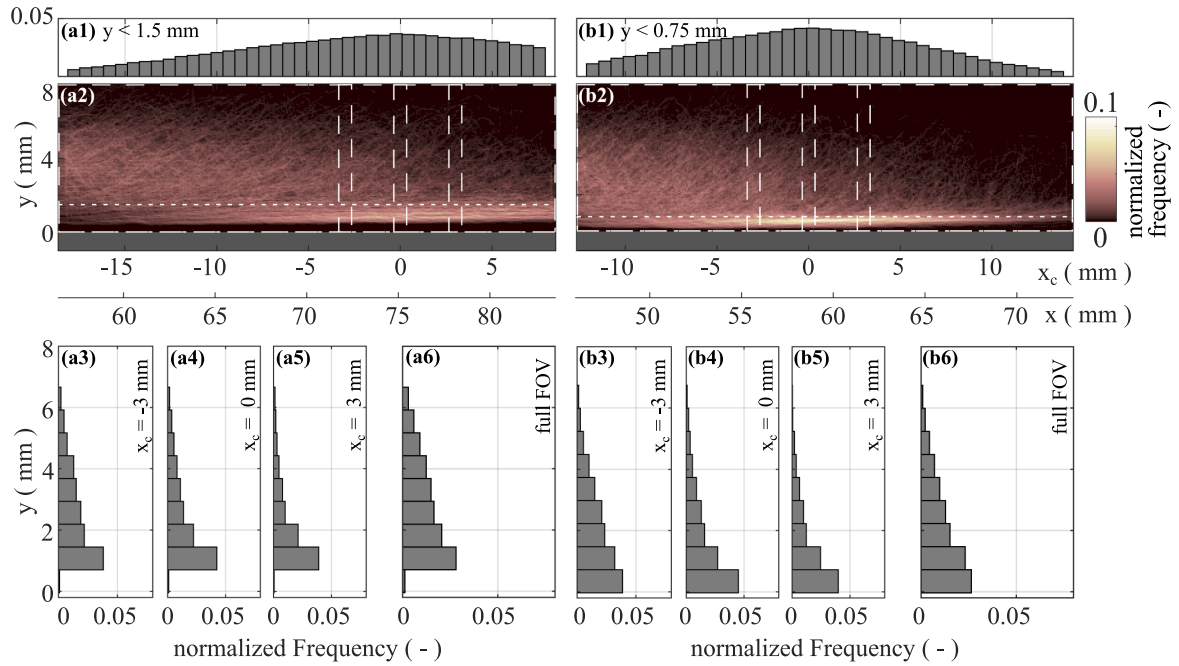

Fig. 11. Flame front statistics of the 1 bar (a•) and 3 bar operating case (b•). Flame brush (•2) derived from 1000 samples (in each operating case) recorded at 50 Hz repetition rate. Wall-normal (•3 - •6) and wall-parallel (•1) distributions of normalized frequencies derived from several regions (highlighted as white dashed rectangles) within the flame brush.

front can be identified. At $t = 1$ ms , reaction zone (I) extinguishes at the wall and the fresh gas pocket (A) vanishes as the unburnt gas mixture is consumed by reaction zone (II). Upstream, two new quenching zones evolve simultaneously as the new reaction zones (II, III) further approach the wall. This FWI event is therefore referred to as *multi-zone quenching scenario*. The fresh gas pocket (B) is now bounded by the wall and the newly formed quenching zones. From $t = 2$ ms to 4 ms , the distance between the wall and the reaction zones (II, III) further decreases and the enclosed pocket of unburnt gas shrinks until it is almost completely vanished at $t = 4$ ms . At the same time another fresh gas pocket (C) bounded by a fourth reaction zone (IV) is carried with the flow in streamwise direction. From $t = 5$ ms on, reaction zones (II) and (III) can hardly be distinguished any more as they are now combined into one single extended wall-parallel reaction zone. Similar to a previous study (Zentgraf et al., 2021a), this FWI event is called *head-on quenching (HOQ)-like scenario*. While reaction zone (IV) and the shrinking fresh gas pocket (C) move further in downstream direction, the wall-parallel reaction zone (II + III) starts to extinguish as chemical reactions are quenched due to enthalpy losses in the vicinity of the wall at $t = 6$ ms . The flame front is now divided into two quenching zones oriented perpendicular (III') and parallel (II') to the wall, respectively. In contrast to the *multi-zone quenching scenario* and according to the post-processing procedure, both quenching zones are not connected but spatially separated by a zone of burnt gas. At $t = 7$ ms , reaction zone (II') is fully extinguished, again resulting in an *SWQ-like scenario.* As reaction zone (IV), which exhibits a wall-parallel flame front, further approaches the wall, the development of a *multi-zone quenching* or *HOQ-like scenario* can be assumed followed by a similar sequence of quenching scenarios (not shown). However, it should be noted that the sequence occurs randomly, as the investigated FWI process is dominated by stochastic events.

For a statistical analysis of the FWI process, flame front positions extracted from 1000 (in each operating case) statistically independent OH-PLIF images recorded at 50 Hz repetition rate are used to determine the flame brush, depicted in Fig. 11(a2) and (b2) for both operating cases. For this purpose, instantaneous two-dimensional binary flame front fields, comprising "ones" at positions where the flame front was detected, and "zeros" at all other locations, were computed for every OH-PLIF image. Averaging all binary fields resulted in a spatial frequency distribution indicating the relative number of flame front occurrences in the data set at a given position. The position of the quenching wall in the binary flame front fields was determined following the procedure described in section 3.1. In addition to the flame brushes, bar charts, derived from the same data, are given, visualizing one-dimensional distributions of normalized frequencies in wall-parallel (•1) and wall-normal (•3 - •6) direction. These distributions are determined for several regions within the flame brush field indicated by rectangles. For the wall-normal frequency distributions (dashed rectangles), frequency values are initially added up in wall-parallel direction within the respective regions and subsequently summed up in $\Delta y = 700$ µm wide bins. While distributions in (•3) to (•5) are derived from data in $\Delta x = 700$ µm wide stripes centered at $x_c = -3$ mm , $x_c = 0$ mm and $x_c = 3$ mm , Fig. 11(a6) and (b6) show the corresponding distributions for the entire FOV. The wall-parallel distributions are determined in an analogous manner, by adding up the frequency values in wall-normal direction first and summing them up in $\Delta x = 700$ µm wide bins subsequently. By dividing the resulting cumulated (absolute) frequency values by the number of pixels in a corresponding bin multiplied with the number of images in the data set (1000), normalized frequency values are determined. Based on the frequency distributions the conditioned x-coordinate x_c, which was already introduced in section 4.2, is calculated. In a first step, the position y_{max} (1.5 mm @ 1 bar; 0.75 mm @ 3 bar) of the bin exhibiting the maximum normalized frequency is identified in distribution (a6) and (b6), respectively. Afterwards, wall-parallel distributions of the normalized frequency are determined as described above based on the flame brush field close to the wall within $y_{max} < y < 0$ (see Fig. 11(•1)). In a final step, the origin of the x_c-scale is placed at the position of the maximum normalized frequency in the

respective wall-normal frequency distribution. This position corresponds to $x = 75.1$ mm in the 1 bar case and $x = 58.6$ mm in the 3 bar case, respectively.

Far upstream of $x_c = 0$ mm , the flame brush is wide extending from close to the wall to about $y = 6$ mm in both operating cases and normalized frequency values do not exceed 3 %. Further downstream, where the frequency of FWI events increases, the flame brush slowly narrows down. Approaching $x_c = 0$ mm , normalized frequency values increase close to the wall and maximum values are reached within a thin, elongated zone oriented parallel to the quenching wall. The shape of this zone could be attributed to HOQ-like scenarios featuring a wall-parallel flame front close to the wall as well as SWQ-like events featuring variable streamwise quenching locations. Comparing both flame brushes, the described zone is more pronounced in the 3 bar case featuring higher maximum values. Moreover, the extent of this zone in wall-normal direction appears to be smaller implying that FWI events are on average limited to a thinner area (in wall-normal direction) close to the wall compared to the atmospheric case. Furthermore, Fig. 11(a2) and (b2) suggest that the flame brush reaches closer to the wall in the 3 bar case as the 0.5 %-isoline of the normalized frequency (not shown) is located at smaller wall distances (1 bar: ≈ 600 μm; 3 bar: ≈ 70 μm). This is in accordance with measured quenching distances of a laminar sidewall quenching flame ($\phi = 0.7$) in a constant volume chamber, which decrease from about 700 μm at 1 bar to about 250 μm at 3 bar (Boust et al., 2007a). An evaluation of the absolute quenching distances is impeded by the uncertainty of the quenching wall position (see section 3.2) being in the same order of magnitude. Comparing the depicted wall-normal frequency distributions, the observed differences in the flame brushes of both operating cases are further clarified. In the 1 bar case, the normalized frequency close to the wall is almost zero, whereas it is maximum in the 3 bar case and the maximum normalized frequency value at $x_c = 0$ mm is slightly higher in the 3 bar case. In order to verify, if the observed differences in the flame brushes are statistically significant, a chi-squared test is performed on the frequency distributions to test if they are based on the same general population. For this purpose, tests are conducted using one frequency distribution of each operating case at a given position with regard to the conditioned coordinate x_c . The chi-squared test statistic is carried out as given in (Sachs, 1999) by comparing the frequency distribution of one operating case to the combined distribution of both operating cases. Thus, in sum, six chi-squared tests were carried out based on the distributions in Fig. 11 (•3), (•4) and (•5). As in all six cases the null hypothesis ("distributions are based on the same general population") was rejected with a 5 % level of significance, the observed differences in both flame brushes are confirmed with statistical significance. A more detailed discussion on the origin of these differences in terms of flame-flow interaction and their impact on properties, like flame surface density and mean reaction rate, is however beyond the scope of this study focussing on a characterization of the novel burner.

5. Conclusion

Within this study, a novel test rig was introduced enabling the investigation of FWI in a pressurized environment at pressures of up to 10 bar and at increased Reynolds numbers in a SWQ configuration. High accessibility to the quenching process is ensured allowing the application of laser diagnostics for detailed assessments of various aspects of FWI, which are needed to supplement previous studies on atmospheric FWI by additional investigations focussing on the impact of conditions that are more relevant to practical combustion devices, e.g. IC engines or gas turbines. This study aimed at the characterization of the combustion process by means of simultaneous high-speed PIV and OH-PLIF measurements for two operating cases featuring turbulent flow conditions at 1 bar and 3 bar, respectively. Methane was used as fuel, as it is easy manageable with regard to the experiment as well as numerical simulations and was therefore suitable for the first operation of the novel test rig. It is expected that the results characterizing the flame front topology and combustion dynamics of the novel test rig are transferable to experiments with more complex fuels, provided that s_l and therefore u_B (constant u_B/s_l ratio) are in the same order of magnitude. In a first step, the flow field data was used to determine the inflow boundary conditions in terms of mean velocities and RMS of velocity fluctuations in the non-reacting flow, which are especially relevant for numerical simulations of the presented SWQ configuration. Normalizing the velocity fluctuations with the laminar flame speed, it was shown that the investigated combustion process is at the transition from the wrinkled to the corrugated flamelet regime. Additional PIV measurements in the non-reacting flow and in the reacting flow at the quenching position were carried out with a focus on the average flow field near the wall. The transient evolution of the near-wall flame front topology was investigated based on OH-PLIF image sequences showing the temporal transition between three different quenching scenarios. Besides SWQ-like and HOQ-like events, which could already be observed in previous studies on atmospheric FWI, a multi-zone quenching scenario could be identified. Flame brushes of both turbulent operating cases (1 bar and 3 bar) derived from statistically independent samples were compared and showed statistically significant differences as confirmed by hypotheses tests performed on one-dimensional frequency distributions deduced from the flame brush data.

CRediT authorship contribution statement

Pascal Johe: Conceptualization, Investigation, Writing – original draft, Writing – review & editing, Visualization, Formal analysis. **Florian Zentgraf:** Conceptualization, Investigation, Writing – review & editing. **Max Greifenstein:** Conceptualization, Investigation, Writing – review & editing. **Matthias Steinhausen:** Conceptualization, Writing – review & editing. **Christian Hasse:** Conceptualization, Writing – review & editing, Supervision. **Andreas Dreizler:** Conceptualization, Writing – review & editing, Supervision.

Declaration of Competing Interest

The authors declare that they have no known competing financial interests or personal relationships that could have appeared to influence the work reported in this paper.

Acknowledgement

This project is funded by the Deutsche Forschungsgemeinschaft (DFG, German Research Foundation) Projektnummer 237267381 TRR 150. The generous financial support is gratefully acknowledged. A. Dreizler is grateful for support through the Gottfried Wilhelm Leibniz program.

Appendix

The algorithm utilized to extract the flame front from OH-PLIF recordings is based on the application of a Canny-edge (CE) filter detecting local maxima of the gradient within the image based on a low and a high threshold (section 3.1). The sensitivity of the low threshold on the flame front statistics is analysed using one-dimensional distributions of normalized frequencies, depicted in Fig. 12. The processing procedure used to derive these distributions is described in section 4.3. The shown distributions are based on the same data set of OH-PLIF raw images (3 bar operating case)

processed with the flame front detection algorithm using either a low threshold of 0 or 0.5. Comparing corresponding distributions at the same position with regard to x_c derived with different low threshold values, it is evident that normalized frequency values decrease with increasing threshold value. Chi-squared homogeneity tests performed on each pair of corresponding distributions moreover indicate that the choice of the threshold value impacts the shape of the distribution, as the null hypothesis ("distributions are based on the same general population") is to be rejected with a level of significance of 5 % in every case. The major contribution to the empirically determined χ^2 value results from both bins closest to the wall indicating that the detection algorithm is more sensitive to the low threshold close to the wall as gradients in the OH-PLIF signal are reduced due to quenching and more likely to be ignored by the CE filter.

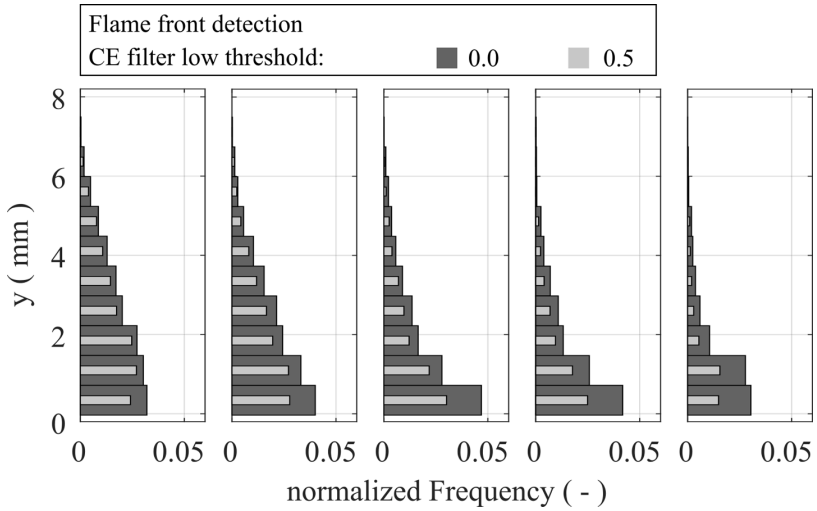

Fig. 12. Sensitivity analysis of flame front detection algorithm by means of flame front statistics for the 3 bar case. Wall-normal distributions of normalized frequencies based on detected flame fronts using a low threshold of either 0.0 or 0.5.

References

Bohlin, A., Mann, M., Patterson, B.D., Dreizler, A., Kliewer, C.J., 2015. Development of two-beam femtosecond/picosecond one-dimensional rotational coherent anti-Stokes Raman spectroscopy: Time-resolved probing of flame wall interactions. Proc. Combust. Inst. 35 (3), 3723–3730. https://doi.org/10.1016/j.proci.2014.05.124.

Bohlin, A., Jainski, C., Patterson, B.D., Dreizler, A., Kliewer, C.J., 2017. Multiparameter spatio-thermochemical probing of flame–wall interactions advanced with coherent Raman imaging. Proc. Combust. Inst. 36 (3), 4557–4564. https://doi.org/10.1016/j.proci.2016.07.062.

Boust, B., Sotton, J., Bellenoue, M., 2007b. Unsteady heat transfer during the turbulent combustion of a lean premixed methane–air flame: Effect of pressure and gas dynamics. Proc. Combust. Inst. 31 (1), 1411–1418. https://doi.org/10.1016/j.proci.2006.07.176.

Boust, B., Sotton, J., Labuda, S.A., Bellenoue, M., 2007a. A thermal formulation for single-wall quenching of transient laminar flames. Combust. Flame 149 (3), 286–294. https://doi.org/10.1016/j.combustflame.2006.12.019.

Canny, J., 1986. A Computational Approach to Edge Detection. IEEE Trans. Pattern Anal. Mach. Intell. PAMI-8 (6), 679–698. https://doi.org/10.1109/TPAMI.1986.4767851.

Dreizler, A., Böhm, B., 2015. Advanced laser diagnostics for an improved understanding of premixed flame-wall interactions. Proc. Combust. Inst. 35 (1), 37–64. https://doi.org/10.1016/j.proci.2014.08.014.

Dreizler, A., Pitsch, H., Scherer, V., Schulz, C., Janicka, J., 2021. The role of combustion science and technology in low and zero impact energy transformation processes. Applications in Energy and Combustion Science 7, 100040. https://doi.org/10.1016/j.jaecs.2021.100040.

Fan, Y., Guo, J., Lee, M., Iki, N., Suzuki, Y., 2021. Quantitative evaluation of wall chemical effect in hydrogen flame using two-photon absorption LIF. Proc. Combust. Inst. 38 (2), 2361–2370. https://doi.org/10.1016/j.proci.2020.06.021.

Escofet-Martin, D., Ojo, A., Mecker, N.T., Linne, M., Peterson, B., 2021. Simultaneous 1D hybrid fs/ps rotational CARS, phosphor thermometry, and CH* imaging to study. Proc. Combust. Inst. 38 (1), 1579–1587. https://doi.org/10.1016/j.proci.2020.06.097.

Ganter, S., Heinrich, A., Meier, T., Kuenne, G., Jainski, C., Rißmann, M.C., Dreizler, A., Janicka, J., 2017. Numerical analysis of laminar methane–air side-wall-quenching. Combust. Flame 186, 299–310. https://doi.org/10.1016/j.combustflame.2017.08.017.

Goodwin, David G., Speth, Raymond L., Moffat, Harry K., Weber, Bryan W. (2021): Cantera: An Object-oriented Software Toolkit for Chemical Kinetics, Thermodynamics, and Transport Processes: Zenodo.

Greifenstein, M., Dreizler, A., 2021. Investigation of mixing processes of effusion cooling air and main flow in a single sector model gas turbine combustor at elevated pressure. Int. J. Heat Fluid Flow 88, 108768. https://doi.org/10.1016/j.ijheatfluidflow.2020.108768.

Greifenstein, M., Hermann, J., Boehm, B., Dreizler, A., 2019. Flame–cooling air interaction in an effusion-cooled model gas turbine combustor at elevated pressure. Exp. Fluids 60 (1). https://doi.org/10.1007/s00348-018-2656-3.

Heinrich, A., Ries, F., Kuenne, G., Ganter, S., Hasse, C., Sadiki, A., Janicka, J., 2018. Large Eddy Simulation with tabulated chemistry of an experimental sidewall quenching burner. Int. J. Heat Fluid Flow 71, 95–110. https://doi.org/10.1016/j.ijheatfluidflow.2018.03.011.

Jainski, C., Rißmann, M., Böhm, B., Dreizler, A., 2017a. Experimental investigation of flame surface density and mean reaction rate during flame–wall interaction. Proc. Combust. Inst. 36 (2), 1827–1834. https://doi.org/10.1016/j.proci.2016.07.113.

Jainski, C., Rißmann, M., Böhm, B., Janicka, J., Dreizler, A., 2017. Sidewall quenching of atmospheric laminar premixed flames studied by laser-based diagnostics. Combust. Flame 183, 271–282. https://doi.org/10.1016/j.combustflame.2017.05.020.

Karrer, M., Bellenoue, M., Labuda, S., Sotton, J., Makarov, M., 2010. Electrical probe diagnostics for the laminar flame quenching distance. Exp. Therm Fluid Sci. 34 (2), 131–141. https://doi.org/10.1016/j.expthermflusci.2009.10.002.

Li, F., Yang, H., Huo, J., Wang, X., Jiang, L., Zeng, X., Zhao, D., 2019. Interactions between the flame and different coatings in a slit burner. Fuel 253, 420–430. https://doi.org/10.1016/j.fuel.2019.05.033.

Mann, M., Jainski, C., Euler, M., Böhm, B., Dreizler, A., 2014. Transient flame–wall interactions: experimental analysis using spectroscopic temperature and CO concentration measurements. Combust. Flame 161 (9), 2371–2386. https://doi.org/10.1016/j.combustflame.2014.02.008.

Kosaka, H., Zentgraf, F., Scholtissek, A., Hasse, C., Dreizler, A., 2020. Effect of Flame-Wall Interaction on Local Heat Release of Methane and DME Combustion in a Side-Wall Quenching Geometry. Flow Turbul. Combust. 104 (4), 1029–1046. https://doi.org/10.1007/s10494-019-00090-4.

Peters, N., 1988. Laminar flamelet concepts in turbulent combustion. Symposium (International) on Combustion 21 (1), 1231–1250.

Ojo, A.O., Escofet-Martin, D., Collins, J., Falconetti, G., Peterson, B., 2021. Experimental investigation of thermal boundary layers and associated heat loss for transient engine-relevant processes using HRCARS and phosphor thermometry. Combust. Flame 233, 111567. https://doi.org/10.1016/j.combustflame.2021.111567.

Pope, S.B., 2012. Turbulent Flows. Cambridge University Press.

Rivera, J.E., Gordon, R.L., Talei, M., 2019. Flame-wall interaction of a forced laminar premixed propane flame: Flame dynamics and exhaust CO emissions. Proc. Combust. Inst. 37 (4), 5385–5392. https://doi.org/10.1016/j.proci.2018.07.030.

Dabov, K., Foi, A., Katkovnik, V., Egiazarian, K., 2006. Image denoising with block-matching and 3D filtering. Proc. SPIE 6064, Image Processing: Algorithms and Systems, Neural Networks, and Machine Learning, 606414.

Rißmann, M., Jainski, C., Mann, M., Dreizler, A., 2017. Flame-Flow Interaction in Premixed Turbulent Flames During Transient Head-On Quenching. Flow Turbul. Combust. 98 (4), 1025–1038. https://doi.org/10.1007/s10494-016-9795-5.

Sachs, L., 1999. Angewandte Statistik. Springer, Berlin Heidelberg, Berlin, Heidelberg.

Saggau, B., 1985. Temperature profile measurements at head-on quenched flame fronts in confined CH4/Air and CH3OH/Air mixtures. Symp. (Int.) Combust. 20 (1), 1291–1297. https://doi.org/10.1016/S0082-0784(85)80619-6.

Schlichting, H., Gersten, K., 2017. Boundary-Layer Theory. Springer Berlin Heidelberg, Berlin, Heidelberg.

Sotton, J., Boust, B., Labuda, S.A., Bellenoue, M., 2005. Head-on quenching of transient laminar flame: heat flux and quenching distance measurements. Combust. Sci. Technol. 177 (7), 1305–1322. https://doi.org/10.1080/00102200590950485.

Smith, G.P., Golden, D.M., Frenklach, M., Moriarty, N.W., Eiteneer, B., Goldenberg, M. et al., 2011. GRI-Mech 3.0. http://www.me.berkeley.edu/gri_mech/.

Wan, S., Fan, Y., Maruta, K., Suzuki, Y., 2019. Wall chemical effect of metal surfaces on DME/air cool flame in a micro flow reactor. Proc. Combust. Inst. 37 (4), 5655–5662.

Wu, Y.i., Modica, V., Rossow, B., Grisch, F., 2016. Effects of pressure and preheating temperature on the laminar flame speed of methane/air and acetone/air mixtures. Fuel 185, 577–588. https://doi.org/10.1016/j.fuel.2016.07.110.

Zentgraf, F., Johe, P., Cutler, A.D., Barlow, R.S., Böhm, B., Dreizler, A., 2021a. Classification of flame prehistory and quenching topology in a side-wall quenching burner at low-intensity turbulence by correlating transport effects with CO_2, CO and temperature. Combustion and Flame, 111681. https://doi.org/10.1016/j.combustflame.2021.111681.

Zentgraf, F., Johe, P., Steinhausen, M., Hasse, C., Greifenstein, M., Cutler, A.D., Barlow, R.S., Dreizler, A., 2021b. Detailed assessment of the thermochemistry in a side-wall quenching burner by simultaneous quantitative measurement of CO_2, CO and temperature using laser diagnostics. Combustion and Flame 235, 111707. https://doi.org/10.1016/j.combustflame.2021.111681.

A.2 Paper II

Laser-based investigation of flame surface density and mean reaction rate during flame-wall interaction at elevated pressure

P. Johe, F. Zentgraf, M. Greifenstein, R. S. Barlow, A. Dreizler. Laser-based investigation of flame surface density and mean reaction rate during flame-wall interaction at elevated pressure. *Proceedings of the Combustion Institute,* 39(2):2159–2168, 2023. https://doi.org/10.1016/j.proci.2022.09.016

Declaration on the contribution to the scientific publication
Erklärung zum Eigenanteil der wissenschaftlichen Veröffentlichung

Pascal Johe, M.Sc.

Paper

P. Johe, F. Zentgraf, M. Greifenstein, R. S. Barlow, A. Dreizler: Laser-based investigation of flame surface density and mean reaction rate during flame-wall interaction at elevated pressure.
Proceedings of the Combustion Institute Volume 39, 2 (2023). https://doi.org/10.1016/j.proci.2022.09.016

Co-Authors

Florian Zentgraf, Dr.-Ing.
Max Greifenstein, Dr.-Ing.
Robert Barlow, Dr.
Andreas Dreizler, Prof. Dr. habil.

Individual Contributions

- **Pascal Johe**
  - Operated the pressurized side-wall quenching burner test rig and performed the experiments.
  - Conducted post-processing and analysis of the experimental data.
  - Served as main and corresponding author of the paper, performed literature research, wrote the manuscript and managed the review process.
- **Florian Zentgraf**
  - Supported P. Johe setting up and conducting the experiments.
  - Proofread the manuscript.
- **Max Greifenstein**
  Advised on the design of the experiment; proofread the manuscript.
- **Robert Barlow and Andreas Dreizler**
  Supported the interpretation and discussion of the results; proofread the manuscript.

Overall Contribution of Pascal Johe

A leading role in the conceptualization and conduction of the experiments, data analysis and main author of the manuscript.

Use of paper contents in other dissertations

This publication is not the subject of any ongoing or completed dissertation.

Available online at www.sciencedirect.com

ScienceDirect

Proceedings of the Combustion Institute 39 (2023) 2159–2168

Proceedings of the Combustion Institute

www.elsevier.com/locate/proci

Laser-based investigation of flame surface density and mean reaction rate during flame-wall interaction at elevated pressure

Pascal Johe [a,*], Florian Zentgraf [a], Max Greifenstein [a], Robert S. Barlow [b], Andreas Dreizler [a]

[a] *Technical University of Darmstadt, Department of Mechanical Engineering, Reactive Flows and Diagnostics, Otto-Berndt-Str. 3, Darmstadt 64287, Germany*
[b] *Barlow Combustion Research, Livermore, USA*

Received 4 January 2022; accepted 16 September 2022
Available online 23 October 2022

Abstract

Velocities and flame front locations are measured simultaneously in a turbulent, side-wall quenching (SWQ) V-shaped flame during flame-wall interaction (FWI) at 1 and 3 bar by means of particle image velocimetry (PIV) and planar laser-induced fluorescence of the OH radical (OH-PLIF). The turbulent flame brush is characterized based on the spatial distribution of the mean reaction progress variable and a common direct method is used to derive the flame surface density (FSD) from the two-dimensional data by image processing. As the near-wall reaction zone is limited to a smaller region closer to the wall at higher pressure, higher peak values are observed in the FSD at 3 bar. A second definition of the FSD adapted for flames exposed to quenching is utilized similar to previous studies emphasizing the impact of FWI. The influence of the wall on the flame front topology is investigated based on a flame front-conditioned FSD and its variability within the data set. In a last step, an estimate of the mean reaction rate is deduced using an FSD model and evaluated in terms of integral and space-averaged values. A decreasing trend of integral mean reaction rate in regions with increasing flame quenching is observed for both operating conditions, but more pronounced at 3 bar. Space-averaged mean reaction rates, however, increase in the quenching region, as the size of the reaction zone decreases.

Keywords: Flame-wall interaction; Pressurized combustion; Flame surface density; Mean reaction rate; LIF

1. Introduction

The interaction of flames with solid surfaces, denoted as flame-wall interaction (FWI), is relevant to many technical combustion system, as recently summarized by Dreizler and Böhm [1], Luo and Liu [2]. These processes are characterized

* Corresponding author.
E-mail address: johe@rsm.tu-darmstadt.de (P. Johe).

https://doi.org/10.1016/j.proci.2022.09.016

by high near-wall temperature gradients causing undesirable wall heat losses which can lead to local (or global) quenching of the chemical reaction progress. This results in reduced thermodynamic efficiency and increased emission of pollutants like unburned hydrocarbons and carbon monoxide (CO). With regard to real combustion devices, experimental and numerical investigations focusing on these aspects of turbulent combustion at increased pressure are needed.

In the context of the flamelet concept for premixed turbulent combustion, the flame surface density (FSD), representing the local ratio of flame surface to volume, is a central quantity to characterize the effect of the flow field to wrinkle the flame and thus increase its surface [3]. Furthermore, it is commonly used to derive the mean reaction rate in the flame [4,5]. In numerical simulation, the FSD may be described by an exact, but unclosed, transport equation, called Σ-equation [3]. Closures of this equation need to be modeled and validated against Direct Numerical Simulation (DNS) or experimental data. In the past, several models for closure of these terms were proposed, as reviewed by Veynante and Vervisch [6]. With regard to FWI, these models, however, need to be adapted to account for wall effects. This was, for example, done based on DNS-results for model derivation/validation by Bruneaux et al. [7] for a flame propagating normal to the wall (head-on quenching, HOQ). More recently, Sellmann et al. [8] investigated the influence of Lewis number effects on the FSD in turbulent head-on quenching using DNS data. Corresponding experimental investigations were carried out by Tayebi et al. [9] and Jainski et al. [10] for a V-shaped flame in an SWQ configuration. Considering the impact of increased pressure on FSD, previous numerical and experimental studies are limited to unbounded flames not exposed to FWI to the authors' best knowledge. Allauddin et al. [11], for example, recently studied algebraic FSD closures for large eddy simluation (LES) of turbulent Bunsen flames up to 10 bar and compared results with experimental data provided by Kobayashi et al. [12].

In this work, a previous investigation on flame surface density in an atmospheric side-wall quenching configuration by Jainski et al. [10] is continued, focusing on the impact of increased pressure. Instantaneous flame front positions of a turbulent V-shaped flame are determined based on planar laser-induced fluorescence of the OH radical (OH-PLIF) in a novel, pressurized SWQ burner at atmospheric and 3 bar pressure. Flame surface density is derived from this data and the mean reaction rate is estimated subsequently. The velocity field is simultaneously measured by means of two-component particle image velocimetry (PIV).

To facilitate further investigations, underlying data of selected figures are available on the institutional repository of Technical University of Darmstadt *TUdatalib* (https://tudatalib.ulb.tu-darmstadt.de/handle/tudatalib/3607).

Table 1
Operating conditions. *Re* defined according to Johe et al. [13].

p (bar)	u_B (m/s)	s_L (m/s)	Re (−)	T_W (K)
1	3.8	0.2725	8200	353
3	2.3	0.167	15000	353

2. Experimental approach

2.1. Pressurized side-wall quenching burner test rig

The main components of the burner, described in detail in Johe et al. [13], are depicted in Fig. 1. Its design is inspired by the atmospheric SWQ burner investigated in previous studies (e.g. Jainski et al. [10]). The burner is partially enclosed by a pressure vessel featuring quartz glass windows on the top and on both sides for optical access. Fuel and dry air are mixed outside the burner and fed into an inlet plenum (not shown). A set of grids and meshes (not shown) is used to homogenize the flow before it enters a converging Morel type nozzle (only partially shown) with rectangular cross-section (≈ 30 × 60 mm^2 at nozzle outlet). Issuing from the nozzle outlet, the premixed gas flow enters the flame tube which is equipped with three quartz glass windows (top and both sides, 180 × 60 mm^2 viewing area). A stainless-steel quenching wall is located at the bottom of the flame tube with its upper surface aligned to the surface of the Morel nozzle. To ensure enhanced optical access, the flat surface of the quenching wall transitions into a convex, cylindrically curved surface (300 mm radius in y-z-plane). The resulting flow cross-section within the flame tube is indicated as red solid line in Fig. 1(b). A turbulence generating grid (perforated plate, solidity 51 %) is positioned in the premixed gas flow. A ceramic rod (1.0 mm diameter) is placed 36 mm downstream the nozzle outlet and 10 mm above the quenching wall to stabilize the V-shaped flame. The lower flame branch impinges on the surface of the quenching wall which is temperature-controlled by circulating water through a cooling duct. Thermocouples positioned about 0.4 mm beneath the surface of the quenching wall are used to monitor the temperature. To minimize shear effects and shield the windows from the reacting gas flow, a dry air co-flow is guided through a sintered bronze structure into the flame tube.

Operating conditions for the two cases investigated within this study are summarized in Table 1. The governing parameter is the flame tube internal pressure p and the operating cases are therefore also referred to as 1 bar (or atmospheric) case and 3 bar case in the following. Operation at 3 bar was

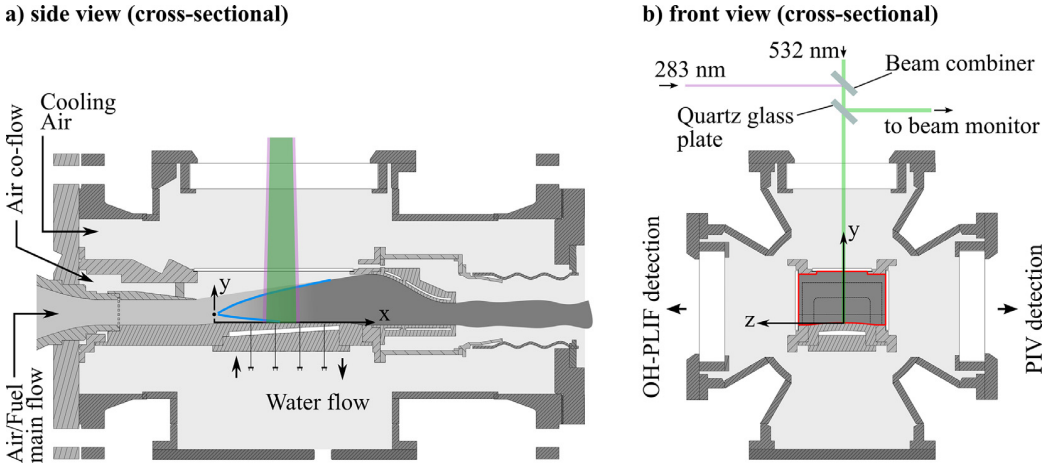

Fig. 1. Cross-sectional side (a) and front (b) view of the pressurized SWQ burner with parts of the laser diagnostic setup.

chosen as a compromise to keep obstructive effects arising from beam steering within manageable limits while achieving an adequate pressure increase for this study of FWI. Methane was used as fuel at an equivalence ratio of 0.8 and the temperature of the quenching wall was stabilized at 353 K. The bulk velocities u_B of the premixed main flow are adapted in both cases with regard to the laminar flame speed s_L to achieve a constant u_B/s_L-ratio, aiming at an almost unchanged streamwise position where quenching occurs in average. This, in turn, leads to different Reynolds numbers in both cases. Varying Reynolds numbers are, however, unavoidable as different pressure dependencies of u_B (or density ρ) and s_L would result in flashback events at 3 bar or flame quenching outside (downstream) of the optically accessible area at 1 bar for Re = constant. However, as the flames are propagating at turbulent flame speed which depends on s_L and flame wrinkling, the mean quenching position is shifted about 12 mm in upstream direction in the 3 bar case.

2.2. Laser diagnostics and post-processing

Fig. 1 also shows parts of the laser diagnostics setup for simultaneous two-component PIV and OH-PLIF measurements at 50 Hz repetition rate. All images were recorded at the central (symmetry) plane of the burner which is equivalent to the x-y-plane ($z = 0$ mm) of the test-rig-fixed coordinate system depicted in Fig. 1(a) and (b). The origin of this coordinate system is defined by the surface of the quenching wall ($y = 0$ mm) and the position of the ceramic rod ($x = 0$ mm). While the x-axis indicates the streamwise position parallel to the wall, the y-axis displays the distance normal to the wall.

PIV measurements were conducted by recording Mie-scattering of alumina particles (Al_2O_3, Martoxid MR52, $d_{50} = [1, 1.7]$ μm) seeded to the premixed gas flow and illuminated by two individual diode-pumped solid state Nd:YAG lasers (Edgewave GmbH, Innoslab IS16II-E). The laser pulses were temporally separated by 30 µs and formed into light sheets of approximately 300 µm thickness. The scattered light was collected using a high-speed CMOS camera (Vision Research, Phantom v2640) equipped with a 180 mm macro lens (Sigma APO Macro EX DG IF HSM, f/8). Velocity vector fields were calculated using DaVis 10.0.5 (LaVision GmbH) based on interrogation windows (IRW) of 24 × 24 pixel size with 75 % overlap (≈ 288 µm IRW size, 72 µm vector spacing).

For qualitative OH-PLIF measurements, the $Q_1(6)$ transition at 35334.38 cm^{-1} was excited using a frequency doubled dye laser (Sirah Lasertechnik GmbH, Allegro) operated with Rhodamine 6G and pumped by a diode-pumped solid state Nd:YAG laser (Edgewave GmbH, Innoslab IS 8II-E). The UV laser pulse ($\lambda \approx 283$ nm) was formed into a light sheet featuring a thickness of 80 µm and overlapped with the PIV light sheets using a beam combiner. The laser energy per pulse was about 0.3 mJ. The coefficient of variation of the laser system used is typically about 10%. Overlap was verified by means of low-energy reflections originating from a quartz glass plate within the beam path and captured by a beam monitor. A high-speed CMOS camera (Photron Fastcam SA-X2) equipped with a dual-stage high-speed image intensifier (LaVision GmbH, HS-IRO, 200 ns gate), a 100 mm UV lens (Sodern CERCO 2073, f/2.8) and an interference filter (305–340 nm transmission) was utilized to record the emitted fluorescence. The optics were positioned as close as possible to the windows of the test rig to attain the maximum achievable magnification (35 µm/pixel, 20 µm pixel size). The resulting field of view (FOV) was about 35 ×

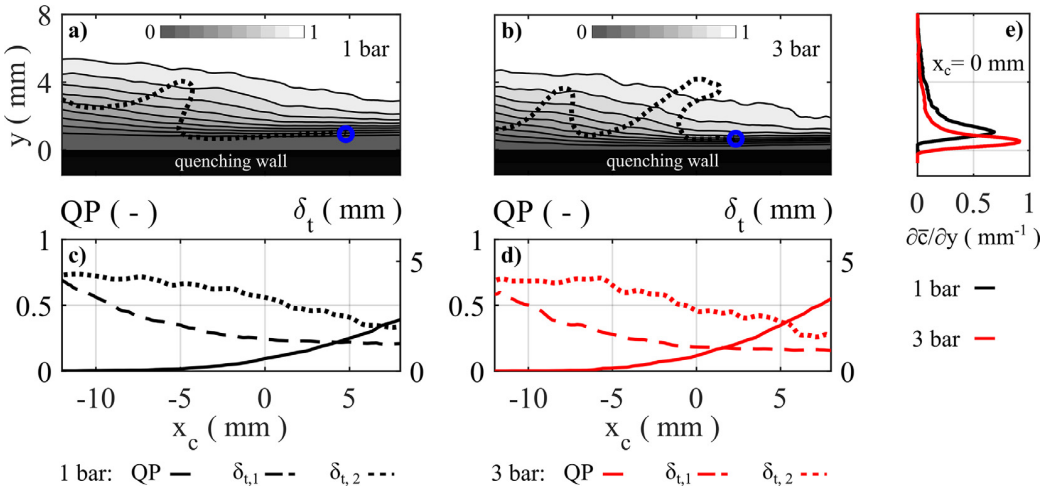

Fig. 2. Spatial distribution of the mean progress variable $\bar{c}$ at 1 bar (a) and 3 bar (b). Profiles of quenching probability (QP) and flame brush thickness $\delta_{t,1}$, $\delta_{t,2}$ at 1 (c) and 3 bar (d). Wall-normal profiles of the partial derivative $\partial\bar{c}/\partial y$ (e).

35 mm^2. Post-processing for flame front detection was implemented in MATLAB 2020b (The MathWorks, Inc.) and included 2 × 2 binning, block-matching and 3D filtering (BM3D) [14] for spatial noise reduction and Canny-edge (CE) filtering to detect local maxima of the intensity's spatial gradient within the OH-PLIF images. Based on the identified edges (assumed to be equivalent to the flame front), the instantaneous spatial reaction progress c was derived by dividing the OH-images in regions of unburnt ($c = 0$) and burnt ($c = 1$) gas.

3. Results

3.1. Reacting flow and flame characteristics

Fig. 2 (a) and (b) visualize the flame brush of the turbulent flame in the 1 bar and 3 bar case, respectively, by means of contour plots of the mean reaction progress variable $\bar{c}$ derived by averaging instantaneous binarized OH-PLIF images. Isolines are shown for $\bar{c} = 0.1$ to $\bar{c} = 0.9$. Since flame quenching in average occurs at slightly different streamwise positions in both operating cases, a quenching-fixed streamwise coordinate x_c is used. This axis indicates the streamwise position with the highest probability to detect a flame front close to the wall at $x_c = 0$ mm and therefore allows for better comparison of both cases. For a detailed description of the determination of x_c based on flame front statistics see [13]. From both spatial distributions of $\bar{c}$ it is evident, that upstream the flame brush extends over a wider range but narrows down at farther downstream positions where the flame interacts with the wall more frequently. To illustrate the spatial distributions of $\bar{c}$-isolines in wall-normal direction, Fig. 2(e) shows wall-normal profiles of the partial derivative of $\bar{c}$ with respect to y ($\partial\bar{c}/\partial y$) for both operating conditions at $x_c = 0$ mm. Based on the maximum of $\partial\bar{c}/\partial y$ the flame brush thickness $\delta_{t,1}$ is derived for every streamwise position according to Namazian [15] ($\delta_{t,1} = 1/\max(\partial\bar{c}/\partial y)$) and shown for both operating cases in Fig. 2(c) and (d). For comparison, the flame brush thickness $\delta_{t,2}$, defined as vertical distance between $\bar{c} = 0.9$ and $\bar{c} = 0.1$ (for example [5]) is also shown in Fig. 2(c) and (d). Comparing both operating cases, it can be seen, that both definitions indicate a slightly reduced flame brush thickness at 3 bar at all streamwise positions x_c. Moreover, it can be deduced that the reaction zone in the 3 bar case is limited to a smaller area closer to the wall.

To give an impression of the flame front topology, an arbitrary, instantaneous flame front is depicted (dashed line) for each operating case in Fig. 2(a) and (b), respectively. For larger wall distances, the flame fronts are noticeably wrinkled in both cases, indicating, however, that flame wrinkling might be more pronounced in the 3 bar case. Approaching the wall, flame wrinkling is reduced and an extended near-wall, wall-parallel reaction zone develops and is finally quenched (not shown) due to wall heat losses. The farthest downstream position of the flame front, the *quenching point*, is indicated by a blue dot in Fig. 2(a) and (b).

The probability of an instantaneous flame front to be already quenched at a certain streamwise position due to its interaction with the wall is depicted by means of streamwise profiles of the quenching probability (QP) in Fig. 2(c) and (d). This quantity is derived by determining the percentage of samples exhibiting a flame front that is already quenched at a given position x_c using the position of the quenching point in each sample. While the quenching probability tends to zero far upstream of $x_c =$

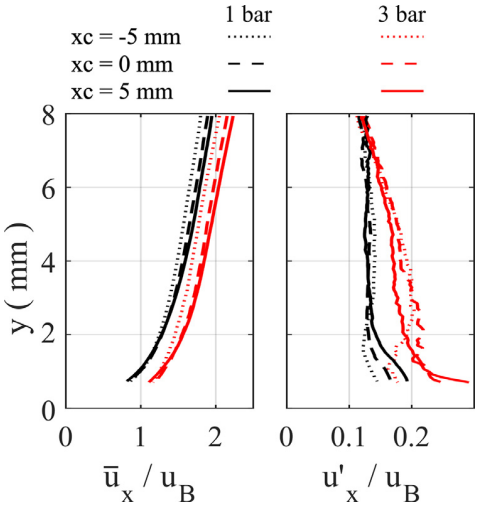

Fig. 3. Wall-normal profiles of mean normalized velocities (a) and normalized RMS of fluctuations (b) in the reacting flow.

0 mm where interaction of flame and wall is rare, it increases farther downstream as flame-wall interaction becomes more frequent. Since the quenching probability remains significantly below 1, it is clear that the shown section (-12 mm $< x_c <$ 8 mm) does not capture the full streamwise range where quenching occurs. Considering the spatial variation of the quenching point position and the spatial extent of the FWI region of the instantaneous flame fronts in Fig. 2, it was not possible to fully capture all quenching events as well as the pre-quenching region within the available FOV, which was limited to achieve the maximum possible spatial magnification.

The velocity field of the reacting flow is characterized for both cases by means of wall-normal profiles of the mean streamwise velocity $\overline{u_x}$ and RMS (root mean square) of velocity fluctuations u'_x both normalized with the corresponding bulk velocity u_B. Wall-normal profiles are shown for $x_c = \{-5, 0, 5\}$ mm (dotted, dashed, solid line, respectively) and both operating cases in Fig. 3(a) and (b). For complementary non-reacting flow conditions (not shown in the manuscript), the PIV setup is capable to resolve the boundary layer down to $y^+ \approx 2$. The thickness of the viscous sublayer (associated with $y^+ = 5$) is about 450 µm at 1 bar and about 300 µm at 3 bar. For reacting conditions, however, no data is depicted for $y < 0.7$ mm as the individual PIV recordings were strongly affected by beam steering (especially at 3 bar) impeding a reliable velocity vector calculation. The boundary layer is therefore not fully resolved down to the viscous sublayer.

While the profiles of $\overline{u_x}/u_B$ exhibit an almost identical shape for both operating cases, they are shifted towards higher values in the 3 bar case. Comparing profiles of one case with regard to their streamwise position, a slight increase of $\overline{u_x}/u_B$ in the downstream direction can be observed.

At 3 bar, normalized velocity fluctuations are increased by a factor of 1.5 to 2 compared to the 1 bar case, and the profiles suggest a slight increase at decreasing wall distances. Accordingly, highest velocity fluctuations align with the flame brush which approaches the wall gradually causing increased velocity fluctuations near the wall by an intense shear layer and increased flame intermittency. At larger wall distances where the frequency of a flame front occurrence decreases (increasing distance between $\tilde{c}$-isolines) and the mean reaction progress approaches unity, velocity fluctuations might lessen due to the increasing viscosity of the fluid. Considering the ratio of bulk velocities used for normalization $(u_B)_{1\text{ bar}}/(u_B)_{3\text{ bar}} = 1.7$, absolute velocity fluctuations are comparable for both operating cases. However, with respect to the absolute mean velocity, velocity fluctuations are considerably increased at 3 bar.

3.2. Flame surface density

The evaluation of the FSD is performed by means of a two-dimensional approximation described by Donbar et al. [16] and Dumont et al. [5] which was previously used by Jainski et al. [10]. Following this procedure, the instantaneous FSD Σ is derived according to Eq. (1) based on the flame front perimeter P in a square control area (CA) with area Δx^2. CAs exhibiting no flame front are assigned a Σ value of zero. The CAs are oriented parallel to the wall.

$$\Sigma = \lim_{\Delta x \to 0} \frac{P}{\Delta x^2} \tag{1}$$

For the practical implementation of this procedure to determine the FSD from flame front images, Δx is set to a finite value. According to Donbar et al. [16], for this purpose, Δx should be (1) larger than the thickness of the reaction zone but should (2) not exceed 1/5 of "the visually observed brush thickness" to ensure that the ensemble-averaged (mean) FSD $\overline{\Sigma}$ is independent of Δx. By choosing $\Delta x = 0.5$ mm for this study the first condition is clearly met as laminar (thermal) flame thicknesses of atmospheric methane flames are in the order of 0.5 mm and decrease at higher pressures (≈ 0.27 mm, estimated from [17] using CANTERA simulations). Considering the flame brush thickness $\delta_{t,2}$ in Fig. 2, which is assumed to best satisfy the definition used by Donbar et al., the second condition is also fulfilled in most parts of the flame brush field. Similar to Jainski's approach [10], two slightly different definitions of the mean FSD, i.e. $\overline{\Sigma}$ and $\overline{\Sigma}_R$, are used to take into account the characteristics of FWI and the associated flame quenching. While $\overline{\Sigma}_R$ is derived by averaging in-

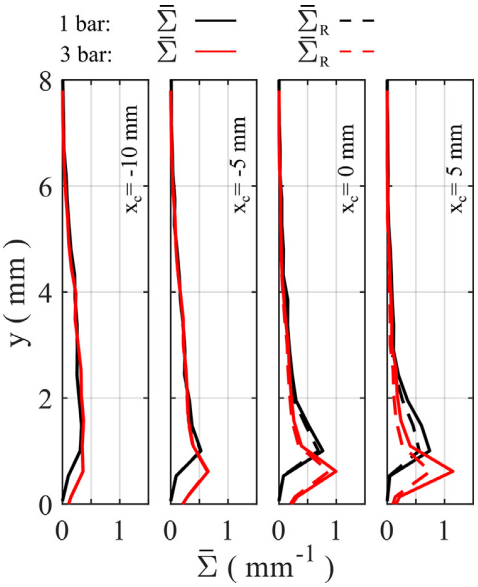

Fig. 4. Wall-normal profiles of $\overline{\Sigma}$ and $\overline{\Sigma}_R$.

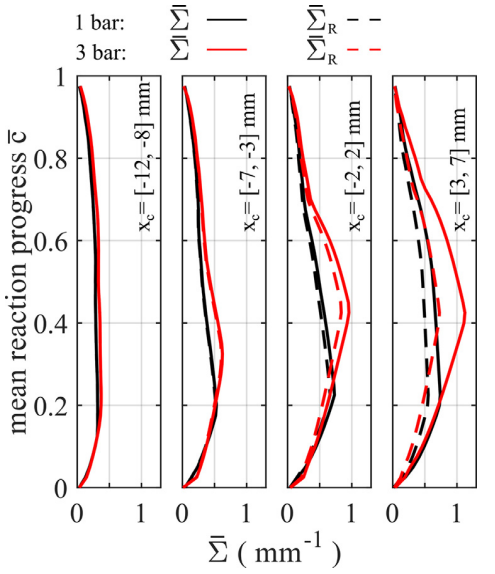

Fig. 5. Wall-normal profiles of $\overline{\Sigma}$ and $\overline{\Sigma}_R$ as function of $\bar{c}$ derived by averaging within segments of 4 mm length in streamwise direction.

stantaneous Σ values of all corresponding CAs of all samples, $\overline{\Sigma}$ is only based on Σ values belonging to CAs that are located upstream of the instantaneous quenching point. Accordingly, $\overline{\Sigma}_R$ is smaller than or equal to $\overline{\Sigma}$ (as potentially more CAs featuring a Σ value of zero are considered for averaging) and differences between mean FSD definitions become more significant with increasing quenching probability. For a more comprehensive derivation of $\overline{\Sigma}$ and $\overline{\Sigma}_R$ the reader is referred to Jainski et al. [10].

Fig. 4 shows wall-normal profiles of $\overline{\Sigma}$ and $\overline{\Sigma}_R$ at different streamwise positions for both operating cases. At $x_c = -10$ mm, all four profiles reveal a broad distribution of the mean FSD, as the flame brush expands over a large range in wall-normal direction (see Fig. 2(a) or (b) and (c) or (d), respectively). Since the quenching probability is nearly zero, no significant difference between $\overline{\Sigma}$ and $\overline{\Sigma}_R$ of the same operating case is evident. Comparing both cases, it can be seen that the profiles differ only slightly at smaller wall distances, where $\overline{\Sigma}$ and $\overline{\Sigma}_R$ are increased in the 3 bar case. As the distributions are slighlty skewed towards smaller wall distances, they deviate from a Gaussian shaped profile, which was previously observed in freely propagating V-shaped flames [18]. Accordingly, it can be assumed that the flame is already influenced by the presence of the wall, even though the quenching probability is close to zero. Farther downstream, as the reaction zone in average is located closer to the wall (see Fig. 2(a) and (b)), the skewness of the profiles increases and a peak close to the wall can be observed featuring a slightly higher maximum value in the 3 bar case. Following theoretical considerations by Donbar et al. [16] assuming an idealized wrinkled flame (triangular wave shape) oscillating within a spatial area of width δ_t, $\overline{\Sigma}$ is proportional to the wrinkledness (ratio of surface areas of turbulent flame and laminar flame located at mean flame position) of the flame and the inverse of the turbulent flame brush thickness δ_t. As will be shown later, in this case the increase of $\overline{\Sigma}$ close to the wall is rather attributed to a reduction of the flame brush thickness $\delta_{t,1}$ or $\delta_{t,2}$, than to a rising flame wrinkling. Since the flame front is in average located within a smaller near-wall region, the decreasing flame brush thickness corresponds to an increasing probability to detect a flame front within a CA close to the wall. Moving farther downstream, the observed peaks are getting more pronounced in both $\overline{\Sigma}$-profiles and the difference in peak heights becomes more significant. This well reflects the relation between the FSD and the flame brush thickness, which is slightly increased in the 1 bar case (at $x_c = 5$ mm: $\delta_{t,1} \approx 1.3$ mm; $\delta_{t,2} \approx 2.5$ mm) compared to the 3 bar case (at $x_c = 5$ mm: $\delta_{t,1} \approx 1.0$ mm; $\delta_{t,2} \approx 2.2$ mm). From $x_c = 0$ mm on, $\overline{\Sigma}_R$ starts to deviate from $\overline{\Sigma}$ as the frequency of flame quenching occurrences rises. With increasing quenching probability the difference between both profiles becomes even more pronounced at $x_c = 5$ mm.

As some of the models used for closure of the Σ-equation rely on a functional relationship of Σ with the reaction progress variable c, profiles of $\overline{\Sigma}$ over $\bar{c}$ are shown in Fig. 5. The profiles are derived by averaging $\overline{\Sigma}(\bar{c})$ and $\overline{\Sigma}_R(\bar{c})$, respectively, in streamwise direction within segments of 4 mm length. In accor-

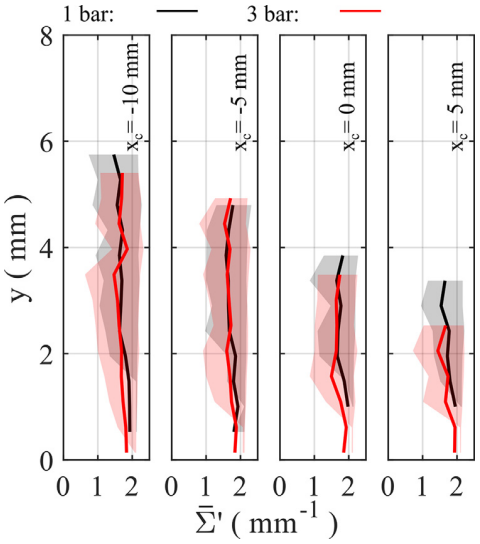

Fig. 6. Wall-normal profiles of mean flame front-conditioned FSD $\overline{\Sigma}'$. Boundaries of colored areas indicate 0.25- and 0.75-quantiles.

dance with observations by Jainski et al. [10] and Shepherd [19], the profiles are almost symmetric, exhibiting a parabolic shape at $x_c = -10$ mm where the flame is almost unaffected by the presence of the wall. Farther downstream, the distributions of $\overline{\Sigma}(\bar{c})$ and $\overline{\Sigma}_R(\bar{c})$ become asymmetric featuring a maximum at smaller $\bar{c}$ values. This trend however, is more pronounced in the 1 bar case. At $x_c = 5$ mm in the 3 bar case, the profile seems to develop a symmetric shape again.

For a *flame front-conditioned* evaluation of the FSD, only those CAs that contain a segment of the instantaneous flame front, therefore being associated with a Σ value greater than zero, are considered for the following statistical analysis. CAs exhibiting no flame front are omitted. By averaging Σ of corresponding CAs a flame front-conditioned mean FSD $\overline{\Sigma}'$ is evaluated. Fig. 6 depicts profiles of $\overline{\Sigma}'$ (solid lines) for the same four streamwise positions analyzed in Fig. 4. Furthermore, 0.25- and 0.75-quantiles are represented by the boundaries of black (1 bar) and red (3 bar) colored areas. CAs featuring less than 50 non-zero Σ values within the data set are not considered within Fig. 6, and no data is shown at the corresponding position. Therefore, as the flame brush narrows down moving in downstream direction, the profiles are limited to a shrinking range close to the wall. Despite it being more common to use a combination of median and quantiles to describe a probability distribution, the mean of the distribution is utilized here as it is more relevant to the calculation of $\overline{\Sigma}$: Multiplying $\overline{\Sigma}'$ with the frequency of flame front occurrences in a given CA yields $\overline{\Sigma}$.

At higher wall distances, Fig. 6 shows that the variability of the flame front-conditioned FSD is high indicated by the increased interquartile range (IQR), i.e. the widths of the colored areas, of the corresponding distributions of Σ values. Depending on their magnitude, the instantaneous Σ values can be associated with different local flame front topologies. As the local flame front curvature κ (flame front perimeter divided by the shortest distance of crossing points of flame front with edges of CA) is in average about 1.015 (in the whole field), its impact on the FSD evaluation is considered negligible and the local flame front within a CA can be assumed as straight line. Therefore, Σ values close to the theoretical value of 2.1 mm^{-1} can in most cases be associated with a straight flame front oriented horizontally or vertically within the corresponding CA ($P = \Delta x$) as the calculation of the FSD according to Eq. (1) reduces to $\Sigma = \frac{1}{\Delta x}$. Considering flame fronts deviating from a horizontal or vertical orientation, Σ values up to 2.98 mm^{-1} (corresponding to diagonally oriented flame front) and below 2.1 mm^{-1} (flame front passes CA only partly) can also occur. Based on this, the increased variability of the flame front-conditioned FSD far from the wall can be assigned to a higher temporal variation of the local flame front orientation and might be associated with increased large-scale flame front wrinkling.

Approaching the wall, the variability of the flame front-conditioned FSD decreases and the IQR is limited to a smaller range around 2.1 mm^{-1}. This is mainly due to an increase of the 0.25-quantiles, while 0.75-quantiles remain almost constant. The corresponding $\overline{\Sigma}'$ values slightly increase with decreasing wall distance and converge towards 2.1 mm^{-1}, corresponding to a horizontal/vertical flame front. As one might expect, an evaluation of the local flame front orientation indicates that a wall-parallel flame front is the dominant flame front topology in the vicinity of the wall. Accordingly, the described trends can be attributed to flame fronts increasingly aligning parallel to the wall. This might be again associated with flame wrinkling decreasing in the vicinity of the wall. Similar observations were made by Jainski et al. [10] with regard to the evolution of a flame front-conditioned $\overline{\Sigma}'$ close to the wall converging towards the theoretical value associated with a wall-parallel flame front. Moving in downstream direction from $x_c = -10$ mm to $x_c = -5$ mm, a comparable trend of decreasing variability is identified as the IQR close to the wall is reduced. This is ascribed to a more frequent interaction between flame and wall, consistent with a rising QP (see Fig. 2).

Comparing both operating cases, it is evident that profiles of $\overline{\Sigma}'$ at 3 bar are shifted towards smaller wall distances reflecting the trend of decreasing quenching distances at increasing pressure [20]. Accordingly, an increased near-wall variability

of the flame front-conditioned FSD is observed in the 3 bar case.

3.3. Mean reaction rate

Following Trouvé and Poinsot [3] and Bruneaux et al. [7], the mean reaction rate $\bar{\dot{\omega}}$ can be derived using Eq. (2) based on the mean FSD, the density of the unburnt gas ρ_u, the initial fuel mass fraction $Y_{F,u}$ and the local consumption speed s_c which is averaged over the area of the laminar flamelet indicated by the operator $\langle \ldots \rangle_S$.

$$\bar{\dot{\omega}} = \rho_u Y_{F,u} \langle s_c \rangle_S \overline{\Sigma} = \rho_u Y_{F,u} \overline{s_c \Sigma} \tag{2}$$

According to Pope [21], $\langle s_c \rangle_S$ may be replaced by a standard ensemble average of s_c weighted with the FSD, $\overline{s_c \Sigma}/\overline{\Sigma}$. A similar expression for the mean reaction rate is given by Dumont et al. [5], based on an ensemble-average of the local product of flamelet velocity and FSD. Effects of flame curvature and stretch are accounted for in both approaches by the consumption speed and the flamelet velocity, respectively. However, as stated by Dumont et al. [5], by replacing these quantities with the laminar flame speed of the undisturbed flame s_L, an approximation for the mean reaction rate can be obtained neglecting these effects. According to Bruneaux et al. [7] this is acceptable for a broad spectrum of turbulent flows far from walls and should be reasonable in this case as the main focus is on comparing two operating cases to examine trends related to pressure variation. However, close to the wall, considerable deviations from the laminar flame speed of the undisturbed flame due to wall heat losses and fuel depletion were observed by Wichman and Bruneaux [22]. Therefore, following the approach of Janiski et al. [10] who investigated the dependency of the consumption speed with respect to the wall distance in a comparable atmospheric SWQ configuration, a linear decrease of the flame consumption speed with decreasing wall distance is assumed for $y < 2$ mm (although this trend might be limited to smaller wall distances at 3 bar). At $y > 2$ mm, the laminar flame speed of the undisturbed flame ($s_L = 0.273$ m/s at 1 bar, $s_L = 0.167$ m/s at 3 bar) is presumed. Fig. 7(a) shows profiles of the integral (in wall-normal direction) mean reaction rate as a function of the streamwise position x_c. Similar profiles of the mean reaction rate space-averaged in wall-normal direction within the reaction zone, i.e. the flame brush ($y(\bar{c} = 0.1)$ to $y(\bar{c} = 0.9)$) are shown in Fig. 7(b). By replacing $\overline{\Sigma}$ with $\overline{\Sigma}_R$ in Eq. (2), the impact of flame quenching on the reaction rate may be considered.

Since the flame front is in average located closer to the wall for increasing x_c (see Fig. 4), the effect of decreasing consumption speed in the vicinity of the wall is intensified resulting in a clearly decreasing integral $\bar{\dot{\omega}}(\overline{\Sigma})$ in Fig. 7(a). Comparing the two operating cases, the integral $\bar{\dot{\omega}}(\overline{\Sigma})$ is at a higher level at 3 bar due to the increased nominal

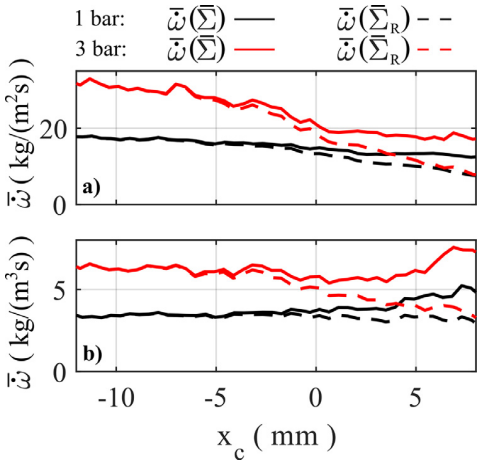

Fig. 7. Profiles of integral (a) and space-averaged (b) mean reaction rate $\bar{\dot{\omega}}$. Due to the spatial integration the unit of $\bar{\dot{\omega}}$ in (a) is kg/(m^2 s).

massflow exhibiting a more pronounced decrease in downstream direction. This reduction is further intensified for $\bar{\dot{\omega}}(\overline{\Sigma}_R)$ as quenching is considered. Comparing the profiles of the flame surface density in Fig. 4, the higher (integral and space-averaged) mean reaction rates observed at 3 bar (see Fig. 7) are presumably caused by the higher gas density and not by an increased flame surface density. This is confirmed by an evaluation of the integral FSD (integrated in wall-normal direction) which is only increased by about 10% at 3 bar at all streamwise positions, while the integral $\bar{\dot{\omega}}(\overline{\Sigma})$ is larger by a factor of almost 2 at upstream positions.

In the case of space-averaged $\bar{\dot{\omega}}(\overline{\Sigma})$, the impact of decreasing consumption speed close to the wall is outweighed by the decreasing reaction zone size relevant for averaging. This results even in a slight increase of $\bar{\dot{\omega}}(\overline{\Sigma})$ in the quenching region. Space-averaged $\bar{\dot{\omega}}(\overline{\Sigma}_R)$, however, is reduced (3 bar) or remains constant (1 bar), respectively.

As the integral heat release is increased at 3 bar and on average takes place within a thinner area (reduced extent in wall-normal direction) closer to the wall (see the flame brush in Fig. 2), higher space-averaged heat release rates can be observed. This might be accompanied by a higher thermal expansion resulting in an increased acceleration of the fluid close to the wall which in turn leads to higher velocity fluctuations by increased shear (see Fig. 3).

4. Conclusions

The flame structure of a turbulent V-shaped flame at ambient and 3 bar pressure, as well as its alteration due to flame-wall interaction, is assessed by means of a statistical analysis of instantaneous

flame front positions. Comparison of both operating cases is simplified by a quenching-fixed streamwise axis. Based on the flame brush represented by the spatial distribution of the mean reaction progress variable, it is shown that the reaction zone in the quenching region is limited to a smaller region closer to the wall in the 3 bar case. These observations were supported by the spatial distribution of the FSD $\overline{\Sigma}$ as corresponding wall-normal profiles are increasingly skewed towards smaller wall distance exhibiting higher and narrower peaks at higher pressure. Following approaches of previous studies on near-wall FSD, a second definition of the mean FSD $\overline{\Sigma}_R$ is used to better visualize the impact of flame quenching. An evaluation of flame front-conditioned FSD showed a vanishing variability of instantaneous Σ values close to the wall, and it could be deduced that the near-wall flame front is primarily oriented wall-parallel. Accordingly, the increase in $\overline{\Sigma}$ close to the wall was associated with the decreasing flame brush thickness, corresponding to locally increasing frequencies of flame front occurence, rather than increased flame wrinkling. In a last step, the mean reaction rate was deduced for both operating conditions using the FSD. Higher integral and space-averaged values at 3 bar could be associated with the increased gas density and the higher nominal massflow, respectively, rather than an increased FSD. Due to the higher heat release and thermal expansion within a smaller area at increased pressure, higher acceleration of the fluid and increased shear close to the wall are assumed and associated with higher velocity fluctuations measured simultaneously.

Declaration of Competing Interest

The authors declare that they have no known competing financial interests or personal relationships that could have appeared to influence the work reported in this paper.

Acknowledgments

This project is funded by the Deutsche Forschungsgemeinschaft (DFG, German Research Foundation) Projektnummer 237267381 TRR 150. The generous financial support is gratefully acknowledged. A. Dreizler is grateful for support through the Gottfried Wilhelm Leibniz program.

References

[1] A. Dreizler, B. Böhm, Advanced laser diagnostics for an improved understanding of premixed flame-wall interactions, Proc. Combust. Inst. 35 (1) (2015) 37–64, doi:10.1016/j.proci.2014.08.014.

[2] M. Luo, D. Liu, Pollutants emissions of CO and soot from flame-wall interactions in fundamental and practical energy conversion systems: A Review, ES Energy Environ. (2018), doi:10.30919/esee8c218.

[3] A. Trouvé, T. Poinsot, The evolution equation for the flame surface density in turbulent premixed combustion, J. Fluid Mech. 278 (1994) 1–31, doi:10.1017/S0022112094003599.

[4] K. Bray, Studies of the turbulent burning velocity, Proc. R. Soc. Lond. 1982 (1990) 315–335.

[5] J. P. Dumont, D. Durox, R. Borghi, Experimental study of the mean reaction rates in a turbulent premixed flame, Combust. Sci. Technol. 89 (1–4) (1993) 219–251, doi:10.1080/00102209308924110.

[6] D. Veynante, L. Vervisch, Turbulent combustion modeling, Prog. Energy Combust. Sci. 28 (3) (2002) 193–266, doi:10.1016/S0360-1285(01)00017-X.

[7] G. Bruneaux, T. Poinsot, J.H. Ferziger, Premixed flame–wall interaction in a turbulent channel flow: budget for the flame surface density evolution equation and modelling, J. Fluid Mech. 349 (1997) 191–219, doi:10.1017/S0022112097006769.

[8] J. Sellmann, J. Lai, A.M. Kempf, N. Chakraborty, Flame surface density based modelling of head-on quenching of turbulent premixed flames, Proc. Combust. Inst. 36 (2) (2017) 1817–1825, doi:10.1016/j.proci.2016.07.114.

[9] B. Tayebi, C. Galizzi, J.-F. Leone, D. Escudié, Topology structure and flame surface density in flame-wall interaction, in: 5th European Thermal–Sciences Conference, 2008.

[10] C. Jainski, M. Rißmann, B. Böhm, A. Dreizler, Experimental investigation of flame surface density and mean reaction rate during flame–wall interaction, Proc. Combust. Inst. 36 (2) (2017) 1827–1834, doi:10.1016/j.proci.2016.07.113.

[11] U. Allauddin, S.R.R. Lomada, M. Pfitzner, Investigation of pressure and the lewis number effects in the context of algebraic flame surface density closure for LES of premixed turbulent combustion, Theor. Comput. Fluid Dyn. 35 (1) (2021) 17–37, doi:10.1007/s00162-020-00543-x.

[12] H. Kobayashi, T. Nakashima, T. Tamura, K. Maruta, T. Niioka, Turbulence measurements and observations of turbulent premixed flames at elevated pressures up to 3.0 MPa, Combust. Flame 108 (1–2) (1997) 104–117, doi:10.1016/S0010-2180(96)00103-4.

[13] P. Johe, F. Zentgraf, M. Greifenstein, M. Steinhausen, C. Hasse, A. Dreizler, Characterization of flow field and combustion dynamics in a novel pressurized side-wall quenching burner using high-speed PIV/OH-PLIF measurements, Int. J. Heat Fluid Flow 94 (2022) 108921, doi:10.1016/j.ijheatfluidflow.2021.108921.

[14] K. Dabov, A. Foi, V. Katkovnik, K. Egiazarian, Image denoising with block-matching and 3D filtering, in: Image Processing: Algorithms and Systems, Neural Networks, and Machine Learning, 606414, Proc. SPIE 6064, 2006, pp. 354–365.

[15] M. Namazian, I.G. Shepherd, L. Talbot, Characterization of the density fluctuations in turbulent V-shaped premixed flames, Combust. Flame 64 (3) (1986) 299–308, doi:10.1016/0010-2180(86)90147-1.

[16] J.M. Donbar, J.F. Driscoll, C.D. Carter, Reaction zone structure in turbulent nonpremixed jet flames—From CH-OH PLIF images, Combust. Flame

122 (1–2) (2000) 1–19, doi:10.1016/S0010-2180(00)00098-5.

[17] T. Poinsot, D. Veynante, Theoretical and Numerical Combustion, R.T. Edwards, Inc., 2001.

[18] D. Veynante, J. Piana, J.M. Duclos, C. Martel, Experimental analysis of flame surface density models for premixed turbulent combustion, Symp. (Int.) Combust. 26 (1) (1996) 413–420, doi:10.1016/S0082-0784(96)80243-8.

[19] I.G. Shepherd, Flame surface density and burning rate in premixed turbulent flames, Symp. (Int.) Combust. 26 (1) (1996) 373–379, doi:10.2172/132644.

[20] B. Boust, J. Sotton, S.A. Labuda, M. Bellenoue, A thermal formulation for single-wall quenching of transient laminar flames, Combust. Flame 149 (3) (2007) 286–294, doi:10.1016/j.combustflame.2006.12.019.

[21] S.B. Pope, The evolution of surfaces in turbulence, Int. J. Eng. Sci. 26 (5) (1988) 445–469, doi:10.1016/0020-7225(88)90004-3.

[22] I.S. Wichman, G. Bruneaux, Head-on quenching of a premixed flame by a cold wall, Combust. Flame 103 (4) (1995) 296–310, doi:10.1016/0010-2180(95)00100-X.

A.3 Paper III

Effects of elevated pressure on thermochemical states of turbulent flame-wall interaction studied by multi-parameter laser diagnostics

P. Johe, F. Zentgraf, M. Greifenstein, B. Böhm, A. Dreizler. Effects of elevated pressure on thermochemical states of turbulent flame-wall interaction studied by multi-parameter laser diagnostics. *Combustion and Flame*, 260, 113214, 2024. https://doi.org/10.1016/j.combustflame.2023.113214

Declaration on the contribution to the scientific publication
Erklärung zum Eigenanteil der wissenschaftlichen Veröffentlichung

Pascal Johe, M.Sc.

Paper

P. Johe, F. Zentgraf, M. Greifenstein, B. Böhm, A. Dreizler: Effects of elevated pressure on thermochemical states of turbulent flame-wall interaction studied by multi-parameter laser diagnostics.
Combustion and Flame, Volume 260 (2024) 113214. https://doi.org/10.1016/j.combustflame.2023.113214

Co-Authors

Florian Zentgraf, Dr.-Ing.
Max Greifenstein, Dr.-Ing.
Benjamin Böhm, Dr.-Ing.
Andreas Dreizler, Prof. Dr. habil.

Individual Contributions

- **Pascal Johe**
  - Operated the pressurized side-wall quenching burner test rig and performed the experiments.
  - Conducted post-processing and analysis of the experimental data.
  - Served as main and corresponding author of the paper, performed literature research, wrote the manuscript and managed the review process.
- **Florian Zentgraf**
  - Supported P. Johe setting up and conducting the experiments.
  - Proofread the manuscript.
- **Max Greifenstein**
  Advised on the design of the experiment; proofread the manuscript.
- **Benjamin Böhm and Andreas Dreizler**
  Supported the interpretation and discussion of the results; proofread the manuscript.

Overall Contribution of Pascal Johe

A leading role in the conceptualization and conduction of the experiments, data analysis and main author of the manuscript.

Use of paper contents in other dissertations

This publication is not the subject of any ongoing or completed dissertation.

Combustion and Flame 260 (2024) 113214

Contents lists available at ScienceDirect

Combustion and Flame

journal homepage: www.sciencedirect.com/journal/combustion-and-flame

Effects of elevated pressure on thermochemical states of turbulent flame-wall interaction studied by multi-parameter laser diagnostics

Pascal Johe *, Florian Zentgraf, Max Greifenstein, Benjamin Böhm, Andreas Dreizler

Department of Mechanical Engineering, Reactive Flows and Diagnostics, Technical University of Darmstadt, Otto-Berndt-Str. 3, Darmstadt 64287, Federal Republic of Germany

ARTICLE INFO

Keywords:
Flame-wall interaction
Turbulence
Pressurized combustion
Thermochemistry
Dual-pump CARS
LIF

ABSTRACT

Effects of increased pressure on the thermochemistry of turbulent flame-wall interaction (FWI) were investigated within this study. Quantitative, pointwise measurements of three state parameters, i.e., gas-phase temperature, CO_2 and CO mole fraction, were performed by means of dual-pump coherent anti-Stokes Raman spectroscopy (CARS) and two-photon laser-induced fluorescence (LIF) of CO. The flame front was simultaneously tracked by planar OH-LIF imaging. The measurements were carried out in a fully premixed methane-air flame in an enclosed side-wall quenching burner test rig under atmospheric and pressurized conditions (3 bar absolute pressure). An evaluation of near wall flame front topologies showed that the interaction of the flame with the wall is predominantly characterized by one single, extended reaction zone, similar to a so-called head-on quenching configuration. The dominance of this quenching scenario occurred most likely due to the confined burner configuration preventing an unhindered expansion of the hot exhaust gases. Thermochemical states were studied using pairwise correlations of temperature, CO_2 and CO mole fraction. Regarding the measurements at atmospheric pressure, an overall good agreement with other studies on atmospheric FWI in a similar unconfined burner was observed considering differences concerning the flow field and the burner configuration. For the thermochemistry measurements at elevated pressure, similar trends as for the atmospheric measurements were identified. A comparison of both operating cases suggested that FWI processes were more strongly affected by heat losses at elevated pressure, but differences are moderately pronounced. To the authors' best knowledge, these experiments are the first attempt to explore the near-wall thermochemistry of FWI processes at elevated pressure using multi-parameter measurements. As the near-wall measurements were further complicated by effects arising with increasing pressure, e.g., intensified beam steering and reduced length scales, implications on the application of the laser diagnostics are reported.

1. Introduction

Although the transition to a climate-neutral energy economy requires the predominant use of renewable energy sources, which drives a progressing electrification of all areas of society and industry, the thermal conversion of chemical energy sources will most likely continue to play an important role in our future energy system. On the one hand, in some areas, e.g., aviation or high-temperature industry processes, there is still no alternative to the energy conversion by combustion in the near future anyhow. On the other hand, in areas such as power generation, chemical energy carriers (produced from renewable energy sources) could also help to meet the challenges posed by the increasing share of renewable energy, e.g., by acting as energy storage to compensate for the volatility of renewable energy sources. The development of clean combustion systems, which are optimized in terms of combustion efficiency, pollutant emission and safe operation, is consequently still of great importance. This in turn implies the need for further fundamental research providing detailed insights into the underlying processes which are incorporated into the predictive design process of such technologies.

In enclosed combustion systems that rely on internal combustion of chemical energy carriers, like gas turbines or IC engines, these processes are typically influenced to a large extent by the interaction of the flame with a cold, solid surface, e.g., the combustion chamber walls. These so-called flame-wall interactions (FWI) result in high heat losses causing local flame quenching and incomplete combustion, which in turn promotes the local formation of pollutants, like carbon monoxide and unburnt hydrocarbons, and lowers the overall efficiency. Due to the

* Corresponding author.

https://doi.org/10.1016/j.combustflame.2023.113214
Received 18 August 2023; Received in revised form 21 November 2023; Accepted 22 November 2023
Available online 22 December 2023

resulting high relevance for the overall performance of the combustion process, investigations in this research field have been conducted for several decades [1]. Therefore, as FWI are characterized by a complex, mutual interaction of flow field, flame and wall, generic experimental configurations were developed enabling the exploration of various aspects of FWI independently at well-defined and reproducible boundary conditions. As summarized in [1], experimental data on thermal (heat losses and quenching distances) and fluid-mechanical (velocity boundary layer phenomena) properties of FWI as well as flame topologies have been reported so far for head-on quenching (HOQ) and side-wall quenching (SWQ) flames. This also includes experiments at turbulent flow conditions or elevated pressure, as for example presented in [2,3]. Regarding thermochemical properties (i.e., gas-phase temperatures and species) during FWI, however, only a few studies addressing this aspect exist which are mostly related to experiments at laminar flow conditions and almost exclusively carried out at atmospheric conditions.

The first experiments on near-wall thermochemical states in premixed flames date back to the 1980s and were carried out by Clendening et al. [4] and Saffmann [5] in an SWQ configuration. Raman-scattering measurements were performed close to an isothermal cold plate which was placed perpendicular to the outlet of a McKenna-type burner operated with a premixed fuel/air mixture under laminar and atmospheric conditions. Profiles of the gas-phase temperature and relative hydrocarbon number densities were derived from Raman spectra and effects of wall temperature, surface material and fuel type were investigated in a parametric study. First measurements in a confined HOQ configuration were carried out by Saggau [6] soon after providing temperature profiles across laminar methane/air and methanol/air flames propagating towards a wall at varying pressure, ranging from 0.5 to 1 bar. More recently, a burner configuration similar to that used in [4,5] was used by Fuyuto et al. [7] to investigate the laminar quenching boundary layer by measuring distributions of gas-phase temperature, using multi-line NO laser-induced fluorescence (LIF) thermometry, as well as OH, CH_2O and CO by means of single-photon and two-photon LIF, respectively. Further studies on FWI under laminar flow conditions were carried out by Mann et al. [8] in a HOQ burner and Janiski et al. [9] as well as Kosaka et al. [10] in an SWQ burner by simultaneous quantification of gas-phase temperatures and mole fractions of CO using coherent anti-Stokes Raman spectroscopy (CARS) and two-photon CO-LIF. By enhancing the CARS technique to a dual-pump CARS approach, Zentgraf et al. [11] additionally quantified CO_2 mole fractions in the side-wall quenching flame. Moreover, ultrabroadband CARS was applied by Bohlin et al. [12] for simultaneous, one-dimensional imaging of temperature and major species (N_2, O_2, CO,CO_2, CH_4) in a similar SWQ burner configuration.

With regard to turbulent flow conditions, however, experiments on thermochemical states of FWI are scarce and have only emerged in the near past. While some of the last-mentioned publications address the impact of turbulence on thermochemistry to some extent [8,10], the only experimental study, known to the author, that focusses on the investigation of near-wall turbulence-chemistry interaction based on multi-parameter measurements was carried out by Zentgraf et al. [13]. Using a laser diagnostic setup similar to that in [11], gas-phase temperature as well as CO_2 and CO mole fractions were probed simultaneously in an atmospheric, turbulent dimethyl ether/air flame at small wall distances and the gathered information was combined with flow field data collected in a separate study.

Considering operating conditions of real combustion devices, besides the flow configuration (laminar/turbulent), also the influence of elevated pressure on combustion processes is of great interest. While investigations on thermochemical states of pressurized flames based on multi-parameter measurements are reported [14–16], these studies, often related to gas turbine research, are focusing on other aspects of combustion than FWI. Studies related to FWI processes at elevated pressure by Escofet-Martin et al. [17] and Ojo et al. [18] focus on thermal boundary layer phenomena. To the authors' best knowledge, effects of elevated pressure on near-wall thermochemical states during FWI have not been investigated experimentally so far.

The state of research concerning numerical simulations on FWI is at a similar stage. While there is a larger number of studies on near-wall flames at laminar flow conditions, for example [19–22], fewer studies are covering turbulent FWI. Gruber at al. [23] investigated effects of the turbulent boundary layer on the structure and the near-wall propagation of a premixed hydrogen/air flame using direct numerical simulation (DNS) with detailed chemical kinetics and observed a regime change from thin to thickened flames at decreasing wall distance. Thermochemical states in a turbulent side-wall quenching flame were studied by Steinhausen et al. [24] to evaluate a flame-vortex interaction mechanism that was observed before in experiments [11]. Based on these findings, a novel chemistry manifold was presented to account for this mechanism. Other recent studies on turbulent FWI have been presented by Jiang et al. [25], Niemietz et al. [26] and Palulli et al. [27]. Effects of elevated pressure are occasionally included, but only for laminar flow conditions [28,29]. The interaction between near-wall turbulence and chemistry at higher pressures and Reynolds numbers has not yet been numerically investigated in detail.

Within this study, quantitative multi-parameter measurements of gas-phase temperature, CO_2 and CO mole fractions (T, X_{CO_2} and X_{CO}) are carried out in an enclosed SWQ configuration at atmospheric and 3 bar absolute pressure. The location of the flame front is simultaneously tracked providing information on the position of the probe volume with respect to the reaction zone. Therefore, a laser diagnostic approach similar to that in [13], including simultaneous dual-pump CARS, CO-LIF and OH-PLIF measurements, is applied. The scope of this study can be divided into three major aspects: (1) It is intended that this study contributes to a better understanding of the influence of elevated pressures and increased Reynolds numbers on FWI processes. (2) Furthermore, the experimental data may be used for model development and validation of numerical simulations. (3) The feasibility of the laser-diagnostics setup for the investigation of the SWQ process at elevated pressure is to be assessed. Properties of FWI at elevated pressure further complicate experimental investigations as, for example, length scales are reduced. Moreover, measurements are more strongly affected by beam steering effects resulting from steeper temperature gradients close to the wall compared to the atmospheric case.

To facilitate further investigations, underlying data of selected figures are available on the institutional repository of Technical University of Darmstadt TUdatalib (https://tudatalib.ulb.tu-darmstadt.de/handle/tudatalib/4066).

2. Experimental approach

2.1. Test rig

The essential components of the pressurized side-wall quenching burner test rig as well as its operation are outlined in the following. Since the test rig was previously introduced and characterized with regard to flow conditions and flame dynamics in [30], a more detailed description of it can be found there.

The test rig is shown in Fig. 1 with two cross-sectional views. During reacting operation, the fully premixed dried air/fuel main flow enters the inlet plenum of the burner and is guided through a set of honeycombs and meshes for flow homogenization (both not shown). The main flow is then accelerated within a converging Morel type nozzle (only partly shown) with rectangular cross-section ($\approx 30 \times 60$ mm^2 at nozzle outlet) resulting in an almost top-hat velocity profile at the nozzle outlet. To increase turbulence intensities, a turbulence-generating grid (3, perforated plate, 3.8 mm bore diameter, 51 % solidity) is placed at the nozzle outlet. A ceramic rod (4, 1.0 mm diameter) is positioned 36 mm downstream of the nozzle outlet within the flame tube (1) to stabilize a V-shaped flame whose lower branch interacts with the surface of a temperature-controlled stainless-steel quenching wall (2). To enable the

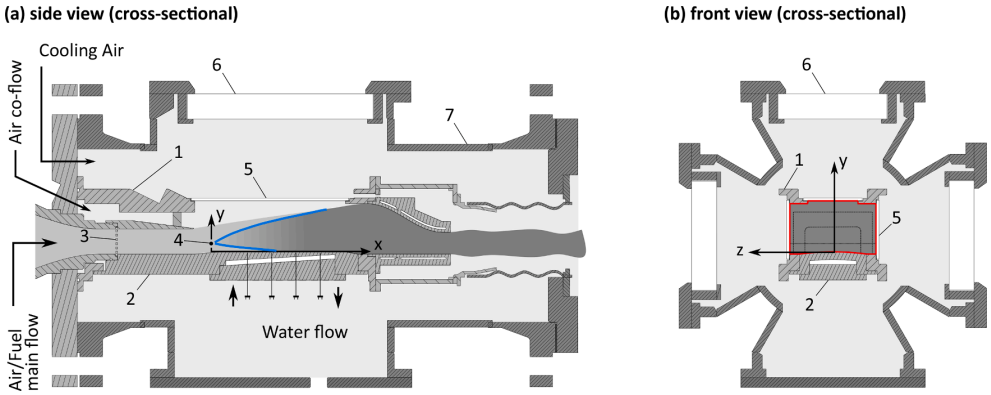

Fig. 1. Cross-sectional views of the pressurized side-wall quenching burner test rig. The red line in (b) indicates the flow cross-section of the main flow and co-flow within the flame tube. Numbers denoting individual components are referred to in the text.

application of laser diagnostics as close to the wall as possible, the upper surface of the quenching wall is slightly curved (300 mm radius) in the y-z-plane. The surface of the quenching wall was manufactured by precision milling resulting in a surface roughness typical in the order of a few microns or less. The flame tube and all components downstream of the Morel type nozzle are enclosed by a pressure vessel (7) to allow for operation at increased pressure. Optical access to the combustion process is guaranteed by quartz glass windows (5 & 6) on three sides of the test rig.

Measurements were carried out for two different operating cases at pressures ranging from 1 to 3 bar absolute. The cases investigated are consistent with previous studies at this test rig [30,31] and relevant parameters of the operating conditions are summarized in Table 1. The ratio of bulk velocity u_B of the premixed main flow and the laminar flame speed s_L were kept constant to achieve an almost unchanged streamwise position where FWI occurs in average. However, the resulting difference in Reynolds number was unavoidable due to limitations with respect to the possible operating conditions [30]. The burner was operated with methane as fuel at an equivalence ratio of 0.8. The operating cases are in the following referred to as atmospheric (1 bar) pressure case and elevated pressure (3 bar) case. The laminar flame speeds listed in Table 1 are obtained from a CANTERA [32] simulation of a one-dimensional, adiabatic, freely-propagating, laminar flame using the GRI3.0 mechanism [33]. This simulation is used as a reference throughout this study and in the following referred to as *adiabatic simulation*.

2.2. Laser diagnostics

The laser-diagnostic setup as well as processing procedures are outlined in the following subsections. The basic concept of the setup is similar to previous experiments on an unconfined, atmospheric SWQ burner [11,13], with respect to the simultaneous application of DP-CARS, CO-LIF and OH-PLIF. Modifications were necessary due to altered measurement requirements resulting from differences between the unconfined and the confined burner configuration. A simplified schematic visualization of the setup is displayed in Fig. 2. Essential components of the test rig relevant for the application of laser diagnostics, i.e., the windows of the pressure vessel (WP) and the flame tube (WF) as well as the quenching wall, are depicted. Since the test rig was stationary in space, a major part of the optical setup, including laser optics and detection systems for CO-LIF and OH-PLIF, was mounted on a traversing unit to allow for varying measurement positions. Therefore, the individual laser beams needed to be aligned parallel to the three axes of the traversing unit. In Fig. 2, components of the optical setup within the area defined by the dashed line were fixed to the traversing unit and could thus be moved in all spatial directions. Temporal synchronization of the individual laser diagnostic techniques was achieved using two pulse generators (*Quantum Composer Inc., 9520 Series*) and a real-time embedded controller equipped with an FPGA module (*National Instruments Corporation, CompactRIO 9074*). While the repetition rate was set to 10 Hz for all lasers, the detection systems were operated at 20 Hz to provide images without signal at every second recording which were used for background subtraction within the post-processing procedures.

Table 1
Operating conditions of the pressurized SWQ burner. Reynolds numbers are calculated using the hydraulic diameter of the nozzle exit, the bulk flow velocity u_B and the kinematic viscosity of air at 25 °C. Wall temperatures T_{wall} indicate the temporal mean and standard deviation of the wall temperature measured with a thermocouple positioned right below the surface of the quenching wall.

p (bar)	u_B (m/s)	s_L (m/s)	Re (−)	T_{wall} (K)
1	3.8	0.27	8200	319 ± 1.6
3	2.3	0.17	15,000	359 ± 2.4

2.2.1. Dual-pump coherent anti-Stokes Raman spectroscopy (DP-CARS)

Three Q-switched, frequency-doubled Nd:YAG lasers operating at 532 nm served as light sources of the setup. Two of them (*Spectra Physics, PIV 400*, PIV-overlap removed resulting in two individual lasers at 532 nm) were used to pump two dye lasers: (1) The custom-built broad-band modeless Stokes laser (following design principles by Ewart [34]) operated with a dye mixture of Rhodamine 610 and 640 to provide laser emission with a spectral profile of ≈ 6.6 nm FWHM and a central wavelength around 608 nm and (2) a narrow-band dye laser (*Radiant Dyes Laser & Accessories GmbH, NarrowScan*) operated with Rhodamine 590 at 560.7 nm (in air) serving as one pump laser within the DP-CARS process. The remaining Nd:YAG laser (*Spectra Physics, Quanta-Ray Pro-270*) provided the second pump wavelength at 532 nm. The energy of the three beams was adjusted by means of combinations of half-wave plates and polarizing beam splitter cubes. Matching of the focal positions in direction of beam propagation was achieved using telescopes consisting of spherical lenses. To minimize the effect of varying ambient temperature on the laser operation, both dye lasers (560.7 nm & 608 nm) and the corresponding two pump lasers were operated in an air-conditioned (temperature and humidity) laboratory room close to the test rig resulting, however, in beam path lengths of >10 m between laser output and test rig. The third Nd:YAG laser, in contrast, was positioned outside of the air conditioned laboratory room closer to the test rig. For this laser, the impact of negative effects associated with such long beam paths, such as degradation of the far-field beam profile, was considered more disruptive on laser operation than

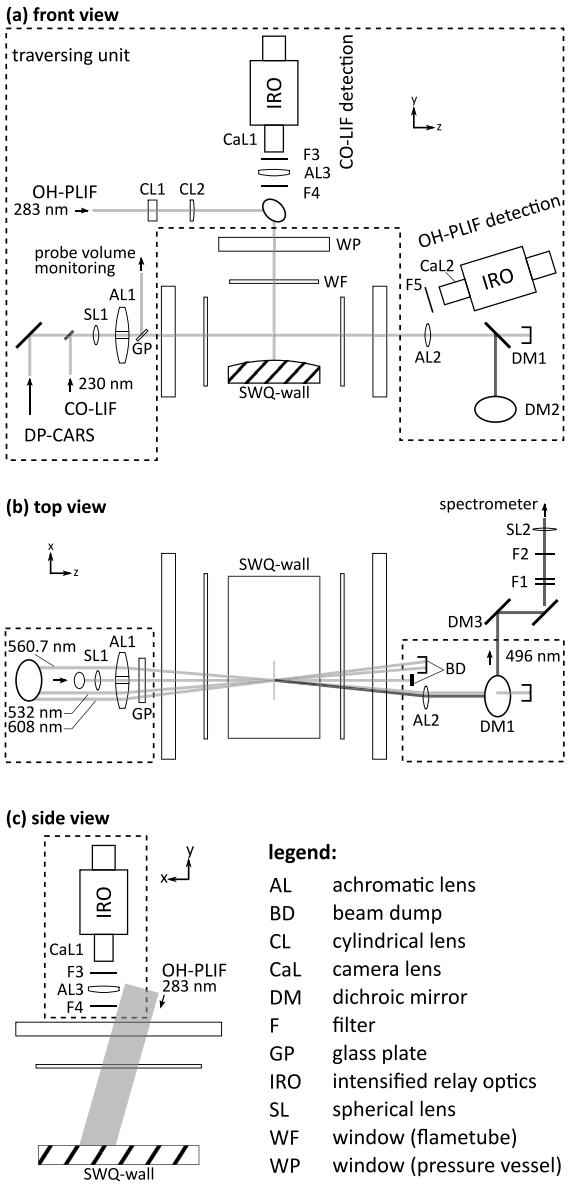

Fig. 2. Laser diagnostic setup.

the influence of changing environmental conditions. At the test rig, the three individual beams were guided to the traversing unit, aligned to each other and focused using a spherical, achromatic lens (AL1, $f = 250$ mm, 2″ diameter) to overlap in the region of interest (ROI) and satisfy the phase matching condition of a planar BOXCARS arrangement parallel to the surface of the wall. The resulting DP-CARS probe volume was about 50 µm in diameter (x- and y-direction), deduced from beam monitor recordings of the individual beams. By traversing the probe volume through a glass plate of 100 µm thickness, an interaction length of about 0.9 mm (z-direction) was measured through the identification of the positions where the non-resonant signal was reduced to $1/e^2$ of its maximum value. Pulse energies in the measurement volume were about 15 mJ (532 nm), 12 mJ (560.7 nm) and 10 mJ (608 nm), respectively. For the collection of the coherent DP-CARS signal at around 496 nm, an achromatic lens (AL2, $f = 250$ mm) of 1″ diameter was used to save space for the positioning of the OH-PLIF detection system (see Fig. 2). The DP-CARS signal was subsequently guided towards the spectrometer using three lowpass dichroic mirrors (DM1-3, *Thorlabs Inc., DMLP550L*), to separate it from the overlapping pump/probe laser at 560.7 nm, and one broadband dielectric mirror. Remaining undesired radiation was removed by means of a short-pass interference filter (F2, *Thorlabs Inc., FESH0550*). Depending on the DP-CARS signal intensity, additional neutral density filters (0.5 % or 10 % transmission, mounted on a filter wheel) were positioned into the beam path, or removed from it respectively, to adjust the signal intensity to the dynamic range of the detector avoiding saturation. A spherical lens (SL2, $f = +100$ mm) was used to focus the DP-CARS signal to the slit of a Czerny-Turner spectrometer (*McPherson, Model 209*, 1.33 m focal length), which was equipped with a 2400 lines/mm grating. Spectra were recorded using a backside-illuminated, cooled CCD camera (*Princeton Instruments, Pixis 400*) operated with on-chip hardware binning of 30 pixels in vertical direction (parallel to the entrance slit of the spectrometer). In the horizontal (wavelength) direction, the full chip (1340 pixels) was read out corresponding to a wavelength range of about 493 to 499 nm (one pixel corresponding to 0.19 cm^{-1} in spectral wavenumber domain). Non-resonant DP-CARS spectra for normalization were recorded in pure methane several times throughout the measurement day.

The DP-CARS processing sequence to deduce gas-phase temperature and CO_2 mole fraction was adopted with minor modifications from Zentgraf et al. [13] and is outlined briefly in the following. The pre-processing steps of the procedure included filtering out spectra of bad quality (e.g., due to saturation or breakdowns), mean background subtraction, normalization to a mean non-resonant signal and square root extraction of the signal intensity. A dispersion calibration was carried out by fitting averaged experimental DP-CARS spectra recorded in the burnt gas of the V-shaped laminar flame (assuming equilibrium conditions) to a simulated spectrum to optimize the parameters of a second-order polynomial describing the wavenumber axis. Temperature and CO_2 mole fraction were subsequently obtained by processing the single-shot spectra using a spectral fitting algorithm [35]. Within post-processing, unphysical samples originating from weak CO_2 signal intensities were removed by a thresholding criterion applied to the first prominent CO_2 feature (i.e., the $00^{\circ}0$–$10^{\circ}0$ band of CO_2). Based on this criterion all samples featuring an absolute baseline to peak difference of $\Delta\sqrt{I_{CO_2}} < 0.6$ were omitted from further analysis. Similar to [13], the procedure was validated based on (X_{CO_2}, T) data measured in a unbounded laminar V-shaped flame of a validation/calibration case which was compared to results of a CANTERA simulation (see Section 2.2.4). In a last step, an additional calibration was applied to the X_{CO_2} data to further improve the accuracy of the measurement. While at lower temperatures, (absolute) differences between uncalibrated X_{CO_2} and corresponding values of the simulation are rather small, deviations increase for temperatures higher than 1000 K (for both operating pressures; for detailed information on accuracy and precision of the uncalibrated CO_2 data see Section 2.2.4). Therefore, a temperature dependent calibration function was derived by comparing curve-fitted experimental data of the validation/calibration case with simulation data with regard to the (X_{CO_2}, T) state space evolution. For temperatures above 1000 K, the experimental single-shot X_{CO_2} were finally corrected using this calibration function based on the corresponding temperature value. In the temperature range below 1000 K however, a calibration was not necessary and could even impair the accuracy of the measurement, as X_{CO_2} of both, experimental and simulation data, tend towards zero resulting in a flawed calibration function.

2.2.2. Two-photon laser-induced fluorescence of carbon monoxide (CO-LIF)

Two-photon CO-LIF was applied to measure CO mole fractions by excitation of CO molecules with two photons at 230.09 nm using the

$B^1\Sigma^+ \leftarrow\leftarrow X^+\Sigma^+(0,\ 0)$ transition within the Hopfield–Birge bands at 115.05 nm and subsequent detection of the emission of the transition $B^1\Sigma^+ \rightarrow A^1\Pi_u(0,\ 1)$ in the Ångström bands. The laser radiation used for the LIF process was provided by a narrow-band dye laser (*Sirah Lasertechnik GmbH, Precision Sca*n, 2400 lines/mm grating) operated with Pyridine 1, which was pumped by a Q-switched, frequency doubled Nd:YAG laser (*Spectra Physics, GCR 4*). A second and a third harmonic generation stage were utilized for frequency tripling of the fundamental laser emission at 690.27 nm resulting in laser radiation at 230.09 nm. Stability of the excitation wavelength was ensured by continuously measuring the fundamental dye laser emission to control the grating position of the dye laser. A quartz glass plate was placed into the UV beam path and the reflections at the front and the back side were guided onto an energy meter (*Coherent Inc., EM USB J-10MT-10KHZ*) and a beam monitor (*DataRay Inc., WinCamD*) for energy reference and beam profile monitoring. Based on these recordings, no visible change in the intensity distribution of the UV beam was observed throughout the measurements. The UV beam was deflected by a small rectangular mirror ($10 \times 20\ mm^2$), positioned between the laser beams for DP-CARS, to a small spherical lens ($f = 300$ mm, ½" diameter) used to focus it through a hole of the DP-CARS focusing lens (AL1) to the ROI within the test rig. The resulting probe volume size was about 130 μm in diameter (x- and y-direction). Average pulse energies in the measurement volume were about 2.5 mJ. The fluorescence signal was recorded using a CCD camera (*Basler AG, piA2400-17gm*) equipped with an intensified relay optics (*IRO, LaVision GmbH, low speed IRO*, GaAsP photocathode) and a combination of a camera lens (*Nikon* 85 mm *f/1.4G AF-S Nikkor*) focused to infinity and an achromatic doublet lens (AL3, *Newport, PAC095,* $f =$ 250 mm, 3″ diameter). To suppress flame luminosity while also compensating for a slightly increased temporal jitter of the laser, the IRO was gated at 300 ns. Flame luminosity was further attenuated by means of an interference bandpass filter (*Laser Components GmbH, LC-HBP 490/20-75*) which selectively transmitted light within the wavelength range of 480 to 500 nm (>95 % transmission). The CCD camera was operated with 4 × 4 hardware binning resulting in one pixel bin corresponding to about 80 μm.

Post-processing of the data for converting the raw signal into quantitative mole fractions followed a proven procedure which was applied for similar measurements in the context of FWI in the past [9,10,31] and further developed over the time. A detailed description of the procedure applied in this study may be found in [13]. Therefore, the post-processing procedure is outlined only briefly in the following. The different steps can be summarized by the following equation [13]:

$$X_{CO} = I_{LIF} \cdot \frac{1}{a + b \cdot E^n} \cdot \frac{T}{T_0} \cdot \frac{1}{W(x,y)} \cdot \frac{fit_{CO,sim}(T)}{fit_{CO,exp}(T)}$$

In a first step, a scalar raw LIF intensity I_{LIF} was obtained by integrating the two-dimensional, background and baseline corrected intensity distribution within a region of 0.9 mm length in z-direction (matching the interaction length of the DP-CARS probe volume). In the 1 bar case, the integrated LIF intensity was then corrected with respect to shot-to-shot variations of the laser energy E. The parameters of the energy dependency ($n = 1.51$) were determined by varying the laser energy while acquiring data in the burnt gas of the V-shaped flame. Regarding the measurements at 3 bar pressure, however, no laser energy correction was performed on the LIF intensities, as an undetected failure of the energy monitoring system occurred during the measurements. Correction of the LIF intensity for the local density was subsequently achieved by multiplication with the instantaneous temperature T (provided by the DP-CARS measurement) divided by a reference temperature $T_0 = 300$ K. Furthermore, a correction function $W(x,y)$ is applied to account for reflections at the quenching wall resulting in an increased LIF signal at small wall distances. This correction function was derived from LIF intensities measured within the test rig at varying positions with respect to the quenching wall in a homogeneous calibration gas (1 % CO, 99 % N_2). The corrected LIF intensity was finally turned into mole fractions using a temperature-dependent calibration function $fit_{CO,sim}(T)/fit_{CO,exp}(T)$ deduced from a CANTERA simulation and curve-fitted experimental data recorded in an adiabatic validation/calibration case (see Section 2.2.4). When applying this procedure to the experimental data of the non-adiabatic near-wall measurements, different chemical compositions compared to the adiabatic validation/calibration case may affect the quenching rate and thus the calibration. Based on an evaluation of the quenching rate Q and the ionization R using an in-house CO-LIF simulation code (based on [36] with quenching data from [37], using an ionization cross-section of 10^{17} cm^{-1} [38] and a laser power density of 1.5 GW/cm^2), R is estimated to be higher than Q for the given conditions in a methane/air flame at 1 bar. With the pressure increased to 3 bar, the quenching rate increases but is still estimated below the ionization rate ($\sim 10^9\ s^{-1}$ vs. $\sim 10^{10}\ s^{-1}$). Accordingly, as pointed out in [13], it is argued that the effect of different quenching rates on the fluorescence quantum yield is reduced by a factor of about two or more. The production of CO by photolytic dissociation of CO_2 is another effect that can also impact the calibration, as discussed in [13,16]. For the measurements at small wall distances, which are the most relevant here, it is expected that the effect of photolytic dissociation of CO_2 on the CO-LIF calibration is small, since for laser wavelengths > 227 nm dissociation of CO_2 is only possible from higher vibrational states, which are less populated with decreasing temperature [39].

Although no laser energy correction of the LIF intensities was performed for the data of the 3 bar case, it is assumed that the described calibration procedure is still valid provided that the average laser energy was the same for both, the near-wall measurement and the validation/calibration case. This assumption is supported by a comparison of corrected LIF intensities (not laser energy-corrected) of the near-wall measurements and the adiabatic validation/calibration case being in the same order for thermochemical states associated with a completed chemical reaction. Furthermore, the influence of the laser energy correction within the overall calibration procedure was found to be of minor importance by comparing data of the 1 bar case calibrated first using the laser energy correction (i.e., the data as it is shown later in Section 3.2.1) and then without using the laser energy-correction (not shown). A detailed description on the impact of the shot-to-shot energy correction on the CO-LIF intensity quantification is given in Appendix A in the supplementary material.

2.2.3. Planar laser-induced fluorescence of hydroxyl radical (OH-PLIF)

Planar LIF measurements were carried out for qualitative imaging of the hydroxyl radical OH to identify the position of the flame front. The fundamental wavelength of 565.86 nm (air) of a narrow-band dye laser (*Sirah Lasertechnik GmbH, Double Dye*) operated with Rhodamine 590 and optically pumped by a Q-switched, frequency doubled Nd:YAG laser (*Spectra Physics, PIV 400*) was frequency doubled to 282.93 nm and used to excite the $Q_1(6)$ transition of OH at 35,334.35 cm^{-1}. The UV beam was guided from the exit of the laser, which was operated within an air-conditioned laboratory room, to the test rig using high reflective dielectric mirrors. Due to space limitations, only two cylindrical lenses were used to expand (CL1, $f = -150$ mm) the beam in one dimension and to compress (CL2, $f = +400$ mm) it in the other forming a light sheet with a thickness of about 200 μm ($1/e^2$) in the ROI. In order not to impair the CO-LIF detection, the light sheet for OH-PLIF was guided into the ROI from above slightly inclined with respect to the y-axis (see Fig. 2 (c)). The fluorescence signal was captured using a CCD camera (*Basler, scA1400-17gm*) in combination with an IRO (*LaVision GmbH, low speed IRO*) gated at 125 ns, which was equipped with an objective lens (*Sodern, CERCO 2073, f/2.8*) and an interference filter (*Laser Components, BP300-325*). The CCD camera was operated at 10 ms exposure time and 2 × 2 hardware binning (one 12.9 μm sized pixel bin corresponding to 54 μm in physical space). The OH-PLIF detection system was positioned above the DP-CARS signal beam slightly inclined with respect

to the z-axis.

The post-processing of the OH-PLIF images for determination of the flame front position followed the procedure already used in previous studies [30,31]. It involved block-matching and 3D filtering (BM3D) [40] to achieve noise reduction while preserving spatial gradients, e.g., in the vicinity of the flame front, and Canny-edge (CE) filtering [41] (built-in function in *Matlab R2022b, The MathWorks, Inc.*) to detect edges in the image based on local maxima of the LIF intensity's spatial gradient. The threshold for CE filtering was determined based on the frequency distribution of the spatial gradient magnitude in an image area dominated by image noise. In a last step, edges resulting from a striped pattern on the laser light sheet (see Fig. 6) were detected based on a Hough transform (built-in function in *Matlab R2022b*) and subsequently removed. Remaining edges detected by the processing algorithm reliably marked the position of the flame front. This post-processing procedure was applied to both the 1 bar and 3 bar case without further adjustment. Based on this information, the position of the DP-CARS/CO-LIF probe volume relative to the flame front is derived subsequently. Therefore, the minimum distance d_F of the probe volume to the nearest flame front segment is deduced. A visualization of the determination of d_F is shown in Fig. 6(d).

2.2.4. Spatial matching of the laser diagnostics and identification of the wall surface position

To ensure spatial matching of the different laser diagnostics, the laser beams for DP-CARS and CO-LIF were guided through a 100-µm pinhole to achieve spatial overlap of both probe volumes in the central plane of the burner (x/y-plane). Recordings of the same pinhole captured with the OH-PLIF detection system were used to determine the position of the DP-CARS/CO-LIF probe volume within the instantaneous flame front images.

The distance of the probe volume from the wall was determined following the procedure described in [13] (supplementary material). By moving the probe volume (DP-CARS beams only) in small steps closer to the wall until first breakdowns occurred, the position of the wall surface was identified. Assuming that first breakdowns happen when the $1/e^2$-isoline of the intensity distribution within the probe volume reaches the wall surface, the distance of the probe volume to the wall at this position was expected to be equal to half of the probe volume diameter. This procedure was initially carried out at non-reacting conditions to get a first estimate of the wall surface position and subsequently repeated under reacting conditions to account for thermal expansion in the steady state of the burner operation. At 3 bar pressure, however, the determination of the distance of the probe volume from the wall is impeded by strongly increased beam steering effects resulting in an unknown systematic error, as described in more detail in Section 3.2.2. The wall distances given in this paper (i.e., the position of the probe volume with respect to the quenching wall) are therefore to be understood as *nominal* wall distances.

2.3. Validation/calibration reference case

Thermochemistry measurements of an adiabatic reference case were carried out for (1) calibration of the two-photon CO-LIF data and (2) an evaluation of accuracy and precision of the setup. Therefore, a calibration burner was used, which was designed and used by Greifenstein and Dreizler before for a similar purpose [16]. Switching to a calibration burner was necessary to generate stable laminar flames as needed for calibration purposes at 1 bar and 3 bar. The burner consisted of an 8-mm pipe (inner diameter) fed with a fully premixed methane/air mixture (equivalence ratio 0.8) and a second surrounding coaxial pipe carrying an N_2 flow to minimize shear effects at the burner outlet. A 1-mm steel-rod positioned at the outlet of the inner pipe served as flame holder for a V-shaped flame. The calibration burner was positioned within the flame tube of the enclosed test rig by inserting it from upstream in positive x-direction through the base plate of the inlet plenum. Measurements were carried out in one branch of this small-sized calibration V-flame, which was positioned far off the quenching wall, at 1 bar and 3 bar pressure and were supplemented by the adiabatic simulation introduced in Section 2.1.

The results of the measurements at 1 bar and 3 bar pressure are summarized in Figs. 3 and 4, respectively. The top row (subfigures (a)–(c)) shows pairwise correlations of experimental, post-processed T, X_{CO_2} and X_{CO} as well as the corresponding simulation data. Absolute single-shot residua of X_{CO_2} and X_{CO} with respect to the corresponding simulation data are depicted in (d) and (e). Relative accuracy and precision of the CO_2 and CO measurements are given in (f) and (g) by the relative mean $\mu_{rel}(r)$ and the relative standard deviation $\sigma_{rel}(r)$, respectively, of the single-shot residua r within temperature bins of 50 K, scaled with the corresponding mole fraction value of the simulation. For both operating pressures, thermochemical states (based on post-processed data) well match the trace of the simulation data, shown in Figs. 3 and 4(a)–(c). With regard to the CO_2 mole fraction measurement, for the uncalibrated data (directly resulting from the spectral fitting algorithm) a mean $\mu_{rel}(r)$ over the full temperature range of ≈19 % for the 1 bar case and ≈26 % for the 3 bar case is derived. This accuracy is significantly improved by an additional calibration of the data to the simulation (see Section 2.2.1) resulting in a mean $\mu_{rel}(r)$ in the order of 2 % in both cases (subfigures (f)) for temperatures higher than 1000 K. Mean $\sigma_{rel}(r)$ of the X_{CO_2} data is about 22 % in the 1 bar case and approximately 25 % for the data acquired at 3 bar. This slight increase might be due the stronger impact of beam steering effects at higher pressure, which could lead to increased stochastic changes of the overlap of the three laser beams within the DP-CARS probe volume. $\mu_{rel}(r)$ and $\sigma_{rel}(r)$ of the gas-phase temperature derived from DP-CARS measurements at equilibrium conditions in the fully burnt gas is about 3 % and 4 %, respectively in both cases. With respect to X_{CO}, as of the procedure, a good relative accuracy is achieved as the CO-LIF raw data is calibrated based on the simulation data. For both operating pressures, $\mu_{rel}(r)$ is almost constant over the full temperature range and only slightly increases for temperatures above 1700 K while its mean value is below 2 %. The relative standard deviation $\sigma_{rel}(r)$ shows a similar trend with increasing temperature for both operating pressures as it first decreases for temperatures below about 1000 K and then rises again for temperatures above 1700 K. For the lower temperature range this is due to the increasing absolute CO concentration while the variance of the residuum, i.e., the width of the scatter in Figs. 3 and 4(e), remains constant. At higher temperatures, the deteriorated relative precision is mainly caused by the steeper gradient of X_{CO} with respect to temperature resulting in an increased variance of the data within one averaging bin. Overall, the precision is slightly reduced in the 3 bar case compared to the measurements at 1 bar (mean $\sigma_{rel}(r)$: ≈12 % (1 bar) / ≈16 % (3 bar)) which is to some extent due to the slightly lower precision of the gas-phase temperature that is used within the CO-LIF calibration procedure.

To further discuss the accuracy and precision of the temperature measurement (which was only evaluated based on equilibrium conditions) as well as the spatial resolution of the laser diagnostic setup in relation to spatial gradients in the reaction zone, a representation of the thermochemistry data in the spatial domain is shown in Fig. 5. The spatial evolution of T, X_{CO_2} and X_{CO} within the reaction zone of a laminar flame is displayed for 1 bar pressure in the top row and for 3 bar in the bottom row. The experimental data, which was measured by traversing the DP-CARS/CO-LIF probe volume through the flame front, is averaged for every traversing location and the mean temperature $\mu(T)$ (green triangles) is plotted over the simulation data (red, solid line). Error bars indicate the standard deviation $\sigma(T)$ of the experimental data at each measurement location. For the 1 bar case, the averaged experimental temperature data only falls below the simulation data for low temperatures (< 500 K) but matches it very well for higher temperatures. The spatial gradients in the temperature trace are reproduced very well by the experimental data indicating that the limited resolution of the DP-

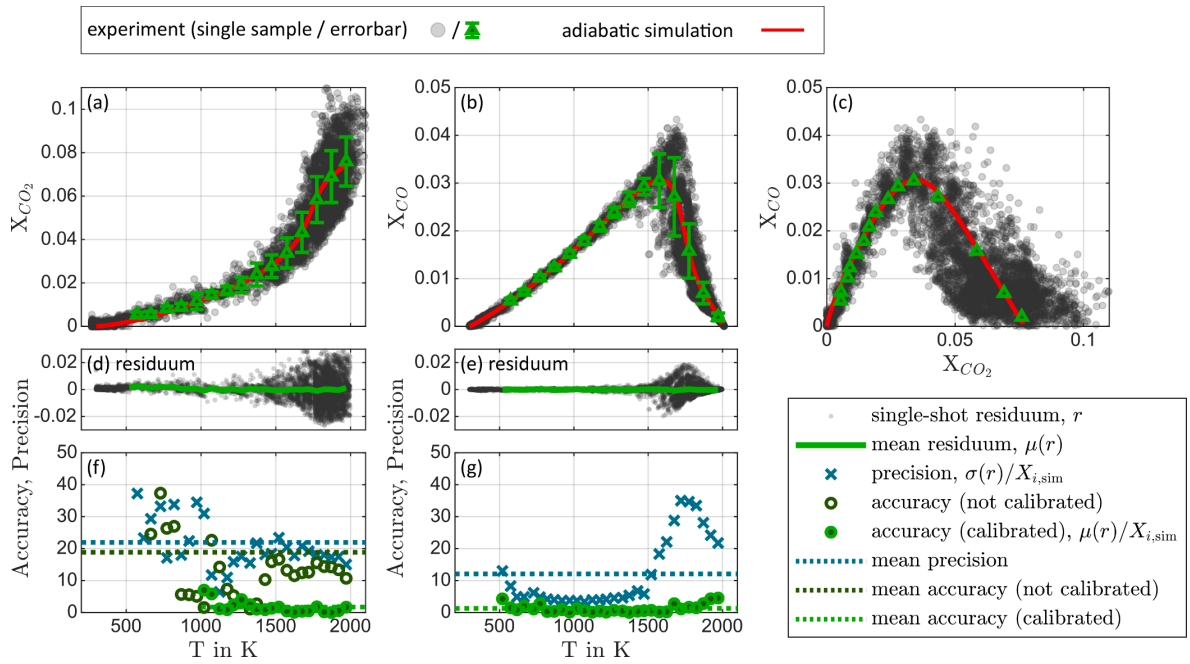

Fig. 3. Assessment of the laser diagnostic setup regarding accuracy and precision of the CO_2 and CO mole fraction measurement based on the validation/calibration case at atmospheric pressure. State-space correlations are shown in (a)–(c), single-shot residua in (d) & (e) and relative accuracy and precision in (f) & (g). Number of individual samples: 8162.

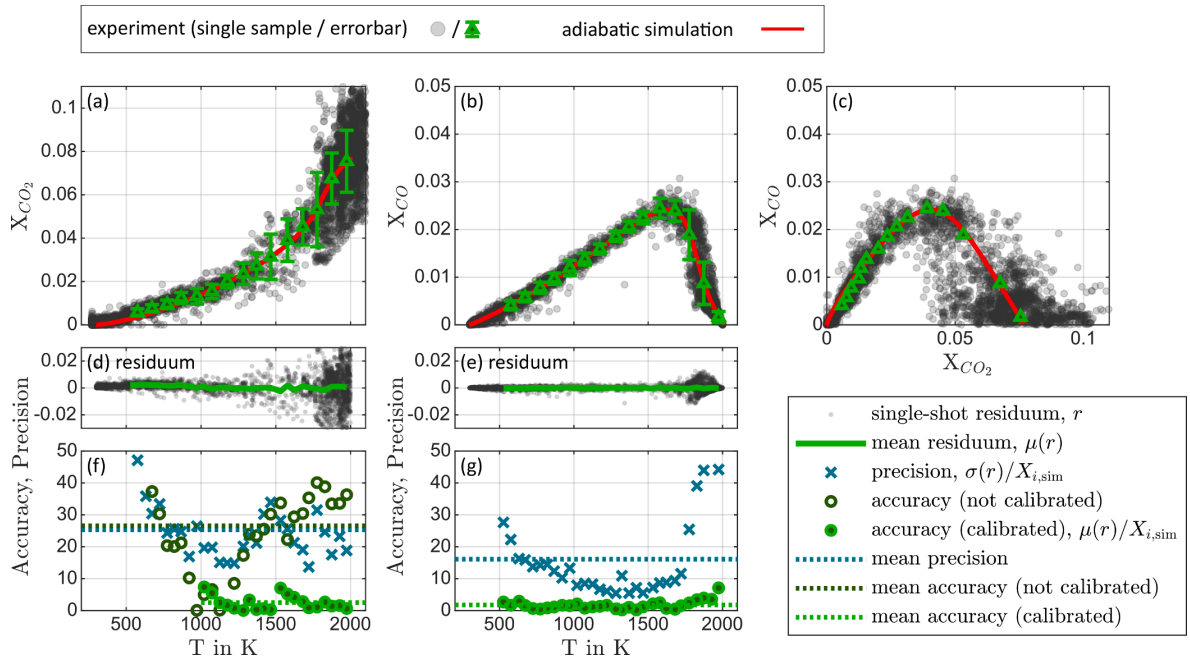

Fig. 4. Assessment of the laser diagnostic setup regarding accuracy and precision of the CO_2 and CO mole fraction measurement based on the validation/calibration case at elevated pressure (3 bar). State-space correlations are shown in (a)–(c), single-shot residua in (d) & (e) and relative accuracy and precision in (f) & (g). Number of individual samples: 7049.

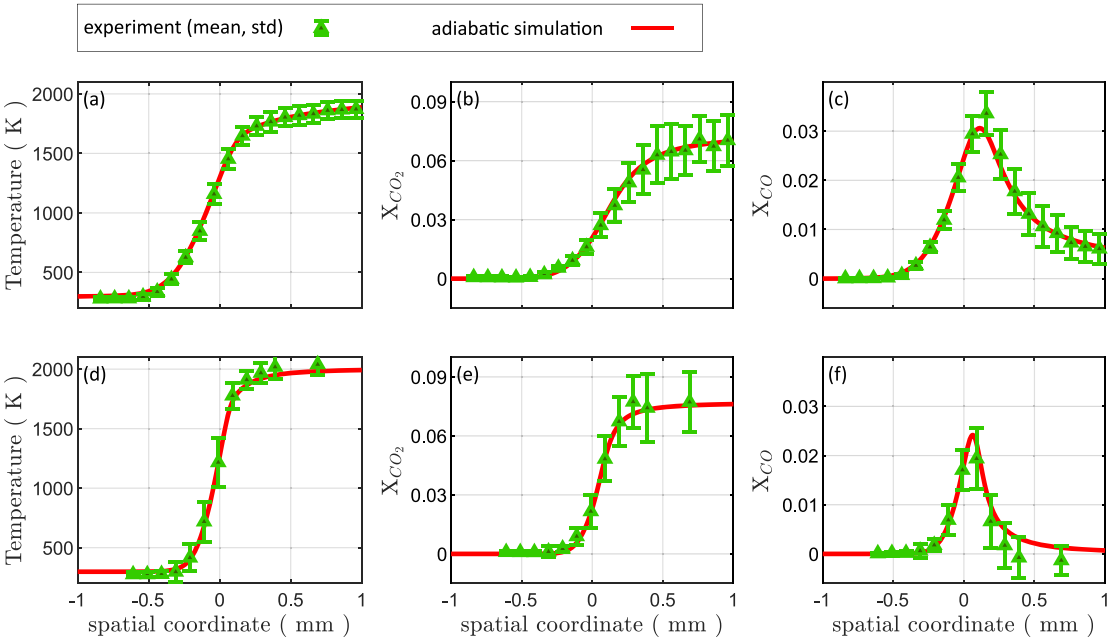

Fig. 5. Evolution of temperature, CO_2, and CO mole fraction in a laminar flame of validation/calibration case shown in the spatial domain at atmospheric (top row) and elevated (3 bar) pressure (bottom row).

CARS setup, i.e., the size of the probe volume, is not limiting the accuracy (i.e., the relative mean of the single-shot residua) of the measurement, which is below 10 % within the full temperature range. The relative standard deviation of the temperature $\sigma_{rel}(T)$ (scaled with the corresponding temperature value of the simulation, not shown) first increases and then slowly decreases above 1000 K. Especially in the temperature range between 500 K and 1500 K, due to the steep spatial gradient, minor fluctuations of the flame location might be the dominant factor for an increased variation in the temperature data. For regions with small temperature gradients, $\sigma_{rel}(T)$ is in the order of 5 % and below. For the temperature data acquired at 3 bar, the averaged experimental data is still in good agreement with the simulation even though the flame thickness is reduced by a factor of about two (from about 0.5 mm at 1 bar pressure to about 0.27 mm at 3 bar, estimated from [42] using the adiabatic simulation) and gradients are increased correspondingly. However, in the higher temperature range, average values of the temperature measurement slightly overshoot the simulation by about 2.5 % (>1800 K). For $\sigma_{rel}(T)$ a similar trend with increasing temperature like in the 1 bar case is observed. The increase in standard deviation at temperatures between 500 K and 1500 K, however, is clearly more pronounced as spatial gradients are significantly increased due to the elevated pressure. Within regions of smaller temperature gradients, the $\sigma_{rel}(T)$ is in the order of 5 %. Regarding the spatial evolution of X_{CO_2} and X_{CO}, a good overall agreement of experimental and simulation data is observed as well for both operating pressures. Larger deviations are only evident for the oxidization zone of CO at 3 bar pressure, as experimental data clearly falls below the simulation. As temperatures of these states are slightly overpredicted, the CO-LIF calibration is deteriorated resulting in this discrepancy. However, since most of the FWI processes take place at lower temperatures, the distorting effect on the results presented in Section 3 is assumed to be negligible. Since accuracy and precision of X_{CO_2} and X_{CO} were already analyzed in detail based on representations in the state space, they are not further discussed here.

3. Results and discussion

3.1. Flame front characteristics and quenching scenarios

Based on the flame front topology in close vicinity of the wall, where the interaction of the reaction zone with the wall takes place, every recorded flame-wall interaction event is assigned to one out of three quenching scenarios. These are shown in Fig. 6 for the 3 bar case for demonstration: (1) The side-wall quenching (SWQ)-like scenario is characterized by an almost point-like near-wall region of flame-wall interaction (i.e., the quenching point), while the flame front and the wall form an acute angle in most cases. (2) In the head-on quenching (HOQ)-like scenario one single, extended (in wall-parallel direction) near-wall reaction zone interacts with the wall. (3) The multi-zone quenching (MZQ) scenario exhibits multiple regions of flame-wall interaction which are spatially separated by pockets of unburnt gas. While the SWQ- and HOQ-like scenarios were already observed in the unconfined, atmospheric SWQ burner and introduced in [11], the MZQ scenario most likely results from the increased Reynolds number which is an inherent characteristic of the pressurized SWQ burner operation. A time sequence visualizing the linking of these three quenching scenarios including a detailed discussion is presented in [30]. For the automated classification of the individual quenching events in the processing algorithms, segments of the flame front in a region close to the wall were identified. This region was defined by the flame front section of minimum wall distance within the full FOV. Based on the number and the lengths of connected flame front segments within this near-wall region each event was finally assigned to one of the three quenching scenarios applying the criteria in Table 2.

Applying this classification to all statistically independent quenching events, the HOQ-like scenario is clearly identified as predominant quenching scenario in the studied burner (about 90 %), regardless of operating pressure. In contrast, only a marginal number of events are classified as either SWQ-like (about 7 %) or MZQ scenarios (about 3 %). Thus, the statistics of quenching scenarios clearly differs from a similar analysis of quenching events in the unconfined, atmospheric SWQ

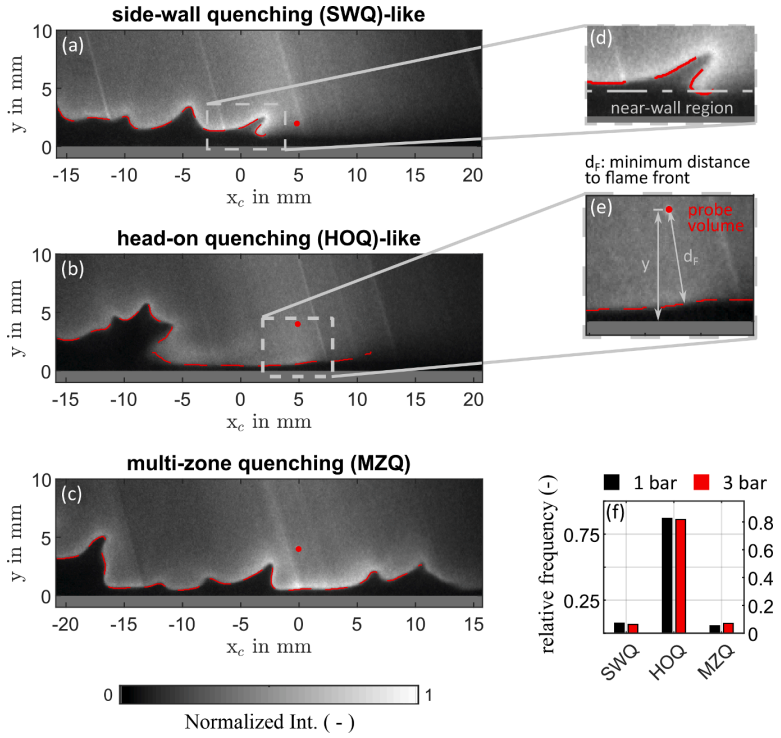

Fig. 6. Instantaneous OH-PLIF recordings of quenching scenarios exemplarily shown for the 3 bar case in (a), (b) and (c). The streamwise coordinate x_c indicates the position with the highest probability to detect a flame front close to the wall and was derived following the procedure described in [30]. The classification of the individual events was carried out based on the number and lengths of flame front segments in a near-wall region exemplarily shown for the SWQ-like case in (d). The near-wall region is defined by the dashed-dotted line. The identification of the minimum distance between the probe volume (red dot) and the flame front d_F is visualized in (e). The position of the probe volume was varied to probe thermochemical states at multiple wall distances. For the example OH-PLIF image in (b), the probe volume was positioned 4 mm from the wall. Relative frequencies of occurrence of quenching scenarios are displayed in (f).

Table 2
Criteria for the classification of quenching scenarios.

	Number of near-wall reaction zone (s)	Length of reaction zone (s)
SWQ-like scenario	1	≤1 mm
HOQ-like scenario	1	>1 mm
MZQ scenario	>1	Not relevant

burner revealing a ratio of 1:1 between SWQ-like and HOQ-like scenarios [11]. This difference is most likely due to the confined burner configuration preventing an unhindered expansion of the exhaust gases which in turn results in the flame front being pushed towards the wall. Furthermore, the higher bulk velocity of the main flow (3.8 m/s vs. 2.2 m/s in [11]) together with a slightly lower laminar flame speed (0.27 m/s vs. ≈0.35 m/s in [11] for a lean DME/air flame at equivalence ratio of 0.83, cf. [43]) in average leads to a decreased angle between flame front and the wall promoting the development of HOQ-like scenarios. Finally, the pressurized burner is oriented differently in the gravitational field than the unconfined configuration (main flow direction horizontal instead of vertical). All these aspects, are expected to impact the statistical share between the possible quenching scenarios. Possible consequences of these differences on the near-wall thermochemistry measurements are discussed in Section 3.2.

To provide a link to previous studies on FWI carried out at identical operating conditions [30,31], a spatial distribution of the mean reaction progress variable representing the flame brush is derived from the OH-PLIF data in a second step. For this purpose, all instantaneous images are first binarized by dividing the OH-PLIF field-of-view (FOV) into regions of burnt and unburnt gas (separated by the flame front which is identified following the procedure described in Section 2.2.3) and subsequently averaged. Fig. 7 shows the flame brush for both operating

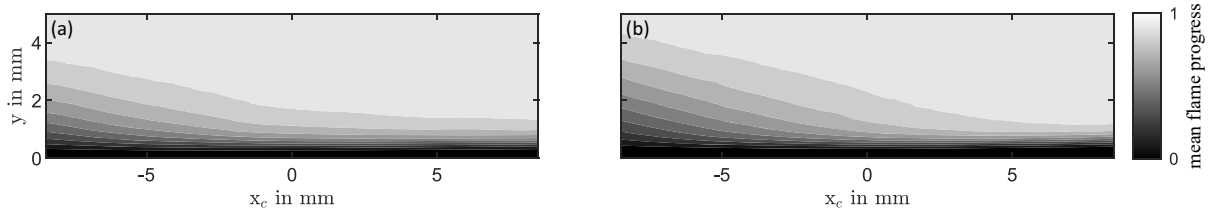

Fig. 7. Spatial distribution of the mean reaction progress in the 1 bar (a) and 3 bar case (b).

conditions. The streamwise coordinate x_C was derived similarly to previous studies [30,31] and indicates the location with the highest probability of a flame front occurrence at $x_c = 0$mm. In both cases, the flame brush is wide upstream but narrows downstream. In the 1 bar case, the thickness of the flame brush is slightly narrower at the upstream positions compared to the 3 bar case, and decreases more gradually with increasing x_c. Despite a constant ratio of bulk flow velocity and laminar flame speed (see Section 2.1), the mean streamwise position of FWI is shifted slightly upstream in the 3 bar case due to increased turbulence causing in average the flame to strike the quenching wall at a slightly increased angle. Far downstream, the flame brush exhibits a reduced thickness at higher pressure which is in good accordance with a previous study [31].

3.2. Thermochemical states

In the following sections, results of the near-wall thermochemistry measurements are presented. Pairwise correlations of T, X_{CO_2} and X_{CO} are visualized by means of scatter plots. As measurement locations near the wall were of greater interest, fewer experimental samples were recorded farther from the wall. Since one quenching scenario was identified as the predominant scenario (more than 90 % HOQ-like events, see Section 3.1), no classification of the thermochemistry data with respect to the quenching scenario was applied. The results presented in the following sections hence give a representative picture of the thermochemistry of HOQ-like events. First, the 1 bar case is discussed and reference is made to results of previous studies on transient HOQ flames in an impinging-jet burner by Mann et al. [8], laminar SWQ flames by Jainski et al. [9] and Kosaka et al. [10] and turbulent SWQ flames by Zentgraf et al. [11] (the latter three studies were carried out in the unconfined, atmospheric SWQ burner). Subsequently, the results of the measurements at 3 bar operating pressure are presented. To emphasize the impact of the wall resulting in non-adiabaticity, thermochemical states of an adiabatic, laminar flame derived from the adiabatic simulation (see Section 2.1) are also shown. In a last step, differences between both operating cases are highlighted and the impact of increasing pressure on near-wall thermochemistry is discussed.

3.2.1. Atmospheric pressure case

Fig. 8 shows the distribution of thermochemical states in the 1 bar case for the measurement location at minimum nominal wall distance $y = 0.1$ mm. For comparison, thermochemical states of the adiabatic simulation are visualized as red solid line. The color-coding of the scatter indicates the minimum distance d_F of the probe volume to the flame front for each sample. While negative values (blue) of d_F are associated with a measurement in the unburnt gas, positive values (yellow) indicate that the probe volume was in the burnt gas. The value $d_F = 0$mm corresponds to probe volumes located exactly on the flame front. For the data shown in Fig. 8 measured at a fixed location close to the wall, the transition from dark blue to light blue scatter (representing statistically independent measurements) in average recreates the scenario of a flame front approaching the wall. To some extent, this is comparable to a transient head-on quenching event, since head-on quenching is the predominant scenario. For higher d_F values (dark blue color-coded scatter), the gas temperature is low but increases as the flame approaches the probe volume (light blue color-coded scatter), evident from the X_{CO_2}/T-correlation in Fig. 8(a). Close to the flame front, the temperature reaches maximum values but does not exceed 1000 K for almost any sample, clearly deviating from the trace of the adiabatic simulation due to the influence of heat losses to the wall. Despite this trend, the spread of temperature for thermochemical states of similar d_F is still wide. Besides of turbulent mixing effects, this might also be partly attributed to the limited resolution of the OH-PLIF detection system reducing the precision of the derivation of d_F. Thermochemical states measured clearly in the burnt gas ($d_F > 0$mm) are either associated with SWQ-like events or an HOQ-like flame that is already quenched at the probe volume location. The high variance in X_{CO_2} of these states is again a sign for turbulent mixing in the post-quenching zone. With regard to X_{CO_2}, almost no correlation with d_F is observed, as mole fractions range between 0 and 0.08 independent of the distance between probe volume and flame front. Regarding increased X_{CO_2} at low temperatures (< 400 K) in regions of unburnt gas, similar observations were made in the unconfined, atmospheric turbulent side-wall quenching flame (comparable to the flame front topology in Fig. 6(a)). These thermochemical states (high X_{CO_2} at low temperatures) have been attributed to a transport mechanism, where turbulent eddies transport burnt exhaust gas upstream through the gap between the flame tip and the wall, mixing with approaching fresh gas [11]. However, due to the different near-wall flame front topology (mostly HOQ-like events) within this study, other transport effects leading to these thermochemical states cannot be excluded. From the X_{CO}/T- and X_{CO}/X_{CO_2}-scatter plots in Fig. 8(b) and (c), it can be deduced that these states feature mostly low X_{CO}, meaning that there is no correlation between X_{CO} and X_{CO_2} which supports the assumption that these states originate from (almost) fully burnt gas

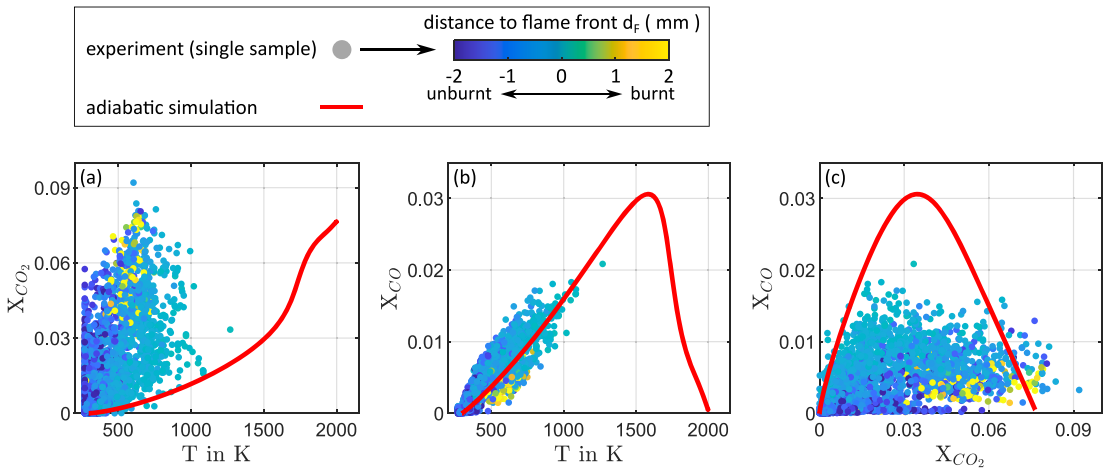

Fig. 8. Thermochemical states of atmospheric FWI under turbulent flow conditions at a wall distance of 0.1 mm. The data is color-coded with respect to the minimum distance d_F of the probe volume to the instantaneous flame front and presented by means of correlations of X_{CO_2}/T, X_{CO}/T and X_{CO}/X_{CO_2} shown in (a), (b) and (c), respectively. Number of individual samples: 3128.

mixtures being cooled down.

Following the evolution of thermochemical states for increasing d_F in the X_{CO}/T-scatter plot (Fig. 8(b)), temperatures and CO mole fractions first rise as d_F approaches zero and then decrease again for the states farther in the burnt gas. The influence of heat losses on the thermochemistry are clearly evident, as thermochemical states are shifted to lower temperatures and maximum X_{CO} values are significantly reduced compared to the adiabatic simulation. Together with turbulent mixing effects, this leads to the observation that a clear distinction between a CO production and an oxidation branch is hardly possible anymore. Based on d_F, however, it can be assumed that thermochemical states on the left side of the scatter ($d_F < 0$mm) might be associated with CO production, while states on the right ($d_F > 0$mm) are rather related to oxidation. Following this assumption, it is evident that the CO oxidation is significantly more strongly affected than the production. This is in good agreement with previous studies on FWI (laminar & turbulent, SWQ & HOQ) [8–11] and attributed to larger chemical time scales of the CO oxidation process [10]. While for the transient HOQ flame in [8] almost no impact of non-adiabaticity on the CO production was observed, a slight shift of the corresponding states to smaller temperatures and a clearly reduced X_{CO} peak value is visible in Fig. 8(b). Besides the differences between the burner configurations, these differing observations might be due to increased turbulence levels leading to an increased convective heat transfer corresponding to smaller time scales of heat transfer (see discussion on time scales in [10]).

The evolution of the scatter plots for different wall distances in the 1 bar case is visualized in Fig. 9. Correlations of X_{CO_2}/T, X_{CO}/T and X_{CO}/X_{CO_2} are shown for five selected wall distances ranging from 0.35 mm to 4 mm. Each column in Fig. 9 corresponds to one fixed wall distance of the probe volume. Comparing the distribution of thermochemical states in the X_{CO_2}/T-state space at increasing wall distances (Figs. 8(a) and 9 (a)–(e)), it is clearly evident that the impact of wall heat losses on the quenching flame diminishes, as the scatter of experimental data approaches the thermochemical states of the adiabatic simulation. Maximum temperatures in the experimental data rise and converge to the adiabatic flame temperature. Maximum X_{CO_2} values of thermochemical states at lower temperatures ($T < 400$K) decrease until there is no deviation from the adiabatic simulation within this temperature range visible anymore at wall distances of $y \geq 0.65$mm. The impact on CO production and oxidation decreases as well, as peak X_{CO} values in the experimental data reach the maximum value of the adiabatic simulation and production/oxidation branch become discriminable. While at $y =$

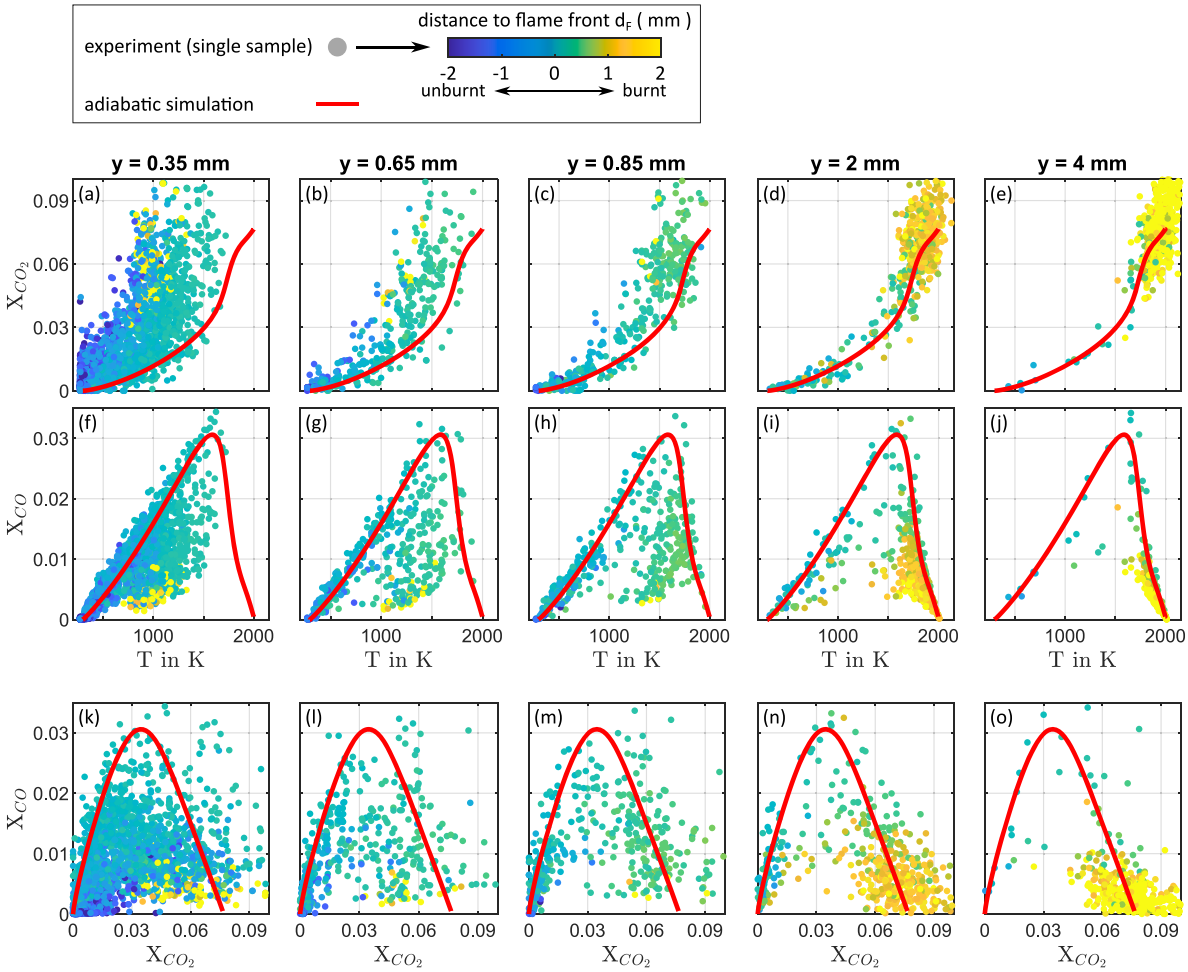

Fig. 9. Thermochemical states of atmospheric FWI under turbulent flow conditions at varying wall distances. The data is color-coded with respect to the minimum distance d_F of the probe volume to the instantaneous flame front and presented by means of correlations of X_{CO_2}/T, X_{CO}/T and X_{CO}/X_{CO_2} shown in (a)–(e), (f)–(j) and (k)–(o), respectively. Number of individual samples ranging between 425 and 2572, depending on the wall distance.

0.85 mm, a weak influence of the wall on the thermochemistry is still observed, the flame seems to be mostly unaffected by heat losses at wall distances of 2 mm and beyond.

3.2.2. Elevated pressure case

The results on the near-wall thermochemistry for the 3 bar case are outlined in Fig. 10 in terms of X_{CO_2}/T, X_{CO}/T and X_{CO}/X_{CO_2} correlations as for the 1 bar case in Section 3.2.1. Scatter plots are shown for five different nominal wall distances ranging from 0.4 mm to 4 mm. At 3 bar pressure, measurements in reactive flows are increasingly affected by beam steering effects. Correspondingly, at decreasing wall distances the laser beams are increasingly deflected resulting in a high proportion of distorted single-shot samples. Furthermore, as the deflected beams occasionally impinge on the quenching wall, the intense broadband radiation emitted during spark formation could potentially cause damage to the CO-LIF, OH-PLIF and DP-CARS detection systems. This behavior impairs the accuracy of the determination of the wall position during reacting conditions as first breakdowns due to laser light impinging on the quenching wall are occasionally observed at rather large wall distances (about 0.45 mm, estimated from the position of the wall determined during non-reacting conditions). By moving the probe volume closer to the wall, the ratio of breakdowns continuously increases and a distinct position where breakdowns abruptly occur can therefore not be identified. The indicated nominal wall distances in the 3 bar case are therefore based solely on the identification of the wall surface position in the non-reacting flow done shortly before the near-wall measurements (according to the procedure described in Section 2.2.4). Accordingly, thermal expansion of the wall at reacting conditions is not accounted for as in the 1 bar case and might result in a systematic error added to the wall distance. In the 1 bar case, for reference, the identified wall surface position is shifted by about 0.05 mm in positive y-direction comparing the non-reacting and the reacting flow. The systematic error related to the wall distance in the 3 bar case is assumed to be of a similar order resulting in a slight overestimation of the wall distance. To avoid damages to the detection systems, measurements at nominal wall distances smaller than 0.4 mm were not carried out for the 3 bar case.

With respect to increasing wall distances, the evolution of the scatter plots shows trends similar to those observed for the 1 bar case. At $y = 0.4$mm the experimental data clearly deviates from the adiabatic simulation as thermochemical states are shifted to lower temperatures. As in the 1 bar case, an average trend of increasing temperature with decreasing $|d_F|$ (i.e., a flame front approaching the probe volume) is

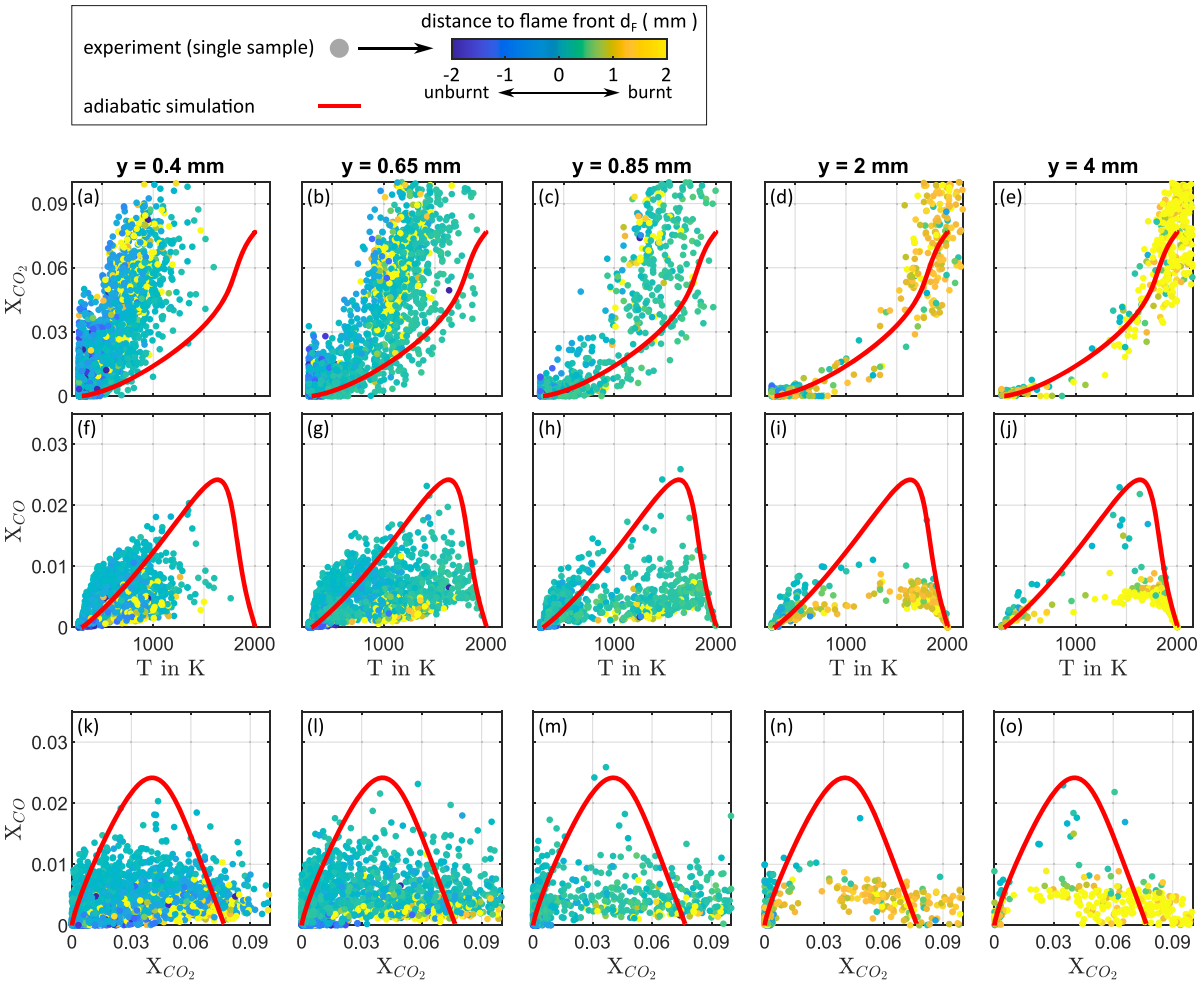

Fig. 10. Thermochemical states of FWI at elevated pressure (3 bar) under turbulent flow conditions at varying wall distances. The data is color-coded with respect to the minimum distance d_F of the probe volume to the instantaneous flame front and presented by means of correlations of X_{CO_2}/T, X_{CO}/T and X_{CO}/X_{CO_2} shown in (a)–(e), (f)–(j) and (k)–(o), respectively. Number of individual samples ranging between 617 and 2837, depending on the wall distance.

observed. This correlation, however, is less distinct for the data at 3 bar shown in Fig. 10. The main reason for this is most likely again an increasing impact of beam steering effects at elevated pressure resulting in an impaired spatial matching of the DP-CARS and OH-PLIF diagnostics, as the DP-CARS/CO-LIF probe volume is stochastically shifted with respect to the OH-PLIF detection. This in turn affects the correlation of T, X_{CO_2} and X_{CO} with d_F even more, as the width of the reaction zone is reduced (see Fig. 5). At lower temperatures, similar to the 1 bar case, thermochemical states featuring increased X_{CO_2} values are observed in Fig. 10(a), which again supports the hypothesis on a convective transport of burnt gas into upstream regions of unburnt gas. With increasing wall distance, these states continuously vanish as the maximum CO_2 mole fraction within this temperature range ($<$ 400 K) decreases. Furthermore, the influence of wall heat losses diminishes since thermochemical states are more and more shifted towards the trace of the adiabatic simulation.

Based on Fig. 10(f), the impact of heat losses on production and formation of CO is also evident as, close to the wall, the majority of thermochemical states is limited to temperatures below 1300 K and CO mole fractions $X_{CO} < 0.015$. Thermochemical states featuring higher X_{CO} occur very rarely in the experimental data and highest values still fall below the peak value of the adiabatic simulation. This could imply that states exhibiting maximum X_{CO} just do not exist at these wall distances as the reaction is quenched due to heat losses. At this point, however, it also needs to be considered that thermochemical states associated with higher X_{CO} might be measured less frequently due to properties of the optical measurement technique and the FWI process itself. This can as well be observed in the X_{CO}/T-state spaces for larger wall distances shown in Fig. 10(g) to (j) as the share of thermochemical states exhibiting increased X_{CO} is still low. On the one hand, this might result from increased beam steering effects at spatial locations of high X_{CO} in the flame which are also characterized by high temperature gradients. On the other hand, it might be just less likely to probe these states in the turbulent flame, comparing the size of the reaction zone (further reduced at elevated pressure, see Fig. 5) with the thickness of the flame brush (see Fig. 7). At larger wall distances, as the total number of experimental samples is reduced, the absolute number of high X_{CO} states would even further decrease. Inhomogeneities of the CO-LIF raw signal in the direction of propagation of the UV beam (z-direction), might also play a non-negligible role. Based on an analysis of the two-dimensional CO-LIF raw data, the coefficient of variance (COV) of the background- and baseline-corrected raw intensity in principal beam direction (z-direction) is shifted towards highest values in the 3 bar case. While at atmospheric pressure the COV is in average about 13.6 %, the corresponding averaged value in the 3 bar case is about 21 %. The 90 %-quantiles of the underlying distributions of the COV are about 27 % and 45 %, at atmospheric and elevated pressure, respectively. These inhomogeneities might be due to increased flame front wrinkling resulting in a higher variation of the flame front orientation at the measurement location. Due to the finite size of the probe volume, the binned CO-LIF signal is reduced, if the flame front is not oriented parallel to the main axis of the probe volume (i.e., the direction of propagation of the UV beam), as in this case a continuous range of thermochemical states is probed. Within the temperature range (1400 K $< T <$ 1800 K) where the occurrence of maximum values of X_{CO} would be expected, the COV is in both operating cases rather small (equivalent with a homogeneous signal). The reason for this could be that an inhomogeneous mixture within the overlapped DP-CARS/CO-LIF probe volume would result in a significant reduction of the temperature measured by the DP-CARS approach due to the dependency of the signal to the number density of the participating molecules squared. At larger wall distances, where the effect of heat losses seems to vanish ($y >$ 2mm), the thermochemical states approach the results of the adiabatic simulation and the number of intermediate states due to turbulent mixing is reduced.

3.2.3. Comparison of both operating cases

For an analysis of possible effects due to increasing pressure on the near-wall thermochemistry, the data presented in Sections 3.2.1 and3.2.2 is further examined with regard to variations between both operating cases in the following. To emphasize differences, thermochemistry data (T&X_{CO_2}) of both cases is combined in Fig. 11 by means of conditional averages. Temperatures and CO_2 mole fractions are therefore averaged within bins of $\Delta X_{CO_2} = 0.01$ width. Fig. 11(a) shows conditionally averaged thermochemical states for wall distances smaller than 1 mm. Thermochemistry data at larger wall distances (2 mm & 4 mm) is depicted in Fig. 11(b). For similar nominal wall distances the same symbol is used for thermochemistry data of both operating cases. The trace of the adiabatic simulation for both operating conditions is shown for reference. From the conditionally averaged data in Fig. 11(a) it can be deduced that close to the wall, thermochemical states are more strongly affected by the presence of the wall in the 3 bar case. While the traces of the adiabatic simulations are quite similar, the thermochemical states of the near-wall measurement are in average shifted further towards lower temperatures in the 3 bar case. Comparing for example the thermochemistry of both operating cases at similar nominal wall distances of $y = 0.35$ mm (1 bar) and $y = 0.4$ mm (3 bar), respectively, temperatures are hence clearly reduced in the 3 bar case. Accordingly, conditionally averaged thermochemical states of the 1 bar case at that wall distance ($y = 0.35$ mm), are close to thermochemistry data of the 3 bar case recorded at $y = 0.65$ mm, i.e. a larger wall distance. Comparing the estimated systematic error of the wall distance specification at elevated pressure (cf. Section 3.2.2) in the order of -0.05 mm (resulting in a slight overestimation of the wall distance), the trends described above are still valid despite this uncertainty. With increasing wall distance, the differences in the near-wall thermochemistry of both operating cases diminish as the impact of the wall decreases and experimental thermochemical states approach the trace of the adiabatic simulation. Far from the wall, at $y = 2$ mm and $y = 4$ mm (Fig. 11(b)), no influence of wall heat losses on the thermochemistry is observed anymore for either operating condition. Conditionally averaged thermochemical states match the adiabatic simulation and can be primarily attributed to conditions in the fresh or burnt gas.

Fig. 11: Comparison of the near-wall thermochemistry at atmospheric and elevated pressure by means of conditionally averaged (within bins of $\Delta X_{CO_2} = 0.01$) thermochemical states plotted in the X_{CO_2}/T-state space for wall distances $y \leq 0.85$ mm in (a) and $y \geq 2$ mm in (b). Conditional averages are only shown for bins containing at least 30 individual samples.

Regarding correlations of X_{CO} and T, the main difference between both operating cases is the reduced number of thermochemical states featuring peak X_{CO} in the 3 bar case (see Fig. 10(h), for example). Possible reasons for this observation are discussed in Section 3.2.2. Besides that, comparing Figs. 9(f)–(h) and 10(f)–(h), close to the wall, the formation of CO appears to be slightly more impacted by wall heat losses and turbulent mixing effects in the 3 bar case, as thermochemical states deviate slightly more from the trace of the adiabatic simulation towards lower temperatures.

4. Conclusion

In this study quantitative, multi-parameter measurements were conducted in a turbulent side-wall quenching flame at atmospheric and elevated pressure (3 bar, absolute) to investigate the impact of pressure effects on flame-wall interaction (FWI). Gas-phase temperatures as well as CO_2 and CO mole fractions were measured by means of dual-pump coherent anti-Stokes Raman spectroscopy (DP-CARS) and laser-induced fluorescence (LIF) of CO. In addition, the instantaneous location of the flame front was tracked using planar OH-PLIF providing information on the relative position of the CO/DP-CARS probe volume with respect to the location of the reaction zone. Based on the near-wall flame front topology, the individual FWI events were categorized into

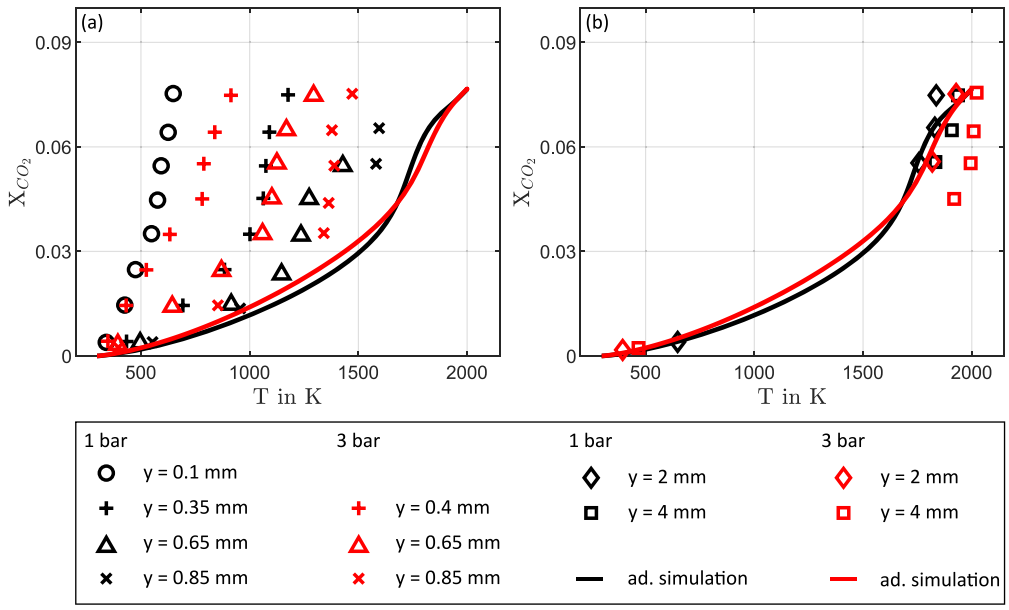

Fig. 11. Comparison of the near-wall thermochemistry at atmospheric and elevated pressure by means of conditionally averaged (within bins of $\Delta X_{CO_2} = 0.01$) thermochemical states plotted in the X_{CO_2}/T-state space for wall distances $y \leq 0.85$ mm in (a) and $y \geq 2$ mm in (b). Conditional averages are only shown for bins containing at least 30 individual samples.

three different quenching scenarios. This analysis showed that for both operating pressures the head-on quenching (HOQ)-like scenario, characterized by one single, extended (in wall-parallel direction) near-wall reaction zone that interacts with the wall, was the predominant quenching scenario associated with about 90 % of all FWI events. Differences in that regard to studies on an unconfined, atmospheric side-wall quenching flame configuration reporting a significantly lower share of HOQ-like scenarios were mainly attributed to the confined burner configuration used within this study. The near-wall thermochemistry was investigated for both operating pressures by means of pairwise correlations of gas-phase temperature, CO_2, and CO mole fraction for varying wall distances. Regarding the measurements under atmospheric conditions, thermochemical states were measured down to a minimum nominal wall distance of 0.1 mm. For this operating pressure, an overall good agreement of the near-wall thermochemistry data presented in this work with results of other studies (carried out in a similar unconfined, atmospheric side-wall quenching flame configuration) was observed. While close to the wall, a significant impact of wall heat losses on thermochemical states was evident, this effect diminished with increasing wall distance. Furthermore, the observation of high CO_2 mole fractions at rather low temperatures measured in the unburnt gas supported the hypothesis (stated in the literature) of hot exhaust gas being cooled down as it is transported in the upstream direction. Beyond that, results of the measurements at 3 bar were shown, representing the first attempt, to the authors' best knowledge, to explore the near-wall thermochemistry during FWI at elevated pressure. As these operating conditions resulted in significantly increased beam steering effects, especially in the vicinity of the wall, where temperature gradients are large, implications on the application of the laser diagnostics and the measurement results were reported. These effects may lead to a reduced spatial matching of the individual laser-diagnostics impairing the overall precision of the measurement. In addition, as the procedure to determine the wall surface position was affected, the reported distance of the probe volume from the wall was associated with an increased uncertainty. Despite these challenging conditions, the evolution of near-wall thermochemistry with increasing wall distance could be analyzed and trends similar to the measurements at atmospheric pressure were observed. At small wall distances, for example, the presence of thermochemical states featuring high CO_2 mole fractions and low temperatures were reported. The comparison of the results with regard to the operating pressure was impaired by the difficulties of the measurement at elevated pressure and differences between both operating cases are moderately pronounced. Considering the uncertainties of the measurements, however, the near-wall thermochemistry appears to be more strongly affected by the presence of the wall at elevated pressure as effects associated with heat losses are intensified due to increased convective transport resulting from enhanced turbulence.

To summarize, the contributions of this study to the research on FWI may be divided into two main aspects. On the one hand, the results provide a first insight into the thermochemistry of FWI at elevated pressure and increased Reynolds numbers, i.e., conditions more relevant to real combustion devices. On the other hand, challenges of near-wall measurements in reactive flows arising with increasing pressure are reported which may be helpful for further studies in this field.

Novelty and significance

Flame-wall interactions (FWI) have been investigated in numerous studies over the last decades. Most of these experiments, however, were carried out at atmospheric pressure and laminar flow conditions and the number of studies providing quantitative information on important state variables, such as temperature and species concentration, are even less. The experiments presented in this manuscript address both of these aspects as gas-phase temperature, CO_2 and CO mole fraction are measured quantitatively and simultaneously in a turbulent side-wall quenching methane/air flame at atmospheric and 3 bar absolute pressure. To the best of our knowledge, these experiments represent the first attempt to explore the thermochemistry of FWI at elevated pressure and turbulent flow conditions.

CRediT authorship contribution statement

Pascal Johe: Conceptualization, Data curation, Writing – original draft, Methodology. **Florian Zentgraf:** Conceptualization, Methodology, Writing – review & editing. **Max Greifenstein:** Conceptualization, Writing – review & editing. **Benjamin Böhm:** Conceptualization, Writing – review & editing. **Andreas Dreizler:** Conceptualization, Data curation, Writing – review & editing.

Declaration of Competing Interest

The authors declare that they have no known competing financial interests or personal relationships that could have appeared to influence the work reported in this paper.

Acknowledgments

This project is funded by the Deutsche Forschungsgemeinschaft (DFG, German Research Foundation) Projektnummer 237267381 TRR 150. The generous financial support is gratefully acknowledged. Andreas Dreizler is grateful for support through the Gottfried Wilhelm Leibniz program.

Supplementary materials

Supplementary material associated with this article can be found, in the online version, at doi:10.1016/j.combustflame.2023.113214.

References

[1] A. Dreizler, B. Böhm, Advanced laser diagnostics for an improved understanding of premixed flame-wall interactions, Proc. Combust. Inst. 35 (2015) 37–64.
[2] B. Boust, J. Sotton, S.A. Labuda, M. Bellenoue, A thermal formulation for single-wall quenching of transient laminar flames, Combust. Flame 149 (2007) 286–294.
[3] Y. Zhang, K.N.C. Bray, B. Rogg, Temporally and spatially resolved investigation of flame propagation and extinction in the vicinity of walls, Combust. Sci. Technol. 113 (1996) 255–271.
[4] C.W. Clendening, W. Shackleford, R. Hilyard, Raman scattering measurements in a side-wall quench layer, Symp. (Int.) Combust. 18 (1981) 1583–1590.
[5] M. Saffman, Parametric studies of a side wall quench layer, Combust. Flame 55 (1984) 141–159.
[6] B. Saggau, Temperature profile measurements at head-on quenched flame fronts in confined CH_4/Air and CH_3OH/Air mixtures, Symp. (Int.) Combust. 20 (1985) 1291–1297.
[7] T. Fuyuto, H. Kronemayer, B. Lewerich, J. Brübach, T. Fujikawa, K. Akihama, T. Dreier, C. Schulz, Temperature and species measurement in a quenching boundary layer on a flat-flame burner, Exp. Fluids 49 (2010) 783–795.
[8] M. Mann, C. Jainski, M. Euler, B. Böhm, A. Dreizler, Transient flame–wall interactions: experimental analysis using spectroscopic temperature and CO concentration measurements, Combust. Flame 161 (2014) 2371–2386.
[9] C. Jainski, M. Rißmann, B. Böhm, J. Janicka, A. Dreizler, Sidewall quenching of atmospheric laminar premixed flames studied by laser-based diagnostics, Combust. Flame 183 (2017) 271–282.
[10] H. Kosaka, F. Zentgraf, A. Scholtissek, L. Bischoff, T. Häber, R. Suntz, B. Albert, C. Hasse, A. Dreizler, Wall heat fluxes and CO formation/oxidation during laminar and turbulent side-wall quenching of methane and DME flames, Int. J. Heat Fluid Flow 70 (2018) 181–192.
[11] F. Zentgraf, P. Johe, A.D. Cutler, R.S. Barlow, B. Böhm, A. Dreizler, Classification of flame prehistory and quenching topology in a side-wall quenching burner at low-intensity turbulence by correlating transport effects with CO_2 CO and temperature, Combust. Flame 239 (2022), 111681.
[12] A. Bohlin, C. Jainski, B.D. Patterson, A. Dreizler, C.J. Kliewer, Multiparameter spatio-thermochemical probing of flame–wall interactions advanced with coherent Raman imaging, Proc. Combust. Inst. 36 (2017) 4557–4564.
[13] F. Zentgraf, P. Johe, M. Steinhausen, C. Hasse, M. Greifenstein, A.D. Cutler, R. S. Barlow, A. Dreizler, Detailed assessment of the thermochemistry in a side-wall quenching burner by simultaneous quantitative measurement of CO_2 CO and temperature using laser diagnostics, Combust. Flame 235 (2022), 111707.
[14] L. Wehr, W. Meier, P. Kutne, C. Hassa, Single-pulse 1D laser Raman scattering applied in a gas turbine model combustor at elevated pressure, Proc. Combust. Inst. 31 (2007) 3099–3106.
[15] H. Ax, O. Lammel, R. Lückerath, M. Severin, High-momentum jet flames at elevated pressure, C: statistical distribution of thermochemical states obtained from laser-Raman measurements, J. Eng. Gas Turb. Power 142 (2020) 71011.
[16] M. Greifenstein, A. Dreizler, Influence of effusion cooling air on the thermochemical state of combustion in a pressurized model single sector gas turbine combustor, Combust. Flame 226 (2021) 455–466.
[17] D. Escofet-Martin, A.O. Ojo, N.T. Mecker, M.A. Linne, B. Peterson, Simultaneous 1D hybrid fs/ps rotational CARS, phosphor thermometry, and CH* imaging to study transient near-wall heat transfer processes, Proc. Combust. Inst. 38 (2021) 1579–1587.
[18] A.O. Ojo, D. Escofet-Martin, J. Collins, G. Falconetti, B. Peterson, Experimental investigation of thermal boundary layers and associated heat loss for transient engine-relevant processes using HRCARS and phosphor thermometry, Combust. Flame 233 (2021), 111567.
[19] M. Chauvy, B. Delhom, J. Reveillon, F.-X. Demoulin, Flame/wall interactions: laminar study of unburnt HC formation, Flow Turbul. Combust. 84 (2010) 369–396.
[20] P. Popp, M. Baum, Analysis of wall heat fluxes, reaction mechanisms, and unburnt hydrocarbons during the head-on quenching of a laminar methane flame, Combust. Flame 108 (1997) 327–348.
[21] Z. Wei, H. Liu, Z. Chen, Z. Liu, H. Zhen, Quenching distance, wall heat flux and CO/NO thermochemical states in the wall vicinity of laminar premixed biogas-hydrogen impinging flame, Fuel 307 (2022), 121849.
[22] M. Steinhausen, Y. Luo, S. Popp, C. Strassacker, T. Zirwes, H. Kosaka, F. Zentgraf, U. Maas, A. Sadiki, A. Dreizler, C. Hasse, Numerical investigation of local heat-release rates and thermo-chemical states in side-wall quenching of laminar methane and dimethyl ether flames, Flow Turbul. Combust. 106 (2021) 681–700.
[23] A. Gruber, R. Sankaran, E.R. Hawkes, J.H. Chen, Turbulent flame–wall interaction: a direct numerical simulation study, J. Fluid Mech. 658 (2010) 5–32.
[24] M. Steinhausen, T. Zirwes, F. Ferraro, A. Scholtissek, H. Bockhorn, C. Hasse, Flame-vortex interaction during turbulent side-wall quenching and its implications for flamelet manifolds, Proc. Combust. Inst. 39 (2023) 2149–2158.
[25] B. Jiang, D. Brouzet, M. Talei, R.L. Gordon, Q. Cazeres, B. Cuenot, Turbulent flame-wall interactions for flames diluted by hot combustion products, Combust. Flame 230 (2021), 111432.
[26] K. Niemietz, L. Berger, M. Huth, A. Attili, H. Pitsch, Direct numerical simulation of flame-wall interaction at gas turbine relevant conditions, Proc. Combust. Inst. 39 (2023) 2209–2218.
[27] R. Palulli, D. Brouzet, M. Talei, R. Gordon, A comparative study of flame-wall interaction and flame-cooling air interaction, Int. J. Heat Fluid Flow 92 (2021), 108888.
[28] C. Hasse, M. Bollig, N. Peters, H.A. Dwyer, Quenching of laminar iso-octane flames at cold walls, Combust. Flame 122 (2000) 117–129.
[29] C.K. Westbrook, A.A. Adamczyk, G.A. Lavoie, A numerical study of laminar flame wall quenching, Combust. Flame 40 (1981) 81–99.
[30] P. Johe, F. Zentgraf, M. Greifenstein, M. Steinhausen, C. Hasse, A. Dreizler, Characterization of flow field and combustion dynamics in a novel pressurized side-wall quenching burner using high-speed PIV/OH-PLIF measurements, Int. J. Heat Fluid Flow 94 (2022), 108921.
[31] P. Johe, F. Zentgraf, M. Greifenstein, R.S. Barlow, A. Dreizler, Laser-based investigation of flame surface density and mean reaction rate during flame-wall interaction at elevated pressure, Proc. Combust. Inst. 39 (2022) 2159–2168.
[32] D.G. Goodwin, R.L. Speth, H.K. Moffat, B.W. Weber, Cantera: an object-oriented software toolkit for chemical kinetics, thermodynamics, and transport processes: version 2.1.0. 10.5281/zenodo.170284, 2021, http://www.cantera.org.
[33] G. Smith, D. Golden, M. Frenklach, N. Moriarty, B. Eiteneer, M. Goldenberg, C. Bowman, R. Hanson, S. Song, W. Gardiner Jr., et al., GRI-mech 3.0, 2011, http://www.me.berkeley.edu/grimech.
[34] P. Ewart, A modeless, variable bandwidth, tunable laser, Opt. Commun. 55 (1985) 124–126.
[35] A.D. Cutler, E.C.A. Gallo, L.M.L. Cantu, WIDECARS spectra fitting in a premixed ethylene-air flame, J. Raman Spectrosc. 47 (2016) 416–424.
[36] O. Carrivain, Etude De La Spectroscopie LIF à Deux Photons De La Molécule CO Pour Des Mesures En Flammes à Haute Pression, Ph.D. Thesis, Universite Pierre et Marie Curie, 2015.
[37] T.B. Settersten, A. Dreizler, R.L. Farrow, Temperature- and species-dependent quenching of CO B probed by two-photon laser-induced fluorescence using a picosecond laser, J. Chem. Phys 117 (2002) 3173–3179.
[38] L. Voigt, J. Heinze, M. Korkmaz, K.P. Geigle, C. Willert, Planar measurements of CO concentrations in flames at atmospheric and elevated pressure by laser-induced fluorescence, Appl. Phys. B 125 (2019), https://doi.org/10.1007/s00340-019-7181-4.
[39] A.P. Nefedov, V.A. Sinel'shchikov, A.D. Usachev, A.V. Zobnin, Photochemical effect in two-photon laser-induced fluorescence detection of carbon monoxide in hydrocarbon flames, Appl. Opt. 37 (1998) 7729–7736.
[40] K. Dabov, A. Foi, V. Katkovnik, K. Egiazarian, E.R. Dougherty, J.T. Astola, K. O. Egiazarian, N.M. Nasrabadi, S.A. Rizvi, Image denoising with block-matching and 3D filtering, in: Proceedings of the Image Processing: Algorithms and Systems, Neural Networks, and Machine Learning, SPIE, 2006, 606414.
[41] J. Canny, A computational approach to edge detection, IEEE Trans. Pattern Anal. (1986) 679–698. PAMI-8.
[42] T. Poinsot, D. Veynante, Theoretical and Numerical Combustion, RT Edwards, Inc., 2005.
[43] J. de Vries, W.B. Lowry, Z. Serinyel, H.J. Curran, E.L. Petersen, Laminar flame speed measurements of dimethyl ether in air at pressures up to 10atm, Fuel 90 (2011) 331–338.